Measurements of the Standard Model Higgs boson in the WW decay mode with the ATLAS detector



Hayden Alexander Smith
St. Cross College
University of Oxford

A thesis submitted for the degree of
Doctor of Philosophy

Trinity 2022

Abstract

The discovery of a Standard Model-like Higgs boson in July 2012 signalled the beginning of a new realm of high energy physics research at the CERN Large Hadron Collider. The decade since has involved studying this new particle in several final states and in challenging kinematic regimes. Measurements are performed with increasing precision, which help to understand the Higgs boson and its role within the Standard Model of particle physics, narrowing down the possible existence of new physical phenomena.

This thesis presents measurements of the Standard Model Higgs boson production cross sections through gluon-gluon fusion and vector-boson fusion using the $H \to WW^*$ decay mode. The measurements are performed with a data set collected from proton-proton collisions occurring at $\sqrt{s} = 13$ TeV by the ATLAS detector during Run 2 of the Large Hadron Collider (2015–2018), corresponding to an integrated luminosity of 139 fb^{-1}. Given the size of the Run 2 data set, the measurements are extended to measure production cross sections of the Higgs boson in distinct kinematic fiducial regions using the Simplified Template Cross Section framework. Good agreement with the predictions of the Standard Model are observed within the uncertainty of the measurements.

Acknowledgements

Reflecting on the past twenty years of education I am privileged to have received, I realise the magnitude of people who have supported and inspired me is too long to list concisely. So I thank all of the school teachers, friends, family, and others, that I have been fortunate enough to have known and learnt from, without whom I would not be the person I am today. Nevertheless, I give particular gratitude to those who have formed a core part of my doctoral experience.

Firstly, thank you to my supervisor, Chris Hays. I was quickly bought up to speed with $H \to WW^*$ when I started in Oxford, and given the academic freedom to pursue this research for the course of my doctorate, for which I am grateful. I am also grateful for your attention to detail in reviewing my research over the years, always ensuring that I was producing results to a high standard.

Thank you to the *HWW couplings analysis* team: in particular to Federica Pasquali, Robin Hayes, Benjamin Jäger, Konstantin Lehmann, and Tae Hyoun Park, as well as our convenors and analysis contacts: Kristin Lohwasser, Yun-Ju Lu, David Shope, and Benedict Winter. I am thankful for all of the ever-friendly, intense, and enjoyable physics discussions (always across multiple timezones), and the unending support for each other that helped us to get through the approval process of this analysis. I learnt a lot from each one of you and it was a pleasure to have collaborated with you all.

In the Oxford ATLAS group and beyond, I have been lucky enough to cross paths (often only fleetingly) with some superb people over the course of my doctorate. In particular, thank you to James Grundy and Luke Scantlebury-Smead: our weekly wine and cheese evenings in Geneva were always a highlight. Thank you to Chris Pollard, for providing feedback on this thesis and for the supervision of my qualification task. And to my housemate, Maria Mironova: thank you for the brilliant friendship, support, and memorable times. I am sure that discussing each of our fit results whilst watching one our favourite musicals is an experience that will not be replicated any time soon.

Thank you to Sue Geddes, Jennifer Matthews, and Kim Proudfoot for always helping me with administration-matters throughout my doctorate so promptly (even when I was not).

And thank you to the Science and Technology Facilities Council for financially supporting me for the duration of my doctorate.

My time in particle physics began during my undergraduate under the supervision of Veronique Boisvert and Tracey Berry. I thank them for their invaluable guidance in my early days and preparing me for doctoral research. I also thank Jordan Palmer, without whose enduring friendship (and regular reminders to revise) would have made my undergraduate days significantly harder.

Lastly, thank you to my family: my parents, Caroline and Nick; my sister, Abi; my grandmother, Sandra; and my late-grandfather, John. You have always believed in me, even when I have not believed in myself, and unconditionally loved and supported me in life and my education. I dedicate this thesis to Grandad. He was always so interested and proud to hear about my research. I am sure he would have delighted in reading this.

H. A. Smith
June 2022

Preface

Modern particle physics research is only possible due to the collaborative efforts of many thousands of scientists worldwide. The measurements presented in this thesis are one such example of the joint effort of a number of individuals who form the ATLAS Collaboration at the CERN Large Hadron Collider (LHC). Chapters 2 and 3 provide an overview of the theoretical and experimental background that are necessary to perform the measurements presented in this thesis. Results obtained by others are clearly indicated as such. Chapters 4–7 provide a detailed description of the published $H\to WW^*$ measurements and my original work therein. Results and illustrations that are not referenced are produced by myself, or if labelled *ATLAS*, are produced by myself in collaboration with others. My contributions to the ATLAS collaboration during my doctorate are summarised below.

Measurement of the Higgs boson in the $H\to WW^*$ decay mode
The main focus of my doctoral research was contributing to the measurement of the gluon-gluon fusion (ggF) and vector-boson fusion (VBF) production cross sections of the Higgs boson in the $H\to WW^*$ decay mode. This research used the full Run 2 data set of proton-proton collisions produced at $\sqrt{s} = 13$ TeV during the years 2015–2018, corresponding to 139 fb^{-1} of integrated luminosity. I was one of the main analysers of these measurements and, in particular, introduced and focused on the measurement of ggF production of the Higgs boson in association with high jet multiplicity (the so-called ggF-enriched $N_{\text{jet}} \geq 2$ category). Events of this type of topology were previously included in measurements of the Higgs boson in the $H\to WW^*$ decay mode that utilised the data set collected by the ATLAS detector during Run 1 (2009–2013) of the LHC, operating at $\sqrt{s} = 7$–8 TeV and corresponding to ∼20 fb^{-1} of integrated luminosity, but had not been studied with the full Run 2 data set. Additionally, the data analysis in this thesis is extended such that measurements of Higgs boson production cross sections are performed in distinct kinematic fiducial regions using the Simplified Template Cross Section (STXS) framework. This is the first time that STXS measurements are performed by the ATLAS Collaboration exclusively using the $H\to WW^*$ decay mode. More specifically, my contributions are summarised as follows:

- I designed and studied the set of selection requirements that are used to construct a ggF-enriched $N_{\text{jet}} \geq 2$ category. This also included defining regions of the data set enriched in major background processes which could be used to make a reliable and data-driven estimate of the background yields in the signal region.

- I extended the strategy of the ggF-enriched $N_{\text{jet}} \geq 2$ category such that STXS measurements could be performed.
- I derived the necessary theoretical uncertainties for all important signal and background processes in the ggF-enriched $N_{\text{jet}} \geq 2$ category, including the STXS measurement, and improved the estimate of the $t\bar{t}$ background uncertainties.
- I developed and optimised the statistical analysis of the ggF-enriched $N_{\text{jet}} \geq 2$ category, as well as the statistical analysis of the STXS measurement, including many studies to design an accurate statistical model. In addition to this, I also performed the statistical analysis for a combined measurement using all regions to derive an inclusive measurement of the $H \to WW^*$ signal normalisation using both the ggF and VBF production modes.
- I contributed to the documentation of the analysis and was responsible for many of the figures and tables produced to visualise the results and illustrate the measurement strategy.

My above contributions are incorporated in three publications by the ATLAS Collaboration:

arXiv:2207.00338 [hep-ex]

The measurements presented in this thesis are published in this paper, which is submitted to *Physics Review D*. This publication supersedes the two documents below and includes several small optimisations to the measurements as well as the combined measurement of ggF and VBF production of the Higgs boson, which was performed by myself.

ATLAS-CONF-2021-014

This document was published as a short note for the *Moriond EW* conference in March 2021 and supersedes the document below. The complete set of measurements described in this thesis, including the ggF measurement as well as the STXS measurement, were first presented in this publication.

ATLAS-CONF-2020-045

This short note was published for the *ICHEP2020* conference in July 2020. It reported the first observation of VBF production of a Higgs boson in the $H \to WW^*$ decay mode.

Improvements for the $H \to WW^*$ analysis

In addition to my contributions to the published measurements above, I also studied several potential improvements which could increase the precision of future measurements. I studied the possible addition of same-flavour leptons to the measurements. Events with same-flavour leptons had not been studied by the ATLAS Collaboration in this decay

mode since Run 1 of the LHC, and in particular, had never been studied in the ggF-enriched $N_{\text{jet}} \geq 2$ category. This study shows that same-flavour leptons could increase the precision of measurements of the Higgs boson produced at high transverse momentum. Additionally, I studied the reduction of top quark background in the ggF-enriched $N_{\text{jet}} \geq 2$ category by optimising the rejection of jets which contain b-quarks. These two pieces of work are described in Chapter 8.

Smoothing of flavour tagging efficiency scale factors

During my qualification task to gain authorship of ATLAS publications, I worked on improvements of the heavy-flavour jet tagging calibrations. In particular, I focused on the smoothing of the tagging efficiency scale factors, which are derived to adjust for differences in efficiency measurements in data and Monte Carlo simulation. To this end, I developed a new method for optimising the smoothing parameters automatically to ensure smooth and well-behaved calibration scale factors that are applied to jets in all measurements performed by ATLAS which make use of heavy-flavour jet tagging. This work is described in Appendix A, and is also documented in an ATLAS PUB note, ATL-PHYS-PUB-2020-004, of which I was the primary author.

Contents

1 Introduction 1

2 Theoretical framework 4

2.1 A theory of fundamental particles . . . 5

2.1.1 Particle content of the Standard Model . . . 5

2.1.2 Symmetry . . . 7

2.1.3 Quantum electrodynamics . . . 9

2.1.4 Quantum chromodynamics . . . 10

2.1.5 Electroweak unification . . . 11

2.1.6 Spontaneous symmetry breaking . . . 15

2.1.7 The Brout-Englert-Higgs mechanism . . . 17

2.1.8 The Standard Model of particle physics . . . 18

2.2 Phenomenology of hadron collisions . . . 19

2.2.1 Partonic cross section . . . 20

2.2.2 Parton distribution functions . . . 21

2.2.3 Parton showering . . . 22

2.2.4 Hadronisation . . . 22

2.2.5 Underlying event . . . 22

2.2.6 Pileup . . . 23

2.3 Monte Carlo simulation . . . 23

2.3.1 Event generators . . . 23

2.3.2 Matching and merging . . . 24

2.4 Higgs boson physics at the LHC . . . 25

2.4.1 Production modes . . . 25

2.4.2 Decay modes . . . 26

2.4.3 Signal strengths and cross section measurements . . . 28

2.4.4 Simplified template cross section measurements . . . 31

2.4.5 Status of Higgs boson physics . . . 32

3 The LHC and the ATLAS experiment **37**
3.1 The Large Hadron Collider . . . 37
3.1.1 LHC operation . . . 37
3.1.2 Luminosity . . . 38
3.2 The ATLAS detector . . . 41
3.2.1 Coordinate system . . . 41
3.2.2 Magnet system . . . 43
3.2.3 Inner detector . . . 43
3.2.4 Calorimeters . . . 45
3.2.5 Muon spectrometer . . . 47
3.3 Expected detector performance . . . 48
3.4 Trigger and data acquisition . . . 49
3.5 Event reconstruction . . . 50
3.5.1 Tracks and vertices . . . 51
3.5.2 Electrons . . . 53
3.5.3 Muons . . . 56
3.5.4 Jets . . . 58
3.5.5 Heavy-flavour jet identification . . . 62
3.5.6 Missing transverse momentum . . . 65

4 Analysis strategy **68**
4.1 Overview of analysis . . . 68
4.1.1 Categorisation and measurements . . . 70
4.1.2 Background processes . . . 71
4.1.3 Higgs boson signal characteristics . . . 76
4.2 Data and simulated samples . . . 79
4.2.1 Data samples . . . 79
4.2.2 Simulated samples . . . 79
4.3 Object identification and selection . . . 82
4.3.1 Leptons . . . 82
4.3.2 Jets . . . 83
4.3.3 Missing transverse momentum . . . 84
4.3.4 Overlap removal . . . 84
4.4 Observables . . . 85
4.4.1 Topological observables . . . 85
4.4.2 Background rejection . . . 86
4.4.3 VBF observables . . . 87
4.4.4 STXS observables . . . 89
4.5 Event selection . . . 89
4.5.1 Preselection . . . 90

4.5.2 ggF $N_{\text{jet}} = 0$ . . . 96
4.5.3 ggF $N_{\text{jet}} = 1$ . . . 96
4.5.4 ggF-enriched $N_{\text{jet}} \geq 2$ . . . 96
4.5.5 VBF-enriched $N_{\text{jet}} \geq 2$ . . . 100
4.6 Background estimation . . . 104
4.6.1 Non-resonant WW background . . . 110
4.6.2 Top quark background . . . 114
4.6.3 Z/γ^* background . . . 118
4.6.4 W+jets and QCD multi-jet background . . . 121
4.7 Simplified template cross sections . . . 122
4.7.1 STXS stage 1.2 . . . 122
4.7.2 Reduced STXS stage 1.2 . . . 125
4.7.3 STXS event selection . . . 125
4.7.4 STXS background estimation . . . 127

5 Systematic uncertainties **132**
5.1 Experimental uncertainties . . . 132
5.2 Theoretical uncertainties . . . 136
5.2.1 Sources of theoretical uncertainty . . . 136
5.2.2 Process-specific theoretical uncertainties . . . 139

6 Statistical analysis **144**
6.1 Maximum likelihood estimation . . . 144
6.2 Hypothesis testing . . . 147
6.3 Validation tools . . . 149
6.3.1 Pulls of nuisance parameters . . . 149
6.3.2 Estimates of uncertainties . . . 150
6.3.3 Ranking of uncertainties . . . 150
6.3.4 Asimov data set . . . 151
6.3.5 Validation studies . . . 151

7 Results **155**
7.1 Inclusive measurements . . . 155
7.2 STXS measurement . . . 164

8 Improvements and prospects **169**
8.1 Optimising the b-jet tagging efficiency . . . 169
8.2 Same-flavour leptons . . . 172
8.2.1 Event selection . . . 173
8.2.2 STXS sensitivity . . . 176
8.3 Prospects . . . 177

9 Conclusions **180**

Bibliography **183**

Appendices

A Smoothing of b-jet identification efficiency and mistag rate scale factors **195**
A.1 Local polynomial kernel regression 196
A.2 Bandwidth optimisation 197
A.3 Results for b-jets 200

B Invariant mass reconstruction of a τ-lepton pair **202**

1
Introduction

The 4th July 2012 is an historic date in humankind's understanding of the universe it resides in. This was the date that the observation of a new particle was announced to the world by the ATLAS [1] and CMS [2] Collaborations. The particle that was discovered had been theorised in the 1960s. At that time, the Standard Model (SM) of particle physics, a collection of mathematical equations and relations that describe the interactions and dynamics of fundamental particles, was coming together. However, an important missing piece of the SM was the mechanism through which fundamental particles acquire a non-zero mass. The theories that formed the SM were mathematically forbidden from allowing particles to have a mass, a consequence which contradicted experimental fact. For example, the existence of atoms would not be possible if the electron was massless. This mathematical quandary was solved with the development of the Brout-Englert-Higgs (BEH) mechanism, which introduced the necessary mathematics to incorporate massive particles into the SM. Out of the mathematics emerged a new particle, which has since come to be known as the Higgs boson. It is the BEH mechanism which gives fundamental particles their mass, and interactions with the Higgs boson are predicted to occur with a strength proportional to the particle mass; an entirely new kind of force of nature.

Since its formulation, the SM has enjoyed remarkable success in accurately describing physical phenomena that have been measured experimentally. The predicted existence of the SM Higgs boson, however, went experimentally undetected for decades. After the discovery of the tau neutrino in 2000, the Higgs boson became the last undiscovered particle in the SM, and as such, its discovery drove the physics programme of the CERN laboratory, in Geneva, Switzerland. The Large Hadron Collider (LHC) was constructed to collide beams of protons together at unprecedented energies, the outcomes of which would be measured and recorded by state-of-the-art particle detectors, developed and maintained by the largest scientific collaborations in the world. Only after all of this decades of work was an SM-like Higgs boson finally detected experimentally, with a mass of $\sim$$125$ GeV.

In the decade since its discovery, a new realm of high energy physics research has begun at the LHC, and the Higgs boson has been studied in great detail by the ATLAS and CMS Collaborations. Far from concluding that high energy physics research is complete, the two collaborations have devoted the past decade to validating that the measured properties of the newly discovered particle are consistent with the predictions of the SM. This is not only to increase confidence that the observed particle is indeed the particle predicted by the SM, but also because the SM is far from a theory that is able to describe all fundamental physics phenomena. Most obvious is the inability of the SM to describe the force of gravity, the asymmetry in the amount of matter and anti-matter in the universe, and the existence of dark matter (which comprises a significant fraction of the energy density of the universe). Additionally, several recent experimental measurements have shown tension with the corresponding SM predictions, including measurements of lepton flavour universality at LHCb [3] and the measurement of $g-2$ at Fermilab [4]. These aspects of high energy physics have also driven the physics programme of the experiments at the LHC, with many searches looking for signs of new particles in the data that are not described by the current SM. In regard to the Higgs boson, measuring the properties of a newly discovered particle is an ideal starting point for probing effects from new physics phenomena. As such, measurements of the Higgs boson performed by the ATLAS and CMS Collaborations have included verifying that it is produced in the proton collisions at the rate predicted by the SM, that it decays at the rate predicted by the SM, and that other properties, such as its spin, are consistent with the SM prediction. The collection of ten years of measurements of the Higgs boson suggest that it is indeed the Higgs boson of the SM; no deviations from the SM have yet been observed. Nevertheless, with the increasing size of the data set available for measurements produced during each run of LHC operations, and aided by advanced techniques in data analysis, measurements of the Higgs boson are reaching an unprecedented precision. This means that the effect of new physics phenomena can be strongly constrained by improvements in the ability of measurements to probe currently unexplored regions of the collected data.

This thesis presents measurements of the SM Higgs boson in its decay to a pair of W bosons, as observed with the ATLAS detector. The $H\to WW^*$ decay mode occurs with the second largest probability of about 21%. At the time of its discovery and despite its observation in several decay modes, measurements of the Higgs boson using the $H\to WW^*$ decay mode were the most precise [5, 6]. The measurements presented in this thesis represent the latest endeavour to measure the production of a Higgs boson and subsequent $H\to WW^*$ decay, which uses a data set collected during the years 2015 through 2018 from proton-proton (pp) collisions occurring at a centre-of-mass energy of $\sqrt{s} = 13$ TeV, corresponding to an integrated luminosity of 139 fb^{-1} (the full LHC Run 2 data set).

With respect to the previous measurement of Higgs boson production using the $H \to WW^*$ decay mode [7] that was performed using a data set collected during the years 2015 and 2016, several improvements and additions are incorporated into the analysis strategy to improve the precision of the measurements presented in this thesis. These include the use of advanced analysis techniques, such as multivariate analysis, to enhance the Higgs boson signal event yield, and the inclusion of events which are produced in association with high jet multiplicities. In addition to performing an inclusive measurement of Higgs boson production rates, measurements of its production rates are measured simultaneously in distinct kinematic fiducial regions that directly probes effects from possible new physics phenomena, particularly at high transverse momentum, using the Simplified Template Cross Section (STXS) framework. This is the first time that STXS measurements are performed by the ATLAS Collaboration exclusively using the $H \to WW^*$ decay mode.

This thesis is structured as follows. Chapter 2 outlines the theoretical language of the SM, the predictive tools that are necessary to understand the Higgs boson in pp collisions at the LHC, the expected properties of the Higgs boson and measurement strategies at colliders like the LHC, and a summary of the status of current measurements of the Higgs boson. The experimental apparatus of the LHC and ATLAS detector, as well as the methods that are used to reconstruct particles originating from the high energy pp collisions, are described in Chapter 3. Chapter 4 summarises the general strategy of the measurements presented in this thesis, including the selection of $H \to WW^*$ events and the estimation of important SM processes contaminating the selected event yields. Chapters 5 and 6 discuss the sources of systematic uncertainty in the measurements and the statistical analysis that is performed to infer meaningful information about the SM and extract the results of the measurements, reported in Chapter 7. Finally, two possible improvements to the analysis strategy are briefly discussed in Chapter 8 and prospects for future measurements are outlined. Concluding remarks are given in Chapter 9.

2

Theoretical framework

A theoretical framework is required to make measurements of and to infer knowledge about the fundamental structures from which the universe is built. The collection of theories which aim to describe sub-atomic particles and their interactions are collectively called the *Standard Model of Particle Physics* (SM). The SM represents the progression of knowledge over the course of decades, combining developments from theory as well as experimental measurements. It is therefore able to describe, with a remarkable precision, a wide range of physical phenomena that characterise the very fabric of the universe.

A crucial question of the SM, for which the proposed solution lacked experimental verification for 50 years, is the origin of non-zero particle masses. Despite the experimental observations that fundamental particles were massive, symmetries in the SM forbid a theoretical construction in which this was the case. Theorised in the 1960s, the Brout-Englert-Higgs (BEH) mechanism provided an elegant solution to this problem through the process of electroweak symmetry breaking. This mechanism predicted the existence of an entirely new particle, called the *Higgs boson*, that interacts with other particles of the SM in a way unlike that of any of the other known interactions. The search for the Higgs boson was the primary goal of the physics programme of CERN entering the 21st century, and drove the construction and design of the LHC and its associated detectors, particularly ATLAS and CMS.

A general overview of the SM, including its particle content, the interactions which govern it, and the BEH mechanism, is provided in Section 2.1. The theoretical basis of hadron collisions and the tools used to simulate such collisions are described in Sections 2.2 and 2.3. Finally, a summary of the expected behaviour of the SM Higgs boson at the LHC, its measured properties to date, and a description of the type of measurements of the Higgs boson performed in this thesis, are presented in Section 2.4.

2.1 A theory of fundamental particles

The SM is a self-consistent and predictive relativistic quantum field theory that provides a unified description of the kinematics of sub-atomic particles[1] and their interactions with three fundamental forces of nature: strong, weak, and electromagnetic [8–11]. Specifically, the SM is formulated using the mathematical language of group theory, and can be described as a non-abelian gauge quantum field theory which follows the $\mathrm{SU(3)_C} \otimes \mathrm{SU(2)_L} \otimes \mathrm{U(1)_Y}$ symmetry groups. The force of gravity, despite it being a fundamental force of nature, is not described by the SM and is generally ignored in high energy physics since the force of gravity between particles is significantly smaller than the other forces of nature. The following descriptions are based on Refs. [12–17].

2.1.1 Particle content of the Standard Model

The particle content of the SM is illustrated in Figure 2.1. Generally, particles are defined and characterised by a unique set of quantum numbers which are used to define and construct a coherent framework. First, two broad categories of particles are defined: *fermions* and *bosons*. All matter is comprised of the fermions, which have half-integer spin. Fermions generally have a corresponding anti-particle; a particle which is otherwise identical (i.e. the same mass and spin) but has an opposite electric charge and other quantum numbers. Forces, otherwise interpreted as interactions between particles, are defined by the exchange of a boson, which have integer spin.

Fermions are further categorised into *quarks* (q) and *leptons* (ℓ), which differ in the types of interactions they participate in; quarks are those particles which experience the strong, weak, and electromagnetic forces, whilst leptons only participate in interactions involving the weak and electromagnetic forces. The fermions naturally organise themselves into three generations, or *flavours*, increasing in mass. Second- and third-generation fermions are unstable and eventually decay into first-generation fermions, which are responsible for comprising all known stable matter.

Each generation of quark and lepton is composed of two particles that form a doublet. A lepton doublet comprises an electrically charged particle and an associated electrically neutral particle. The electrically charged leptons are electrons (e), muons (μ), and taus (τ), and their electrically neutral partners are the neutrinos, $\nu_{e,\mu,\tau}$. Since neutrinos are electrically neutral, they only participate in the weak interaction. Leptons possess a quantum number known as the lepton number, which has a value of $+1$. Lepton number is conserved between generations in interactions in the SM.

[1] In this context, *sub-atomic* refers to particles which are fundamental and point-like with no internal structure, in the sense that they are not composite particles of smaller, more elementary particles. Sub-atomic particles are simply referred to as particles in this thesis.

Quarks have an electric charge which is a signed fraction of the electron charge. A quark doublet comprises an up-type quark with $+2/3$ electric charge, and a down-type quark with a $-1/3$ electric charge. The up-type quarks include the up (u), charm (c), and top quarks (t), whilst the down-type quarks include the down (d), strange (s), and bottom (b) quarks. Since quarks also interact through the strong force, they each carry a charge under this interaction: *colour*. Colour charge exists in three flavours: red (R), green (G), and blue (B). Leptons do not carry colour charge. It is experimentally evident that particles with non-zero colour charge are not observed in nature; all observed particles are colour-singlets. The phenomenon of *colour confinement* describes this process and means that quarks are not observed as free particles. Instead, quarks form composite particles called *hadrons*. Hadrons are categorised into *mesons*, which contain a quark and anti-quark of the same colour charge, and *baryons*, which are bound states of three quarks. Baryon number is a quantity which is conserved in the SM, and has a value of $+1$ for baryons, so that quarks have a baryon number of $+1/3$.

The interactions of fermions through the strong, weak, and electromagnetic forces, is defined by the exchange of a spin-1 gauge boson[2]. There are several gauge bosons in the SM with spin-1, which include the photon (γ), gluon (g), Z boson, and $W^{\pm}$ boson. The photon is massless, electrically neutral, and responsible for mediating electromagnetic interactions, the force describing the interactions between electrons and atomic nuclei. Electromagnetic interactions are described by the theory called *quantum electrodyamics*. The gluon is also massless and electrically neutral, and is responsible for mediating the strong force between quarks. The strong force is described by the theory called *quantum chromodynmamics*. The Z and $W^{\pm}$ bosons are the massive gauge bosons responsible for mediating the weak force. All fermions possess a weak charge and can participate in the weak interaction. The Z boson mediates *neutral current* interactions, which conserve flavour and electric charge. The $W^{\pm}$ bosons mediate *charged current* interactions taking place between particles within a fermion doublet which changes the electric charge by one unit. The $W^{\pm}$ boson, having a non-zero electric charge, is also able to interact with the photon and take part in electromagnetic interactions. The weak and electromagnetic forces originate from one theory in the SM, called the *electroweak* theory. The gluon possesses colour charge, whilst the $W^{\pm}$ bosons possess weak charge. These charged force-carriers are a consequence of the non-abelian nature of the description of these forces, meaning they can interact with each other, unlike the electrically neutral photon. In particular, eight gluons are realised in nature, each with a colour+anti-colour charge.

Finally, the Higgs boson is the only known fundamental spin-0 (scalar) boson. Interactions

[2]Gauge bosons are so-called because the description of forces in the SM is based on the concept of gauge invariance.

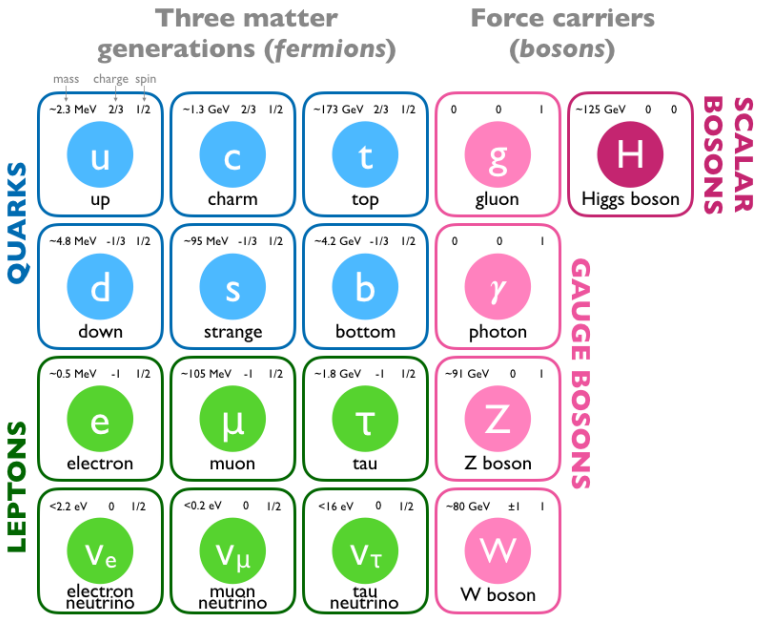

Figure 2.1: Summary of the fundamental particle content of the Standard Model of particle physics, including the mass, electric charge, and spin of the particles. The particles are grouped into three generations of fermions and five gauge bosons.

of particles with a Higgs boson are what allows particles to acquire a non-zero mass. The Higgs boson also has the ability to interact with itself.

The constituent particles of the SM arise from *fields*, with local excitations of a field corresponding to their interpretation as a particle. The dynamics of the SM are thus encoded in a Lagrangian density function.

2.1.2 Symmetry

The dynamics of a physical system are defined by the relation of energy, E, and momentum, $\mathbf{p}$, of a particle. Classically[3], this relation is given by $E = \mathbf{p}^2/2m$, where m is the particle mass. In a quantum but non-relativistic regime, this relation is given by the Schrödinger equation:

$$-\frac{\boldsymbol{\nabla}^2}{2m}\psi = i\partial_t\psi, \tag{2.1}$$

where energy and momentum are replaced by the operators $i\partial_t$ and $-i\boldsymbol{\nabla}$, respectively. In the quantum regime, the system is described by a wavefunction, ψ.

The relativistic equivalent of the energy-momentum relation in the quantum regime is called a quantum field theory (QFT). In a QFT, the constituent particles of the SM are

[3]That is to say in a non-quantum and non-relativistic regime.

described by the local excitation of a field, ϕ. The energy-momentum relation of a field in a QFT is given by the *Klein-Gordon equation*:

$$(\partial^\mu \partial_\mu + m^2)\phi = 0, \tag{2.2}$$

where energy and momentum are the components of a four-vector, p_μ, which is defined by the operator $i\partial_\mu = i\frac{\partial}{\partial x^\mu}$. The process of defining a consistent energy-momentum relation in these different regimes is called quantisation.

The description of the system using fields means that the dynamics of SM particles can be encoded in a *Lagrangian density*, $\mathcal{L}$. The Lagrangian density (also known simply as the Lagrangian) is a function of the fields and their partial derivatives with respect to space-time, $\mathcal{L}(x) = \mathcal{L}(\phi, \partial_\mu \phi)$. The integral of the Lagrangian over all space-time is called the *action*, defined by

$$S = \int \mathrm{d}^4 x \mathcal{L}(\phi, \partial_\mu \phi), \tag{2.3}$$

which gives rise to the equations of motion of a system using the principle of least action. This formulation is similar to classical Euler-Lagrange mechanics. The equations of motion are given by

$$\partial_\mu \left(\frac{\partial \mathcal{L}}{\partial(\partial_\mu \phi)} \right) - \frac{\partial \mathcal{L}}{\partial \phi} = 0. \tag{2.4}$$

Symmetries of the Lagrangian are the basis of the structure of the SM. In this context, a symmetry is a transformation, or group of transformations, on the fields in the system which does not change the Lagrangian (i.e. it is invariant). Symmetries of this type are called *gauge transformations* and can be global or local in nature. A global symmetry is one which is applied to a field at all points in space-time; local symmetries are those transformations which depend on the particular space-time point.

A consequence of symmetries in a Lagrangian is Noether's theorem [18]. Simply put, Noether's theorem states that a continuous symmetry transformation for a field will correspond to a conserved quantity in the system (i.e. that this quantity is time-independent). This means that a conservation law originates from a symmetry that exists in nature. Common examples of this include the conservation of energy which originates from invariance of the Lagrangian with respect to translations in time. Mathematically, a conserved current exists, $\partial_\mu J^\mu = 0$, where $J^\mu = \frac{\partial \mathcal{L}}{\partial(\partial_\mu \phi)} \delta\phi$. The conserved quantity, or *charge*, is given by

$$Q = \int \mathrm{d}^3 x J^0, \tag{2.5}$$

where J^0 is the zeroth component of J^μ.

The SM is constructed from a Lagrangian which is invariant under local transformations of the $\mathrm{SU(3)_C} \otimes \mathrm{SU(2)_L} \otimes \mathrm{U(1)_Y}$ symmetry group. The first part describes QCD, with the subscript *C* indicating that colour charge is the conserved quantity. The $\mathrm{SU(2)_L} \otimes \mathrm{U(1)_Y}$ part refers to the unification of the weak and electromagnetic interactions, where the subscript *L* refers to the conserved quantities of weak hypercharge (y) and weak isospin (T), which act on left-handed fields.

2.1.3 Quantum electrodynamics

The Klein-Gordon equation of motion in Eq. 2.2 describes spin-0 particles, since the solutions are given by scalar-valued fields, ϕ. A Lagrangian describing spin-$\frac{1}{2}$ particles, $\psi(x)$, is given by

$$\bar{\psi}(x)(i\gamma^\mu\partial_\mu - m)\psi(x). \tag{2.6}$$

In this construction, γ^μ are the Dirac matrices which require $\psi(x)$ to have some dimensionality, and are called *spinor fields*. The quantity $\bar{\psi}(x)$ $(= \psi(x)^\dagger\gamma^0)$ describes anti-fermions. The Dirac matrices satisfy an anti-commutation relation of $\{\gamma^\mu, \gamma^\nu\} = \gamma^\mu\gamma^\nu + \gamma^\nu\gamma^\mu = 2g^{\mu\nu}$, where $g^{\mu\nu}$ is the metric tensor. The Euler-Lagrange equations result in the *Dirac equation*, given by

$$(i\gamma^\mu\partial_\mu - m)\psi(x) = 0, \tag{2.7}$$

which describes the motion of a fermion. The Dirac Lagrangian is invariant under a global gauge transformation $\psi \to e^{iq\theta}\psi$. Here, θ is a real-valued constant and q is called the *generator* of the symmetry group that contains the gauge transformation. In this case, the symmetry group is called U(1) because q is a real-valued constant. If the gauge transformation were space-time dependent, i.e. $\psi \to e^{iq\theta(x)}\psi$, the Lagrangian would no longer be invariant. However, invariance can be restored by replacing the derivative, ∂_μ, by the covariant derivative, D_μ, which itself transforms under the local gauge transformation to cancel terms which break the invariance. This is achieved by defining the covariant derivative as

$$D_\mu \equiv \partial_\mu + iqA_\mu(x), \tag{2.8}$$

where a new field, $A_\mu(x)$, is introduced that is required to transform as $A_\mu \to A_\mu - \frac{1}{q}\partial_\mu\theta(x)$. The requirement of local gauge invariance introduces a new term:

$$-q\bar{\psi}(x)\gamma^\mu A_\mu(x)\psi(x), \tag{2.9}$$

which describes an interaction of the fields ψ and A_μ which occurs with a strength proportional to the charge, q. This interaction strength is typically called a *coupling strength*. In this case, the interaction term describes the electromagnetic interaction of a

fermion with electric charge q interacting with a photon, described by the field $A_\mu(x)$.

As a corollary, the Lagrangian of a spin-1 field like $A_\mu(x)$ is given by the *Proca Lagrangian*:

$$\mathcal{L}_{\text{Proca}} = -\frac{1}{16\pi}F^{\mu\nu}F_{\mu\nu} + \frac{1}{8\pi}m_A^2 A^\mu A_\mu, \tag{2.10}$$

where $F_{\mu\nu} = \partial_\mu A_\nu - \partial_\nu A_\mu$. The mass term, given by $\frac{1}{8\pi}m_A^2 A^\mu A_\mu$, is not invariant under the local U(1) gauge transformation, meaning the photon mass must be zero in order to preserve the $\mathrm{U}(1)$ gauge symmetry.

2.1.4 Quantum chromodynamics

The symmetry transformations which leave the QCD Lagrangian invariant are those of the $\mathrm{SU}(3)_\mathrm{C}$ group, where the subscript *C* indicates colour charge (the charge responsible for the interactions between gluons and quarks). The dynamics of a free quark are described by a Lagrangian given by

$$\sum_f \bar{q}_f(i\gamma^\mu\partial_\mu - m_f)q_f, \tag{2.11}$$

where $q_f = (q_f^R, q_f^G, q_f^B)^\mathrm{T}$ and $\bar{q}_f = (\bar{q}_f^{\bar{R}}, \bar{q}_f^{\bar{G}}, \bar{q}_f^{\bar{B}})$ define quark colour triplets. The quark flavour is denoted by f and runs from 1 to 6. Global transformations of this Lagrangian under the $\mathrm{SU}(3)_\mathrm{C}$ symmetry group leave it invariant, where the transformations take the form

$$q(x) \to Uq(x) = e^{i\frac{\lambda_a}{2}\theta_a}q(x). \tag{2.12}$$

The transformations, U, are 3×3 unitary matrices with a determinant of one. A particular representation of these matrices, the so-called fundamental representation, is given by the generators of the $\mathrm{SU}(3)$ group, $\frac{\lambda_a}{2}$, with $a = 1, \ldots, 8$. These matrices are the Gell-Mann matrices, which have zero trace and have a commutation relation given by

$$[\lambda_a, \lambda_b] = if_{abc}\lambda_c, \tag{2.13}$$

where f_{abc} are the totally anti-symmetric *structure functions* of $\mathrm{SU}(3)$. The fact that the $\mathrm{SU}(3)$ generators do not commute makes QCD non-abelian.

In a similar fashion as for QED, the $\mathrm{SU}(3)$ gauge transformation can be local, in which the parameters, θ_a, take on space-time-dependent values. There are eight generators of $\mathrm{SU}(3)$, meaning eight gauge fields must be introduced into the covariant derivative to maintain invariance. The QCD covariant derivative is defined by

$$D_\mu \equiv \partial_\mu + ig_s\frac{\lambda_a}{2}G_\mu^a(x), \tag{2.14}$$

where the gauge fields transform as

$$G_\mu^a \to G_\mu^a - \frac{1}{g_s}\partial_\mu\theta_a - f_{abc}\theta_b G_\mu^c. \tag{2.15}$$

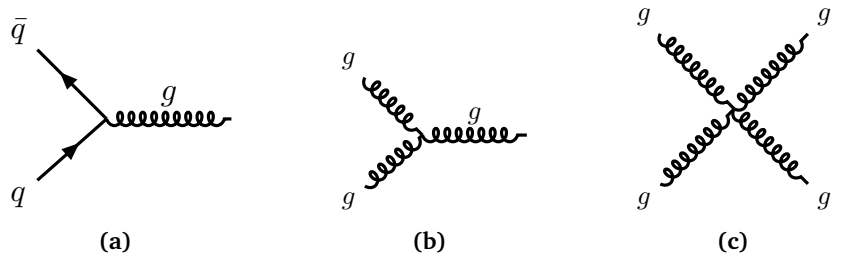

Figure 2.2: Feynman diagrams illustrating QCD interactions between particles which carry colour charge.

The parameter g_s is the strong coupling constant. The gauge-invariant QCD Lagrangian is then given by

$$\mathcal{L}_{\mathrm{QCD}} = \sum_f \bar{q}_f(i\gamma^\mu\partial_\mu - m_f)q_f - g_s\sum_f(\bar{q}_f\gamma^\mu\frac{\lambda_a}{2}q_f)G^a_\mu - \frac{1}{4}G^a_{\mu\nu}G^{\mu\nu}_a, \tag{2.16}$$

where $G^a_{\mu\nu} = \partial_\mu G^a_\nu - \partial_\nu G^a_\mu - g_s f_{abc} G^b_\mu G^c_\mu$ is a gauge-invariant term describing the dynamics of the gluon fields. The interaction term between quarks and gluons is given by the second term. However, unlike in QED, there is a term which describes the self-interaction of the gluon fields, given by the third term in the expression of $G^a_{\mu\nu}$. This self-interaction terms gives rise to interactions involving three and four gluons which are illustrated in Figure 2.2. Similarly to QED, gauge invariance means the gluons must have zero mass.

The self-interaction term of the gluon fields has consequences for the strong force which results in a very different behaviour to QED. The first consequence is *asymptotic freedom*. This phenomenon occurs because of the energy dependence of the strong coupling, g_s[4] (which can also be thought of as a dependence on the distance over which the interaction takes place). At very high energies, or short distances, the strong coupling, $\alpha_{\mathrm{S}} = g_s^2/4\pi$, is very small. This has the effect that quarks and gluons interacting at very high energy behave like free particles. At very low energy, or large distances, the strong coupling is very large. This is the reason for the phenomenon of confinement: at low enough energy, quarks and gluons cease to exist as free particles and instead form composite hadrons.

2.1.5 Electroweak unification

Weak interactions were first observed in nuclear β-decay and muon decay and accurately describe processes up to energies of $\mathcal{O}(1\ \mathrm{TeV})$. Fermi interpreted weak interactions as a point-like interaction, with a coupling strength proportional to the Fermi constant, $G_{\mathrm{F}} = 1.166 \times 10^{-5}\,\mathrm{GeV}^{-2}$ [19]. A more complete description of the weak interactions

[4]Coupling constants in the SM, as well as particle masses, are no longer constant when higher-order effects are incorporated into effective terms in the Lagrangian. In order for calculations in the SM to yield finite predictions, parameters in the SM have to be *renormalised*, which forces coupling constants and masses to depend on the energy scale of an interaction. This concept is discussed further in Section 2.2.1.

involved the introduction of charged vector bosons (the $W^{\pm}$ bosons) to act as mediators of the weak force. These bosons had to be massive, with a mass that scaled like $G_{\rm F} \sim g^2/m_W^2$, where g is the coupling strength of the vector boson, such that the weak interaction strength was suppressed at low energies. However, massive gauge bosons break the invariance of Lagrangians under local gauge transformations. An additional complication in unifying the weak and electromagnetic interactions is that parity violation had been observed in β-decay of cobalt-60 atoms [20]. This meant that only fermions (anti-fermions) with left-handed (right-handed) helicity participate in weak interactions. Helicity refers to the projection of the spin of a fermion onto its direction of motion, where left-handed refers to the case where the the spin and momentum are in the opposite directions, whilst right-handed helicity is where the spin and momentum are in the same direction. The solution was to describe fermion spinors in terms of left- and right-handed components, which are obtained with the application of projection operators:

$$\psi_{\rm L,R}(x) = P_{\rm L,R}\psi(x) = \frac{1}{2}(1 \mp \gamma^5)\psi(x), \tag{2.17}$$

where $\gamma^5 = i\gamma^0\gamma^1\gamma^2\gamma^3$. A Lagrangian involving Dirac spinors is invariant under $\mathrm{SU}(2)$ gauge transformations, but must also be invariant under $\mathrm{U}(1)$ gauge transformations, $\mathrm{SU}(2)_{\rm L} \otimes \mathrm{U}(1)_{\rm Y}$, if the weak and electromagnetic forces are to be unified in one description. The simplest description of a common electroweak interaction involves fermion fields comprising a doublet of left-handed spinor fields, $\psi_1(x) = (u, d)^{\rm T}_{\rm L}$, and singlets of right-handed spinor fields, $\psi_2(x) = u_{\rm R}$ and $\psi_3(x) = d_{\rm R}$. The fields u and d describe the up- and down-type quarks of a single generation. An equivalent formulation is valid for leptons fields, e and ν_e, and other generations. The Lagrangian describing the free motion of fermions is given by

$$\mathcal{L} = \sum_{j=1}^{3} i\bar{\psi}_j(x)\gamma^\mu\partial_\mu\psi_j(x), \tag{2.18}$$

where there is no explicit mass term which would mix up the left- and right-handed fields (breaking the gauge invariance). Transformations of the $\mathrm{U}(1)$ symmetry group are given by phases,

$$\psi(x) \to e^{iy\beta}\psi(x), \tag{2.19}$$

where β are arbitrary constants and y is the *weak hypercharge*[5]. Transformations of $\mathrm{SU}(2)$ act on the left-handed doublets as

$$\psi(x) \to U_{\rm L}\psi(x) = e^{i\frac{\sigma_a}{2}\alpha_a}\psi(x). \tag{2.20}$$

The $U_{\rm L}$ are 2×2 matrices with unit determinant. The generators of $\mathrm{SU}(2)$ are $\sigma_a/2$, with $a = 1, \ldots, 3$, whose fundamental representation is given by the Pauli matrices. These

[5]Note that this is not the same quantity as the electric charge, q, as in QED.

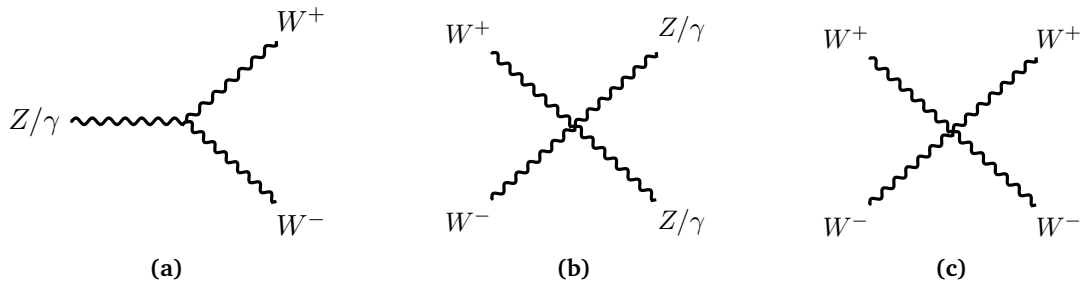

Figure 2.3: Feynman diagrams illustrating electroweak self-interactions between the gauge bosons.

matrices satisfy a commutation relation of $[\sigma_a, \sigma_b] = 2i\epsilon_{abc}\sigma_c$, where ϵ_{abc} is the Levi-Civita symbol. These are the structure constants of $\mathrm{SU}(2)$. Fermion fields then transform as

$$\begin{aligned}\psi_1(x) &\to e^{i\frac{\sigma_a}{2}\alpha_a + iy_1\beta}\psi_1(x),\\ \psi_2(x) &\to e^{iy_2\beta}\psi_2(x),\\ \psi_3(x) &\to e^{iy_3\beta}\psi_3(x).\end{aligned} \tag{2.21}$$

As before, the transformations are required to be local in space-time, such that $\alpha_a = \alpha_a(x)$ and $\beta = \beta(x)$. The partial derivatives are replaced with the covariant derivatives which introduces four gauge fields. Three gauge fields, W^1_μ, W^2_μ, and W^3_μ, represent the gauge fields of the $\mathrm{SU}(2)$ transformation, whilst a single gauge field, $B_\mu(x)$, represents the gauge field of the $\mathrm{U}(1)$ transformation. This leads to covariant derivatives given by

$$\begin{aligned}D_\mu\psi_1(x) &\equiv \left[\partial_\mu + ig'y_1B_\mu(x) + ig\frac{\sigma_a}{2}W^a_\mu(x)\right]\psi_1(x),\\ D_\mu\psi_2(x) &\equiv \left[\partial_\mu + ig'y_2B_\mu(x)\right]\psi_2(x),\\ D_\mu\psi_3(x) &\equiv \left[\partial_\mu + ig'y_3B_\mu(x)\right]\psi_3(x),\end{aligned} \tag{2.22}$$

where g' and g are the coupling strengths corresponding to the $\mathrm{U}(1)$ and $\mathrm{SU}(2)$ transformations, respectively. Kinematic terms of the gauge fields are defined to maintain gauge invariance, and take the form

$$B_{\mu\nu} \equiv \partial_\mu B_\nu - \partial_\nu B_\mu, \tag{2.23}$$

$$W^a_{\mu\nu} \equiv \partial_\mu W^a_\nu - \partial_\nu W^a_\mu - g\epsilon_{abc}W^b_\mu W^c_\mu. \tag{2.24}$$

Similarly to QCD, the non-abelian nature of $\mathrm{SU}(2)$ introduces an interaction term between gauge bosons, illustrated in Figure 2.3. The electroweak Lagrangian is then given by

$$\mathcal{L}_{\text{electroweak}} = \sum_{j=1}^{3} i\bar{\psi}_j(x)\gamma^\mu D_\mu\psi_j(x) - \frac{1}{4}B_{\mu\nu}B^{\mu\nu} - \frac{1}{4}W^a_{\mu\nu}W^{\mu\nu}_a. \tag{2.25}$$

The covariant derivative also introduces two interaction terms between the fermions and gauge bosons:

$$-g\bar{\psi}_1(x)\gamma_\mu\frac{\sigma_a}{2}W_\mu^a\psi_1(x) - g'B_\mu\sum_{j=1}^{3}y_j\bar{\psi}_j(x)\gamma^\mu\psi_j(x). \tag{2.26}$$

The first interaction term gives rise to the so-called charged-current interactions, whilst the second term gives rise to the neutral-current interactions. The gauge-field component of the first term can be written

$$\frac{\sigma_a}{2}W_\mu^a = \frac{1}{2}\begin{pmatrix} W_\mu^3 & \sqrt{2}W_\mu^+ \\ \sqrt{2}W_\mu^- & -W_\mu^3 \end{pmatrix}, \tag{2.27}$$

where $W_\mu^\pm = (W_\mu^1 \mp iW_\mu^2)/\sqrt{2}$. Charged-current interactions occur through interactions of fermions with the $W_\mu^\pm$ fields, which are identified with the physical $W^\pm$ gauge bosons. In the basis of the physical fields, and projecting out the left-handed components of the fermion fields, the Lagrangian of charged-current interactions, $\mathcal{L}_{\mathrm{CC}}$, is written as

$$\mathcal{L}_{\mathrm{CC}} = -\frac{g}{2\sqrt{2}}\{W_\mu^+[\bar{u}\gamma^\mu(1-\gamma^5)d + \bar{\nu}_e\gamma^\mu(1-\gamma^5)e] + \mathrm{h.c.}\}, \tag{2.28}$$

The charged-current interactions have the form $\bar{\psi}\gamma^\mu(1-\gamma^5)\psi$, which is different to the structure of electromagnetic interactions, $\bar{\psi}\gamma^\mu\psi$. Under the transformation of parity (spatial inversion), γ^μ transforms as a vector, i.e. $P(\gamma^\mu) = -\gamma^\mu$. The product, $\gamma^\mu\gamma^5$, transforms as an axial-vector, i.e. $P(\gamma^\mu\gamma^5) = \gamma^\mu\gamma^5$. The structure of the electroweak interactions are thus referred to as V–A, since it combines vector and axial-vector couplings. The introduction of the axial-vector interaction is what causes weak interactions to violate parity. The interaction term for the charged-current is illustrated in Figure 2.4a.

The physical photon field, A_μ, and Z boson field, Z_μ, are obtained through a mixing of the remaining W_μ^3 and B_μ fields:

$$\begin{pmatrix} Z_\mu \\ A_\mu \end{pmatrix} = \begin{pmatrix} \cos\theta_{\mathrm{W}} & -\sin\theta_{\mathrm{W}} \\ \sin\theta_{\mathrm{W}} & \cos\theta_{\mathrm{W}} \end{pmatrix}\begin{pmatrix} W_\mu^3 \\ B_\mu \end{pmatrix}, \tag{2.29}$$

where θ_{W} is known as the *weak mixing angle*, or Weinberg angle. In the basis of the physical fields, and projecting out the left-handed components of the fermion fields, the Lagrangian of neutral-current interactions, $\mathcal{L}_{\mathrm{NC}}$, is written as

$$\mathcal{L}_{\mathrm{NC}} = -\sum_j \bar{\psi}_j\gamma^\mu\left[A_\mu\left(g\frac{\sigma_3}{2}\sin\theta_{\mathrm{W}} + g'y_j\cos\theta_{\mathrm{W}}\right) + Z_\mu\left(g\frac{\sigma_3}{2}\cos\theta_{\mathrm{W}} - g'y_j\cos\theta_{\mathrm{W}}\right)\right]\psi_j. \tag{2.30}$$

In the low energy limit, electromagnetism is described by QED, which means the interaction of fermions with the photon in Eq. 2.9 must equate with the term in Eq. 2.30. This means the following hold:

$$g\sin\theta_{\mathrm{W}} = g'\cos\theta_{\mathrm{W}} = e \quad \text{and} \quad y = Q - T_3, \tag{2.31}$$

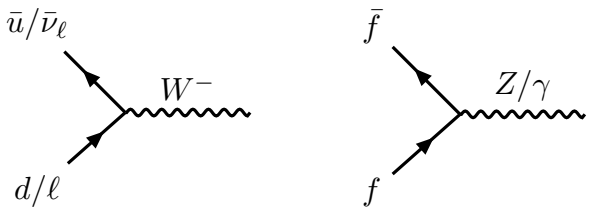

(a) **(b)**

Figure 2.4: Feynman diagrams of the basic electroweak interactions between fermions and the physical $W^\pm$ bosons (charged-current) and the Z boson or photon (neutral-current).

where e is the electric charge, Q is the electromagnetic charge operator, and $T_3 \equiv \sigma_3/2$. The neutral-current Lagrangian comprises an interaction term with the photon and an interaction term with the Z boson. The former term is the usual QED Lagrangian. The remaining terms indicate the interaction of fermions with the Z boson, given by

$$\mathcal{L}_{\mathrm{NC}}^{Z} = -\frac{e}{2\sin\theta_{\mathrm{W}}\cos\theta_{\mathrm{W}}} Z_\mu \sum_f \bar{f}\gamma^\mu (c_V^f - c_A^f \gamma^5) f, \tag{2.32}$$

where f is the fermion spinor field, with summation over all fermions, and c_V and c_A are the vector and axial-vector couplings, given by $c_V^f = T_3^f - 2Q^f \sin^2\theta_{\mathrm{W}}$ and $c_A^f = T_3^f$. The interaction term for the neutral-current is illustrated in Figure 2.4b.

2.1.6 Spontaneous symmetry breaking

The unification of the weak and electromagnetic forces does not yet describe the interactions observed in nature. This is because the four gauge bosons are required to be massless to preserve gauge invariance, making the electroweak interaction a long-range force. Mass terms for fermions are forbidden, since gauge transformations would generate mixed terms involving left- and right-handed fermions. These statements contradict experimental observation, since in addition to massive fermions, the $W^\pm$ and Z gauge bosons were experimentally measured to have masses of around $m_W \sim 80$ GeV [21, 22] and $m_Z \sim 91$ GeV [23, 24] following their direct observation in 1983. The generation of masses in the SM is achieved through a process called *spontaneous symmetry breaking* (SSB).

SSB begins with a complex scalar field, $\phi(x)$, described by the Lagrangian

$$\mathcal{L}_{\mathrm{SSB}} = \partial_\mu \phi^\dagger \partial^\mu \phi - V(\phi), \tag{2.33}$$

where $V(\phi) = \mu^2 \phi^\dagger \phi + \lambda(\phi^\dagger \phi)^2$. The scalar field is invariant under global $\mathrm{U}(1)$ phase transformations:

$$\phi(x) \to e^{i\theta}\phi(x). \tag{2.34}$$

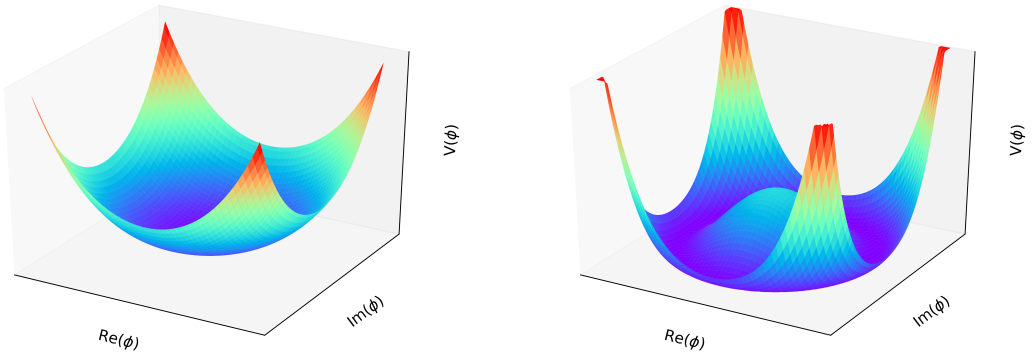

(a) **(b)**

Figure 2.5: The potential, $V(\phi)$, of a complex scalar field for (a) $\mu^2 > 0$ and (b) $\mu^2 < 0$.

The parameter λ is greater than zero to ensure the existence of the ground state, although the parameter μ could assume positive or negative values with differing consequences, as illustrated in Figure 2.5. For $\mu^2 > 0$, the ground state of the system is given by $\phi = 0$, and the system describes a particles of mass μ. For $\mu^2 < 0$, the minimum of the system is defined by

$$|\phi_0| = \sqrt{\frac{-\mu^2}{2\lambda}} \equiv \frac{v}{\sqrt{2}} > 0. \tag{2.35}$$

However, there are an infinite number of ground states, defined by $\phi_0(x) = \frac{v}{\sqrt{2}} e^{i\theta}$, because of the global $\mathrm{U}(1)$ invariance of $\mathcal{L}_{\mathrm{SSB}}$. Choosing one of the infinitely possible ground states, for example $\theta = 0$, the symmetry is said to be *spontaneously broken*. The excitations of the system around this ground state can be expanded as

$$\phi(x) \equiv \frac{1}{\sqrt{2}}(v + \varphi_1(x) + i\varphi_2(x)), \tag{2.36}$$

where φ_1 and φ_2 are real fields. The potential, $V(\phi)$, has the form

$$V(\phi) = -\frac{\lambda}{4}v^4 - \mu^2\varphi_1^2 + \lambda v\varphi_1(\varphi_1^2 + \varphi_2^2) + \frac{\lambda}{4}(\varphi_1^2 + \varphi_2^2)^2. \tag{2.37}$$

This system, with $\mu^2 < 0$, leads to the existence of a massive state, φ_1, with mass $-2\mu^2$, and a massless state described by φ_2. The state described by φ_2 represents excitations of ϕ in the azimuthal direction of the ground state, or those excitations which do not change the energy of the ground state, which explains the zero mass of the state described by φ_2. The existence of massless excitations arising from the spontaneous breaking of a symmetry of the Lagrangian is a result of the *Goldstone theorem* [25], which states that a number of massless bosons are generated in a theory which has SSB, where the number corresponds to the number of generators, or number of gauge bosons, of the symmetry that is broken.

2.1.7 The Brout-Englert-Higgs mechanism

The concept of SSB still does not yet describe the generation of masses in the SM. The application of local SSB to the SM, or its application to non-abelian and local gauge symmetries, is called the *Brout-Englert-Higgs* (BEH) mechanism [26–31], after three of the contributors to this sector of the SM.

The BEH mechanism starts by introducing a complex scalar field which is an isospin doublet:

$$\phi(x) = \begin{pmatrix} \phi^+ \\ \phi^0 \end{pmatrix} = \frac{1}{\sqrt{2}} \begin{pmatrix} \phi_1 + i\phi_2 \\ \phi_3 + i\phi_4 \end{pmatrix}. \tag{2.38}$$

Two terms are added the SM Lagrangian, a kinetic term and a potential term, which take the form

$$(D_\mu \phi)^\dagger (D^\mu \phi) - V(\phi^\dagger \phi), \tag{2.39}$$

where

$$D_\mu \phi = \left(\partial + ig \frac{\sigma_a}{2} W_\mu^a - ig' y_\phi B_\mu \right) \phi \tag{2.40}$$

$$V(\phi^\dagger \phi) = -\mu^2 \phi^\dagger \phi + \lambda (\phi^\dagger \phi)^2, \tag{2.41}$$

where the hypercharge of the scalar field, y_ϕ, is given by $y_\phi = Q_\phi - T_3 = \frac{1}{2}$. This value is constrained by the couplings of the scalar field, ϕ, to the photon, A_μ, such that the photon has no interaction with the ϕ^0 component and has an interaction with the ϕ^+ component with a strength proportional to the electric charge, e.

Similarly to before, there are an infinite number of ground states with energy $\sqrt{\frac{-\mu^2}{2\lambda}} \equiv \frac{v}{\sqrt{2}}$. Only the neutral component of the complex scalar field, ϕ^0, should acquire a non-zero vacuum expectation value since the electric charge is a conserved quantity. The choice of a ground state breaks the $\mathrm{SU(2)_L} \otimes \mathrm{U(1)_Y}$ symmetry to $\mathrm{U(1)_{QED}}$. The Goldstone theorem indicates that there should be three massless states, corresponding to the three generators of the broken $\mathrm{SU(2)}$ symmetry.

The complex scalar doublet can be parameterised as

$$\phi(x) = e^{i \frac{\sigma_a}{2} \theta^a(x)} \frac{1}{\sqrt{2}} \begin{pmatrix} 0 \\ v + H(x) \end{pmatrix}, \tag{2.42}$$

consisting of four fields: $\theta^a(x)$ and $H(x)$. The local $\mathrm{SU(2)_L}$ invariance of the Lagrangian means the dependence on $\theta^a(x)$ can be absorbed into the transformation of the gauge bosons fields in the so-called *unitary gauge*, and are the Goldstone boson fields generated through the SSB. Interactions between the complex scalar doublet and the gauge bosons

of the $\mathrm{SU(2)_L} \otimes \mathrm{U(1)_Y}$ symmetry are generated by the covariant derivative, $(D_\mu\phi)^\dagger D^\mu\phi$, which in the unitary gauge (with $\theta^a = 0$) has the expression

$$\frac{1}{2}\partial_\mu H \partial^\mu H + (v+H)^2\left(\frac{g^2}{4}W_\mu^- W^{+,\mu} + \frac{g^2}{8\cos^2\theta_\mathrm{W}}Z_\mu Z^\mu\right). \tag{2.43}$$

Picking out the terms with a v^2, mass terms for the $W^\pm$ and Z bosons appear, having been generated by the non-zero vacuum expectation value. The mass terms are related by

$$m_Z \cos\theta_\mathrm{W} = m_W = \frac{1}{2}vg. \tag{2.44}$$

As such, the SM Lagrangian, which is invariant under $\mathrm{SU(3)_C} \otimes \mathrm{SU(2)_L} \otimes \mathrm{U(1)_Y}$ gauge transformations, experiences SSB and the Higgs field acquires a non-zero vacuum expectation value. The broken generators of the symmetry breaking, equivalent to the appearance of massless Goldstone bosons, are eliminated from the Lagrangian through the chosen gauge. The photon remains massless because the $\mathrm{U(1)_{QED}}$ symmetry is not broken. Before SSB, there are six degrees of freedom in electroweak theory (the two polarisations of three massless, spin-1 gauge bosons), and four real scalar fields comprising the complex scalar doublet. Once the vacuum acquires a non-zero value, the three gauge bosons acquire masses, giving them each one more additional (longitudinal) polarisation, and a scalar particle, H - the Higgs boson. The three Goldstone bosons are said to have been "eaten" by the gauge bosons, preserving the number of degrees of freedom in the theory.

2.1.8 The Standard Model of particle physics

The SSB of the $\mathrm{SU(2)_L} \otimes \mathrm{U(1)_Y}$ symmetry introduces a new scalar particle, H, which is called the Higgs boson. Terms in the SM Lagrangian which interact with the Higgs boson include

$$\begin{aligned}\mathcal{L}_\mathrm{H} =& \frac{1}{2}\partial_\mu H \partial^\mu H - \frac{1}{2}m_H^2 H^2 - \frac{m_H^2}{2v}H^3 - \frac{m_H^2}{8v^2}H^4 \\ &+ m_W^2 W_\mu^+ W^{-,\mu}\left(1 + \frac{2}{v}H + \frac{H^2}{v^2}\right) + \frac{1}{2}m_Z^2 Z_\mu Z^\mu\left(1 + \frac{2}{v}H + \frac{H^2}{v^2}\right),\end{aligned} \tag{2.45}$$

where the Higgs boson mass, m_H, is given by $m_H = \sqrt{-2\mu^2} \equiv \sqrt{2\lambda}v$. The introduction of a Higgs boson into the SM induces an entirely new type of force that is unlike the forces of QED or the strong and weak forces. Interactions with a Higgs boson are proportional to the squared mass of the gauge bosons and the vacuum expectation value; the Higgs boson couples to mass.

However, no masses have yet been generated for fermions, which are otherwise forbidden by the requirement of local gauge invariance. Terms are introduced to the SM Lagrangian which couple the complex scalar doublet to fermion fields:

$$\mathcal{L}_Y = c_1(\bar{u}, \bar{d})_L \begin{pmatrix}\phi^+ \\ \phi^0\end{pmatrix} d_R + c_2(\bar{u}, \bar{d})_L \begin{pmatrix}\phi^{0*} \\ -\phi^-\end{pmatrix} u_R + c_3(\bar{\nu}_e, \bar{e})_L \begin{pmatrix}\phi^+ \\ \phi^0\end{pmatrix} e_R + \mathrm{h.c.} \tag{2.46}$$

The second term introduces the charge-conjugate scalar field, defined by $\phi^c \equiv i\sigma_2\phi^*$. Following SSB, $\mathcal{L}_Y$ has the form

$$\mathcal{L}_Y = \frac{1}{\sqrt{2}}(v+H)(c_1\bar{d}_L d_R + c_2\bar{u}_L u_R + c_3\bar{e}_L e_R), \tag{2.47}$$

where fermion masses can be identified as

$$m_d = -c_1\frac{v}{\sqrt{2}}, \quad m_u = -c_2\frac{v}{\sqrt{2}}, \quad m_e = -c_3\frac{v}{\sqrt{2}}, \tag{2.48}$$

which shows the Higgs boson interacts with fermions with a strength that is proportional to the mass of the fermion. The Yukawa couplings, c_i, are unknown, so the values of the fermion masses are not predicted by the BEH mechanism. However, all Yukawa couplings are fixed in terms of the fermion masses.

Lastly, the quark doublets which take part in electroweak interactions are not mass eigenstates but are related by a unitary transformation, V_{CKM}. It is conventional to apply the transformation to the down-type quarks, such that

$$q = \begin{pmatrix} u \\ d' \end{pmatrix}, \begin{pmatrix} c \\ s' \end{pmatrix}, \begin{pmatrix} t \\ b' \end{pmatrix}, \text{where} \begin{pmatrix} d' \\ s' \\ b' \end{pmatrix} = \begin{pmatrix} V_{ud} & V_{us} & V_{ub} \\ V_{cd} & V_{cs} & V_{cb} \\ V_{td} & V_{ts} & V_{tb} \end{pmatrix} \begin{pmatrix} d \\ s \\ b \end{pmatrix}. \tag{2.49}$$

The unitary transformation, V_{CKM}, is known as the *Cabibbo-Kobayashi-Maskawa* (CKM) matrix [32, 33]. Measurements of the CKM matrix indicate that the off-diagonal elements are non-zero. A typical parameterisation of the CKM matrix introduces a complex phase, which is one of the sources of charge and parity (CP) violation in the SM.

2.2 Phenomenology of hadron collisions

The interaction of particles through the exchange of gauge bosons, introduced by requiring invariance under local gauge transformations, are terms representing the potential energy of the system in the Lagrangian (which are in addition to the kinetic terms of freely-propagating particles). Using the possible interactions in the SM, the transition of an initial state to some final state is described by a set of quantum amplitudes, which are mathematical expressions for the different interactions (or scatterings) that can occur in the transition. These amplitudes are typically illustrated with Feynman diagrams, where the diagram with the least number of interaction vertices is the first term in a perturbative series. This is possible because the coupling strengths of the interaction terms are often small, so that the complete description of the state can be considered in a perturbative expansion of the coupling strengths. These quantum amplitudes[6] are translated into a measurable quantity, the cross section, which quantifies the probability that a scattering

[6] Hereafter, the word *process* is generally used to mean a quantum amplitude describing the production and decay of various particles in pp collisions that can be visualised at a fixed order using Feynman diagrams.

process takes place. Many of the processes of interest in collider experiments, such as the production and decay of a Higgs boson, have a high-momentum transfer (or hard scatter) due to the exchange of a heavy, resonant particle. However, in order to make inference on the cross section of the particular process of interest (the *signal process*), the cross sections of all SM processes contributing to the final state (both high- and low-momentum scatters) have to be calculated and taken into account (the *background processes*). This is a complex task, since the LHC is a hadron collider, where QCD describes the interactions of the colliding protons, which comprise three valence quarks and a sea of quarks and gluons (collectively termed *partons*). There is also the fact that several phenomenological aspects of QCD mean there are such effects as parton showering and hadronisation, generating a complex environment that must be taken into account when making predictions of different processes.

2.2.1 Partonic cross section

The first component of pp collisions to define is the partonic cross section of a particular process of interest, $\hat{\sigma}_{ij\to X}$, from the collision of two partons, i and j, to a final state, X. An inclusive partonic cross section is the sum of all terms in the perturbative expansion, including terms with loops in Feynman diagrams. Loop diagrams generally lead to diverging coupling constants and particle masses at high energy, but can be removed in a process called *renormalisation* to yield physical coupling constants and particle masses. This process requires the introduction of an arbitrary *renormalisation scale*, μ_{R}, defining the energy, or scale, at which divergent loop diagrams are absorbed into renormalised quantities. The value of μ_{R} is usually chosen as the energy scale, Q, of the interaction of interest, generating a dependence of coupling constants and particle masses on μ_{R}, which are known as *running couplings*. Whilst μ_{R} facilitates finite calculations in a perturbative QFT, it is not a physical scale, meaning that measurable observables must be independent of it.

The strong coupling constant, α_{S}, is a running coupling, and is large at low energy scales (long distances) but small at high energy scales (short distances). This means that the interactions of quarks and gluons inside the proton are non-perturbative, but the high-momentum transfer interactions generating particles like the Higgs boson can be described by a perturbative expansion in the strong coupling constant,

$$\hat{\sigma}_{ij\to X} = \sum_{n=0}^{\infty} \alpha_{\mathrm{S}}^{m+n} \hat{\sigma}_{ij\to X}^{(n)}, \tag{2.50}$$

where m is the number of QCD vertices for the simplest Feynman diagram of process $ij \to X$, and $\hat{\sigma}_{ij\to X}^{(n)}$ is the nth order cross section in α_{S}. Many predictions of Higgs boson cross sections at the LHC are calculated to a certain order in α_{S}, and are called

fixed-order calculations. Starting at $n = 0$, the prediction is said to be *leading order* (LO) in QCD. For $n = 1$, the prediction is called *next-to-leading order* (NLO) in QCD. For higher n, an additional *next-to* is prepended to the name. Terminating the perturbative expansion at order k means $\hat{\sigma}_{ij\to X}$ has a residual dependence on μ_{R} of the order $\mathcal{O}(\alpha_{\mathrm{S}}^{m+k+1})$. This can be seen by considering that the dependence of $\hat{\sigma}_{ij\to X}$ on μ_{R} is zero, $\mathrm{d}\hat{\sigma}_{ij\to X}/\mathrm{d}\mu_{\mathrm{R}} = 0$, such that

$$\frac{\mathrm{d}}{\mathrm{d}\mu_{\mathrm{R}}} \sum_{n=0}^{k} \alpha_{\mathrm{S}}^{m+n} \hat{\sigma}_{ij\to X}^{(n)} = -\frac{\mathrm{d}}{\mathrm{d}\mu_{\mathrm{R}}} \sum_{n=k+1}^{\infty} \alpha_{\mathrm{S}}^{m+n} \hat{\sigma}_{ij\to X}^{(n)} = \mathcal{O}(\alpha_{\mathrm{S}}^{m+k+1}). \tag{2.51}$$

This means that the effect of missing higher order terms in a fixed-order calculation can be estimated by considering its residual dependence on μ_{R}.

2.2.2 Parton distribution functions

The second component of pp collisions to consider is that partons are the constituents of the protons, so hadronic cross sections to a final state X, $\sigma_{pp\to X}$, should be computed. The non-perturbative physics of the individual hadrons is separated from the perturbative physics of the partonic cross section according to the *factorisation theorem*, which states the pp cross section of an interaction is a convolution of the partonic cross section with so-called *parton distribution functions* (PDFs) of each colliding proton:

$$\sigma_{pp\to X}(p_1, p_2) = \sum_{i,j} \int_0^1 \mathrm{d}x_1 \mathrm{d}x_2 f_a(x_1, \mu_{\mathrm{F}}^2) f_b(x_2, \mu_{\mathrm{F}}^2) \int \hat{\sigma}_{ij\to X}(x_1 p_1, x_2 p_2, \frac{Q^2}{\mu_{\mathrm{R}}^2}, \frac{Q^2}{\mu_{\mathrm{F}}^2}). \tag{2.52}$$

Each f_a term is the PDF of the parton a in one proton, p_i is the momentum of the ith proton, x_i is the momentum fraction of parton i, and Q is the energy scale, or magnitude of momentum transfer, of the partonic interaction. The sum is taken over all contributing parton types: six quark flavours and the gluon. The PDFs encode the probability that a parton inside a proton carries a fraction, x, of the total proton momentum at the energy scale Q. The *factorisation scale*, μ_{F}, has a similar function to the renormalisation scale, μ_{R}, and is the scale at which the non-perturbative functions describing PDFs are distinguished from the perturbative cross section describing the hard interaction. There is a residual dependence of the perturbative expansion on μ_{F}, similar to the residual dependence on μ_{R}, when performing a fixed-order calculation. The PDFs are determined empirically because they describe soft QCD (where the momentum transfer of an interaction is small). At these low energy scales, the strong coupling constant is large and QCD is non-perturbative, meaning PDFs cannot be calculated analytically. Typically, PDFs are measured at a given energy scale using data from deep-inelastic scattering events and are evolved to different energy scales according to the DGLAP equations [34–37]. Several collaborations provide so-called *PDF sets* which differ in experimental data, parameterisation models, treatment of theoretical parameters and values, and uncertainties. These collaborations include CTEQ [38], MRST2007 [39], NNPDF [40], and PDF4LHC [41].

2.2.3 Parton showering

Outgoing partons in a high-momentum transfer interaction will radiate daughter QCD particles, in a process that will repeat until the energy scale of the daughter particles reaches the non-perturbative regime. Fixed order calculations, such as those of the hard scatter, do not accurately take into account low momentum or collinear parton emissions. As such, the evolution of QCD emissions from the hard scatter to the non-perturbative QCD regime is performed using an algorithmic programme called a *parton shower*. Parton showers typically compute the probability of a parton to branch into a further two partons, which could be done in several ways, leading to several different types of parton shower programmes. These include virtuality-ordered and angular-ordered showers. There can also be dipole showers where emission probabilities are computed considering pairs of partons connected by colour charge. It is also possible for partons in the initial state to radiate soft or collinear emissions, which are also modelled with parton shower programmes.

2.2.4 Hadronisation

The non-perturbative regime of QCD occurs at energy scales of $\mathcal{O}(1\text{ GeV})$. At this point, partons experience *confinement* and form a collimated spray of hadrons with zero net colour charge. A hadronisation model describes the confinement of partons into hadrons, of which there are two distinct types. The first is the *Lund string model*, where outgoing partons experience a potential energy which increases with increasing distance. At a specific distance, it is energetically favourable to convert the potential energy into a new $q\bar{q}$ pair and form a hadron, and the process repeats. The second is the *cluster model* whereby gluons are split into $q\bar{q}$ pairs, forming clusters with a net-zero colour charge.

Many of the hadrons produced by the hadronisation model are unstable and decay into lighter hadrons and particles which are measurable in the ATLAS detector. The decay of unstable hadrons[7] must be computed taking into account momentum conservation and known branching ratios. The result of parton showering and hadronisation is that partons in the final state of a hard scatter interaction are experimentally observed in the ATLAS detector as a collimated spray of hadronic activity, which is known as a *jet*. Jets are described in Section 3.5.4.

2.2.5 Underlying event

The underlying event is the collection of interactions which are not the hard scatter. It includes soft hadronic activity caused by other partons in the colliding protons (so-called *multi-parton interactions*) and the beam remnant. The energy scale of the underlying

[7] Also the τ-lepton.

event is less than the energy scale of the hard scatter and is generally represented by a uniform distribution of soft activity in the detector.

2.2.6 Pileup

The LHC collides beams consisting of bunches of several billion protons in quick succession. Inelastic interactions from pp collisions in one bunch, as well as those from pp collisions in an adjacent bunch, give rise to so-called *pile-up*. These are interactions which contribute to the detector signals and affect the reconstruction of the hard scatter process of interest.

2.3 Monte Carlo simulation

State-of-the art Monte Carlo (MC) event generators are used to provide accurate predictions and simulations of pp collision events that can be compared to observed data collected by the ATLAS detector, taking into account all of the above components of a collision event. An illustration of a single collision event is shown in Figure 2.6.

2.3.1 Event generators

Several programmes, each differing in their algorithmic implementation of the contributing physics effects to a pp collision event, are available to simulate a full collision event. The programmes used for the measurements in this thesis include:

PYTHIA

PYTHIA [42] is a multi-purpose event generator that has the ability to compute the partonic cross section, parton shower, hadronisation, and underlying event. The partonic cross section is usually calculated at LO in PYTHIA, so it is typically only used to simulate the parton shower, hadronisation, and underlying event (collectively called the UEPS). The parton shower is simulated using colour-charged dipoles ordered by transverse momentum. The Lund string model is used to simulate hadronisation. The UEPS has been tuned to observed data from several measurements, resulting in good agreement with data, so PYTHIA is used as the nominal UEPS for predictions for the measurements in this thesis.

HERWIG

HERWIG [43] is typically used to compare the UEPS as simulated by PYTHIA. This is because the implementation of the parton shower in HERWIG uses an angular-ordered shower, whilst the hadronisation is performed using the cluster model.

SHERPA

SHERPA [44] is also a general purpose event generator, but can only be used to simulate an entire event, unlike PYTHIA and HERWIG. The UEPS implementation is similar to PYTHIA, using colour-charged dipoles ordered by transverse momentum.

The hadronisation is performed using the cluster model. SHERPA typically generates the partonic cross section at NLO where additional partonic emissions to Feynman diagrams are explicitly included in the calculation. This makes SHERPA the preferred generator for simulating events with additional hadronic activity.

MADGRAPH

MADGRAPH [45] is an event generator that calculates partonic cross sections at LO or NLO. It is typically interfaced to a separate programme to simulate the UEPS, usually PYTHIA.

POWHEG

POWHEG [46] is an event generator that simulates partonic cross sections at NLO or above. Similarly to MADGRAPH, it is interfaced to PYTHIA to simulate the UEPS.

2.3.2 Matching and merging

A complication arises in the case where a partonic cross section is determined at NLO or above and combined with a programme that simulates a parton shower. This is because there can be double-counting of emissions in the parton shower with emissions from the partonic cross section. An NLO calculation will include LO diagrams, as well as virtual corrections in the form of loop diagrams, but also diagrams with additional emissions. The additional emissions can be doubly counted when adding a parton shower to the NLO calculation. To avoid the double-counting, two prescriptions exist, implemented in different forms, called *matching* and *merging*.

In the case of matching, the double-counting can be avoided by modifying the NLO calculation. The partonic cross section is then dependent on the particular parton shower that is used. This is the approach taken in the MADGRAPH5_aMC@NLO generator [45]. Alternately, in programmes such as POWHEG, the emission with the highest momentum is required to have been simulated in the partonic cross section. The parton shower emission probabilities are modified in the combination of the partonic cross section with the parton shower.

Parton showers are generally supposed to model low momentum collinear emissions, rather than high momentum emissions. High momentum emissions are better simulated using fixed-order calculations. There can be double-counting in the combination of a partonic cross section with the parton shower (matching), but there can also be double-counting from merging exclusive partonic cross sections with different emission multiplicities. The SHERPA event generator uses the CKKW-L algorithm, as well as the MEPS@NLO algorithm [47–50]. In these algorithms, the two highest parton shower emissions are corrected to match the emissions in the partonic cross section. Several

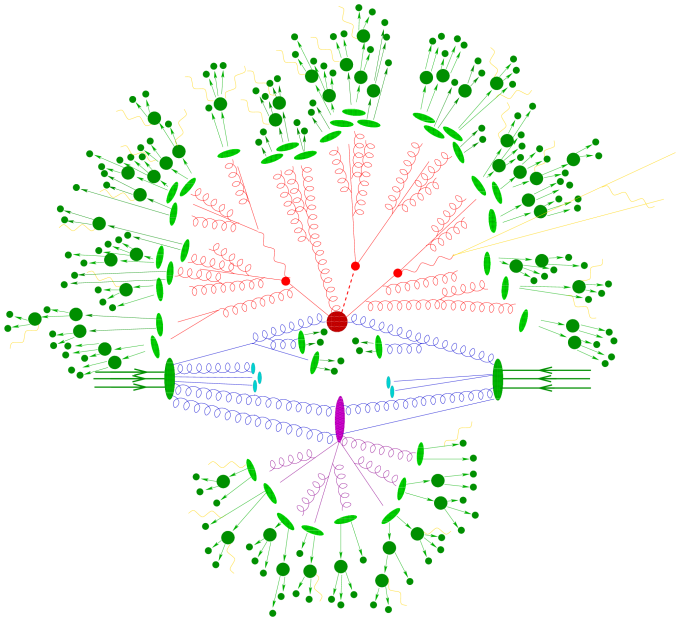

Figure 2.6: Illustration of a single pp collision event simulated using an MC event generator in several stages. The hard scatter is shown by the large red circle. Particles radiated from partons in the initial and final state are shown in blue and red. The transition below the perturbative regime of QCD is when hadronisation occurs and partons are confined into colour-singlet hadrons, shown by the green circles. The confinement of the partons inside the initial state protons are shown by the bigger green ovals. The beam remnant and underlying event are shown by the blue and purple ovals. Photons and leptons which are radiated from electrically charged particles are shown in yellow. Sourced from Ref. [51].

thresholds are introduced to determine the point above which hadronic activity is simulated using the partonic cross section or whether the parton shower is used.

2.4 Higgs boson physics at the LHC

In the SM, the Higgs boson is the quantum oscillation of the Higgs field, and is predicted to be a spin-0, electrically neutral, colourless particle. It interacts with other SM particles with a probability proportional to their masses, whilst its own mass, m_H, is a free parameter of the SM. Once the vacuum energy of the Higgs field is determined, the interaction strength, or couplings, of the Higgs boson to other SM particles are predicted.

2.4.1 Production modes

In a hadron collider such as the LHC, a Higgs boson is produced through several possible production processes, or *modes*, which are illustrated at LO in QCD in Figure 2.7. The predicted cross-section of each production mode is shown in Figure 2.8a. The two dominant production cross sections, gluon-gluon fusion (ggF) and vector-boson fusion (VBF), are the subject of the measurements in this thesis.

The production modes include:

gluon-gluon fusion (ggF)

The ggF mode occurs when two gluons collide and a virtual fermion loop produces a Higgs boson. The Higgs boson does not interact with gluons directly since they are massless in the SM. Top quarks have the largest contribution to the fermion loop due to their heavy mass. This process occurs with a significantly larger relative contribution than other production modes because of the larger colour factors associated with vertices involving gluons, the large top quark Yukawa coupling, and because this process operates in an energy regime where the gluon PDF is dominant.

vector-boson fusion (VBF)

The VBF mode has the second largest production cross section, and proceeds via the radiation of two vector bosons (W or Z) from colliding quarks to produce a Higgs boson. The colliding quarks are spectators in the interaction, with no exchange of colour charge, leading to a distinctive final state topology in which two high-energy jets of hadrons are found at small angles to the beam line.

associated production (Higgs-strahlung or VH)

A Higgs boson is radiated from a vector boson (W or Z) produced from the annihilation of two colliding quarks. A gluon loop, similar to ggF, contributes to the ZH mode. This process is referred to as Higgs-strahlung due to its similarity with bremsstrahlung radiation. Whilst occurring with a small predicted cross section, the vector boson in the final state gives rise to additional particles that can be selected in events to increase experimental discrimination of this process.

top quark fusion ($t\bar{t}H$)

The $t\bar{t}H$ process occurs when two colliding gluons produce a $t\bar{t}$ pair, where one from each pair fuse to produce a Higgs boson. A Higgs boson could also be radiated from a top quark when a $t\bar{t}$ pair is produced in a collision. Similar processes occur that involve b-quarks. These production processes occur with the smallest cross sections at the LHC.

2.4.2 Decay modes

Once a Higgs boson is produced, it is predicted to exist for a very short time before decaying into other particles, and is thus never observed directly in the ATLAS detector. The predicted decay width is $\Gamma_H = 4.1$ MeV[8] calculated for a Higgs boson with mass $m_H = 125.09 \pm 0.24$ GeV [53]. The *branching ratio* (BR) of a Higgs boson decaying to a final state f, $\mathcal{B}_f$, is defined as the ratio of the partial decay width to the final state f, $\Gamma(H \to f)$, to the total width, Γ_H,

$$\mathcal{B}_f = \frac{\Gamma(H \to f)}{\Gamma_H}, \tag{2.53}$$

[8]This corresponds to a mean lifetime, τ, of $\tau = 1.6 \times 10^{-22}$ s calculated from $\tau = \hbar/\Gamma_H$.

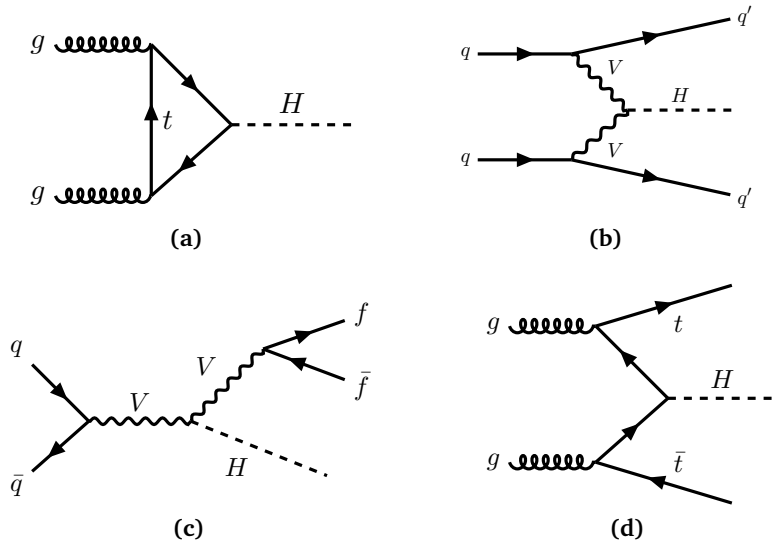

Figure 2.7: Example Feynman diagrams at LO showing the production of an SM Higgs boson via (a) gluon-gluon fusion (ggF), (b) vector-boson fusion (VBF), (c) associated vector boson (Higgs-strahlung), VH, with $V = \{W,\ Z\}$, and (d) top quark fusion ($t\bar{t}H$).

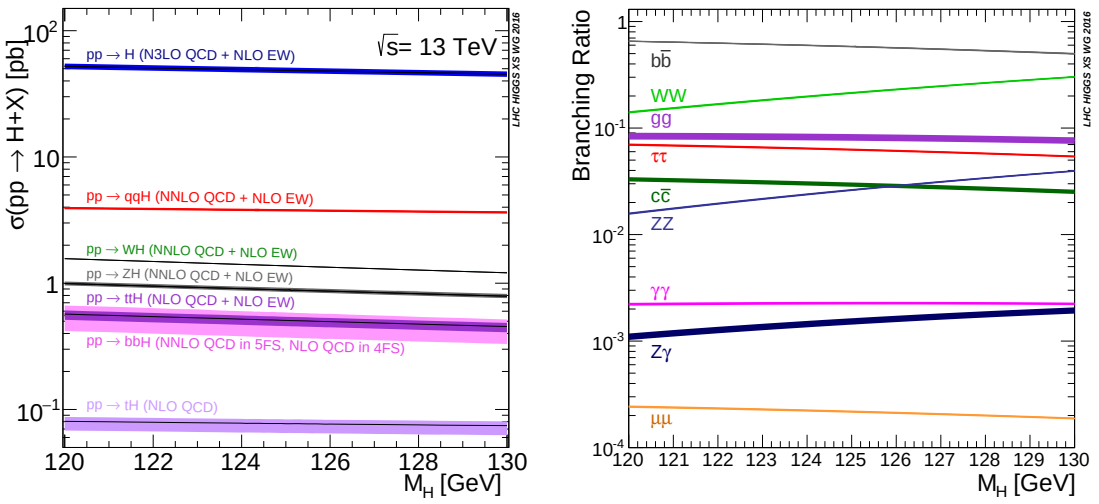

Figure 2.8: Calculations in the SM, as a function of the Higgs boson mass, m_H, of (a) several Higgs boson production cross sections, and (b) several Higgs boson branching ratios. Sourced from Ref. [52].

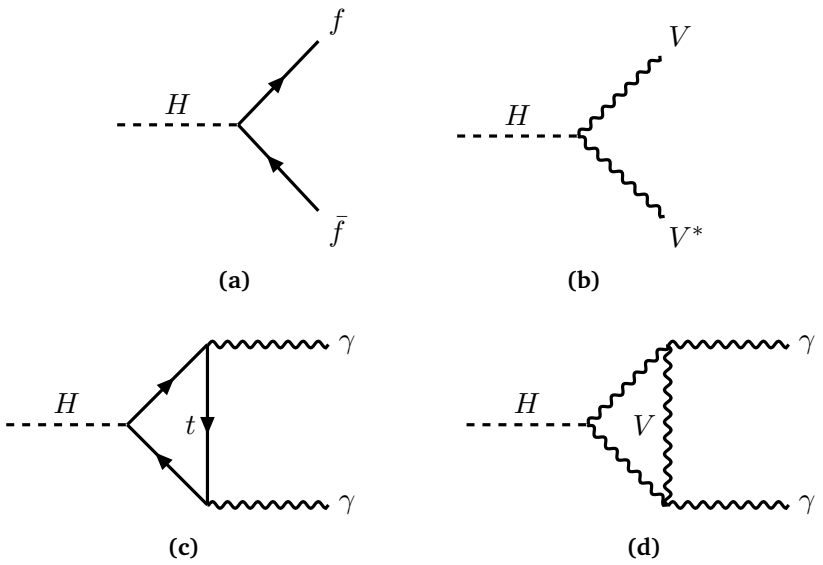

Figure 2.9: Example Feynman diagrams at LO showing Higgs boson decays to (a) pairs of fermions (dominantly $f\bar{f} = \{b\bar{b},\ \tau\tau,\ c\bar{c},\ \mu\mu\}$), (b) pairs of massive vector bosons (where $VV^* = \{WW^*,\ ZZ^*\}$), (c) pairs of photons via a virtual fermion loop, and (d) pairs of photons via a virtual vector boson loop. The photon pair could be replaced with a gluon pair in (c) or a $Z\gamma$ pair in (d) to give rise to the $H \to gg$ and $H \to Z\gamma$ decay modes, respectively.

and has the interpretation of the probability of the Higgs boson to decay into final state f. Higgs boson decay BRs are shown in Figure 2.8b as a function of the Higgs boson mass. The shown decay modes include WW and ZZ pairs, where, in this range of Higgs boson masses, one of the gauge bosons is off-shell due to its large mass ($m_H < 2m_V$). Also shown are decays to massless particles (photons and gluons) that proceed through loop diagrams. Several possible Feynman diagrams of the Higgs boson decay modes are illustrated at LO in QCD in Figure 2.9.

2.4.3 Signal strengths and cross section measurements

Measurements of the production and decay of the Higgs boson at the LHC are typically performed using the concept of categorisation. With this approach, a large data set of events, which have been selected because they contain final state particles that are reconstructed in the detector corresponding to the final state of the Higgs boson production and decay mode of interest, are divided into mutually exclusive partitions of the data set. This partitioning is usually achieved by defining kinematic quantities (observables) using the four-momenta of final-state particles reconstructed in the detector (electrons, muons, etc.) for each event. Distributions of observables, such as the invariant mass of and opening angles between reconstructed particles, are then used to make selection requirements, resulting in smaller and mutually exclusive data sets that are enriched in events of the particular physics process of interest. MC simulation is often used to predict the event yields and distributions of observables of the physics processes that populate

each category. In a final step, the different categories are combined in a statistical model, which will typically contain several parameters that can adjust the yields and distributions of the MC-simulated predictions in light of the data. The use of categories improves the precision of the measurements of parameters associated with the production and decay of Higgs bosons since the categories will generally have different purities of Higgs boson and background processes, as well as different compositions of events from different Higgs boson production modes. A framework for extracting parameters from data associated with the production and decay of Higgs bosons has been (and continues to be) developed during the past decade since the Higgs boson discovery. Detailed descriptions can be found in Refs. [53] and [54].

The parameters associated with Higgs boson production and decay that can adjust the predicted event yields of Higgs bosons in light of the data are called *signal strengths*, μ_i^f. They are defined by

$$\mu_i^f = \mu_i \times \mu_f = \frac{\sigma_i}{\sigma_i^{\text{SM}}} \times \frac{\mathcal{B}_f}{\mathcal{B}_f^{\text{SM}}}, \tag{2.54}$$

where $\mu_i = \sigma_i/\sigma_i^{\text{SM}}$ and $\mu_f = \mathcal{B}_f/\mathcal{B}_f^{\text{SM}}$ are the measured cross section of production mode i and BR of decay mode f, normalised to their SM predictions, respectively. This form of the signal strength utilises the narrow-width approximation whereby the production cross section of a Higgs boson is factorised from its decay. In the SM, both μ_i and μ_f are equal to unity, although a measurement of either is experimentally inaccessible; only measurements of the product of μ_i and μ_f are possible without making an assumption about the Higgs boson decay width or the production cross sections.

In any analysis, the measured number of events of Higgs boson production mode i and decay mode f in a category k, N_{ik}, is given by

$$\begin{aligned} N_{ik}^f = N_{\text{data},k} - N_{\text{bkg},k} &= \mathcal{L}_k \times (\sigma_i \cdot \mathcal{B}_f) \times (A \cdot \epsilon)_{ifk}^{\text{SM}} \\ &= \mathcal{L}_k \times \mu_i^f \times (\sigma_i \cdot \mathcal{B}_f)^{\text{SM}} \times (A \cdot \epsilon)_{ifk}^{\text{SM}}, \end{aligned} \tag{2.55}$$

where $\mathcal{L}_k$ is the integrated luminosity of category k, $N_{\text{data},k}$ and $N_{\text{bkg},k}$ are the event yields obtained in data and the measured event yields from background processes in category k, and $(A \cdot \epsilon)_{ifk}^{\text{SM}}$ are the acceptance and efficiency of selecting and reconstructing events in category k. The acceptance and efficiency terms are predicted assuming SM Higgs boson production and decay in MC simulation[9]. A signal strength measurement can be

[9] These quantities are defined as the ratio of the number of Higgs boson events satisfying a set of selection requirements to the total number of Higgs boson events prior to the set of selection requirements. The efficiency term accounts for both efficiencies and migration of events between categories (due to detector response and resolution).

converted into an inclusive cross section measurement through

$$\begin{aligned}\sigma_i \cdot \mathcal{B}_f &= \hat{\mu}_i^f \times (\sigma_i \cdot \mathcal{B}_f)^{\text{SM}} \\ &= \frac{N_{\text{data}} - N_{\text{bkg}}}{\mathcal{L} \times (A \cdot \epsilon)_{if}^{\text{SM}}},\end{aligned} \tag{2.56}$$

where $\hat{\mu}_i^f$ is the measured signal strength, and a sum over k categories is implied.

Signal strength measurements strongly depend on the state-of-the-art theoretical prediction of $(\sigma_i \cdot \mathcal{B}_f)^{\text{SM}}$ available at the time the measurement is performed. An inclusive cross section measurement removes this dependency, but must correct for inefficiency that is accrued due to event selection requirements on kinematic distributions or the inability of the detector to measure all particles with absolute accuracy. The measured event yields are said to have been recorded at *detector-level* (or reconstruction-level), which refers to the set of signals reconstructed in the detector. However, it is possible to consider the set of events prior to any interaction with the detector material to define so-called *truth-levels*. First, the *particle-level* refers to the set of long-lifetime particles ($\gtrsim 10^{-10}$ s) which are usually those which will go on to interact with the detector material. Second, the *parton-level* refers to the set of particles as defined in the Lagrangian before any hadronisation or parton shower modelling is assumed. A measurement corrected to a truth-level that is similar in definition to detector-level requires less assumptions on theoretical predictions than a detector-level measurement and can be directly compared to the output of theoretical calculations.

In order to correct a detector-level measurement to the particle-level, a *fiducial volume* is defined. This refers to a set of event selection requirements on kinematic distributions at particle-level. Typically, the fiducial volume is defined as closely as possible to the detector-level selection requirements to ensure that the theoretical dependence on events which are not selected by either the fiducial volume or detector-level selection requirements is minimised ($A_{if}^{\text{SM}} \sim 1$). A fiducial cross section, $(\sigma_i \cdot \mathcal{B}_f)^{\text{fid.}}$, is defined by

$$\begin{aligned}(\sigma_i \cdot \mathcal{B}_f)^{\text{fid.}} &= \hat{\mu}_i^f \times (\sigma_i \cdot \mathcal{B}_f)^{\text{SM}} \times A_{if}^{\text{SM}} \\ &= \frac{N_{\text{data}} - N_{\text{bkg}}}{(\mathcal{L} \cdot \epsilon_{if}^{\text{SM}})}.\end{aligned} \tag{2.57}$$

Fiducial cross sections have the least dependence on theoretical predictions. It is also possible to perform *differential fiducial* cross section measurements in which a fiducial cross section is measured in several bins of a kinematic distribution. However, minimising the dependency of a measurement on theoretical predictions often comes at the cost of decreased experimental sensitivity. The reason for this is that advanced analysis techniques, such as using machine learning for classification of Higgs boson and background events, are required to increase the precision of measurements beyond the precision obtained

using simple kinematic selection requirements. Typically, however, only simple kinematic selection requirements are emulated in a fiducial volume.

The acceptance and efficiency of Higgs boson events strongly depend on the production mode, due to the different kinematics of events originating from each production mode [55, 56]. Coupled with the increasing luminosity available to perform measurements of the Higgs boson, more granular (differential) measurements can be performed, in addition to inclusive measurements (signal strengths), which should be carried out as a function of the production modes.

2.4.4 Simplified template cross section measurements

The simplified template cross sections (STXS) [53, 54, 57, 58] framework was constructed as a complementary approach to measuring fiducial differential cross sections, as well as an evolution of signal strength measurements. STXS are a set of physical cross sections, as opposed to signal strengths, for several production modes which are measured simultaneously in mutually exclusive kinematic fiducial regions. These mutually exclusive regions, called *bins*, are partitions of the fiducial region for a particular production mode, where the partitions are defined using several kinematic distributions constructed using the physics objects available in the fiducial volume. Within each bin, *templates* (histograms of kinematic distributions) are created. Events in the Higgs boson MC samples are used to generate the templates and are divided amongst the bins, meaning that SM production of a Higgs boson is assumed within each bin. The expected Higgs boson signal yield of a particular bin is associated with its own normalisation parameter, whose value is determined (simultaneously with the expected Higgs boson yield in other bins) from one or more corresponding categories of observed event yields. Any deviation from the SM in a particular part of the fiducial region is then more apparent than in a signal strength measurement and it is in this sense that STXS measurements are differential. In order for STXS measurements to be useful and precise, the definition of the STXS bins are designed to:

- maximise the experimental sensitivity to events containing Higgs bosons;
- reduce the extrapolation uncertainties of measurements to regions which depend strongly on theoretical predictions;
- allow for the combination of measurements from different decay modes and between experiments;
- isolate effects from new physics.

These criteria are achieved by defining the bins with global event quantities, such as the reconstructed Higgs boson transverse momentum, p_{T}^{H}, the number of reconstructed jets,

N_{jet}, and the invariant mass of two jets, m_{jj}. The latter two are often used in the selection requirements of categories in signal strength measurements of different decay modes. Further, since STXS measurements are performed with separate bins for each Higgs boson decay mode, STXS measurements lend themselves to straightforward statistical combination, both between decay modes and between experimental collaborations. Matching the bin definitions to the experimental selection requirements also minimises the dependency on theoretical predictions, although there is a residual dependence by assuming SM kinematics within each bin and from the fact that the fiducial regions are often larger than those in a fiducial measurement. Nevertheless, the use of multivariate analysis in STXS measurements is possible, unlike in fiducial measurements, because of the assumption of SM kinematics in each bin. Lastly, by virtue of their mutual exclusivity, STXS bins can be made more granular by dividing them into sub-bins as more data is collected, further reducing the dependency on theoretical predictions. This leads to the concept of *stages* of STXS measurements, where a stage corresponds to a specific set of partitions of the fiducial region. The definition of the fiducial volume and the STXS bins is outlined in Section 4.7.

2.4.5 Status of Higgs boson physics

Over the past ten years since its discovery, the Higgs boson has been observed and measured with increasing precision in many of the possible production and decay modes accessible at the LHC, in very good agreement with the predictions of the SM. This includes measurements of the ggF, VBF, VH, and $t\bar{t}H$ production cross sections and in final states originating from the $\gamma\gamma$, ZZ^*, WW^*, $b\bar{b}$, and $\tau\tau$ decay modes. Measurements are also now able to begin probing the Higgs boson coupling to second generation fermions such as charm quarks and muons, as well as with decay modes with very small BRs such as $Z\gamma$. Whilst individual measurements of Higgs boson production and decay rates are performed using a single decay mode, such as the measurements presented in this thesis, a global statistical combination of event categories from many Higgs boson measurements is typically performed such that differing and complementary experimental sensitivity from measurements in each decay mode improves the precision of production cross sections and decay BRs.

One such combination has been performed recently by the ATLAS Collaboration using the full Run 2 data set, or only 36 fb^{-1} of Run 2 data for a small number of input measurements [59]. The measurements presented in this thesis are included in this global combination and in the results highlighted in this section. The CMS Collaboration has also performed a global combination of measurements of the Higgs boson resulting in similar precision to the measurements by ATLAS [60]. Figure 2.10a shows the measured inclusive cross sections of ggF, VBF, WH, ZH, $t\bar{t}H$, and tH production modes, normalised to their

SM predictions, which highlights the level of precision that is achieved in such a global combination. The ggF production mode is now measured to a precision of $\sim$7%, the VBF mode to a precision of $\sim$12%, and the WH, ZH, and $t\bar{t}H$ modes to a precision of $\sim$23%. Figure 2.10b shows the global measurement of the ggF, VBF, VH, $t\bar{t}H$, and tH production cross sections in distinct kinematic fiducial regions as defined in the STXS framework. The strengths of the Higgs boson coupling in each decay vertex are also extracted from the global combination and are shown in Figure 2.12 as a function of particle mass using a framework in which a single parameter scales any given coupling strength relative to the SM prediction. The agreement with the SM predictions of the measured cross sections and coupling strengths across several orders of magnitude is impressive to note, and is demonstrative of the robust understanding and calibration of final state particles in the ATLAS detector, developments in theoretical calculations of Higgs boson production and decay rates, and the use of advanced data analysis techniques in the classification of events. Such results give sizeable credibility to the SM and the BEH mechanism as the description through which fundamental particles acquire their mass.

Measurements of Higgs boson production cross sections in several decay modes have differing experimental sensitivity and precision, helping to constrain measurements of the total production cross sections in the global combination, as illustrated in Figure 2.11. From this, it can be seen that the precision of the ggF production mode measurement is primarily driven by the $\gamma\gamma$ and ZZ decay modes. Despite the low BRs of these decay modes, precision measurements are possible because it is easy to identify and obtain a pure set of leptonic final states originating from the ZZ^* decay, whilst it is possible to precisely measure the large continuum diphoton SM background using a function with a small number of parameters in the $\gamma\gamma$ measurement. Measurements of ggF production using the WW^* and $\tau\tau$ are less precise because several SM processes give rise to the same final states which make measurements in these decay modes challenging. However, these decay modes are the most precise measurements of VBF production due to the use of advanced analysis techniques in the measurements and the distinctive final state topology involved. The precision of the WH and ZH production cross sections are driven by the $b\bar{b}$ decay mode. This decay mode has the largest BR but differentiating $H \to b\bar{b}$ events from events with generic hadronic activity produced in pp collisions is challenging. The use of the VH production mode means leptons produced in the decay of the associated vector boson can be used to aid in the identification of the signal. The $t\bar{t}H$ production mode is most precisely measured using the $\gamma\gamma$ and $b\bar{b}$ decay modes. Lastly, measurements of Higgs boson couplings to second generation fermions are increasingly precise, which tests the BEH mechanism across particle generations. The $\mu\mu$ decay mode has confirmed SM-like interactions at the level of 3σ [61] whilst a measurement using the $c\bar{c}$ decay mode has set a limit of 26 times the SM [62].

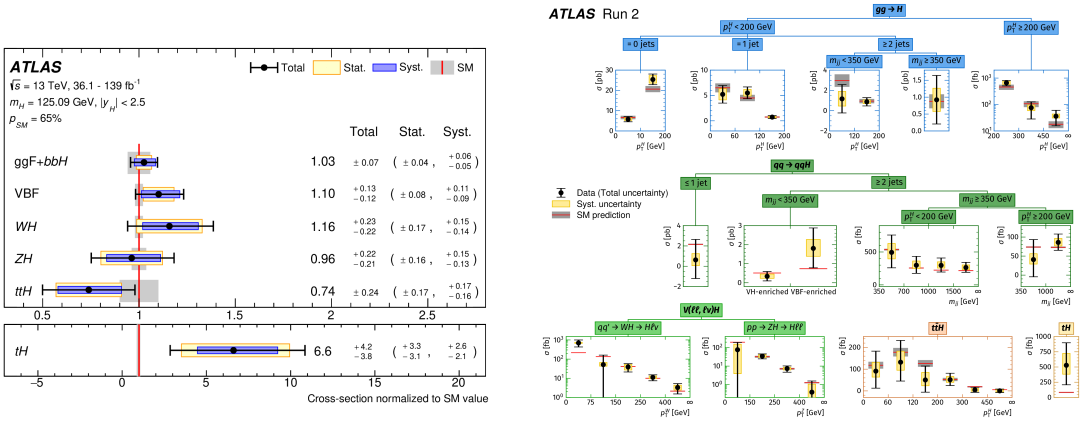

(a) (b)

Figure 2.10: Expected and observed cross section measurements for ggF, VBF, WH, ZH, $t\bar{t}H$, and tH Higgs boson production modes where (a) SM branching ratios are assumed and the measurements are normalised to the SM prediction, and (b) where the measurements are performed in distinct kinematic fiducial regions according to the STXS framework. Sourced from Ref. [59].

Underpinning all measurements of Higgs boson production cross sections and decay BRs is the assumption that the Higgs boson is a spin-0 and CP-even scalar particle (i.e. it is a singular 0^{++} state). In this thesis, this assumption is reflected in event selection requirements to define regions of the data set enriched in Higgs boson signal events where the decay of a heavy scalar and CP-even Higgs boson constrains the expected kinematics of the final state particles. This is discussed in Section 4.1.3. However, both the ATLAS and CMS Collaborations have tested this assumption by studying angles between final state particles and comparing the data to several different spin and CP hypotheses[10], as well as considering the possibility that the Higgs boson is an admixture of CP-even and CP-odd states. The SM hypothesis has been confirmed at the level of up to 3σ in measurements of the Higgs boson in the WW, ZZ, and $\gamma\gamma$ decay modes with Run 1 data (2009–2013) collected at $\sqrt{s} = 7$–8 TeV by both ATLAS [63] and CMS [64]. More recently, spin and CP studies of the Higgs boson have continued to confirm the SM hypothesis with Run 2 data collected at $\sqrt{s} = 13$ TeV in decay modes to vector bosons, but also with the $\tau\tau$ decay mode [65, 66].

[10]The spin-1 hypothesis is essentially ruled out by the observation of $\gamma\gamma$ decays of the Higgs boson, so tested spin hypotheses are typically spin-0 and spin-2 hypotheses.

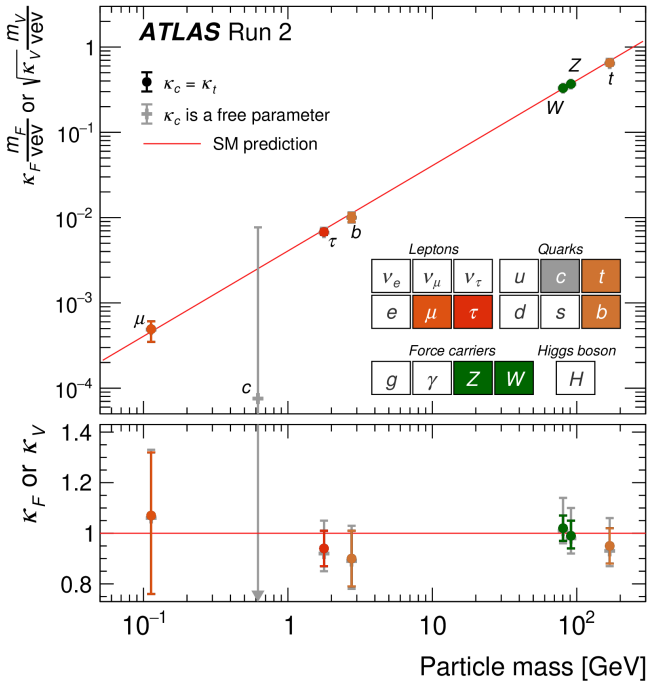

Figure 2.11: Measured coupling strength modifiers, $\kappa_F \frac{m_F}{v}$ and $\sqrt{\kappa_V}\frac{m_V}{v}$, for fermions ($F = t,\ b,\ \tau,\ \mu$) and gauge bosons ($V = W,\ Z$), respectively, as a function of particle mass, m_F and m_V. The vacuum expectation value of the Higgs field, v, is 246 GeV. The red line shows the SM prediction. No contribution from new physics is assumed in either the production or decay of a Higgs boson. The bottom panel shows the ratio of the measured coupling strengths to the SM prediction. Two scenarios are shown where $\kappa_c = \kappa_t$ (circles) and where κ_c is a free parameter (grey cross). Sourced from Ref. [59].

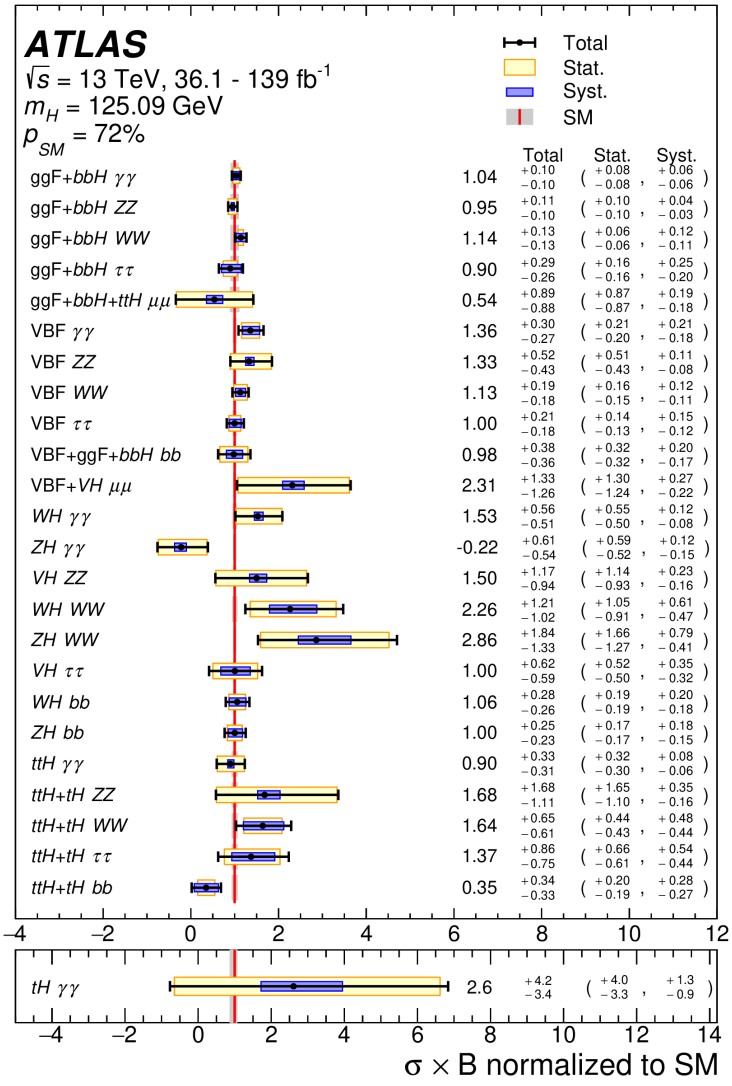

Figure 2.12: Measured Higgs boson production cross sections times branching ratio for several different production and decay modes, normalised to their SM predictions, obtained from a global combination of event categories. Sourced from Ref. [59].

3
The LHC and the ATLAS experiment

One method to measure the various parameters of the SM is to collect the output of as many high energy particle collisions as is technically possible. The LHC, and its various experiments, have been constructed for such a purpose by CERN and its associated member states. Situated 100 m beneath the Franco-Swiss border near Geneva, the LHC is the machine designed to provide the high energy collisions, whilst the experiments (or detectors), located at several points around the LHC, record the outcome of each high energy collision. Both of these components are essential to perform the analysis and make the measurements presented in this thesis, where the data set collected by the ATLAS detector is used. The LHC machine and the ATLAS detector are the subject of this chapter, and are described in Sections 3.1, 3.2, and 3.3. The transformation of the high energy collisions recorded by the ATLAS detector into a format that makes measurements of the SM possible is described in Sections 3.4 and 3.5.

3.1 The Large Hadron Collider

The LHC is an immense scientific apparatus with which to perform high energy physics research in the 21st century. Housed in the tunnels of the former Large Electron Positron (LEP) machine, it is the world's largest and most energetic particle accelerator, with a circumference of 27 km allowing it to reach unprecedented energies. Specifically, the LHC is a circular superconducting synchrotron which accelerates beams of protons[11] in opposite directions. The beams are brought into collision at a centre-of-mass energy, $\sqrt{s}$, of up to 13 TeV[12] at four primary points located around the LHC ring, called the interaction points (IPs). The IPs are the locations of the four LHC detectors: ATLAS, CMS, LHCb, and ALICE.

3.1.1 LHC operation

Protons begin their journey to the desired collision energy not in the LHC machine itself but in an unassuming canister of hydrogen gas. Electrons are removed from hydrogen

[11] Beams of lead ions are also used at the LHC, but are not used for the measurements in this thesis.

[12] The design centre-of-mass energy of particle collisions at the LHC is $\sqrt{s} = 14$ TeV, although the data set for the measurements in this thesis was recorded with collisions operating at $\sqrt{s} = 13$ TeV.

atoms with an electric field and the resulting protons enter the LHC accelerator complex, illustrated in Figure 3.1. Starting with LINAC 2, the protons proceed through sequential stages of acceleration in increasingly large accelerators and centre of mass energy. Two beams of protons pass through the Proton Synchrotron (PS), Super Proton Synchrotron (SPS), and finally enter the LHC at 450 GeV where they circulate in opposite directions and are accelerated up to 6.5 TeV, the collision energy of each proton beam for the data used in this thesis.

The LHC itself consists of several electromagnetic devices to accelerate the proton beams as well as to steer and maintain their orbit. Two beam pipes, each containing one of the counter-circulating beams, are held in an ultra-high vacuum of 10^{-13} atm to minimise collisions with gas molecules. The bending of the counter-circulating beams to maintain their orbits is performed using magnetic fields, generated by 1232 superconducting dipole magnets. They are composed of Niobium-titanium (NbTi) filaments and are 15 m in length. Superfluid helium is used to cool the dipole magnets to 1.9 K[13], where they enter the superconducting phase. In this regime, the dipole magnets are able to generate an electric current of $11\,700$ A, equivalent to a magnetic field of 8.33 T. A series of further 329 quadrupole magnets are interspersed between the dipole magnets to provide corrections to the transverse profile of the beams to maintain their orbits. The most important quadrupoles are those located near the IPs which are used to focus the beam to a small size and increase the chance of a collision. Additional higher multipole magnets are used for further higher-order corrections to the beam profiles. The acceleration is performed using 16 radio-frequency cavities which also act to restore energy losses [67].

In nominal operating conditions, the proton beams are grouped into bunches as opposed to a continuous longitudinal stream, with a bunch consisting of 1.15×10^{11} protons. A total of 2808 bunches are organised into a discrete number of bunch trains, with each bunch in a train separated by 25 ns. At their nominal collision energies, bunches circulate the LHC machine with a frequency of 11.25 kHz, leading to a bunch crossing rate at the ATLAS IP of 31.6 MHz [67].

3.1.2 Luminosity

Many of the physics processes that are searched for and measured by the ATLAS detector, including Higgs boson production, have small cross sections. The production cross section of an interaction i, σ_i, is related to the number of events produced by interaction i, N_i, through

$$N_i = \sigma_i \int L(t)\mathrm{d}t, \tag{3.1}$$

[13]This makes the LHC the coldest known location in the universe and colder than the cosmic microwave background.

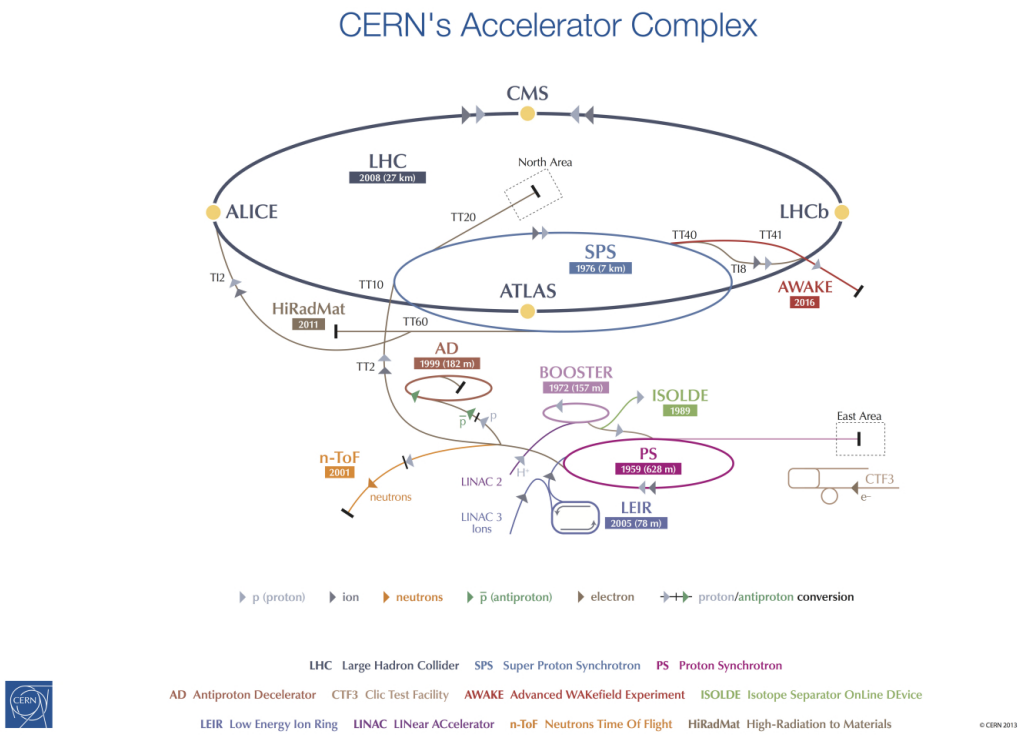

Figure 3.1: The accelerator complex at CERN, of which the LHC is the largest component at 27 km in radius. Sourced from Ref. [68].

where $L(t)$ is the instantaneous luminosity and $\int L(t)\mathrm{d}t = \mathcal{L}$ is the integrated luminosity. Mathematically, the cross section is proportional to the squared matrix element and represents the quantum probability of a transition from some initial state to a final state. Experimentally, the cross section is defined as a number of collisions per unit area and per unit time, divided by the incident flux [69], given in units of barn ($1\,\mathrm{b} = 1 \times 10^{-28}\,\mathrm{m}^2$). The instantaneous luminosity is a key design parameter of a particle collider. It is necessary for the LHC machine to provide a very large instantaneous luminosity such that events from rare physics processes are produced. The instantaneous luminosity is a function of LHC machine parameters, given by

$$L = \frac{N_b^2 n_b f_{\mathrm{rev}}}{4\pi \Sigma_x \Sigma_y} F, \tag{3.2}$$

where N_b is the number of particles in each bunch, n_b is the number of bunches in each beam, f_{rev} is the revolution frequency, $\Sigma_{x(y)}$ is the transverse component of the beam size along the x (y) axis, and F is a factor to account for the fact that the beams cross at an angle at the IP. The beam size is more commonly expressed in terms of the normalised transverse emittance, ϵ_{N}, and the transverse size of the beam at the IP, β^*, to give,

$$\mathcal{L} = \frac{N_b^2 n_b f_{\mathrm{rev}} \gamma_r}{4\pi \epsilon_{\mathrm{N}} \beta^*} F. \tag{3.3}$$

The values of ϵ_{N} and β^* are 3.75 μm and 0.55 m, respectively, resulting in an instantaneous luminosity of $L \sim 10^{34}$ cm$^{-2}s^{-1}$ [67]. The transverse spread of protons within a bunch in position-momentum space defines the transverse emittance, ϵ, of the LHC beams. The normalised transverse emittance is given by $\epsilon_{\text{N}} = \beta\gamma\epsilon$, where $\beta = v/c \sim 1$ and $\gamma = E_{\text{beam}}/m_p$ (E_{beam} is the beam energy and m_p is the mass of the proton). The envelope of all proton trajectories within a beam as the beam is focused and defocused by quadrupole magnets is characterised by the β-function. The minimum value of the β-function at the ATLAS IP is β^* [70].

The duration of time in which proton beams are circulating within the LHC in bunch trains, where bunches in a train are separated by 25 ns, and colliding at the ATLAS IP, is known as a *fill*. Over the course of the Run 2 data-taking years, the LHC machine delivered 156 fb^{-1} of integrated luminosity at the ATLAS IP. ATLAS aims to record as much data as possible within an LHC fill, and the duration of time in which ATLAS is able to continuously collect data is called a *run*. Within a run, *luminosity blocks* (LB) of approximately 60 s duration refer to a time in which the instantaneous luminosity and detector conditions are roughly constant. A set of requirements on the quality of individual LBs then defines a set of LBs which are declared *good for physics* [71]. The ATLAS detector was able to record 94% of the delivered luminosity, of which a total of 139 fb^{-1} is used for the data analysis presented in this thesis. Figure 3.2a shows the delivered and recorded integrated luminosity accumulating with time during Run 2. However, achieving a very high instantaneous luminosity has the drawback that many instances of pp interactions take place per bunch crossing, in addition to the single collision generating a hard scatter of interest. These additional pp interactions create energy flows in the detector material uncorrelated with that of the hard scatter of interest and are called *pile-up*. The average number of interactions per bunch crossing is a measure of the amount of pile-up and is displayed in Figure 3.2b for each data-taking year of Run 2. Pileup interactions originating from the same bunch crossing are typically referred to as *in-time* pile-up. It can also be the case that interactions from successive or preceding bunch crossings are recorded in a single event. This can occur for two reasons: firstly, that the time taken for a detector sub-system to record a signal is longer than the bunch spacing of 25 ns; and secondly, that some particles move slower than the speed of light and are delayed by more than 25 ns relative to relativistic particles. Interactions of this type are called *out-of-time* pile-up. The average number of pile-up interactions per bunch crossing is 33.7 for the full Run 2 data set [72].

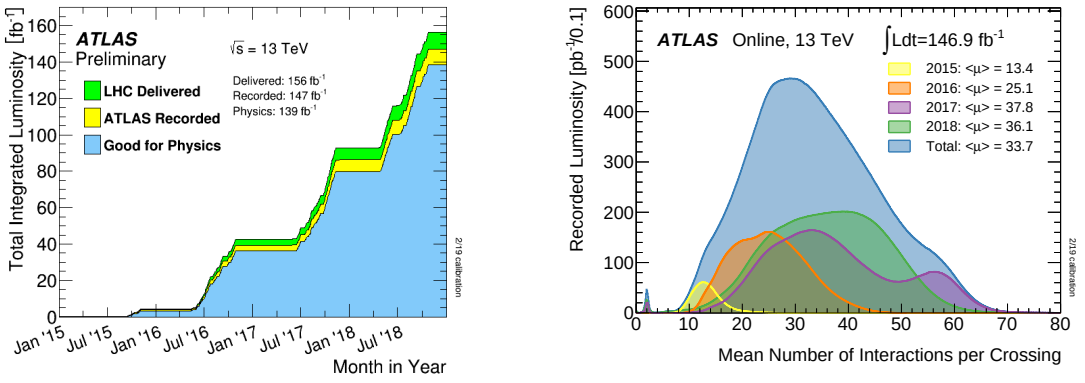

(a) **(b)**

Figure 3.2: Distributions of (a) the total integrated luminosity produced by the LHC and that recorded by the ATLAS detector between 2015 and 2018, and (b) the average number of interactions per bunch crossing between the same years of data-taking. Sourced from Ref. [72].

3.2 The ATLAS detector

The ATLAS (**a** **T**oroidal **L**HC **A**pparatu**S**) detector [73] is a general-purpose particle detector located at one of the four IPs around the LHC ring. The design of the detector reflects its comprehensive physics programme, ranging from precision measurements of SM parameters, searches for new physics phenomena, and (since 2012) precision measurements of the Higgs boson. Several detector components surround the beam line in increasing radii, consisting of a central *barrel* section and closed with two *endcaps* either side, giving ATLAS a cylindrical shape with a diameter of 25 m and length of 44 m. This gives a coverage of almost 4π in solid angle, necessary for accurate measurements of the total momentum transverse to the beam line. Given the scale of the detector and the wide-ranging physics programme, the detector is maintained and operated by an international collaboration of over 3000 people. Figure 3.3 illustrates the different components comprising the ATLAS detector.

3.2.1 Coordinate system

Of central importance to studying the pp collisions collected by the ATLAS detector is a standardised measurement system, and the nomenclature defined in this section is used throughout this thesis. The centre of the coordinate system is defined at the centre of the detector (the IP). The beam line serves as the z-axis, whilst the x- and y-axes define the transverse plane to the beam line, and point toward the centre of the LHC ring and upwards, respectively. More convenient to studying the pp collisions is to use a cylindrical coordinate system: the variables r and ϕ describe the radial distance from and the azimuthal angle around the z-axis, whilst the variable θ describes the polar angle between a particle's trajectory and the z-axis in the x–z plane. Since collisions are between

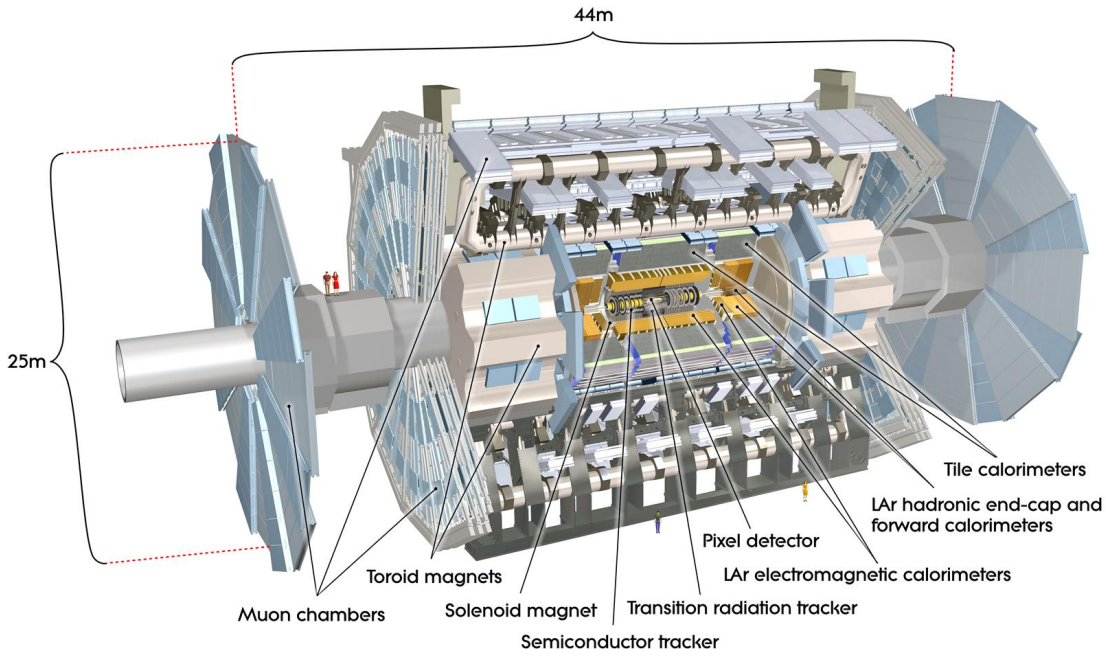

Figure 3.3: Computer generated illustration of the different components comprising the ATLAS detector. Two humans are included to demonstrate the scale. Sourced from Ref. [73].

partons inside the protons, each with an unknown fraction of longitudinal momenta, the angle θ is affected by longitudinal boosts and is not Lorentz-invariant. For this reason, the quantity called pseudorapidity, η, replaces the polar angle and is defined by

$$\eta = -\ln \tan\left(\frac{\theta}{2}\right). \tag{3.4}$$

The pseudorapidity is the massless limit of the rapidity, $y = \frac{1}{2}\log\left(\frac{E+p_z}{E-p_z}\right)$, where p_z is the longitudinal momenta of a particle. These quantities are preferred because differences in them are Lorentz invariant and thus independent of the longitudinal momentum fractions of the colliding partons. The pseudorapidity is defined such that $\eta = 0$ corresponds to the direction perpendicular to the beam line, whilst $|\eta| \to \infty$ corresponds to directions parallel to the beam line.

A geometric distance parameter in the η–ϕ plane, ΔR, is used ubiquitously throughout this thesis, and is defined by

$$\Delta R = \sqrt{\Delta\eta_{ij}^2 + \Delta\phi_{ij}^2}, \tag{3.5}$$

where $\Delta\eta_{ij}$ and $\Delta\phi_{ij}$ are the differences in pseudorapidity and azimuthal angle of two particle trajectories, i and j, in the detector.

Additionally, the momentum of a particle in the detector is typically described in the transverse plane since the average initial transverse momentum of the colliding protons is zero. The transverse momentum, $\boldsymbol{p}_{\mathrm{T}}$ (with magnitude p_{T}), is given by

$$\mathbf{p}_{\mathrm{T}} = (p_x, p_y), \tag{3.6}$$

where p_x and p_y are the momentum components of a particle projected along the x- and y-axes, respectively. The correspondence between three-momentum, $\mathbf{p}$, in Cartesian coordinates and the basis typically used in this thesis is given by

$$\mathbf{p} = (p_x, p_y, p_z) = (p_{\mathrm{T}} \cos\phi, p_{\mathrm{T}} \sin\phi, p_{\mathrm{T}} \sinh\eta), \tag{3.7}$$

where $p_{\mathrm{T}} = \sqrt{p_x^2 + p_y^2}$.

3.2.2 Magnet system

Essential to precision measurements of charged particle momenta within the detector is a magnetic field to bend the trajectories. The magnet system in the ATLAS detector consists of three components: the central solenoid, the barrel toroid, and the endcap toroids. The field lines generated by the magnetic fields are shown in Figure 3.4. The central solenoid is located between the inner detector (ID) and the electromagnetic calorimeter, and generates a 2 T axial magnetic field in the ID. This bends charged-particle trajectories in the plane transverse to the beam line. The barrel and endcap toroids generate toroidal magnetic fields in the muon spectrometer, bending charged particle trajectories longitudinally. Consisting of eight coils, the barrel toroid is 25.3 m in length and located at a radius of 9.4–20.1 m from the beam line. The endcap toroids each consist of eight coils, with a length of 5 m and located at a radius of 1.65–10.70 m. The magnetic field varies as a function of $|\eta|$; the barrel toroid provides 2–6 Tm of bending power in the range $|\eta| < 1.4$, whilst the endcap toroids provide 4–8 Tm in the range $1.6 < |\eta| < 2.7$. The transition region, $1.4 < |\eta| < 1.6$, experiences degraded bending power (up to a factor of 2) from a combination of the barrel and endcap toroidal fields.

3.2.3 Inner detector

The closest detector system to the beam line is the ID, designed to precisely measure the momentum of charged particles. Given the high multiplicity of charged particles in the ID, several high-granularity detector components are used, which include the insertable B-layer (IBL), pixel detector, semiconductor tracker (SCT), and the transition radiation tracker (TRT). In all instances, the components comprise a barrel section made of concentric cylinders, and two endcap sections where discs are positioned in the transverse plane. The ID is immersed in the 2 T axial magnetic field generated by the central solenoid and measures charged-particle trajectories up to $|\eta| < 2.5$. The components of

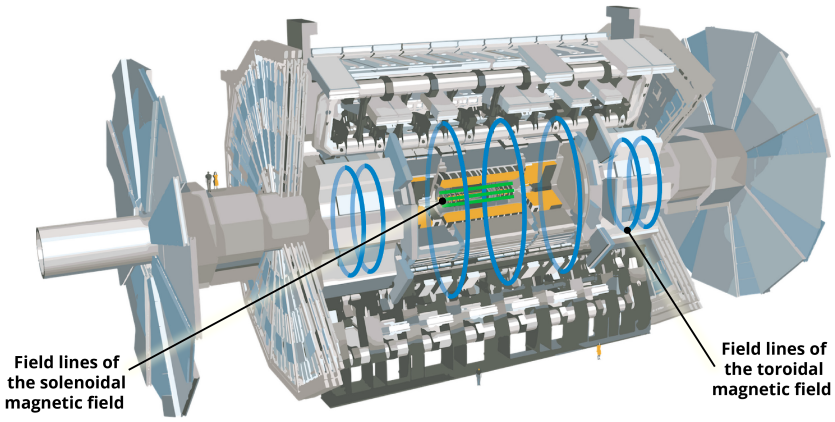

Figure 3.4: Computer generated illustration of the magnetic fields and the directions of the field lines in the ATLAS detector. Sourced from Ref. [74].

the ID are shown in Figure 3.5a and the trajectory of a charged particle as measured by the detector components is shown in Figure 3.5b. Charged-particle trajectories as measured in the ID are typically referred to as *tracks* and the ID and its components are otherwise known as *tracking* detectors.

Pixel detector

The innermost layer of the ID is the pixel detector, located 27.5–122.5 mm from the beam line where the highest charged-particle multiplicity is expected. Silicon pixels, numbering on the order of 80 million, are arranged in three layers in the barrel region ($|\eta| < 1.5$) and three discs in each endcap region ($1.5 < |\eta| < 2.5$). A silicon pixel has a size of 50×400 μm^2 in r–ϕ and z. The resolution of a pixel is 10×115 μm in the transverse and longitudinal directions. The IBL, added to the detector between 2013–2015, adds a fourth layer to the pixel detector in the barrel region, improving the precision of impact parameters of tracks which leads to improvements in the identification of heavy-flavour quarks.

Semiconductor tracker

Between radii of 299–514 mm from the beam line, the charged-particle density is lower than in the pixel detector so larger silicon micro-strips perform tracking in this range. The SCT consists of four layers in the barrel region and nine discs in each endcap region. An SCT module comprises two layers of silicon micro-strip sensors with dimensions of 6–13 cm in length and 80 μm in width. The two layers of an SCT module are rotated by 40 mrad to maintain good spatial resolution, which is 17×580 μm in the transverse and longitudinal directions.

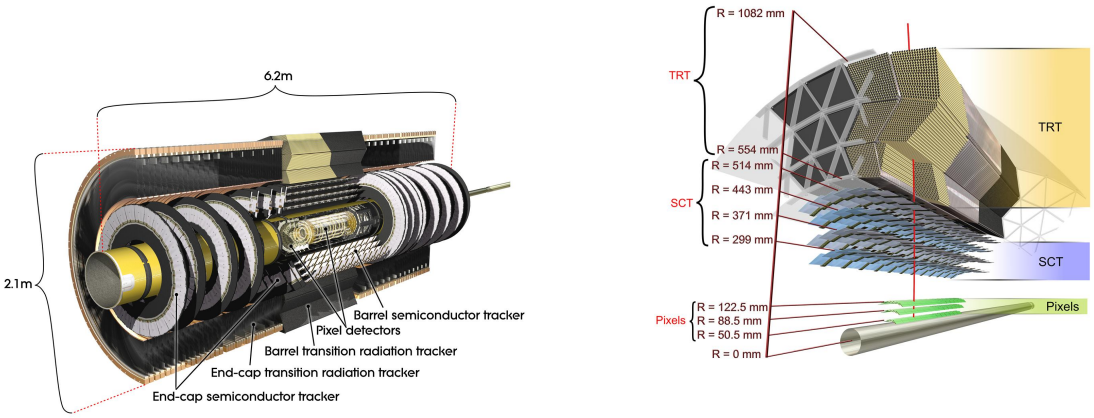

(a) (b)

Figure 3.5: Computer generated illustration of (a) the ID and (b) a trajectory of a charged particle traversing each component of the ID. Illustrations sourced from Ref. [75].

Transition radiation tracker

Finally, in the radial range of 554–1082 mm, tracking is performed by the TRT. The TRT comprises about $300\,000$ tubes, which are parallel with the beam line in the barrel and perpendicular in the two endcaps. The tubes are 4 mm in diameter and filled with xenon gas. A charged particle traversing the TRT ionises the xenon gas producing ions. A negative electric field generated at the walls of the straws accelerates the ions towards wires at the centre of the straws which results in a detectable signal. The drift time is determined and results in a resolution of 130 μm per straw. Only one-dimensional information in r–ϕ (for positive or negative η) is available in the range $|\eta| < 2.0$, with an average of 35 measurements in the TRT per charged-particle track. The TRT complements the pixel and SCT measurements since it is possible to estimate the mass of a charged particle with the TRT and therefore perform particle identification. This is because the amount of transition radiation depends on the particle mass.

3.2.4 Calorimeters

The calorimetry system in the ATLAS detector is located outside of the volume occupied by the ID and central solenoid and absorbs the total energy of all particles except muons and neutrinos. The calorimeters are *sampling* calorimeters, made up of alternating layers of *absorber* and *active* material. The absorber material reduces the energy of the incident particle and generates several other particles in the process, which then traverse the active material where the energy of that sample is measured. This process then repeats for the length of the calorimeter generating a shower of energy, classed as electromagnetic or hadronic.

Energy is typically lost in matter via bremsstrahlung and e^+e^- pair production for high energy electrons and photons, respectively. The radiation length, X_0, is the average distance an electron loses $\frac{1}{e}$ of its energy, and is $\frac{7}{9}$ of the mean free path of a photon. This quantity is the characteristic length scale of electromagnetic showers. Hadrons lose energy in matter via inelastic hadronic interactions, with an electromagnetic component from neutral pion decays. The nuclear interaction length, λ, describes the mean free path of a hadron and is the characteristic length scale for hadronic showers. Both X_0 and λ vary for different materials. The size of the ATLAS calorimetry system is defined by the ability to contain the showers within the detector material, so materials with small values of X_0 and λ are preferred to reduce costs, the overall size, as well as the radiation tolerance of the materials. The calorimeters comprise two components: an electromagnetic calorimeter (ECAL) and a hadronic calorimeter (HCAL), and are illustrated in Figure 3.6. Measurements of particle energy are performed up to $|\eta| < 4.9$ and with complete ϕ-symmetry, providing accurate determination of the total transverse momentum.

Electromagnetic calorimeter

The ECAL measures the energy of electrons and photons up to $|\eta| < 3.2$. Lead is used as the absorber material whilst the active material is liquid argon (LAr). A barrel section is situated in the region $|\eta| < 1.475$ and two endcaps are situated in the region $1.375 < |\eta| < 3.2$. The ECAL makes use of an accordion geometry to ensure uniform coverage in ϕ. The transition region between the barrel and endcap, $1.37 < |\eta| < 1.52$, comprises inactive material and suffers from degraded performance so events with particles in this region are usually discarded.

The radial length of the ECAL is $22X_0$ in the barrel region and $24X_0$ in the endcap regions, corresponding to about half a metre. In the region corresponding to the tracking detectors ($|\eta| < 2.5$), the ECAL is segmented into three layers in depth to perform precision measurements of electrons and photons, and to distinguish $\pi^0 \to \gamma\gamma$ decays. The first layer has a granularity of $\eta \times \phi = 0.003 \times 0.1$ and measures showers initiated upstream of the ECAL. The second layer has a radial length of $16X_0$ and granularity of $\eta \times \phi = 0.025 \times 0.025$; this layer contains the majority of the deposited energy. The third layer has the coarsest granularity of $\eta \times \phi = 0.05 \times 0.025$ and a thickness of $2X_0$. An additional layer, *pre-sampler*, is located before the active material of the ECAL to measure showers initiated upstream of the ECAL. The endcap ECALs beyond $|\eta| > 2.5$ have two segmentations with coarser granularities.

Hadronic calorimeter

The HCAL comprises three components: the tile calorimeter (TileCal) covering $|\eta| < 1.7$, a hadronic endcap (HEC) covering $1.5 < |\eta| < 3.2$, and a forward calorimeter (FCal)

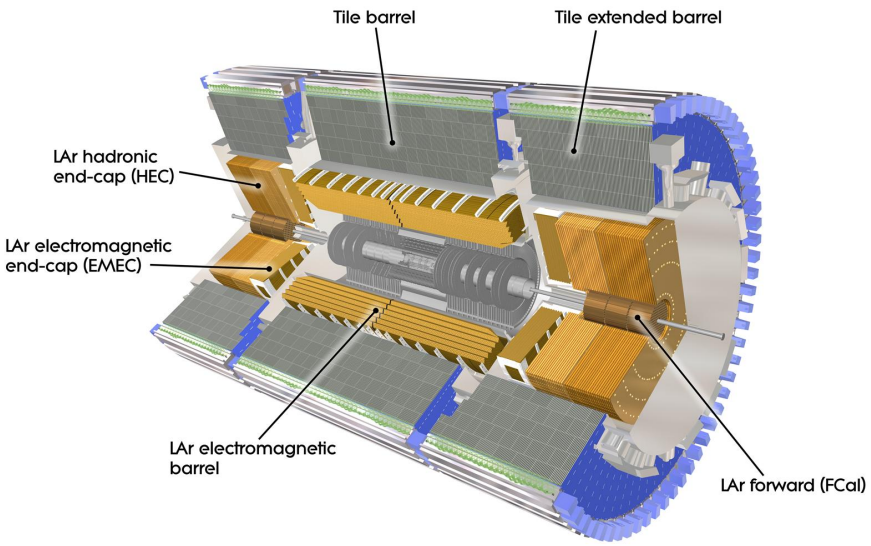

Figure 3.6: Computer generated illustration of the calorimetry systems in the ATLAS detector. Sourced from Ref. [76].

covering $3.1 < |\eta| < 4.9$. The total radial length of the HCAL is about 11λ, or 2 m. The HCAL is larger than the ECAL since hadronic showers are typically wider and longer than electromagnetic showers because of the significant contribution to the shower development from strong interaction scattering processes. The characteristic length scale of hadronic showers is the nuclear interaction length, λ, which is longer than the radiation length, X_0. This is because the hadron-nucleon cross section, occurring through the short-range strong force, is smaller than the cross sections governing the interactions of electrons and photons with detector material. Additionally, the larger masses of incident hadrons lead to large momentum transfer in inelastic nuclear interactions, generating secondary particles with large transverse momentum scattered at large angles. The granularity is $\eta \times \phi = 0.1 \times 0.1$, coarser than the ECAL.

The TileCal consists of a central barrel section ($|\eta| < 1.0$) and two extended barrels ($0.8 < |\eta| < 1.7$). It is composed of steel absorber plates with plastic scintillator tiles serving as the active material. The HEC comprises two LAr wheels per endcap interspersed with copper absorber plates, covering $1.5 < |\eta| < 3.2$. The FCal consists of copper and tungsten absorber plates with LAr active material, completing the $|\eta|$ range up to 4.9.

3.2.5 Muon spectrometer

The final and largest component of the ATLAS detector is the muon spectrometer (MS). Muons produced in pp collisions have a flight length of the order of several kilometres and are typically minimum-ionising particles (MIPs) at the energies they are produced,

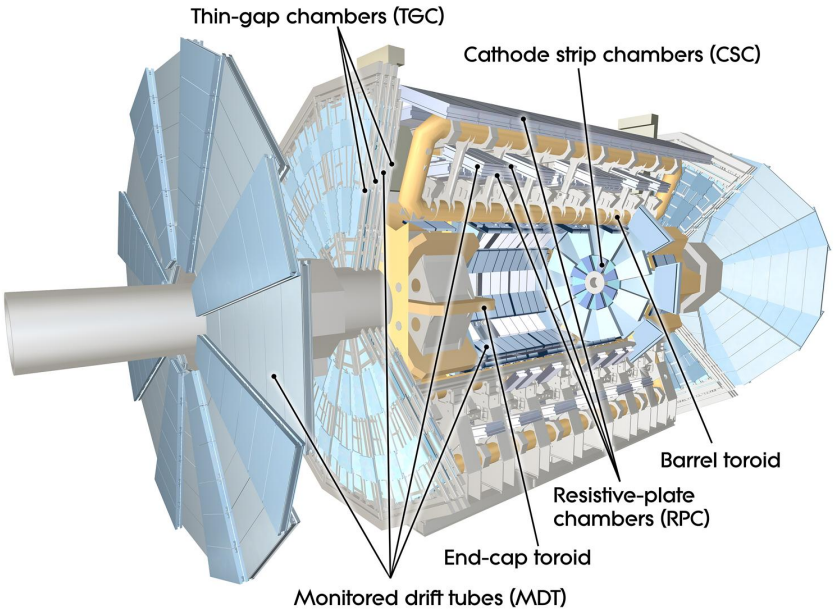

Figure 3.7: Computer generated illustration of the muon spectrometry sub-systems in the ATLAS detector. Sourced from Ref. [77].

meaning they do not generate a shower and instead traverse the entire ATLAS detector. The MS is situated on the periphery of the ATLAS detector, immersed in the toroidal magnetic field, to measure the momenta and electric charge of muons, as well as to provide fast trigger decisions on events containing high energy muons. An illustration of the MS is shown in Figure 3.7.

Measurements of the muon momentum are performed in the range $|\eta| < 2.7$. In the barrel region ($|\eta| < 1.4$), three cylindrical layers are placed around the beam line whilst chambers are placed perpendicular to the beam line in the endcaps. Several types of detector are used and are based on differing technologies. Generally, they rely on the principle of gas ionisation generating drifting electric charge, which can be collected at electrodes and measured. Precision measurements of muon momentum are performed using Monitored Drift Tubes (MDTs) at lower $|\eta|$ and Cathode Strip Chambers (CSCs) at larger $|\eta|$ to tolerate the higher particle multiplicity. The average resolution of these components is about 40 μm in the bending plane. The fast detection of events with high-momentum muons is performed using detectors with faster readout capability: Resistive Plate Chambers (RPCs) and Thin Gap Chambers (TGCs) are used in the barrel and endcap regions, respectively.

3.3 Expected detector performance

The expected performance of the different components comprising the ATLAS detector, as well as the range in $|\eta|$ with which they are used to measure particle momenta and

Table 3.1: The expected performance of the different components of the ATLAS detector with energy and momenta given in [GeV] [73]. The resolution of the MS is independent of any measurements combining tracks from the ID.

Detector component	Resolution	$\lvert\eta\rvert$ coverage
ID	$\sigma_{p_\mathrm{T}}/p_\mathrm{T} = 0.05\% \times p_\mathrm{T} \oplus 1.0\%$	< 2.5
ECAL	$\sigma_E/E = 10\%/\sqrt{E} \oplus 0.7\%$	< 3.2
HCAL	$\sigma_E/E = 50\%/\sqrt{E} \oplus 3.0\%$	< 4.9
MS	$\sigma_{p_\mathrm{T}}/p_\mathrm{T} = 3\%$ (12%) for $p_\mathrm{T} = 10$ (1000) GeV	< 2.7

energy, is shown in Table 3.1. The resolution of the ID has a constant term arising from multiple scattering and a term proportional to the p_T due to degrading resolution as tracks curve less in the magnetic field (limited by the spatial resolution of the detector). The calorimeter resolution has a constant term to account for non-uniformities in the calorimeter response, and a stochastic term proportional to $1/\sqrt{E}$ arising from statistical fluctuations in the development of the particle shower.

3.4 Trigger and data acquisition

The nominal crossing rate of proton bunches in the ATLAS detector is $31.6\,\mathrm{MHz}$, with several pp collisions per bunch crossing. It is therefore impossible to expect to be able to record the outcome of each of these collisions. The ability of the detector to generate a signal and transfer it to permanent storage limits this immediately, but it is also unnecessary to record every collision event since the vast majority will not contain the interesting interactions of the SM that are to be tested and measured with the ATLAS detector. A combination of hardware (built onto the detector) and software, known as the *trigger*, is used to make fast decisions on whether to retain an interesting event, whilst a *data acquisition* (DAQ) system handles the flow of data from the detector to permanent computer storage[14]. The combination of the trigger and DAQ helps to reduce the readout rate and ensure that only interesting events are kept for data analysis. Figure 3.8 shows a flowchart of the interplay between the trigger and DAQ systems, indicating the reduction of the event and data rates with each stage.

The trigger system comprises two components called the Level 1 (L1) and the High Level Trigger (HLT):

Level 1

The L1 trigger makes use of dedicated hardware built into the detector to make a decision on event rejection within 2.5 μs and reduces the event rate to 100 kHz.

[14] Data written to permanent storage by the DAQ system and after passing the trigger are said to be available for *offline* analysis.

The decision is made using information from the calorimeters (with a reduced granularity of $\eta \times \phi = 0.1 \times 0.1$) and trigger chambers in the MS. Regions of interest (RoIs) are built from the η and ϕ coordinates of the locations of significant detector activity and candidate electrons and muons, as well as a measure of the total transverse momentum imbalance, are constructed. Selection requirements based on the isolation, invariant mass, and ΔR between these candidates are also possible. Event data is stored in buffers whilst a decision is made, since the bunch crossing rate is much shorter than the L1 latency.

High Level Trigger

The HLT makes use of software to refine the selected events from L1 and further reduce the event rate to 1.5 kHz. The HLT has a decision latency of about 0.5 s and has the full detector readout available to make a decision. This means that tighter selection requirements and complex algorithms that resemble those used in offline data analysis can be used.

A *trigger menu* is active during operation of the detector, and consists of a set of *trigger chains*. These are strings identifying the set of selection requirements and thresholds used in L1 and HLT, with different trigger chains targeting the predicted signatures of many of the final states searched for in the physics programme. Different trigger chains will additionally have different rates. In some instances, trigger chains are scaled by a factor N, signifying that only one in N events passing the trigger chain is written to permanent storage. This is so as to ensure the HLT output rate stays within 1.5 kHz.

3.5 Event reconstruction

Events accepted by the trigger and DAQ systems are written to permanent storage and undergo offline event reconstruction. This means the complete event information recorded by the detector is passed through a complex chain of algorithms in order to accurately identify and reconstruct the energy and momenta of the particles in the event. Following this reconstruction sequence, an event is described by a collection of candidate objects (e.g. electrons, muons, photons etc.) each with a particular four-momenta. These candidate objects are then calibrated so that they can be used in data analysis. The identification of different particles is achieved by using the expected behaviour of different particles in the detector material. Figure 3.9 shows several distinctive signatures of particles which are measurable in the ATLAS detector. Only a small number of particles are stable enough[15] to be measurable in the ATLAS detector. The rest decay before interacting with the detector material and are thus indirectly measurable through their decay products. The following descriptions highlight the specific physics objects used for the measurements presented in

[15] Stable particles in ATLAS are generally those that have a lifetime $\tau > 10$ ps.

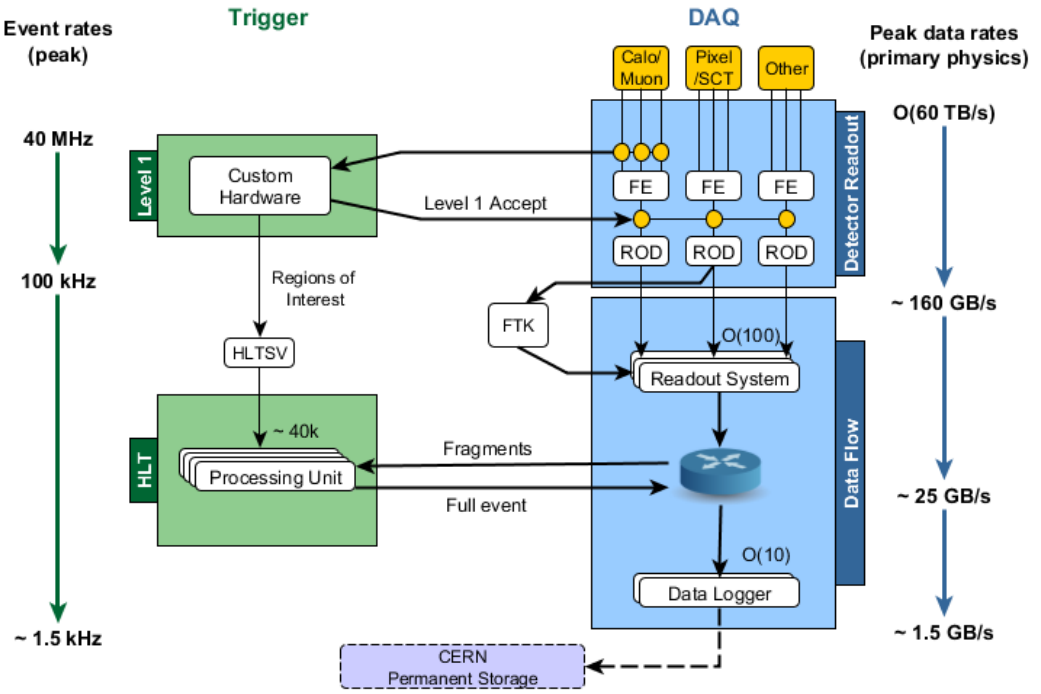

Figure 3.8: Functional diagram of the ATLAS Trigger and Data Acquisition system in Run 2 showing expected peak rates and bandwidths through each component. Sourced from Ref. [78].

this thesis (electrons, muons, jets, and missing transverse momentum). Other objects that can be reconstructed, such as photons and hadronic tau decays, are not discussed.

3.5.1 Tracks and vertices

A *track* is the measured trajectory of a charged particle in the ID. It consists of several *hits*, which are the measurements of the track in each layer of the ID. Whilst they are expected to exhibit a helical shape because of the solenoidal magnetic field, deviation from this expectation can occur due to energy loss and multiple scattering. In order to construct tracks, coordinates from the pixel and SCT detectors, as well as the drift circles from the TRT, are required. A combination of algorithms take this information to build and improve reconstructed tracks [80, 81].

The first is a so-called *inside-out* algorithm. In this algorithm, seed tracks are formed using pixel detector hits and hits in the first layer of the SCT. A Kalman filter [82] is used to find the most likely track trajectory given knowledge of the detector material and the magnetic field. Ambiguity in hits associated to multiple track candidates is resolved by feeding tracks with $p_{\mathrm{T}} > 400$ MeV into the ATLAS Global χ^2 Track Fitter [83]. A further series of quality requirements are also applied to reduce fake tracks, which originate from the high

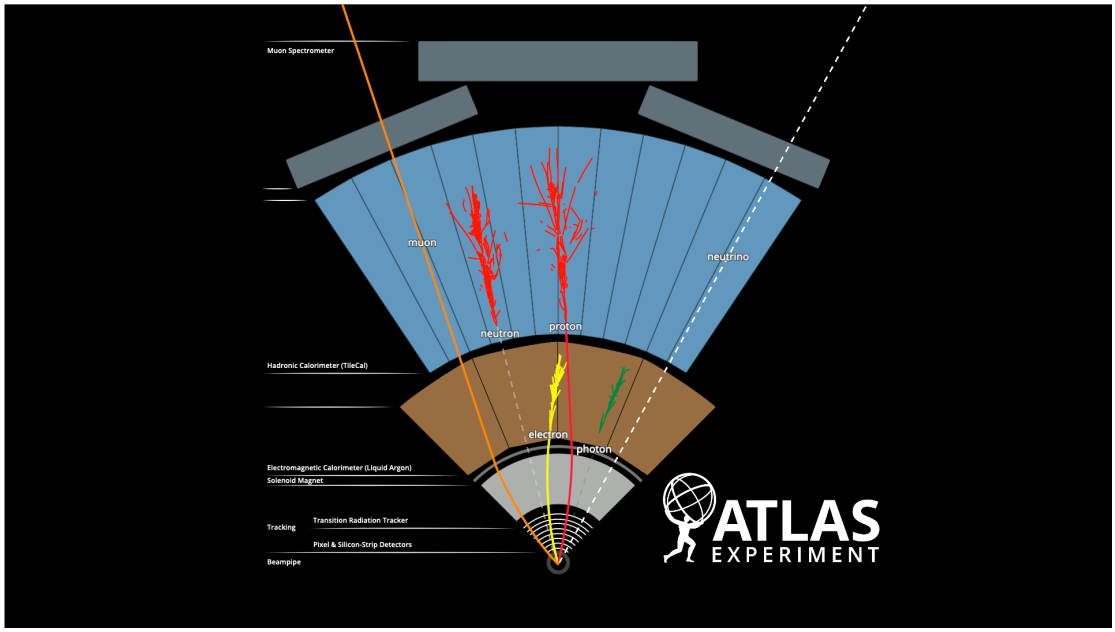

Figure 3.9: Transverse view of a quadrant of the ATLAS detector depicting the behaviour of different particles as they interact with the detector material. Sourced from Ref. [79].

charged-particle multiplicity. These include requiring that tracks have more than nine hits in the pixel and SCT layers, no missing hits for a given track trajectory, and $p_{\mathrm{T}} > 400$ MeV. A second algorithm works backwards (outside-in). This algorithm starts with unused track seeds in the TRT and extrapolates the track trajectory into the SCT and pixel layers. The use of this second algorithm improves the reconstruction of particles with displaced vertices. A track is then described by a set of five parameters, $(d_0, z_0, \phi, \theta, q/p)$, which are depicted in Figure 3.10. The quantities d_0 and z_0 are the transverse and longitudinal impact parameters, describing the minimal distance from the track to the beam line and the distance from the point of the track used to calculate d_0 to the centre of the coordinate system, respectively. The quantity q/p is the ratio of the measured charge of a track to its momentum.

A *vertex* is the spatial location of a pp interaction, defined by the coincidence of at least two reconstructed tracks [70, 84]. *Primary vertices* (PVs) are those vertices associated with the interaction of colliding protons, whilst *secondary vertices* (SVs) are those produced by further particle decays in the detector volume as well as photon conversions into an e^+e^- pair[16]. The reconstruction of vertices proceeds in two steps: vertex finding and vertex fitting, which are performed simultaneously. First, a pool of selected tracks are associated with a candidate vertex and a fit is performed using the impact parameters of the tracks. Incompatible tracks with the candidate vertex are removed and used to seed

[16]Photon conversions into e^+e^- pairs are caused by the interaction of a photon with the detector material in the ID, and are typically found by searching for track(s) that do not point back to the PV or have several missing hits in the first layers of the pixel detector.

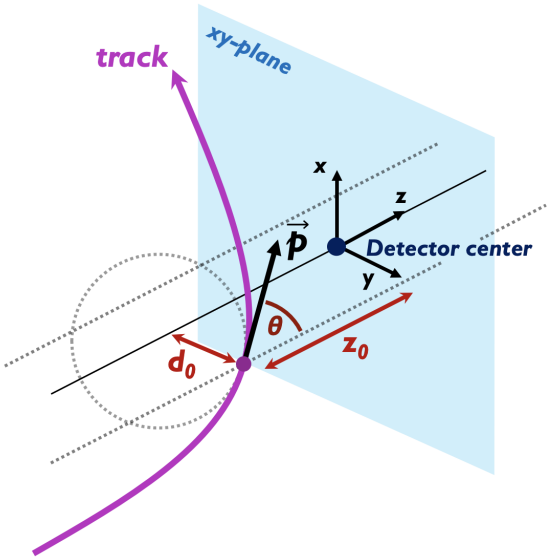

Figure 3.10: Illustration of a charged-particle track in the ATLAS detector and the associated parameters describing its trajectory. Modified from [85].

and fit another vertex. The algorithm then iterates. Each event will contain a number of reconstructed PVs, N_{PV}, which is a measure of the amount of pile-up interactions in each bunch crossing. Out of all reconstructed PVs, the vertex associated with the hard scatter generating the high-p_{T} particles of interest is the vertex with the largest sum of squared p_{T} of associated tracks, $\sum p_{\text{T}}^2$, and with at least three associated tracks. This vertex is hereafter referred to as the primary vertex. Other remaining vertices are pile-up vertices or SVs. The reconstruction of SVs is typically constrained using PV information, such as in the case of heavy-flavour hadron decays or photon conversions.

3.5.2 Electrons

The distinctive signature of electrons traversing the ATLAS detector is that of a reconstructed track in the ID followed by an energy deposit in the ECAL. An illustration of the path of an electron through the detector and the several detector layers it passes through are shown in Figure 3.11. The reconstruction of electron candidates thus relies on close matching of ID tracks to energy deposits in the ECAL to accurately reconstruct the energy and momenta of electrons. Many of the electron candidates reconstructed in the ATLAS detector are mis-identified hadrons, photon conversions, or electrons from heavy-flavour hadron decays [86], and are not of interest for the measurements in this thesis. Therefore, identification and isolation requirements are applied to reconstructed electron candidates to reject events of this type and maximise the number of selected prompt electrons (high-p_{T} electrons originating from the hard scatter of two protons).

The first stage of electron reconstruction is the identification of energy deposits in the

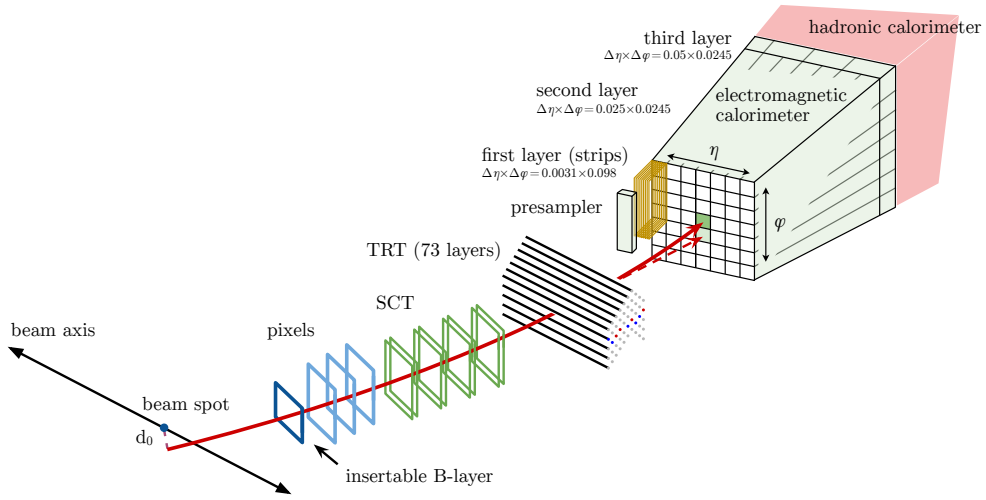

Figure 3.11: Computer generated illustration of the trajectory of an electron, shown in red, as it traverses the ID and calorimetry sub-systems of the ATLAS detector. The dashed red trajectory indicates a radiated photon produced from the interaction of the electron with the detector material in the ID. Sourced from Ref. [90].

ECAL. *Topological clusters* are formed by searching for energy deposits from calorimeter cells that are four times greater than that expected from electronic noise and pile-up. Surrounding cells with more than two times the energy expected from noise and pile-up are also added to the cluster. A requirement on the fraction of energy measured in the ECAL layers with respect to the total measured energy in all calorimeter layers is efficient at rejecting pile-up [87, 88].

Tracks in the ID that are close in the η–ϕ plane to a cluster are extrapolated into the calorimeter using a Gaussian Sum Filter (GSF) algorithm [89] which takes into account significant energy losses from radiated photons (bremsstrahlung). Multiple tracks are ranked based on the number of hits in several layers of the ID and the proximity to the cluster barycentre. Two tracks which are associated with an SV and only have hits in the SCT and TRT detectors are classified as a photon conversion vertex. A candidate electron seed is formed if a cluster has $E_{\mathrm{T}} > 1$ GeV and is associated with a track with at least 4 hits in the SCT detector. Adjacent clusters are added to the electron seed if they are located within a window of size $\eta \times \phi = 0.0075 \times 0.125$[17]. This process leads to the formation of *superclusters* which are labelled as electron candidates, photon candidates, or ambiguous.

An identification algorithm is constructed using a likelihood discriminant to improve the purity of candidate electrons. Probability density functions are built for thirteen discriminating variables, with the final discriminant defined as the natural logarithm of the ratio of

[17] The asymmetric window size, which is larger in the ϕ direction, is because the axial magnetic field bends charged-particle trajectories in the transverse (r–ϕ) plane. Photons, which are electrically neutral, do not bend in the transverse plane, causing electromagnetic showers to have a larger spread in the ϕ direction.

the likelihood functions for electrons originating from signal and background sources [91]. The thirteen variables include the longitudinal and lateral shapes of the electromagnetic showers in the ECAL, several properties of tracks in the ID, and spatial compatibility of the electron track with the cluster in the ECAL [90]. A selection requirement on the likelihood discriminant results in a particular identification efficiency of prompt electrons, and is used to define *working points* (WPs). These WPs are mutually inclusive and are called *Loose*, *Medium*, and *Tight* (in order of increasing prompt lepton purity but decreasing efficiency). The efficiency of the identification algorithm is determined as the ratio of the number of electrons passing each identification WP to the total number of electron candidates and is measured in both MC simulation and data. Figure 3.12 shows the identification efficiency for each WP as a function of the transverse energy, E_{T}, and pseudorapidity, η, of electron candidates in data collected during the years 2015–2017. The efficiencies are measured using a *tag-and-probe* methodology with $J/\psi \to ee$ and $Z \to ee$ events[18]. The identification efficiency is about 72% (88%) at 30 GeV for the Tight (Loose) WP. Ratios of the identification efficiency as measured in data and MC simulation, called *scale factors*, are used in the measurements in this thesis to correct the performance of electrons in MC simulation to that in data and reduce dependence on MC predictions. The use of scale factors corrects for inaccurate predictions of the variables in the LH discriminant causing an increase in the identification efficiency for $E_{\mathrm{T}} < 15$ GeV, for example [91].

Electrons produced in electroweak interactions are typically characterised by little detector activity in their vicinity (i.e. they are *isolated*). This is in comparison to electrons from heavy-flavour hadron decays and mis-identified hadrons. The amount of detector activity in the vicinity of an electron candidate is described by two variables:

$p_{\mathrm{T}}^{\mathrm{varcone20}}$
: The track-based isolation variable sums the p_{T} of tracks with $p_{\mathrm{T}} > 1$ GeV within a cone around the electron candidate track (but not including the electron candidate track) of size $\Delta R = \min(10\ \mathrm{GeV}/p_{\mathrm{T}}\ [\mathrm{GeV}], 0.2)$. The dynamic cone size reflects the expectation that electrons produced in heavy-flavour hadron decays at low p_{T} are located nearby a broader spray of hadronic activity since the hadrons are less boosted.

$E_{\mathrm{T}}^{\mathrm{cone20}}$
: The calorimeter-based isolation sums the E_{T} of ECAL energy clusters in a cone of size $\Delta R = 0.2$; again, not including the energy deposits of the electron candidate.

Several isolation WPs are defined based on these variables. The relevant WP for the measurements in this thesis is the so-called *Tight* WP, requiring that $E_{\mathrm{T}}^{\mathrm{cone20}}/p_{\mathrm{T}} < 0.06$

[18] The identification efficiency obtained with $J/\psi \to ee$ events is measured in the range $5 < E_{\mathrm{T}} < 15$ GeV, whilst $Z \to ee$ events are used for $E_{\mathrm{T}} > 15$ GeV.

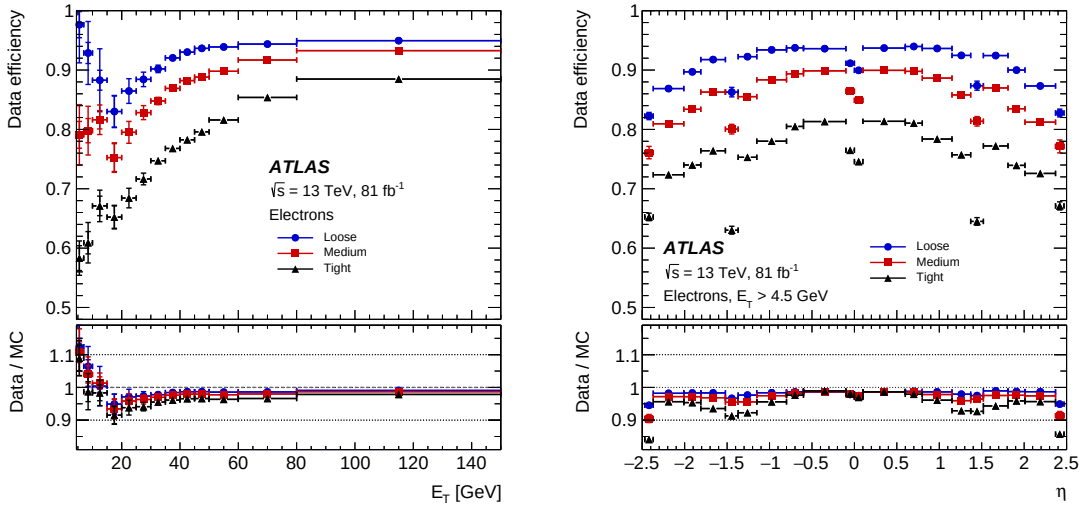

(a) (b)

Figure 3.12: The identification efficiency of reconstructed electron candidates measured in data as a function of (a) E_{T} and (b) η, for several WPs. The efficiency is measured using data obtained in 2015–2017 and using $Z \to ee$ events. The bottom panel displays the ratio of the efficiency measured in data to that measured in MC simulation. The efficiency is obtained by applying the data-to-MC ratio measured in $J/\psi \to ee$ and $Z \to ee$ to $Z \to ee$ simulation. Sourced from Ref. [91].

and $p_{\mathrm{T}}^{\mathrm{varcone20}}/p_{\mathrm{T}} < 0.06$ [91].

3.5.3 Muons

High reconstruction and identification efficiencies of muons are achieved by combining measurements of tracks in the MS with other detector components, such as tracks measured in the ID. The reconstruction of muons proceeds by forming measured hits in the MS into track segments. Track candidates are formed by performing a χ^2 fit that combines track segments in the different layers of the MS. A loose requirement is made on the association of a track candidate in the MS to the IP and several hits in the MS are added or removed to improve the fit quality. At this point, several types of muon reconstruction are defined:

Combined (CB)

CB muons are reconstructed within $|\eta| < 2.5$ by matching MS track candidates to tracks measured in the ID. A fit is performed based on hits in the ID and the MS, and takes into account energy loss in the calorimeters.

Inside-out combined (IO)

A complementary reconstruction method to CB muons starts with tracks measured in the ID and extrapolates the measurement to hits in the MS. A combined fit is performed to hits in the ID, calorimeters, and the MS.

Muon-spectrometer extrapolated (ME)

MS track candidates that are not matched to any ID track are extrapolated to the beam line. This extends the reconstruction of muon beyond the range of the ID and up to $|\eta| = 2.7$.

Segment-tagged (ST)

ID tracks are extrapolated to at least one track segment in the MS and the muon candidate assumes the measurement of the track in the ID.

Calorimeter-tagged (CT)

Tracks in the ID are extrapolated through the calorimeters. If energy deposits in the calorimeters are consistent with energy deposits of a MIP, a CT muon is defined.

All muon types (except for ME muons) are required to have at least 1 (5) hits in the pixel (SCT) detector, with an allowance of a maximum of two hits missing where one would be expected. CB muons represent the majority of reconstructed muon candidates in the ATLAS detector and are used for the measurements in this thesis.

Similarly to electrons, several identification WPs are defined to provide varying levels of efficiency and muon purity by applying several quality requirements on the reconstructed muon candidates. The WPs are defined to reduce the number of muons originating from hadron decays, whilst maximising the yield of muons from the hard scatter interaction. Amongst the WPs include the mutually inclusive WPs called *Loose*, *Medium*, and *Tight* (the Tight WP only makes use of CB and IO muons). These WPs are defined by making selection requirements on several quantities including track impact parameters, the fit quality of the combined track, and the compatibility of the momentum measurements in the ID and MS. The identification efficiencies are measured using the tag-and-probe methodology with samples of events enriched in $J/\psi \to \mu\mu$ and $Z \to \mu\mu$ processes. The identification efficiency of the Tight WP as measured in data and MC simulation is shown in Figure 3.13a as a function of muon candidate p_{T}, showing that the efficiency is greater than 90% for muon candidates with $p_{\mathrm{T}} > 10$ GeV. The identification efficiencies of the Loose, Medium, and Tight WPs are shown in Figure 3.13b as a function of muon candidate $|\eta|$ and with $p_{\mathrm{T}} > 10$ GeV, measured exclusively using $Z \to \mu\mu$ events. A very high efficiency of greater than 95% is measured across the η range[19]. The data-to-simulation scale factors are additionally within a few percent of unity [92].

Further requirements are then made to ensure muon candidates are isolated from nearby detector activity. This is particularly useful in rejecting muons originating from hadron decays. Variables which quantify local detector activity are defined, similarly to those

[19]The drop in efficiency at $\eta \sim 0$ is due to a lack of detectors in the MS in this region, leading to a degradation of measurements in this region.

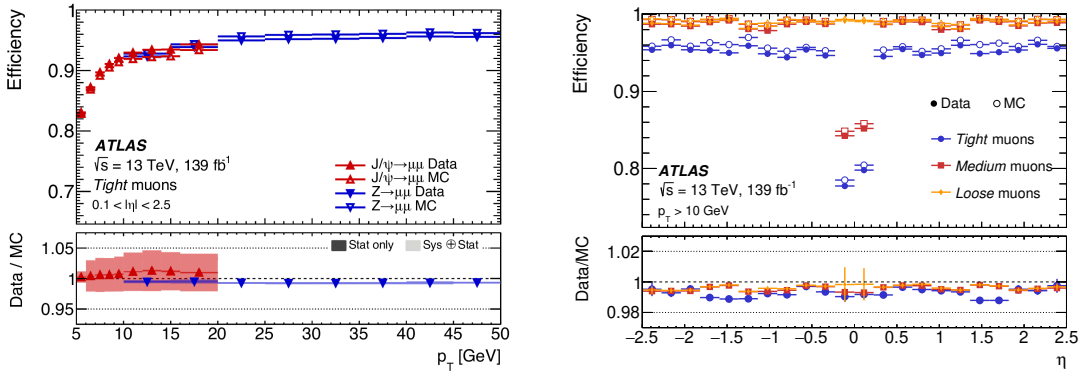

(a) (b)

Figure 3.13: The muon identification efficiencies measured in data and MC simulation for (a) the Tight WP measured as a function of muon candidate p_{T} in the range $0.1 < |\eta| < 2.5$ using event samples enriched in $J/\psi \to \mu\mu$ and $Z \to \mu\mu$ processes and (b) the identification of the Loose, Medium, and Tight WPs as a function of muon candidate $|\eta|$ with $p_{\mathrm{T}} > 10$ GeV measured exclusively with $Z \to \mu\mu$ events. The bottom panels display the ratio of the efficiencies measured in data to that measured in MC simulation. Sourced from Ref. [92].

used for electron candidates, based on tracks measured in the ID or energy deposits in the calorimeters. Several WPs are defined based on the requirements made on these isolation variables. The *Tight* WP, later used in the measurements in this thesis, is defined by

- $p_{\mathrm{T}}^{\mathrm{varcone30}}/p_{\mathrm{T}}^{\mu} < 0.04$,
- $E_{\mathrm{T}}^{\mathrm{cone20}}/p_{\mathrm{T}}^{\mu} < 0.15$,

where $p_{\mathrm{T}}^{\mathrm{varcone30}}$ and $E_{\mathrm{T}}^{\mathrm{cone20}}$ are the sum of tracks with $p_{\mathrm{T}} > 1$ GeV or calorimeter energy deposits in cones of a maximum size of $\Delta R = 0.3$ and $\Delta R = 0.2$, respectively, and not including the muon candidate measurements. The $p_{\mathrm{T}}^{\mathrm{varcone30}}$ is a dynamic cone size, similarly to the isolation variables used for electron candidates. The isolation efficiency is typically greater than 85% for muons with $p_{\mathrm{T}} > 10$ GeV, as measured in $J/\psi \to \mu\mu$ and $Z \to \mu\mu$ events [92].

3.5.4 Jets

Quarks and gluons are particles which experience parton showering and hadronisation due to the non-existence of unbounded particles with a non-zero colour charge. The result of this is that quarks and gluons produced in the final state of an interaction manifest in the ATLAS detector as a collimated spray of hadrons. Charged hadrons, and their decay particles, will leave measurable tracks in the ID, before depositing their energy in the ECAL and HCAL. It is generally impossible to reconstruct individual hadrons in the ATLAS detector due to pile-up and overlapping energy deposits. As such, this spray of energy, centred on a common axis of flight, is summed into one object called a *jet*. Jet objects are then reconstructed and calibrated to infer the initial energy and momenta of the quark or

gluon producing it.

The reconstruction of jets starts with the identification of energy deposits in the calorimeters using a *topological clustering* algorithm, similarly to the clustering performed for electrons in the ECAL. In this algorithm, clusters are seeded by searching for energy deposits in calorimeter cells which exceed the expected noise by a factor of 4. Adjacent cells with energy deposits exceeding the noise by a factor of 2 are then added. In a final step, a ring of cells with no requirement on their energy exceeding the expected noise are added. These form so-called *topo-clusters* [87].

The topo-clusters are then used as input to a new algorithm in use for analysis with the full Run 2 data set: the so-called *particle flow* (PFlow) algorithm [93]. The PFlow algorithm works by combining measurements of track momenta in the ID with corresponding energy measurements of topo-clusters in the calorimeters. The measurement of charged hadron tracks in the ID are typically more precise than those in the calorimeters and more robust against pile-up interactions, so the energy deposited in the calorimeters is removed if an associated charged-hadron track could be used instead. This algorithm is in use for jet momenta up to 100 GeV, since the precision of measurements in the calorimeters exceeds the precision of charged-particle track momenta in the ID beyond this range [94].

Jet reconstruction algorithm

Jets are formed by using an algorithm which combines the set of PFlow topo-clusters into singular objects. The algorithm used for jet reconstruction in data analysis of the full Run 2 data set is the *anti-k_t* algorithm [95]. This algorithm is an example of a *sequential recombination* algorithm, which adds clusters to a jet one at a time according to a given distance metric. Two distance measures are defined as

$$\begin{aligned} d_{ij} &= \min(k_{t,i}^{2p}, k_{t,j}^{2p}) \frac{\Delta R_{ij}^2}{R^2}, \\ d_{iB} &= k_{t,i}^{2p}, \end{aligned} \tag{3.8}$$

where $\Delta R_{ij}^2 = (y_i - y_j)^2 + (\phi_i - \phi_j)^2$ is the angular distance in y–ϕ space of two clusters i and j, and $k_{t,i(j)}$ is the transverse momentum of cluster i (j) with respect to the beam line. The quantities R and p are parameters of the algorithm. The quantity d_{ij} refers to the distance between clusters i and j, whilst d_{iB} refers to the distance between a cluster i and the beam line. The distances are calculated for the full set of PFlow clusters, and the minimum is found. If the smallest value is a d_{ij} then clusters i and j are merged into a single object. If the smallest value is a d_{iB} then the object i is a defined as a jet and is removed from the list of inputs. This algorithm iterates until all clusters have been merged into a jet.

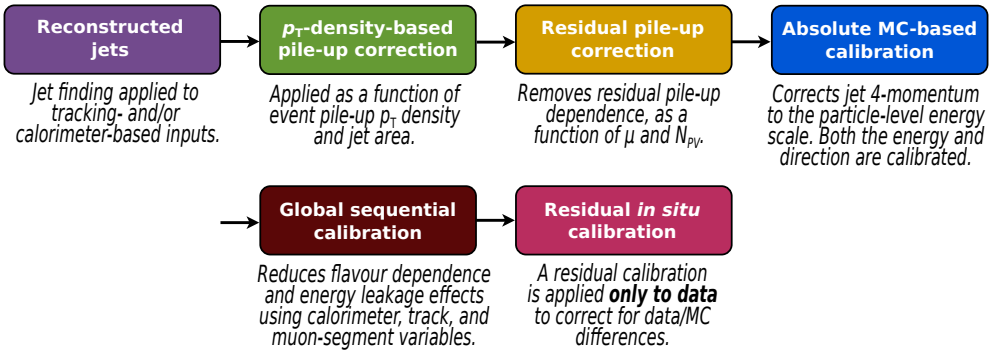

Figure 3.14: Flow chart depicting the stages of the jet energy scale calibration that are applied to the four-momenteum of a jet. Modified from [85].

The parameter R is an effective size of the jet, and assumes a value of $R = 0.4$ for the measurements in this thesis. The parameter p refers to the power of the transverse momenta of objects i and j, and determines the order in which clusters are considered. The anti-k_t algorithm assumes a value of $p = -1$, which means higher momentum clusters are merged into jets first, which results in relatively conical jets which are resilient against soft radiation that could originate from pile-up. Conversely, a value of $p = +1$ is called the k_t algorithm, which starts with lower momentum clusters in the jet reconstruction.

Jet calibration

The energy measurement of cells in the calorimeter is performed at the electromagnetic scale (EM scale), which correctly measures the energy deposited by electrons and photons. The calorimeters in the ATLAS detector have the property that they are *non-compensating*. This means the response to electromagnetic and hadronic showers is different since hadronic showers lose a significant amount of energy through slow neutrons, nuclear excitation, and neutrinos, which escape detection. Jets formed with the anti-k_t algorithm undergo a calibration procedure to correct the jet energy scale (JES) measured in data to that measured in MC simulation [94]. Corrections are applied to the jet four-momenta which affect the jet p_{T}, mass, and energy, and are shown in the flow chart in Figure 3.14. The stages of the jet calibration are as follows:

Origin correction

First, the jet four momentum is recalculated to account for the fact the jet was produced at the PV, as opposed to the centre of the detector which is assumed in the jet reconstruction algorithm.

Jet-area-based pile-up correction

The pile-up contribution is removed event-by-event from the jet p_{T} based on the expected energy density of soft contributions in an area given by the size of the

jet [96]. The expected energy density is determined using jets reconstructed with the k_t algorithm since soft radiation is considered in the clustering first.

Residual pile-up correction

A residual dependence on pile-up is present because the energy density is calculated in a limited region of the detector. The correction is determined in MC simulation and depends on the number of primary vertices, N_{PV}, and the average number of interactions per bunch crossing, μ.

Absolute MC-based calibration

The detector response is corrected to the response in MC simulation to take into account the non-compensation of the calorimeter response, energy loss in passive material, and biases in the $|\eta|$ reconstruction. The latter arises due to transitions in differing technologies and granularity of the ATLAS calorimetry systems. At this point, reconstructed jets are said to have been calibrated to the EM+JES scale.

Global sequential correction

A series of corrections are applied to account for effects including differences in jet evolution when initiated by a quark or gluon, and the flavour composition of hadrons in jets. These corrections modify the resolution of the jet response, but not the energy scale. The combination of measurements from several detector systems, including ID tracks, calorimeter energy deposits, and MS tracks, reduce the effect of punch-through in the MS, a phenomenon where high-momentum jets are not fully contained within the calorimeters and charged particles leave tracks in the MS.

Residual in-situ calibration

The final step in the JES calibration is a correction to take into account any residual differences in the jet response in data and MC simulation. Data-to-simulation scale factors are applied to data and measured in several sets of events enriched in $\gamma+\text{jet}$, Z/γ^*+jets, and multi-jet processes. Figure 3.15 shows the ratio of the average jet response as measured in data and MC simulation.

In addition to the JES, the jet energy resolution (JER) is parameterised and measured as a function of jet p_{T},

$$\frac{\sigma(p_{\text{T}})}{p_{\text{T}}} = \frac{N}{p_{\text{T}}} \oplus \frac{S}{\sqrt{p_{\text{T}}}} \oplus c, \tag{3.9}$$

where N and S represent constants to parameterise the effects of noise and stochastic fluctuation in detector response, and c is a constant term. The JER is measured in events with two jets (dijet events) using a balance methodology. This method uses the fact that dijet events should be perfectly balanced against each other in the transverse plane, such that their momenta can be precisely measured [94].

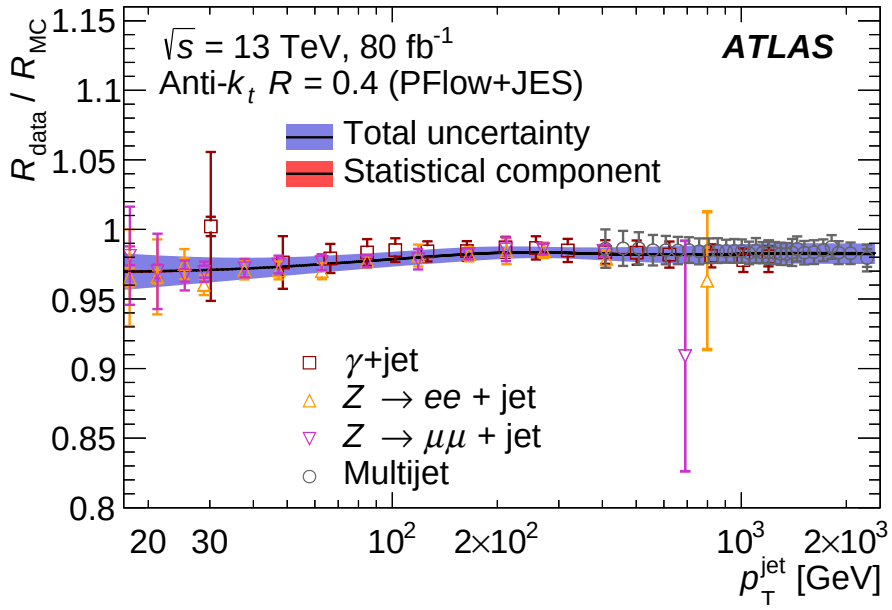

Figure 3.15: Comparison of the jet response as measured in data to that in MC simulation as a function of jet p_{T} for Z/γ^*+jets, γ+jet, and multi-jet events collected in 2015–2017. Sourced from [94].

Pileup jet mitigation

Before using the jets for data analysis as defined and calibrated above, a further requirement is made on a quantity designed to suppress jet activity arising from pile-up interactions. In Run 1, this quantity was the *jet vertex fraction* (JVF) [97]. The JVF computes the fraction of track p_{T} associated to the hard scatter PV out of the track p_{T} associated to all reconstructed PVs. A correction to JVF is defined that takes into account the dependence of the denominator on the number of primary vertices, N_{PV}. A second quantity, $R_{p_{\mathrm{T}}}$, is defined as the ratio of track p_{T} associated with a jet (where tracks must originate from the hard scatter PV) to the total calibrated jet p_{T}. It thus represents the charged-p_{T} fraction for jets from the hard scatter interaction, but is peaked towards zero for pile-up jets where a minimal amount of track p_{T} is expected from the PV of the hard scatter interaction. These two quantities are combined to form a two-dimensional likelihood function called the *jet vertex tagger* (JVT). Values of the JVT towards unity represent a higher likelihood the jet is from the PV of the hard scatter interaction, whilst values closer to zero are more likely to be pile-up jets [98].

3.5.5 Heavy-flavour jet identification

The identification of jets containing b-hadrons, c-hadrons, or neither b- or c- hadrons[20], collectively referred to as b-tagging, is an important task for the physics programme of the ATLAS detector. In particular for the measurements in this thesis, the rejection of events

[20] Jets containing such hadrons are referred to as b-jets, c-jets and light-flavour jets, respectively.

containing top quarks is achieved by rejecting events with b-jets since the decay of a top quark into a W boson and b-quark occurs with almost 100% probability.

Several properties of b-hadrons make them readily identifiable in the ATLAS detector. These properties include the b-hadron's long lifetime (of about 1.5 ps), its high mass (of about 5 GeV), and the high multiplicity of tracks from its decay particles. The long lifetime means a b-hadron will have a flight distance of a few millimetres, resulting in an SV representing the point at which the b-hadron decayed and is distinct to the PV of the hard scatter interaction. A number of algorithms are used to construct a probability that a jet contains a b- or c-hadron, or neither, based on measured tracks in an event and kinematic constraints. These include:

IP2D and IP3D

The IP2D and IP3D algorithms [99] search for tracks within jets that have large impact parameters.

SV1

The SV1 algorithm [100] identifies secondary vertices inside jets that would originate from the decay of a b-hadron.

JetFitter

The JetFitter algorithm [101] reconstructs the decay chain of a b-hadron to a c-hadron and the associated third vertex of the c-hadron decay.

RNNIP

The RNNIP algorithm [102] is a recurrent neural network which takes the impact parameter significances of jet tracks, the p_{T} fraction of tracks normalised to the jet p_{T}, and the angular distance to the jet axis, in order to output a b-jet score for the jet.

A high level b-tagging algorithm called *DL1r* [99, 103], among others, is a deep neural network which takes the output of the above four algorithms to provide a probability that a jet is likely to be a b-jet, c-jet, or light-flavour jet, given by p_b, p_c, and p_l, respectively. These are combined into a score defined by

$$\mathrm{D}_{\mathrm{DL1r}} = \ln\left(\frac{p_b}{f_c p_c + (1 - f_c) p_l}\right), \tag{3.10}$$

where the parameter f_c is set to 0.018 to give a particular discrimination power between b- and c-jets. The output score for the DL1 b-tagging algorithm (equivalent to DL1r but where the output from the RNNIP algorithm is not used and $f_c = 0.08$) is shown in Figure 3.16 for b-jets, c-jets, and light-flavour jets in MC simulation of $t\bar{t}$ events.

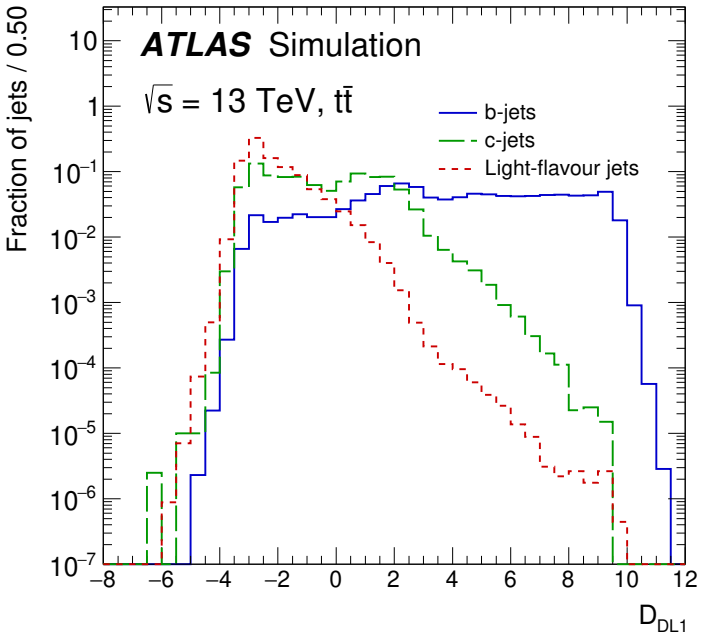

Figure 3.16: Distribution of the output of the DL1 b-tagging algorithm for b-jets, c-jets and light-flavour jets in MC simulation of $t\bar{t}$ events. Sourced from Ref. [103].

WPs are defined by applying a fixed requirement on the output score of DL1r. The requirement is chosen such that a particular average efficiency of identifying b-jets is achieved in MC simulation of $t\bar{t}$ events, and are defined for 60%, 70%, 77%, and 85% b-tagging efficiency. The b-tagging efficiency is measured in data and simulation as a function of jet p_{T} and data-to-simulation scale factors are derived to correct for inaccurate modelling in the simulation due to limited knowledge of b-hadron decays. The b-tagging efficiency is measured in $t\bar{t}$ events where both W bosons decay to a lepton and neutrino [103]. The mistag rate for c-jets (which is the probability a b-tagging algorithm identifies a c-jet as a b-jet) is measured in $t\bar{t}$ events where one W boson decays to a lepton and neutrino whilst the other W boson decays to a c- and s-quark [104]. The light-flavour jet mistag rate is measured using Z/γ^*+jets events [105]. The 85% WP is used for the measurements in this thesis and the scale factors are shown in Figure 3.17. The measurement of the b-tagging efficiency is performed in bins of the jet p_{T}, although the measurement and its uncertainties are smoothed using a non-parametric regression technique before the efficiency scale factors are used in data analysis (Appendix A) [106].

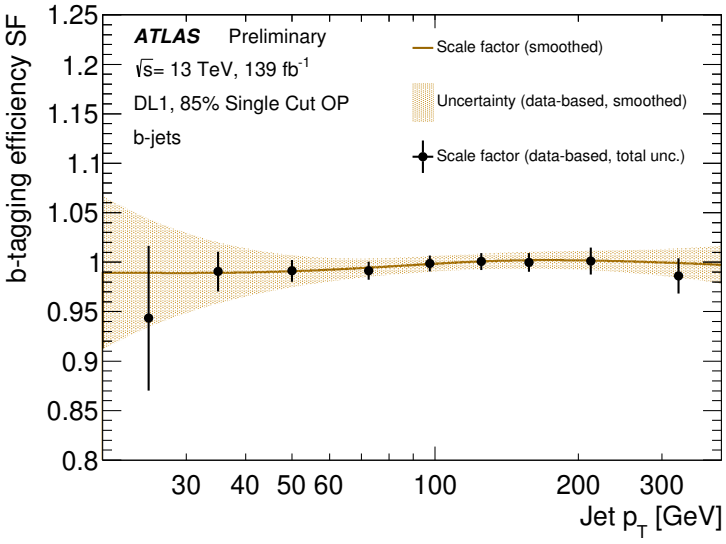

Figure 3.17: The b-tagging efficiency data-to-simulation scale factors for the DL1 85% WP. Sourced from Ref. [106].

3.5.6 Missing transverse momentum

The ATLAS detector covers almost 4π in solid angle so that the total p_{T} of each collision event can be accurately measured. However, some particles, such as neutrinos or weakly interacting hypothetical particles, which only interact through the weak force will pass through the detector material without interacting. Their contribution can be inferred from the measured total p_{T} of particles which do interact with the detector material by considering momentum conservation, since the initial p_{T} of a collision event is zero. The quantity, $\boldsymbol{E}_{\mathrm{T}}^{\mathrm{miss}} = (E_{\mathrm{x}}^{\mathrm{miss}},\ E_{\mathrm{y}}^{\mathrm{miss}})$ with magnitude $E_{\mathrm{T}}^{\mathrm{miss}} = \sqrt{E_{\mathrm{x}}^2 + E_{\mathrm{y}}^2}$, is defined as the negative vector sum of the p_{T} of all particles which interact with and are measured by the ATLAS detector, such that the total p_{T} in an event is zero. The momentum carried by non-interacting particles is then typically assumed to have been accounted for in the calculation of $E_{\mathrm{T}}^{\mathrm{miss}}$. More specifically, $E_{\mathrm{T}}^{\mathrm{miss}}$ is defined as

$$\boldsymbol{E}_{\mathrm{T}}^{\mathrm{miss}} = -\Big\{ \sum_{\text{muons}} \boldsymbol{p}_{\mathrm{T}} + \sum_{\text{electrons}} \boldsymbol{p}_{\mathrm{T}} + \sum_{\text{photons}} \boldsymbol{p}_{\mathrm{T}} + \sum_{\tau} \boldsymbol{p}_{\mathrm{T}} + \sum_{\text{jets}} \boldsymbol{p}_{\mathrm{T}} + \sum_{\text{soft}} \boldsymbol{p}_{\mathrm{T}} \Big\}, \tag{3.11}$$

where each term is calculated using the projections along the x- and y-axes. The contributions to the $E_{\mathrm{T}}^{\mathrm{miss}}$ calculation are muons, electrons, photons, hadronically decaying τ-leptons, and jets, where the fully calibrated detector signals associated with the PV are used. This set of contributions is called the *hard* term because they are typically high p_{T}. The final term, $\sum_{\text{soft}} \boldsymbol{p}_{\mathrm{T}}$, is called the *soft* term and takes into account remaining detector signals which are not associated to any of the high p_{T} objects. The soft term is calculated by considering tracks reconstructed in the ID with $p_{\mathrm{T}} > 500$ MeV, $|z_0 \sin\theta| < 2.0$ mm, and associated to the PV. This term is called the *track-based soft term* (TST). The use of tracks significantly removes contributions from out-of-time pile-up, despite not including

calorimeter energy deposits from neutral particles or energy flow beyond the ID acceptance ($|\eta| > 2.5$) [107].

Two flavours of $E_{\mathrm{T}}^{\mathrm{miss}}$ are used for the measurements in this thesis and are related to the use of measurements from the tracking detectors in the $E_{\mathrm{T}}^{\mathrm{miss}}$ calculation. The standard definition of $E_{\mathrm{T}}^{\mathrm{miss}}$ uses PFlow objects for jets, where these objects make use of a combination of calorimeter energy deposits and tracks in the ID. This flavour is termed $E_{\mathrm{T}}^{\mathrm{miss}}$ in this thesis because of the use of calorimeter deposits. Generally, the use of PFlow jet objects helps to improve the jet energy resolution and reduce the contamination of pile-up jets. However, a second flavour of $E_{\mathrm{T}}^{\mathrm{miss}}$ can be constructed which only uses tracks in the ID and neglects to include signals from the calorimeters or MS. This approach means a stricter association to the PV can be used, which essentially eliminates pile-up contributions. This flavour is termed $p_{\mathrm{T}}^{\mathrm{miss}}$ because of the use of tracks. However, the contribution from neutral particles are not accounted for, nor any momentum flow beyond $|\eta| > 2.5$ [108].

The resolution of reconstructed $E_{\mathrm{T}}^{\mathrm{miss}}$ is generally poor since it depends on the accurate measurements of all particles interacting with the detector material in an event. Inaccuracies in the calibration and resolution of reconstructed objects, as well as contamination from pile-up, degrade the $E_{\mathrm{T}}^{\mathrm{miss}}$ resolution. WPs are defined to reduce the effect of pile-up and are related to the jet inputs for the term $\sum_{\mathrm{jets}} \boldsymbol{p}_{\mathrm{T}}$. The *Tight* WP is used for the measurements in this thesis, where jets are required to have

- $|\eta| < 2.4$: $p_{\mathrm{T}} > 20$ GeV and JVT > 0.2 if $p_{\mathrm{T}} < 60$ GeV,
- $|\eta| > 2.4$: $p_{\mathrm{T}} > 30$ GeV.

The resolution of $E_{\mathrm{T}}^{\mathrm{miss}}$ is taken as the width of the distribution given by the difference in the x- and y-components of the measured $E_{\mathrm{T}}^{\mathrm{miss}}$ and the true $E_{\mathrm{T}}^{\mathrm{miss}}$ obtained using the MC event record. Figure 3.18 shows the $E_{\mathrm{T}}^{\mathrm{miss}}$ resolution for the Tight WP using events with zero expected real $E_{\mathrm{T}}^{\mathrm{miss}}$ ($Z \to ee$) and inclusive in jet multiplicity. The $E_{\mathrm{T}}^{\mathrm{miss}}$ resolution is shown as a function of the average number of interactions per bunch crossing (a metric for the amount of pile-up in each bunch crossing). The data collected during 2017 is compared to the predictions of the SHERPA and POWHEG+PYTHIA 8 MC event generators [109].

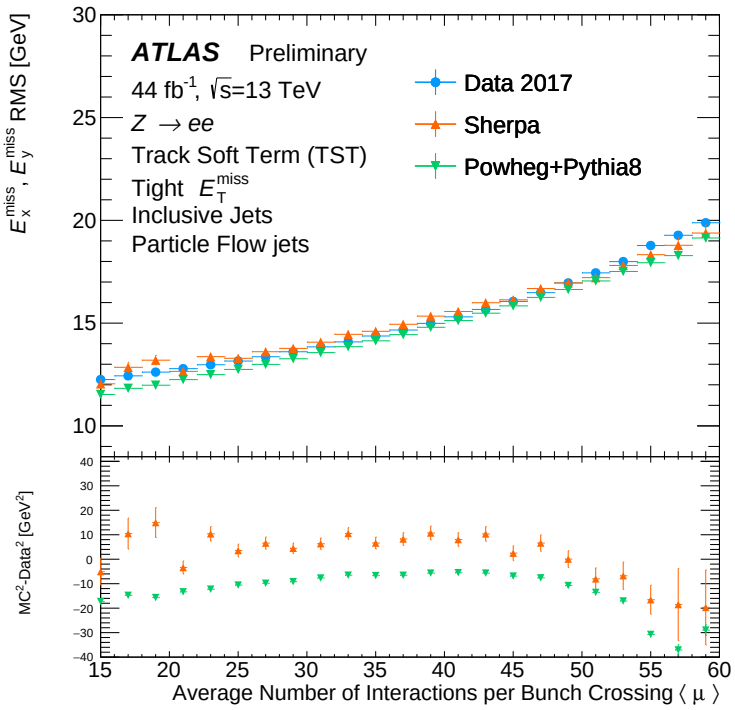

Figure 3.18: The resolution of $E_{\mathrm{T}}^{\mathrm{miss}}$ calculated with the Tight WP as a function of the average number of interactions per bunch crossing shown for data collected in 2017, SHERPA, and POWHEG+PYTHIA 8. Events with zero expected real $E_{\mathrm{T}}^{\mathrm{miss}}$ are selected ($Z \to ee$) and are inclusive in jet multiplicity. The bottom panel shows the quadratic difference between the $E_{\mathrm{T}}^{\mathrm{miss}}$ prediction of the MC simulation and the measured $E_{\mathrm{T}}^{\mathrm{miss}}$. Sourced from Ref. [109].

4
Analysis strategy

The decay of a Higgs boson to a pair of W bosons is an experimentally competitive decay mode to use to perform cross section measurements of the Higgs boson at a hadron collider. This decay mode benefits from a large branching ratio of 21.5% [53], and a sufficiently identifiable experimental signature is achieved by collecting events where both W bosons decay into leptons and neutrinos. This chapter describes the strategy taken to perform the cross section measurements of ggF and VBF Higgs boson production in the WW^* decay mode using pp collisions collected between the years 2015–2018 at a centre-of-mass energy of $\sqrt{s} = 13$ TeV, corresponding to 139 fb^{-1} of integrated luminosity (the full LHC Run 2 data set).

An overview of the measurement strategy and characteristic features of the Higgs boson and SM background processes are described in Section 4.1. The data and Monte Carlo (MC) samples used to perform the measurements are provided in Section 4.2. The reconstruction of detector information into analysis objects, such as electrons, muons, and jets, are described in Section 4.3. Kinematic quantities constructed from these objects (observables) that are utilised in the measurements are defined in Section 4.4. The selection requirements made on distributions of observables to isolate the event yield containing Higgs bosons and to measure important SM background processes are detailed in Sections 4.5 and 4.6, respectively. Lastly, the strategy taken to measure cross sections in the STXS framework is described in Section 4.7.

4.1 Overview of analysis

The Higgs boson has a measured mass of 125.09 GeV [110] and a predicted decay width of 4.1 MeV [53] in the SM. Events containing a Higgs boson must be searched for by considering the final state particles of its possible decay modes, since it will decay before it can interact with the detector material. In this analysis targeting the $H \to WW^*$ decay mode, where one W boson is off-shell given the measured Higgs boson mass, the W bosons will also subsequently decay through several possible modes. These decays are

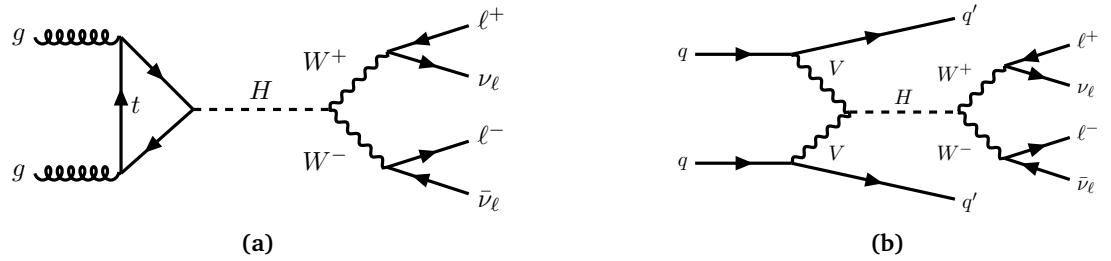

Figure 4.1: Feynman diagrams at LO illustrating the $H \to WW^* \to \ell\nu\ell\nu$ process initiated by (a) ggF and (b) VBF. The final state leptons implicitly include the leptons originating from the decay of τ-leptons.

classified as either hadronic or leptonic, where the former involves final states consisting of quarks and the latter involves final states consisting of a lepton and neutrino pair. The branching ratio of hadronic W boson decays is 67.3%, whereas the leptonic branching ratio is 32.7% [111]. Despite the smaller branching ratio, a final state consisting of two leptons and significant missing transverse energy is a distinctive signature to search for in a hadron collider. An event sample with final state leptons will result in a higher purity of Higgs bosons than hadronic final states since many of the physics processes leading to leptonic final states generally involve electroweak interactions, which occur with a smaller cross section than for QCD processes.

The experimental signature of events selected for analysis is therefore that of two high-p_{T} and isolated leptons, each originating from the leptonic decay of a W boson. The two leptons must have opposite charge and there must be a sizeable amount of $E_{\mathrm{T}}^{\mathrm{miss}}$, originating from the neutrinos. The electrons and muons in leptonic decays of a W boson are directly observable with the detector, whereas a τ-lepton will subsequently decay to two neutrinos and an electron or muon about 35% of the time [111]. Events containing $W \to \tau\nu_\tau \to \ell\nu_\ell\nu_\tau\nu_\tau$ decays are implicitly included with events containing $W \to \ell\nu_\ell$ decays, where ℓ will henceforth denote an electron or muon. The quantum amplitudes describing ggF and VBF production of a Higgs boson, with the subsequent $H \to WW^* \to \ell\nu\ell\nu$ decay, are illustrated in the form of LO Feynman diagrams in Figure 4.1. These quantum amplitudes are referred to as the *signal processes*, or signal.

The two leptons searched for in events collected by the ATLAS detector can be of the *same flavour* or of *different flavour*. Events containing two same-flavour leptons are more likely to have been produced through a process involving the exchange of a Z/γ^* boson. This process has a cross section that is several orders of magnitude larger than that of the Higgs boson signal so the final state leptons in this analysis are required to have different flavour. Events comprising two leptons of the same flavour are considered in Section 8.2.

4.1.1 Categorisation and measurements

As described in Section 2.4.3, measurements of the Higgs boson are performed by defining categories of events, based on selection requirements on kinematic quantities (observables) that are constructed using the four-momenta of final state particles, measured and identified by the detector. After selecting events with two high-p_{T} leptons with opposite charge and different flavour (the preselection), four analysis categories are defined based on jet multiplicity. This is done because of the different background compositions present in each jet-binned category and because the ggF and VBF production modes of the Higgs boson occur with different jet multiplicities: the $N_{\text{jet}} = 0$ and $N_{\text{jet}} = 1$ categories are sensitive to the ggF production mode, whilst the $N_{\text{jet}} \geq 2$ category is split into ggF-enriched and VBF-enriched categories. In the ggF-enriched $N_{\text{jet}} \geq 2$ category, jets originate mainly from parton radiation, whereas the jets are a distinctive feature of the production process for VBF.

A set of selection requirements on distributions of observables are optimised for each analysis category such that the event yield is enriched in the Higgs boson signal process. The event yield following a specific set of selection requirements is called the *signal region* (SR) if the region targets the Higgs boson signal, or a *control region* (CR) if the region targets a specific background process[21]. The use of CRs means that the rates of background processes can be measured simultaneously to the measurement of the Higgs boson signal, reducing the dependency of the background rates in the signal-enriched regions on predictions from MC simulation. In addition to making selection requirements on distributions of observables, a multivariate analysis technique is used in the VBF-enriched $N_{\text{jet}} \geq 2$ category to increase the discrimination of the signal from background processes. This takes the form of a Deep Neural Network (DNN), trained against all background processes including the ggF Higgs boson signal, which evaluates a score quantifying the probability that an event is more VBF-like or more background-like.

With a set of events selected and categorised as above, a statistical analysis is performed, where two different measurements of the Higgs boson production cross sections are performed. The first is the *inclusive* measurement which simultaneously measures the rate of ggF and VBF production of the Higgs boson using the regions categorised by jet multiplicity. The second is the *STXS* measurement where ggF and VBF production of the Higgs boson are measured in 11 distinct kinematic fiducial regions. The regions used to perform the STXS measurement are further partitions of the SRs used for the inclusive measurement, based on observables such as the reconstructed p_{T} of the Higgs boson

[21] The word *category* is used as a general term to define a partition of a set of events, whilst *signal region* and *control region* (or regions) are used to refer to the set of events with which the final measurements are performed.

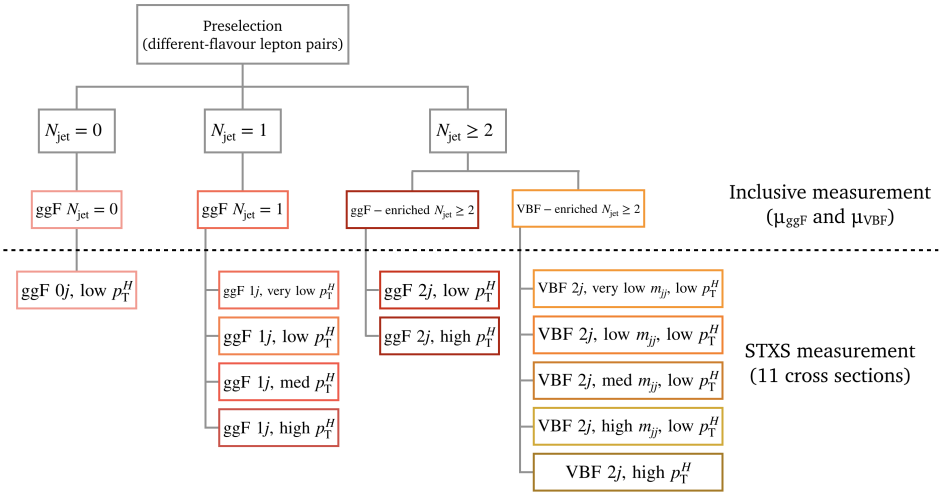

Figure 4.2: Illustration of the categorisation of events with different-flavour lepton pairs based on jet multiplicity (N_{jet}). SRs are defined after making several selection requirements on distributions of observables that are enriched in events containing Higgs bosons produced through the ggF or VBF production modes. The SRs above the dashed line are used to measure the rate of ggF and VBF production of Higgs bosons (inclusive measurement). The inclusive SRs are split further by requirements on the reconstructed Higgs boson candidate p_{T}, p_{T}^H, and the reconstructed invariant mass of two jets, m_{jj}, to define STXS SRs which are used to measure 11 cross sections in distinct kinematic fiducial regions.

candidate and the reconstructed invariant mass of the two highest-p_{T} jets. An illustration of the categorisation of events in this analysis is shown in Figure 4.2.

4.1.2 Background processes

Given the propensity of known particles and the forces giving rise to interactions between particles, several SM processes can result in or mimic the $\ell\ell + E_{\text{T}}^{\text{miss}}(+\text{jets})$ final state signature of the ggF and VBF $H \to WW^* \to \ell\nu\ell\nu$ signal processes. Background processes can be *irreducible* or *reducible*. The irreducible background describes processes where the final state is exactly the $\ell\ell + E_{\text{T}}^{\text{miss}}(+\text{jets})$ final state of the signal process. Reducible background describes processes where the final state is not necessarily identical to the final state of the signal process, but the same final state of the signal process is measured in the detector due to inefficiency in the capability of the detector to identify and reconstruct the kinematics of all particles with absolute accuracy.

Table 4.1 summarises the numerous background sources and the cause of the $\ell\ell + E_{\text{T}}^{\text{miss}}(+\text{jets})$ final state signature. The specific processes that constitute the background in this analysis are categorised into broader classes of background, whose names are given in the first column. Many of these background processes have cross sections which are orders of magnitude larger than the Higgs boson signal cross section, illustrated in Figure 4.3. It is therefore crucial to precisely estimate the background processes which contaminate the

Table 4.1: A list of background processes considered in this analysis that mimic the $\ell\ell+E_{\mathrm{T}}^{\mathrm{miss}}(+\text{jets})$ final state signature of the Higgs boson signal. Modified from Ref. [5].

Name	Physics process	Cause of $\ell\ell + E_{\mathrm{T}}^{\mathrm{miss}}(+\text{jets})$ signature	Estimation method
Other Higgs boson (Other H)			
VH production	$pp \to VH, V = \{W, Z\}$	hadronic V: irreducible leptonic V: lepton(s) not reconstructed	Theoretical predictions
Inclusive ttH	$pp \to t\bar{t}H$	untagged b-jets	
ggF, VBF production of $H \to \tau\tau$	$H \to \tau\tau$	irreducible	
Non-resonant WW			
$qqWW$	$qq \to WW$	irreducible	Data-driven (CR)
$ggWW$	$gg \to WW$	irreducible	Theoretical prediction
Top quarks ($t\bar{t}/Wt$)			
$t\bar{t}$	$t\bar{t} \to WbW\bar{b}$	untagged b-jets	
Wt	Wt	untagged b-jets	Data-driven (CR)
	$t\bar{b}/tq\bar{b}$	q or b reconstructed as ℓ	
Mis-identified leptons (Mis-Id)			
Wj	W + jet(s)	j reconstructed as ℓ	Data-driven (fake factor)
jj	QCD multi-jet	jj reconstructed as $\ell\ell$; fake $E_{\mathrm{T}}^{\mathrm{miss}}$	
Non-WW diboson and triboson			
Other $VV(V)$	$W\gamma$	γ reconstructed as e	Theoretical predictions
	$W\gamma^*,\ WZ,\ ZZ \to \ell\ell\ell\ell$	lepton(s) not reconstructed	
	$ZZ \to \ell\ell\nu\nu$	irreducible	
	$Z\gamma$	γ reconstructed as e; lepton not reconstructed	
	$WWW,\ WWZ,\ ZZZ$	leptons not reconstructed	
Drell-Yan (Z/γ^*)			
$\tau\tau$	$Z/\gamma^* \to \tau\tau \to \ell\nu\nu\ell\nu\nu$	irreducible	Data-driven (CR)
$ee/\mu\mu$	$Z/\gamma^* \to ee/\mu\mu$	fake $E_{\mathrm{T}}^{\mathrm{miss}}$	

event yields of the analysis regions. The most precise theoretical calculations implemented in MC simulation are used to predict the rates of some background processes and their kinematic distributions, whereas data is used to provide a more accurate estimate for background processes with larger contributions to the event yields in the analysis regions. CRs are used to normalise the rate of the non-resonant WW, top quark, and Z/γ^* background processes, whilst an alternative method (the fake factor) is used to estimate the yields of the W+jets and QCD multi-jet processes.

Non-resonant WW

The non-resonant production of W boson pairs, where each W boson decays into a lepton and neutrino, constitutes one of the largest irreducible sources of background. Exclusive production of WW pairs can occur with quarks ($qqWW$) or gluons ($ggWW$), example Feynman diagrams of which are shown in Figures 4.4a and 4.4b, respectively. Despite the presence of two high-p_{T} leptons and a sizeable amount of $E_{\mathrm{T}}^{\mathrm{miss}}$ in the final state, the kinematics of the lepton pair are different with respect to the leptons originating from the Higgs boson decay due to the resonant production of the spin-0 Higgs boson.

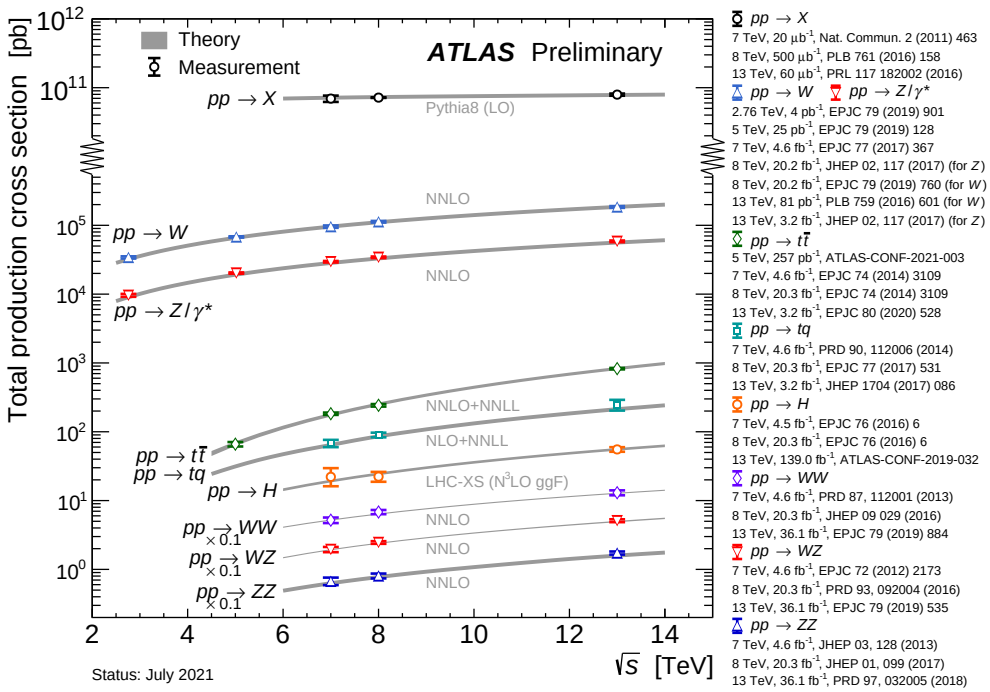

Figure 4.3: Total production cross sections for a selection of processes that are important in this analysis, presented as a function of the centre-of-mass energy, $\sqrt{s}$, from 2.76 to 13 TeV. Measurements of processes involving two bosons are scaled by a factor of 0.1 for visualisation. Sourced from Ref. [112].

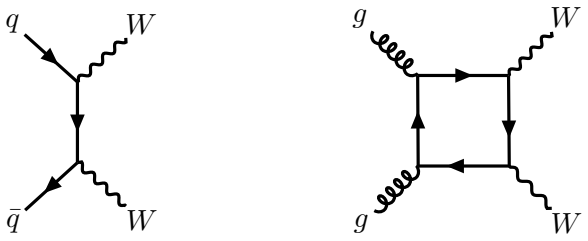

Figure 4.4: Example Feynman diagrams of non-resonant WW production in pp collisions where (a) shows t-channel production with a $q\bar{q}$ initial state, and (b) shows production through gluon fusion.

Top quarks

The production of top quarks at the LHC occurs at a rate significantly larger than that of ggF production of a Higgs boson. Top quarks are typically produced in pairs ($t\bar{t}$) through several LO processes which are illustrated in Figure 4.5. The top quark is the heaviest particle in the SM with a very short lifetime, and thus decays into subsequent particles before it can hadronise and form jets. It almost exclusively decays through the weak interaction into a W boson and a bottom quark. Events where both W bosons decay into a lepton and neutrino pair constitute a large source of background, particularly in analysis categories defined with $N_{\text{jet}} \geq 2$.

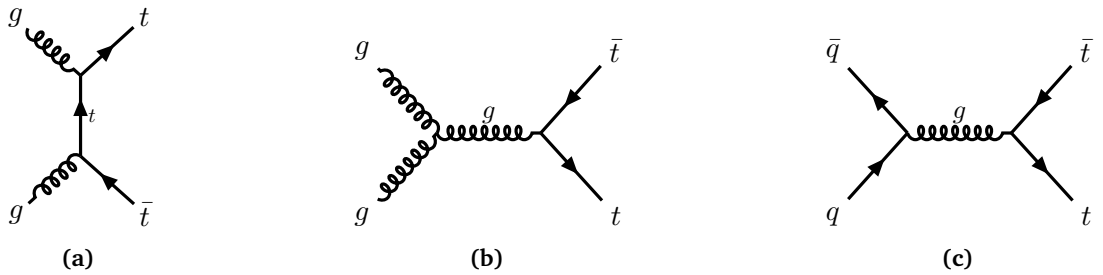

Figure 4.5: Example Feynman diagrams at LO of $t\bar{t}$ production in pp collisions where (a) and (b) show t- and s-channel production with a gg initial state, and (c) shows s-channel production with a $q\bar{q}$ initial state.

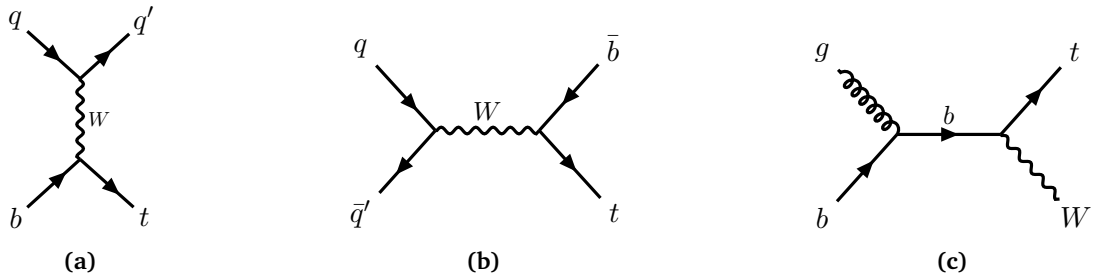

Figure 4.6: Example Feynman diagrams at LO of single-top production in pp collisions where (a) and (b) show t- and s-channel production, and (c) shows s-channel Wt production.

Top quarks are also produced singly, as illustrated in Figure 4.6, through s- and t- channel exchange of a W boson and s-channel production of a W boson and top quark. The latter process (Figure 4.6c) constitutes the largest contamination of single-top quark events to this analysis[22], since this process leads to a final state including $\ell\ell + E_{\mathrm{T}}^{\mathrm{miss}}(+\text{jets})$ and mimics the Higgs boson signal when the associated b-quark is not reconstructed or identified.

In contrast to the Higgs boson signal, top quark production always results in the presence of one or more b-jets. Suppression of top quark events is achieved naturally by defining categories based on jet multiplicity. Further suppression of top quark events is achieved by rejecting events where a jet is identified as having originated from a b-quark. However, the yield of top quark events in all analysis categories is still sizeable due to the large production cross section of top quarks and inefficiencies in the identification of b-jets.

Z/γ^*

The annihilation of a quark and anti-quark can produce a Z boson or virtual photon, which subsequently decays into a lepton pair of opposite charge and with the same flavour.

[22] Background events arising from single-top quark events are collectively termed Wt in this thesis, for this reason.

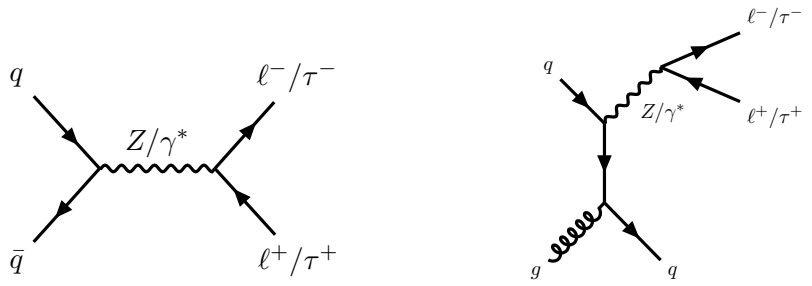

Figure 4.7: Example Feynman diagrams of Z/γ^* production in pp collisions at (a) LO and (b) where an additional parton is produced.

At LO, this process is called Drell-Yan (DY) and is illustrated in Figure 4.7a. Beyond LO, this process is also called Z/γ^*+jets and is illustrated in Figure 4.7b. The cross section for Z/γ^* processes occurs at a significantly higher rate than for the Higgs boson signal.

The $Z/\gamma^* \to \tau\tau$ process, with the two subsequent $\tau \to \ell\nu_\ell\nu_\tau$ decays, is an irreducible background and also the dominant Z/γ^* background. The final state consists of two oppositely charged leptons, not necessarily of the same flavour, and with a significant amount of real $E_{\mathrm{T}}^{\mathrm{miss}}$ due to the neutrinos. The $Z/\gamma^* \to ee/\mu\mu$ process, however, which does not produce real $E_{\mathrm{T}}^{\mathrm{miss}}$, contributes insignificantly to the total Z/γ^* yield after rejecting lepton pairs of the same flavour[23].

W+jets and QCD mulit-jet

Processes which do not contain two *prompt* leptons (leptons originating from a hard scatter interaction) are a non-negligible source of background events in this analysis. The contributing processes consist of W+jets and QCD multi-jet production, of which Feynman diagrams at LO are shown in Figure 4.8. Events originating from these processes can contribute to the background yields in the analysis when a jet is incorrectly identified as a lepton, once in the case of W+jets and twice in the case of QCD multi-jet. Events of this sort are termed *Mis-ID* and the mis-identified leptons themselves are termed *fake* leptons. Sources of fake leptons are numerous and include the leptonic decay of heavy-flavour hadrons inside jets, ambiguity in the profiles of hadronic and electromagnetic showers, and punch-through in the muon spectrometers. Despite the small probability that a jet fakes a lepton, a significant yield of fake lepton background populates the analysis regions due to the fact that the cross sections for W+jets and QCD multi-jet production are several orders of magnitude larger than that to produce a Higgs boson.

[23] For this reason, the Z/γ^* background is often referred to as the $Z/\gamma^* \to \tau\tau$ background (or $Z\tau\tau$) in this thesis.

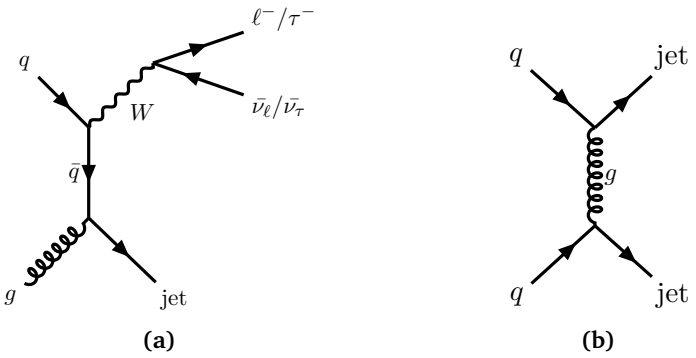

Figure 4.8: Feynman diagrams of (a) W+jets and (b) QCD multi-jet production in pp collisions, where the object labeled *jet* is incorrectly identified as a lepton.

Other backgrounds

There are several other background processes which can enter the analysis regions but which represent a smaller contribution to the total background event yield. One category of these backgrounds includes the other possible Higgs boson production and decay modes, e.g. production modes other than ggF or VBF, as well as the decay of a Higgs boson to a pair of τ-leptons. The other category includes processes with multiple bosons, e.g. $W\gamma$, WZ, ZZ, $Z\gamma$, WWW, WWZ, and ZZZ. Events originating from these processes can enter the analysis regions when final state particles are not reconstructed correctly.

4.1.3 Higgs boson signal characteristics

The two final state leptons originating from the $H\to WW^*\to \ell\nu\ell\nu$ process exhibit different kinematics to leptons produced from background processes due to the resonant production of a spin-0 Higgs boson. The W bosons produced from its decay, which are both spin-1, are back-to-back in the Higgs boson rest frame with anti-parallel spins to conserve angular momentum. The W bosons each then decay into two spin-$\frac{1}{2}$ leptons, where the decay is governed by the V–A structure of the weak interaction: a W boson only exhibits interactions with left-handed (right-handed) fermions (antifermions) in the SM. Therefore, leptons and neutrinos produced by the decay of a W boson are produced anti-parallel to the spin of the W boson, whereas anti-leptons and anti-neutrinos are produced parallel to the spin of the W boson. This leads to a correlation in the direction of the leptons, illustrated in Figure 4.9, whereby the leptons emerge from the $H\to WW^*\to \ell\nu\ell\nu$ decay process with the same direction, resulting in the observation of a small opening angle between (and subsequently a small invariant mass of) the lepton pair in the detector. Lepton pairs originating from background processes are expected to have a broader range of opening angles and invariant masses since they do not originate from the decay of a spin-0 resonance. Figure 4.10 shows detector displays of reconstructed $H\to WW^*\to \ell\nu\ell\nu$ event candidates from each analysis region, where it can be seen that the two leptons are

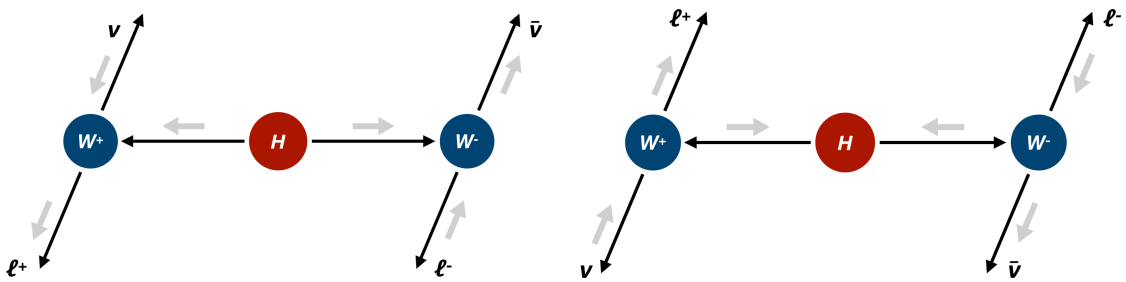

(a) (b)

Figure 4.9: Illustration of the $H \to WW^* \to \ell\nu\ell\nu$ decay and the spin correlations between the final state particles. The black arrow heads depict the direction of motion of the particle and the large grey arrows depict its spin projection. The decay of the spin-0 SM Higgs boson into two spin-1 W bosons with positive helicity is shown in (a), and with negative helicity in (b).

observed to have a small opening angle.

The VBF production mode of a Higgs boson is characterised by the scattering of two quarks inside the protons. There is no exchange of colour charge between these quarks and they do not directly participate in the production or decay of the Higgs boson. The VBF production mode is thus noticeable in the detector by the presence of two highly energetic jets at very large rapidities, with the decay products of the Higgs boson located centrally in the detector (at low values of rapidity). The large opening angle between the two jets means they have a very large invariant mass. This can be seen in Figure 4.10d, which shows a display of an $H \to WW^* \to \ell\nu\ell\nu$ event candidate produced through the VBF production mode. Contrastingly, the jets in the display of an $H \to WW^* \to \ell\nu\ell\nu$ event candidate in the ggF-enriched $N_{\text{jet}} \geq 2$ region (Figure 4.10c) do not display the same characteristic features.

Lastly, the presence of neutrinos in the final state of the Higgs boson signal process, which escape detection, make it impossible to reconstruct the Higgs boson mass from the reconstructed four-momenta of the final state particles. However, it is possible to construct a *transverse mass* to discriminate the Higgs boson signal from background processes, since the transverse momentum components of the visible final state particles and the missing transverse momentum are known. A starting point for defining the transverse mass is

$$m_{\text{T}}^{\text{unique}} = \sqrt{(E_{\text{T}}^{\ell\ell} + E_{\text{T}}^{\nu\nu})^2 - (\mathbf{p}_{\text{T}}^{\ell\ell} + \mathbf{p}_{\text{T}}^{\nu\nu})^2}, \tag{4.1}$$

where $E_{\text{T}}^{\ell\ell(\nu\nu)} = \sqrt{m_{\ell\ell(\nu\nu)}^2 + |\mathbf{p}_{\text{T}}^{\ell\ell(\nu\nu)}|^2}$. The quantities $m_{\ell\ell(\nu\nu)}$ and $\mathbf{p}_{\text{T}}^{\ell\ell(\nu\nu)}$ refer to the invariant mass of the lepton (neutrino) pair and the vector sum of the lepton (neutrino) p_{T}. The quantity $m_{\text{T}}^{\text{unique}}$ is a lower bound on m_H; the two quantities are equal when the rapidity of the lepton pair and neutrino pair are equal or zero. Several assumptions

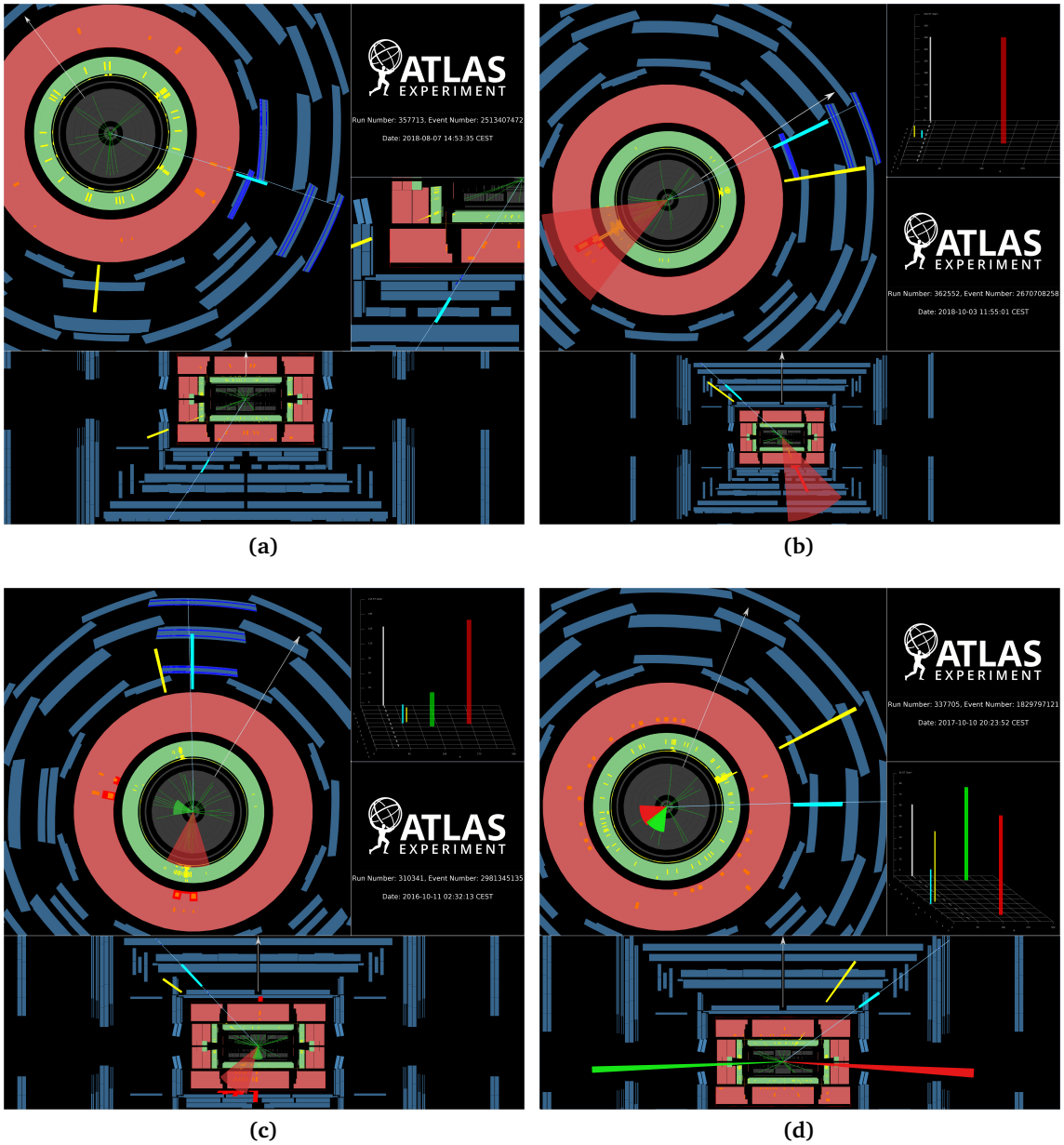

(a) **(b)**

(c) **(d)**

Figure 4.10: Event displays of candidate Higgs bosons from the (a) ggF $N_{\text{jet}} = 0$, (b) ggF $N_{\text{jet}} = 1$, (c) ggF-enriched $N_{\text{jet}} \geq 2$, and (d) VBF-enriched $N_{\text{jet}} \geq 2$ analysis regions. Each display depicts a transverse (top third) and longitudinal (bottom third) view of the ATLAS detector. The measured trajectories of reconstructed electrons and muons are shown in yellow and blue, respectively. The reconstructed missing transverse momentum is shown by the white arrow. Reconstructed jets are shown by red and green cones. Energy deposits in the ECAL and HCAL are also shown by yellow and red squares. Reconstructed tracks are shown by green lines in the ID.

can be made in order to convert $m_{\mathrm{T}}^{\mathrm{unique}}$ into an observable that accounts for the fact that the individual components of each neutrino four-momentum are unknown. In this analysis, the quantities $\mathbf{p}_{\mathrm{T}}^{\nu\nu}$ and $E_{\mathrm{T}}^{\nu\nu}$ are identified with $\boldsymbol{E}_{\mathrm{T}}^{\mathrm{miss}}$ and $E_{\mathrm{T}}^{\mathrm{miss}}$ (the magnitude of $\boldsymbol{E}_{\mathrm{T}}^{\mathrm{miss}}$), respectively, which is equivalent to assuming that $m_{\nu\nu} = 0$. The expression for m_{T} is then given by

$$m_{\mathrm{T}} = \sqrt{(E_{\mathrm{T}}^{\ell\ell} + E_{\mathrm{T}}^{\mathrm{miss}})^2 - (\mathbf{p}_{\mathrm{T}}^{\ell\ell} + \boldsymbol{E}_{\mathrm{T}}^{\mathrm{miss}})^2}. \tag{4.2}$$

This observable is a key tool that is used to measure the Higgs boson signal in the ggF regions, since many of the background processes in Table 4.1 have a different distribution in m_{T} compared to the Higgs boson signal. In the VBF-enriched $N_{\mathrm{jet}} \geq 2$ region however, the output distribution of a Deep Neural Network (DNN) is used to discriminate the Higgs boson signal process from background processes.

4.2 Data and simulated samples

The analysis is performed using the full Run 2 data set, corresponding to an integrated luminosity of 139 ± 2.4 fb^{-1}, or equivalently, approximately 1.1×10^{16} pp collisions. In addition to this data set, the event yields and shapes of distributions of many of the signal and background processes in the different analysis categories are predicted using state-of-the-art theoretical calculations, embedded in MC event generators.

4.2.1 Data samples

The data is selected after passing several trigger requirements. The triggers employed in this analysis search for events with at least one lepton (single lepton triggers), as well as events with pairs of leptons (dilepton triggers). The p_{T} thresholds of the triggers are 20 (24) GeV for electrons (muons) in 2015, which increases to 26 GeV for both electrons and muons in 2016–2018. The specific values of the single lepton trigger p_{T} thresholds depend on the background rate and the trigger latency. Incorporating dilepton triggers means that the efficiency of the trigger at low p_{T} is increased, since the background rate is smaller and the p_{T} thresholds can be lower. The dilepton trigger has a minimum p_{T} threshold of 17 (14) GeV for electrons (muons) in Run 2. This also means that the offline requirement on the p_{T} of the two signal leptons can be lowered. The efficiency of triggers is typically measured using the tag-and-probe method, using a selection of electrons and muons originating from the decay of a Z boson. The trigger efficiency is about 75% for a 31 GeV electron, rising to 96% at 60 GeV [113]. For muons, the trigger efficiency is about 68% (85%) in the barrel (endcap) [114].

4.2.2 Simulated samples

Predictions for the signal and background processes, assuming the SM, are modelled using simulated samples generated with MC. A number of programmes and settings are

Table 4.2: The signal and background processes which are generated with MC for this analysis and the simulation programmes used to generate the matrix element and simulate the UEPS for each process. Alternative programmes (or in some cases quantities) are used to derive systematic uncertainties, which are shown in parentheses.

Process	Matrix element (alternative)	PDF set	UEPS model (alternative model)	Prediction order for total cross section
ggF H	POWHEG-BOX v2 [46, 115–118] NNLOPS [115, 129, 130] (MG5_aMC@NLO) [45, 131]	PDF4LHC15_NNLO [41]	PYTHIA 8 [42] (Herwig 7) [43]	N^{3}LO QCD + NLO EW [53, 119–128]
VBF H	POWHEG-BOX v2 [46, 117, 118, 129] (MG5_aMC@NLO)	PDF4LHC15_NLO	PYTHIA 8 (Herwig 7)	NNLO QCD + NLO EW [132–134]
VH excl. $gg \to ZH$	POWHEG-BOX v2	PDF4LHC15_NLO	PYTHIA 8	NNLO QCD + NLO EW [135–139]
$t\bar{t}H$	POWHEG-BOX v2	NNPDF3.0NLO	PYTHIA 8	NLO [53]
$gg \to ZH$	POWHEG-BOX v2	PDF4LHC15_NLO	PYTHIA 8	NNLO QCD + NLO EW [140, 141]
$qq \to WW$	SHERPA 2.2.2 [142] (Q_{cut})	NNPDF3.0NNLO [143]	SHERPA 2.2.2 [47–50, 144, 145] (SHERPA 2.2.2 [145, 149]; μ_{q})	NLO [146–148]
$qq \to WWqq$	MG5_aMC@NLO [45]	NNPDF3.0NLO	PYTHIA 8 (Herwig 7)	LO
$gg \to WW/ZZ$	SHERPA 2.2.2	NNPDF3.0NNLO	SHERPA 2.2.2	LO [150]
$WZ/V\gamma^*/ZZ$	SHERPA 2.2.2	NNPDF3.0NNLO	SHERPA 2.2.2	NLO [151]
$V\gamma$	SHERPA 2.2.8 [142]	NNPDF3.0NNLO	SHERPA 2.2.8	NLO [151]
VVV	SHERPA 2.2.2	NNPDF3.0NNLO	SHERPA 2.2.2	NLO
$t\bar{t}$	POWHEG-BOX v2 (MG5_aMC@NLO)	NNPDF3.0NLO	PYTHIA 8 (Herwig 7)	NNLO+NNLL [152–158]
Wt	POWHEG-BOX v2 (MG5_aMC@NLO)	NNPDF3.0NLO	PYTHIA 8 (Herwig 7)	NNLO [159, 160]
Z/γ^*	SHERPA 2.2.1 (MG5_aMC@NLO)	NNPDF3.0NNLO	SHERPA 2.2.1	NNLO [161]

used to generate MC samples for most signal and background processes, details of which are shown in Table 4.2. The programmes used for the matrix element calculation, the underlying event and parton shower (UEPS), and the PDF sets, as well as the perturbation order of the total cross-section predictions (used for sample normalisation) are shown. For some processes, an additional sample produced with a different programme is listed in parentheses; these are used to derive systematic uncertainties corresponding to the different steps of sample generation.

Higgs boson signal

Samples of Higgs boson production processes are generated using the POWHEG-BOX v2 programme [46, 115–118] interfaced with PYTHIA 8 [42] for the UEPS, and assume a Higgs boson mass of 125.0 GeV. Whilst ggF and VBF production of a Higgs boson are the primary processes targeted by the analysis, samples are also generated for the WH, ZH, and ttH production processes. Moreover, samples are generated for the decay of a Higgs boson to a pair of τ-leptons.

The ggF, VBF, WH, and ZH samples make use of the PDF4LHC15 PDF set [162] and the PYTHIA 8 AZNLO tune [163]. The $t\bar{t}H$ sample instead uses the NNPDF3.0NLO PDF set [143] and the ATLAS A14 tune [164].

The Higgs boson signal samples are accurate to next-to-next-to-leading order (NNLO)[24] for ggF; next-to-leading order (NLO) for VBF; NLO for VH plus one jet and leading order

[24]The accuracy in perturbation theory is understood to mean QCD here.

(LO) for the loop-induced $gg \to ZH$ process; and NLO for $t\bar{t}H$.

The samples are normalised to state-of-the-art cross section predictions, listed as follows:

- For ggF, the sample is normalised to an N^{3}LO cross section in QCD with electroweak corrections at NLO [53, 119–128];
- For VBF, the sample is normalised to an approximate-NNLO QCD cross section with NLO electroweak corrections [133, 165, 166];
- For WH and ZH, the samples are normalised to cross sections calculated at NNLO in QCD with NLO electroweak corrections [135–139] (including the $gg \to ZH$ process at NNLO).
- For $t\bar{t}H$, the sample is normalised to an NLO cross section in QCD with NLO EW accuracy [53].

Additionally, branching ratios of the Higgs boson are incorporated in the normalisation of the samples. The decay branching ratios are calculated with HDECAY [167–169] and PROPHECY4F [170–172], assuming a Higgs boson mass of $125.09\,\text{GeV}$ [173]. For the $t\bar{t}H$ sample, however, the sample is inclusive in Higgs decay modes and the cross section is computed assuming a Higgs boson mass of $125.09\,\text{GeV}$.

Background processes

Top quark processes ($t\bar{t}$ pair production and single-top quark production) are modelled using POWHEGBOX v2 at NLO with the `NNPDF3.0NLO` PDF set. The simulated events are interfaced to PYTHIA 8 to model the UEPS, which uses the A14 tune. The p_{T} distribution of the highest-p_{T} lepton in each event in the $t\bar{t}$ sample is not well modelled by the simulation, which could be due to missing higher-order corrections in the sample. An NNLO re-weighting is applied [174] to correct the agreement of the simulation with the data whilst keeping the normalisation of the sample unchanged. For the single-top quark sample, the *diagram removal scheme* [175] is used to remove interference and double-counting with $t\bar{t}$ production. For all samples generated with POWHEGBOX v2, bottom- and charm-hadron decays are performed with EVTGEN v1.6.0 [176] for better modelling of the data.

Processes involving multiple bosons are mostly generated using SHERPA [142] which performs both the matrix element generation and the modelling of the UEPS using the `NNPDF3.0NNLO` set of PDFs and a parton shower tune developed by the SHERPA authors. Quark-initiated production of WW, WZ, ZZ, and triboson (VVV) processes are generated using SHERPA 2.2.2, $V\gamma$ processes with SHERPA 2.2.8, and Z/γ^* processes with SHERPA 2.2.1. The WW, WZ, ZZ, and $V\gamma$ samples are accurate to NLO in QCD for up to one additional parton and at LO accuracy for up to three additional parton

emissions, whilst the triboson samples are accurate to NLO inclusively and to LO for up to two additional parton emissions. The Z/γ^* samples are accurate to NLO for up to two partons, and LO for up to four partons. The gluon-initiated WW and ZZ samples are accurate to LO for up to one additional parton emission.

The electroweak production of $\ell\ell qq$ final states through the process $qq \to (Z/\gamma^* \to \ell\ell)qq$ is generated with SHERPA 2.2.1 using LO matrix elements with up to two additional parton emissions. The electroweak production of WW bosons (EW WW) through the process $qq \to (WW \to \ell\ell\nu\nu)qq$ is instead generated using MG5_AMC@NLO [45] with LO matrix elements, interfaced with PYTHIA 8. The `NNPDF3.0NNLO` PDF set and the A14 tune are used.

Samples of W+jets and Z+jets events are generated using POWHEG and MG5_AMC@NLO [45, 131] (both interfaced with PYTHIA 8), and SHERPA 2.2.1 [142]. These samples are used in the data-driven estimate of the W+jets and multi-jet backgrounds.

Pile-up is modelled by generating inelastic pp events with PYTHIA 8.186 [177], the `NNPDF2.3LO` set of PDFs, and the ATLAS A3 tune [178]. These events are overlaid onto each hard scatter interaction in every MC sample. The average number of interactions per bunch crossing in the MC samples is then re-weighted to reflect that in the data, which is only possible after data-taking has finished since this is when the pile-up profile becomes known.

Finally, the simulated samples are fed into a simulation of the ATLAS detector, which is done using GEANT 4 [179]. For some of the alternative samples, a detector simulation is used which employs a parameterisation of the calorimeter response to speed up the computation time [180]. The MC-simulated samples are then fed through the ATLAS reconstruction software [181], similarly to the collision data.

4.3 Object identification and selection

The signals measured in the detector that are combined together to represent the initial four-momenta of final state particles are called *objects*. They must be identified and selected for analysis with a high efficiency and purity. However, ambiguity arises since signals from one source may be reconstructed as multiple objects, necessitating the implementation of an *overlap removal* procedure for the selected objects.

4.3.1 Leptons

The selection of leptons (electrons and muons) aims to maximise the rejection of fake lepton backgrounds, whilst maintaining a high efficiency of signal. The origin of leptons

selected for analysis must be from the PV, which is defined as the vertex with at least two tracks with $p_{\mathrm{T}} > 500$ MeV[25] [70, 84]. Further rejection of fake lepton backgrounds is achieved by requiring $|d_0|/\sigma_{d_0} < 5$ (3) and $|z_0 \sin\theta| < 0.5$ mm for electron (muon) candidates, where d_0 and z_0 are the transverse and longitudinal impact parameters of the lepton track with respect to the PV, and σ_{d_0} is the uncertainty on d_0.

Electrons

Candidate electrons are required to have $p_{\mathrm{T}} > 10$ GeV, $|\eta| < 2.47$. They are required to satisfy different identification WPs depending on their transverse energy, E_{T}, in order to reject mis-identified leptons, where the identification WPs are described in Section 3.5.2. The *Tight* WP is used for electrons with $E_{\mathrm{T}} < 25$ GeV and the *Medium* WP for electrons with $E_{\mathrm{T}} > 25$ GeV. Electron candidates must also satisfy the *Tight* isolation WP, which is inclusive in electron E_{T}. Events are removed if electron candidates have $1.37 < |\eta| < 1.52$ (the transition region between the barrel and an endcap in the ECAL where the resolution is degraded).

Muons

Muon candidates are required to have $p_{\mathrm{T}} > 10$ GeV and $|\eta| < 2.5$. They must pass the *Tight* identification WP and *Tight* isolation WP, as described in Section 3.5.3. The former requirement ensures that tracks in the ID are matched to tracks in the MS, which significantly improves the purity of selected muons.

4.3.2 Jets

Jets are a major component in this analysis since they are used to separate events with a $\ell\ell + E_{\mathrm{T}}^{\mathrm{miss}}(+\text{jets})$ final state into categories defined by the jet multiplicity. Jet candidates are reconstructed using the anti-k_t algorithm with a distance measure in the η–ϕ plane of $R = 0.4$ and using PFlow objects as input, as described in Section 3.5.4. Reconstructed jets are required to have $p_{\mathrm{T}} > 20$ GeV and $|\eta| < 4.5$. A selection of JVT > 0.5, as described in Section 3.5.4, is required for jet candidates with $20 < p_{\mathrm{T}} < 60$ GeV to reject jets originating from pile-up. Jets originating from b-quarks are identified with the DL1r b-tagging algorithm, with a WP defined by an 85% efficiency as measured in simulated dilepton $t\bar{t}$ events, described in Section 3.5.5. These jets, which have $p_{\mathrm{T}} > 20$ GeV and $|\eta| < 2.5$, are referred to as b-jets. Tighter criteria requiring $p_{\mathrm{T}} > 30$ GeV and that the jet is not identified as a b-jet are used for counting the jet multiplicity in an event and therefore to define the analysis categories.

[25] In cases where there is more than one reconstructed PV, the PV with the largest sum of squared track p_{T} is used as the default.

4.3.3 Missing transverse momentum

Two types of $E_{\mathrm{T}}^{\mathrm{miss}}$ are used in this analysis depending on the use of measurements from the tracking detectors in the determination of $E_{\mathrm{T}}^{\mathrm{miss}}$, as described in Section 3.5.6. The first type ($E_{\mathrm{T}}^{\mathrm{miss}}$) uses jets as defined above (with $p_{\mathrm{T}} > 20$ GeV) in the determination of the hard term. The second type ($p_{\mathrm{T}}^{\mathrm{miss}}$) instead uses tracks measured in the ID for all terms in the calculation. Other objects that enter the calculation of $E_{\mathrm{T}}^{\mathrm{miss}}$ or $p_{\mathrm{T}}^{\mathrm{miss}}$ are as defined above. The use of $p_{\mathrm{T}}^{\mathrm{miss}}$ is favourable to reject certain backgrounds due to its better rejection of pile-up. The use of $E_{\mathrm{T}}^{\mathrm{miss}}$ is instead reserved for observables such as m_{T} since it improves the resolution.

4.3.4 Overlap removal

Double-counting of calorimeter energy deposits and tracks can lead to the reconstruction of multiple objects from one source. This is more likely for leptons originating from heavy-flavour hadron decays inside jets or for hard emissions from leptons. Objects originating from sources like this are typically located near a sizeable amount of detector activity. Using a geometric measure, ΔR, of the physical proximity of objects to each other can help to disentangle them. A procedure is applied using the objects defined above to remove overlapping objects that could otherwise degrade the position and energy measurement of the object, and is similar to the isolation requirements applied to the objects. Jets which are identified as having originated from a b-quark according to the description above are not considered for removal.

In the case where two electron candidates share a track in the ID, the electron candidate with lower E_{T} is removed. If a muon candidate shares a track in the ID with an electron candidate, then the electron candidate is removed. This can occur when a muon radiates a photon, causing the energy deposit in the calorimeter to be matched to the muon track and thus considered an electron. If a jet is not identified as a b-jet and is located within $\Delta R = 0.2$ of an electron candidate, the jet is removed. Beyond this ΔR range, it is generally the case that these are real hadronic jets reconstructed in the vicinity of an electron, where the electron likely originates from the decay of a hadron. The electron candidate is removed if it is within $\Delta R = 0.4$ of the jet object, since its energy reconstruction is biased by the proximity of the jet. A muon can overlap with a jet for several reasons, including pile-up, hadron decays, final state radiation, and bremsstrahlung radiation. Jet objects are removed if it is found within $\Delta R = 0.2$ of a muon candidate, has less than three associated tracks with $p_{\mathrm{T}} > 500$ MeV, and the jet is not identified as a b-jet. For remaining jet objects, the muon is removed if it is located within $\Delta R = 0.4$ of the jet object.

4.4 Observables

A single pp collision event can be described as a collection of objects, each with a unique four-momentum, which have been constructed from the signals collected by the detector components, and which satisfy various identification and isolation criteria. A number of analytic quantities can be constructed out of these objects event-by-event (observables). For a set of many events, requirements on distributions of observables can give rise to meaningful separation between the signal and background processes. In this analysis, many observables are defined are are described below. They are categorised into three groups: those which are particularly sensitive to the expected kinematics of the Higgs boson signal process, those which are particularly useful to reject specific background events, and those which are useful at identifying ggF-enriched $N_{\text{jet}} \geq 2$ and VBF-enriched $N_{\text{jet}} \geq 2$ events. All of these observables are used to construct SRs and CRs enriched in signal or background events, or are used as input to the VBF DNN. The selection requirements on observables defining the SRs and CRs are later described in Sections 4.5 and 4.6.

4.4.1 Topological observables

Three observables are defined in order to exploit the expected topology of the signal process:

$\Delta\phi_{\ell\ell}$

The azimuthal angle between the two leptons, $\Delta\phi_{\ell\ell}$, will be smaller for the Higgs boson signal than for background processes, such as non-resonant WW. This is because of the spin correlations between the two leptons for the Higgs boson signal process, as described in Section 4.1.3.

$m_{\ell\ell}$

The invariant mass of the two leptons, $m_{\ell\ell}$, is expected to be smaller for the Higgs boson signal than for background processes for the same reason as $\Delta\phi_{\ell\ell}$.

m_{T}

The transverse mass of the lepton pair, m_{T}, as described in Section 4.1.3, is defined as

$$m_{\text{T}} = \sqrt{\left(E_{\text{T}}^{\ell\ell} + E_{\text{T}}^{\text{miss}}\right)^2 - \left|\boldsymbol{p}_{\text{T}}^{\ell\ell} + \boldsymbol{E}_{\text{T}}^{\text{miss}}\right|^2}, \tag{4.3}$$

where $E_{\text{T}}^{\ell\ell} = \sqrt{|\boldsymbol{p}_{\text{T}}^{\ell\ell}|^2 + m_{\ell\ell}^2}$, $\boldsymbol{p}_{\text{T}}^{\ell\ell}$ is the vector sum of the lepton transverse momenta, and $\boldsymbol{E}_{\text{T}}^{\text{miss}}$ (with magnitude $E_{\text{T}}^{\text{miss}}$) is the missing transverse momentum. This observable is used as the primary discriminating variable for the analysis categories targeting the ggF production mode.

4.4.2 Background rejection

A number of observables are defined to reject events originating from specific background processes, including:

$m_{\tau\tau}$

The invariant mass of the τ-lepton pair, $m_{\tau\tau}$, in $Z/\gamma^* \to \tau\tau$ events, or hypothetical τ-lepton pair otherwise, is reconstructed using the *collinear approximation* method [182]. This method assumes the τ-leptons are highly boosted such that the decay products are collinear to the τ-lepton directions and that the neutrinos are the only source of $E_{\mathrm{T}}^{\mathrm{miss}}$ in the event. Under these assumptions, the fraction of τ-lepton momenta imparted to the visible and invisible decay particles is computed and the invariant mass of the τ-lepton pair is reconstructed. This observable is effective at reducing background from Z/γ^* events, as well as $H\to\tau\tau$ events. Further detail about the di-τ invariant mass reconstruction is given in Appendix B.

$N_{b\text{-jet}}$

The number of jets with $p_{\mathrm{T}} > 20$ GeV and $|\eta| < 2.5$ that are identified as b-jets by the b-tagging algorithm DL1r at the 85% efficiency WP (Section 4.3.2), $N_{b\text{-jet}}$, is effective in reducing the background from top quark events.

$p_{\mathrm{T}}^{\ell\ell}$

The vector sum of the two highest-p_{T} leptons, $p_{\mathrm{T}}^{\ell\ell}$, is typically large for Higgs boson signal events where the two leptons recoil against the two neutrinos. This observable is effective in reducing Z/γ^* events where the leptons are typically back-to-back.

$\Delta\phi(\ell\ell, E_{\mathrm{T}}^{\mathrm{miss}})$

The azimuthal angle between the two highest-p_{T} leptons and $E_{\mathrm{T}}^{\mathrm{miss}}$, $\Delta\phi(\ell\ell, E_{\mathrm{T}}^{\mathrm{miss}})$, is typically back-to-back for Higgs boson signal events and most other background events. Small values of this observable most likely represent mis-measured objects.

$\max(m_{\mathrm{T}}^{\ell})$

The transverse mass of each lepton, $m_{\mathrm{T}}^{\ell_i}$, is defined as

$$m_{\mathrm{T}}^{\ell_i} = \sqrt{2\, p_{\mathrm{T}}^{\ell_i} E_{\mathrm{T}}^{\mathrm{miss}} \left(1 - \cos\Delta\phi\left(\ell_i, E_{\mathrm{T}}^{\mathrm{miss}}\right)\right)}, \tag{4.4}$$

where i represents either of the two highest-p_{T} leptons. This quantity is typically small for Z/γ^* and multi-jet background processes but will be larger for at least one lepton in the Higgs boson signal process due to the presence of at least one real W boson. It is effective to place a lower bound on the maximum value of m_{T}^{ℓ} for the two leptons.

m_{T2}

For the leptonic decay of a W boson, $W \to l\nu$, the transverse mass is given by

$$m_{\mathrm{T}}^2 = m_\ell^2 + m_\nu^2 + 2(E_{\mathrm{T},\ell}E_{\mathrm{T},\nu} - \boldsymbol{p}_{\mathrm{T},\ell} \cdot \boldsymbol{p}_{\mathrm{T},\nu}), \tag{4.5}$$

with $E_{\mathrm{T,x}}^2 = m_x^2 + \boldsymbol{p}_{\mathrm{T,x}}^2$ where $x = \{\ell, \nu\}$. This quantity satisfies $m_{\mathrm{T}} \leq m_W$, with equality when both the lepton and neutrino are entirely in the transverse plane with zero rapidity. For dileptonic $t\bar{t}$ decays, $t\bar{t} \to W(\to \ell\nu)bW(\to \ell\nu)b$, a value of m_{T} can be determined from each branch of the $t\bar{t}$ decay, using the visible ($b\ell$) and invisible (ν) components of the decay. However, only the total missing transverse momentum, $\boldsymbol{E}_{\mathrm{T}}^{\mathrm{miss}}$, is known, and the determination of each neutrino momentum is impossible. The observable m_{T2} extends the concept of m_{T} to decay processes with identical decay branches, a and b, originating from the same parent particles, in order to determine the mass of the parent particle. It can be applied to events originating from dileptonic $t\bar{t}$ decays, as well as dileptonic non-resonant WW decays, in order to estimate the top quark mass or W boson mass. Generally, m_{T2} is defined as

$$m_{\mathrm{T2}} = \min_{\boldsymbol{p}_{\mathrm{T}}^{\mathrm{a}} + \boldsymbol{p}_{\mathrm{T}}^{\mathrm{b}} = \boldsymbol{E}_{\mathrm{T}}^{\mathrm{miss}}} [\max(m_{\mathrm{T}}^{\mathrm{a}}, m_{\mathrm{T}}^{\mathrm{b}})], \tag{4.6}$$

where m_{T} as defined in Equation 4.5 is used (with the terms corresponding to ℓ replaced by the sum of the momenta of measured objects) and the sum of the invisible momenta, $\boldsymbol{p}_{\mathrm{T}}^{\mathrm{a}}$ and $\boldsymbol{p}_{\mathrm{T}}^{\mathrm{b}}$, is constrained to the measured $\boldsymbol{E}_{\mathrm{T}}^{\mathrm{miss}}$. The minimisation over the possible values of $\boldsymbol{p}_{\mathrm{T}}^{\mathrm{a}}$ and $\boldsymbol{p}_{\mathrm{T}}^{\mathrm{b}}$ is to ensure the kinematic constraint that $m_{\mathrm{T2}} \leq m_0$, where m_0 is the mass of the parent particle, which could be a top quark or W boson [183–186]. The term m_ν^2 in m_{T} is set to zero since the invisible particles are neutrinos. The m_{T2} observable is used in the estimation of the non-resonant WW background yields in the ggF-enriched $N_{\mathrm{jet}} \geq 2$ category.

4.4.3 VBF observables

Several observables that are sensitive to the VBF production process are constructed. These are used to define the exclusivity of the ggF-enriched $N_{\mathrm{jet}} \geq 2$ and VBF-enriched $N_{\mathrm{jet}} \geq 2$ regions, as well as in the training of the DNN to discriminate the VBF Higgs boson signal process from background processes. The observables include:

$p_{\mathrm{T}}^{\mathrm{tot}}$

The total transverse momentum, $p_{\mathrm{T}}^{\mathrm{tot}}$, is defined as $\boldsymbol{p}_{\mathrm{T}}{}^{\ell\ell} + \boldsymbol{E}_{\mathrm{T}}^{\mathrm{miss}} + \sum \boldsymbol{p}_{\mathrm{T}}{}^{\mathrm{jets}}$, where the sum over jets runs over all jets which pass the object selection requirements. Large values of this observable are obtained for background events with significant soft gluon radiation. This radiation forms jets which are typically below the $p_{\mathrm{T}} = 30$ GeV threshold for jet counting in this analysis, resulting in an imbalance of the observed transverse momentum in the event.

Δy_{jj}

The presence of two forward, colour-disconnected jets in VBF Higgs boson signal events means there will be a large difference in the rapidity of these jets, Δy_{jj}, with respect to background processes and ggF signal events, where additional hadronic activity is typically very central in the detector.

$m_{\ell_i j_i}$

The invariant masses of four combinations of leptons and jets, $m_{\ell_i j_i}$, with $i = \{1, 2\}$, with 1 and 2 denoting the two highest-p_{T} objects, are used as input to the DNN.

$E_{\mathrm{T}}^{\mathrm{miss}}$ significance

The observable $E_{\mathrm{T}}^{\mathrm{miss}}$ significance is defined, event-by-event, as a ratio of likelihood functions, quantifying the level of agreement with the hypothesis that the measured $\boldsymbol{E}_{\mathrm{T}}^{\mathrm{miss}}$ is consistent with zero true $\boldsymbol{E}_{\mathrm{T}}^{\mathrm{miss}}$, denoted $\boldsymbol{p}_{\mathrm{T}}^{\mathrm{inv}}$. It is defined as

$$\mathcal{S}^2 = 2 \ln \left(\frac{\max_{\boldsymbol{p}_{\mathrm{T}}^{\mathrm{inv}} \neq 0} \mathcal{L}(\boldsymbol{E}_{\mathrm{T}}^{\mathrm{miss}} | \boldsymbol{p}_{\mathrm{T}}^{\mathrm{inv}})}{\max_{\boldsymbol{p}_{\mathrm{T}}^{\mathrm{inv}} = 0} \mathcal{L}(\boldsymbol{E}_{\mathrm{T}}^{\mathrm{miss}} | \boldsymbol{p}_{\mathrm{T}}^{\mathrm{inv}})} \right), \tag{4.7}$$

where $\mathcal{L}(\boldsymbol{E}_{\mathrm{T}}^{\mathrm{miss}} | \boldsymbol{p}_{\mathrm{T}}^{\mathrm{inv}})$ is the likelihood function, maximised given the two hypotheses of $\boldsymbol{p}_{\mathrm{T}}^{\mathrm{inv}} \neq 0$ and $\boldsymbol{p}_{\mathrm{T}}^{\mathrm{inv}} = 0$. The $\boldsymbol{p}_{\mathrm{T}}^{\mathrm{inv}} \neq 0$ hypothesis is assumed to be the expected $\boldsymbol{E}_{\mathrm{T}}^{\mathrm{miss}}$ given the sum of the $\boldsymbol{p}_{\mathrm{T}}$ of the hard objects in an event. The form of the $E_{\mathrm{T}}^{\mathrm{miss}}$ significance takes into account the expected resolution of the objects entering the determination of $\boldsymbol{E}_{\mathrm{T}}^{\mathrm{miss}}$ as well as the correlations between them [187, 188]. Large values of $E_{\mathrm{T}}^{\mathrm{miss}}$ significance imply the measured $\boldsymbol{E}_{\mathrm{T}}^{\mathrm{miss}}$ is not consistent with the resolution of physics objects entering the $\boldsymbol{E}_{\mathrm{T}}^{\mathrm{miss}}$ calculation, and that the event is more likely to have involved unidentifiable particles. This observable is used as an input variable to the DNN and is helpful in suppressing top quark background events.

Central jet veto (CJV)

The jet with the highest p_{T} above 30 GeV that is located between the two VBF jets[26] in pseudorapidity is defined as the central jet. Using this jet, the *central jet veto* (CJV) is defined as

$$\mathrm{CJV} = \begin{cases} 1 & \text{no central jet with } p_{\mathrm{T}} > 30 \text{ GeV in the event.} \\ 0 & \text{there is a central jet with } p_{\mathrm{T}} > 30 \text{ GeV in the event.} \end{cases} \tag{4.8}$$

m_{jj}

Given the distinctive forward nature of the two VBF jets, kinematic arguments imply the invariant mass of the two jets, m_{jj}, is expected to be larger than the invariant mass of two jets in background and ggF Higgs boson signal events.

[26] The VBF jets are the two highest-p_{T} jets per event.

Outside lepton veto (OLV)

Similarly to the CJV above, the OLV determines whether one or both leptons are located within the rapidity gap of the two VBF jets, and is defined as

$$\text{OLV} = \begin{cases} 1 & \text{both leptons located within rapidity gap.} \\ 0 & \text{one or both leptons not located within rapidity gap.} \end{cases} \tag{4.9}$$

$\eta_\ell^{\text{centrality}}$

The location of the two leptons in the detector may be defined with respect to the two VBF jets on the η-axis as:

$$\eta_\ell^{\text{centrality}} = \sum_i 2 \cdot \left| \frac{\eta_{\ell_i} - \bar{\eta}}{\eta_{j_0} - \eta_{j_1}} \right|, \tag{4.10}$$

where $\bar{\eta} = (\eta_{j_0} + \eta_{j_1})/2$ is the average pseudorapidity of the two VBF jets, j_0 and j_1, and ℓ_i is one of the leptons. This observable is used as an input to the DNN.

4.4.4 STXS observables

The STXS framework defines kinematic fiducial regions based on several observables (defined at particle level): p_{T}^H, p_{T}^{Hjj}, m_{jj}, and N_{jet}. To aid in the STXS measurements, the corresponding observables are built using reconstructed objects:

p_{T}^H

The p_{T} of Higgs boson candidates, p_{T}^H, is defined at detector-level as the vector sum of the p_{T} of the lepton pair and $E_{\text{T}}^{\text{miss}}$ i.e.

$$p_{\text{T}}^H = |\mathbf{p}_{\text{T}}^{\ell\ell} + \boldsymbol{E}_{\text{T}}^{\text{miss}}|$$

p_{T}^{Hjj}

Similarly to p_{T}^H, p_{T}^{Hjj} is defined using detector-level inputs as the vector sum of the p_{T} of the lepton pair, $E_{\text{T}}^{\text{miss}}$, and the p_{T} of the two highest-p_{T} jets, j_0 and j_1, i.e.

$$p_{\text{T}}^{Hjj} = |\mathbf{p}_{\text{T}}^{\ell\ell} + \boldsymbol{E}_{\text{T}}^{\text{miss}} + \mathbf{p}_{\text{T}}{}^{j_0} + \mathbf{p}_{\text{T}}{}^{j_1}|$$

4.5 Event selection

A set of selection requirements on distributions of observables is used to define SRs in categories of jet multiplicity. Figure 4.11 shows the jet multiplicity distribution after a common preselection of events, where it can be seen that the fraction of the three largest backgrounds (non-resonant WW, top quark, and Z/γ^*) is different for each bin. Targeted selection requirements in each analysis category are able to reduce the most dominant backgrounds and increase the sensitivity of the analysis to the Higgs boson signal. A summary of the selection requirements defining each SR is shown in Table 4.3. The

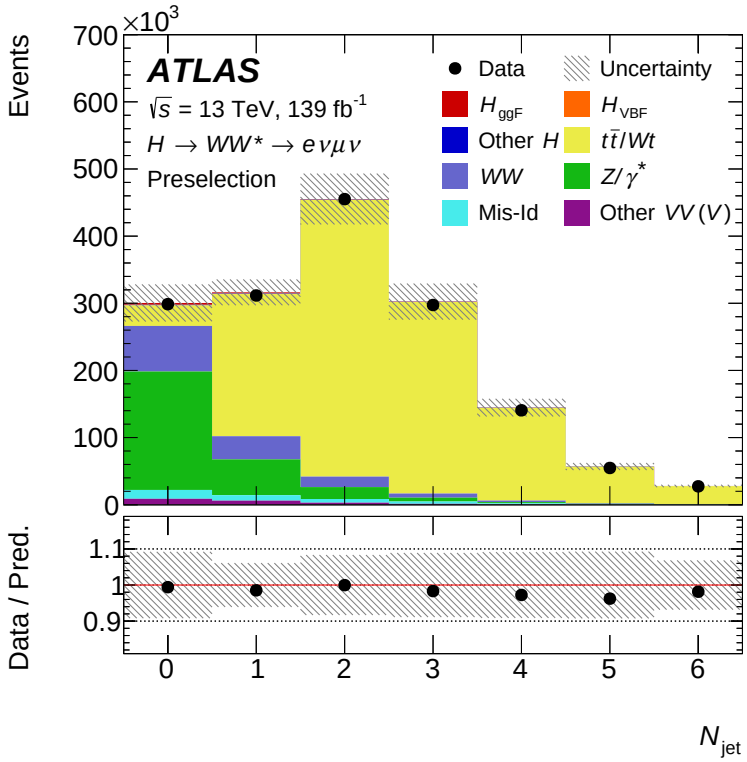

Figure 4.11: Jet multiplicity distribution after the preselection requirements (defined in Section 4.5.1) but before the requirement on $p_{\mathrm{T}}^{\mathrm{miss}}$. The uncertainty band represents the total normalisation uncertainty prior to performing the statistical analysis described in Chapter 6. The background processes are normalised according to the values in Table 4.6.

expected signal and background yields for each selection requirement in the different analysis categories are shown in Table 4.4 and the expected relative contribution of signal and background events in each SR is shown in Figure 4.12. Generally, the specific values of different selection requirements are determined through maximising the expected signal significance, often defined as $S/\sqrt{B}$, where S and B are event yields of the signal and background processes, respectively. This is particularly the case for the ggF-enriched $N_{\mathrm{jet}} \geq 2$ event category which is included in this analysis for the first time since the Run 1 $H \to WW^*$ measurement [6], whereas the analysis strategy for the ggF $N_{\mathrm{jet}} \leq 1$ is mostly identical to the previous measurement with partial Run 2 data [7].

4.5.1 Preselection

The set of requirements considered preselection are those requirements which are common to all analysis categories. The preselection is defined by:

- Exactly two leptons with different flavour and opposite electric charge.
- The highest-p_{T} lepton (leading lepton) is required to have $p_{\mathrm{T}}^{\mathrm{lead}} > 22$ GeV, whilst the second highest-p_{T} lepton (sub-leading lepton) is required to have $p_{\mathrm{T}}^{\mathrm{sublead}} > 15$ GeV.

Table 4.3: The selection criteria made on distributions of observables (defined in Section 4.4) to define the SRs in the analysis.

Category	$N_{\text{jet},(p_T>30\text{ GeV})} = 0$ ggF	$N_{\text{jet},(p_T>30\text{ GeV})} = 1$ ggF	$N_{\text{jet},(p_T>30\text{ GeV})} \geq 2$ ggF	$N_{\text{jet},(p_T>30\text{ GeV})} \geq 2$ VBF
Preselection	Two isolated, different-flavour leptons ($\ell = e, \mu$) with opposite charge $p_T^{\text{lead}} > 22$ GeV , $p_T^{\text{sublead}} > 15$ GeV $m_{\ell\ell} > 10$ GeV			
	$p_T^{\text{miss}} > 20$ GeV			
Background rejection	$N_{b\text{-jet},(p_T>20\text{ GeV})} = 0$			
	$\Delta\phi(\ell\ell, E_T^{\text{miss}}) > \pi/2$	$m_{\tau\tau} < m_Z - 25$ GeV		
	$p_T^{\ell\ell} > 30$ GeV	$\max(m_T^{\ell}) > 50$ GeV		
$H \to WW^* \to e\nu\mu\nu$ topology	$m_{\ell\ell} < 55$ GeV $\Delta\phi_{\ell\ell} < 1.8$			
			fail central jet veto or fail outside lepton veto	central jet veto outside lepton veto $m_{jj} > 120$ GeV
			$\lvert m_{jj} - 85\rvert > 15$ GeV or $\Delta y_{jj} > 1.2$	
Discriminating fit variable	m_T			DNN

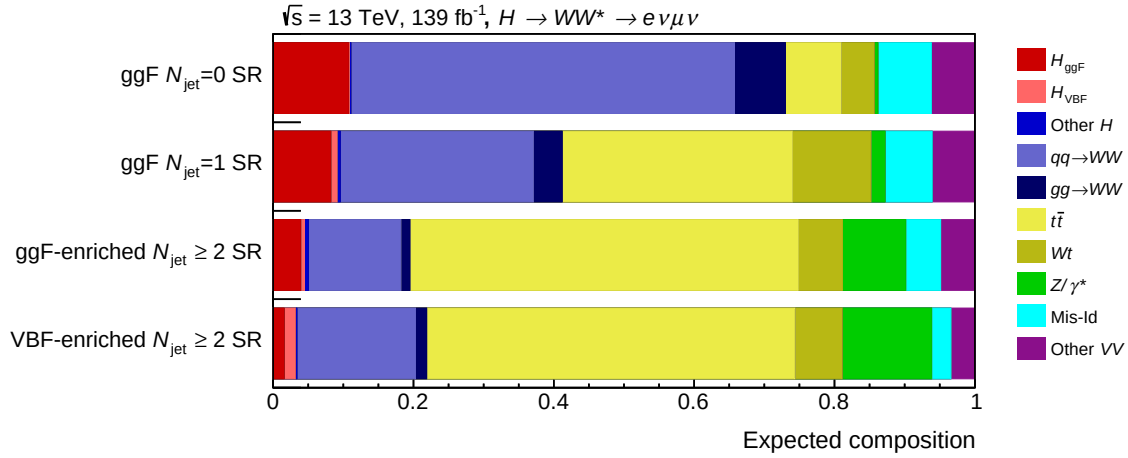

Figure 4.12: The composition of the signal and background processes in each SR. The $qqWW$, top quark, and Z/γ^* background processes are normalised according to the values in Table 4.6.

The asymmetric requirement on the leading and sub-leading lepton p_{T} is due to the fact that only one of the W bosons is generally real.

- A lower bound of $m_{\ell\ell} > 10$ GeV is imposed to suppress background from τ-lepton pairs, originating from low-mass Drell-Yan production and meson resonances (eg. $J/\psi,\ \Upsilon$).

Distributions of the data and MC predictions for the leading and sub-leading lepton p_{T} and η, as well as the invariant mass of the lepton pair, $m_{\ell\ell}$, are shown in Figure 4.13 after applying the preselection criteria.

A further preselection requirement of $p_{\mathrm{T}}^{\mathrm{miss}} > 20$ GeV is applied in the ggF categories in order to reject background from Z/γ^* events, where $p_{\mathrm{T}}^{\mathrm{miss}}$ is used in place of $E_{\mathrm{T}}^{\mathrm{miss}}$ due to a better rejection of Z/γ^* background. The modelling of the data and MC predictions for $E_{\mathrm{T}}^{\mathrm{miss}}$ and $p_{\mathrm{T}}^{\mathrm{miss}}$ is shown in Figure 4.14.

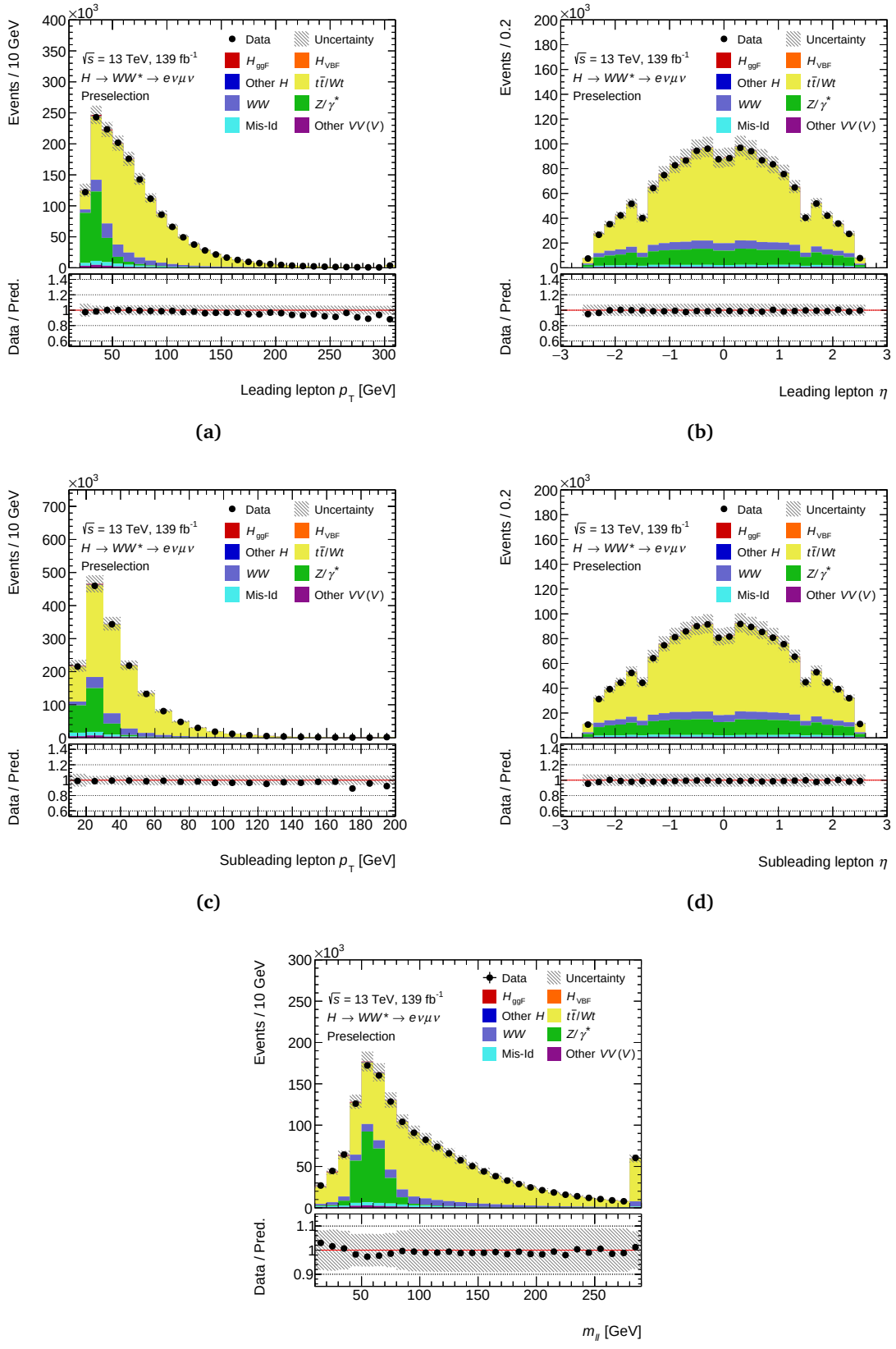

Figure 4.13: Distributions comparing the modelling of the data and MC predictions for the observables used in the common preselection. The uncertainty band represents the total normalisation uncertainty prior to performing the statistical analysis described in Chapter 6. The background processes are normalised according to the values in Table 4.6. The final bin includes events beyond the shown range of the distribution.

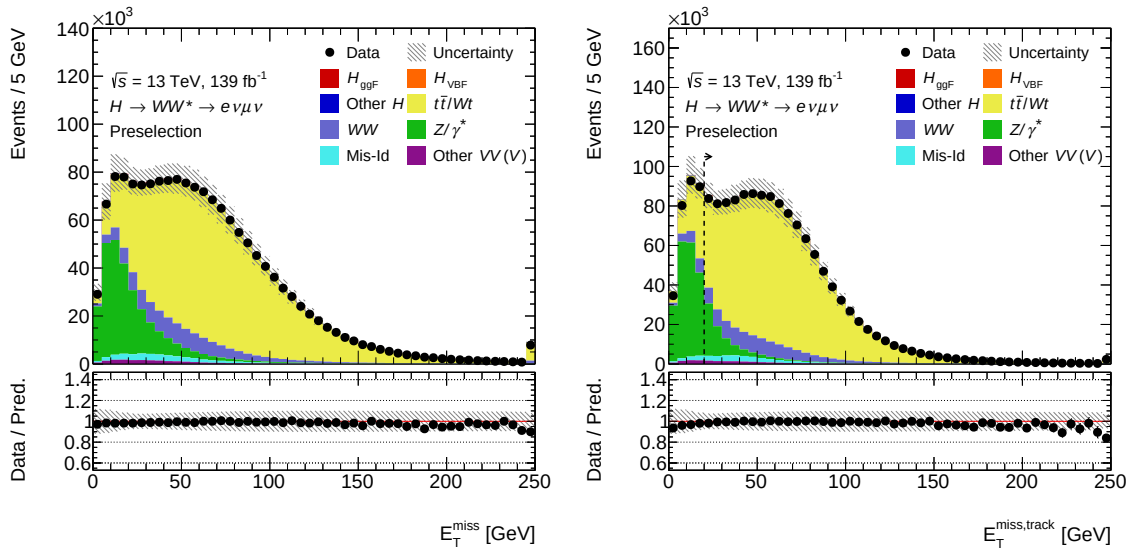

(a) **(b)**

Figure 4.14: Distributions comparing the modelling of the data and MC predictions for (a) $E_{\mathrm{T}}^{\mathrm{miss}}$ and (b) $p_{\mathrm{T}}^{\mathrm{miss}}$. The uncertainty band represents the total normalisation uncertainty prior to performing the statistical analysis described in Chapter 6. The background processes are normalised according to the values in Table 4.6. The final bin includes events beyond the shown range of the distribution. The vertical dashed line and arrow identifies the range of the distribution which is included in the common preselection.

Table 4.4: Event yields of signal and background processes for each selection requirement in each analysis category. The yields correspond to the expectation from MC simulation. Yields for background processes measured with a CR are normalised according to the values in Table 4.6, whilst the yield for Mis-ID is obtained using the data-driven method described in Section 4.6.4. The uncertainties correspond to statistical uncertainty only.

Category	Selection	H_{ggF}	H_{VBF}	Other H	WW	Other $VV(V)$	$t\bar{t}/Wt$	Z/γ^*	Mis-Id	Total Bkg.	Data
	Preselection	5236 ± 8	563 ± 1	1956 ± 2	$108\,155 \pm 99$	$13\,751 \pm 89$	$1\,070\,097 \pm 227$	$68\,604 \pm 238$	$26\,886 \pm 202$	$1\,287\,493 \pm 408$	1 288 321
ggF $N_{jet}=0$	$N_{jet}=0$	2595 ± 6	31 ± 1	326 ± 1	$60\,475 \pm 86$	4853 ± 54	$28\,754 \pm 45$	$28\,815 \pm 160$	9480 ± 89	$132\,378 \pm 215$	134 489
	$\Delta\phi_{\ell\ell,\text{MET}} > 1.57$	2587 ± 6	31 ± 1	315 ± 1	$60\,177 \pm 86$	4641 ± 52	$27\,857 \pm 45$	$27\,401 \pm 154$	9163 ± 87	$129\,239 \pm 208$	131 593
	$p_T^{\ell\ell} > 30$ GeV	2307 ± 5	28 ± 1	168 ± 1	$48\,679 \pm 77$	3246 ± 42	$25\,204 \pm 42$	4428 ± 88	7072 ± 65	$88\,628 \pm 146$	89 907
	$m_{\ell\ell} < 55$ GeV	1958 ± 5	24 ± 1	47 ± 1	$11\,221 \pm 35$	1160 ± 28	3834 ± 17	486 ± 38	1637 ± 29	$18\,337 \pm 68$	20 585
	$N_{b\text{-jet}} = 0$	1920 ± 5	23 ± 1	44 ± 1	$11\,062 \pm 35$	1123 ± 28	2175 ± 13	456 ± 38	1572 ± 28	$16\,387 \pm 66$	18 523
	$\Delta\phi_{\ell\ell} < 1.8$	1778 ± 5	21 ± 1	40 ± 1	$10\,271 \pm 34$	1028 ± 26	2099 ± 13	88 ± 35	1267 ± 26	$14\,753 \pm 62$	16 726
ggF $N_{jet}=1$	$N_{jet}=1$	1654 ± 4	185 ± 1	403 ± 1	$26\,853 \pm 49$	4588 ± 52	$198\,139 \pm 109$	$19\,257 \pm 131$	6876 ± 96	$255\,712 \pm 209$	258 634
	$N_{b\text{-jet}} = 0$	1534 ± 4	171 ± 1	346 ± 1	$25\,256 \pm 48$	4082 ± 50	$37\,192 \pm 50$	$17\,661 \pm 128$	5334 ± 72	$89\,524 \pm 169$	92 658
	$M_T^\ell > 50$ GeV	1296 ± 4	136 ± 1	258 ± 1	$23\,488 \pm 46$	3182 ± 42	$35\,219 \pm 48$	8392 ± 90	4283 ± 63	$74\,565 \pm 136$	76 396
	$m_{\tau\tau} < (m_Z - 25)$ GeV	1220 ± 4	125 ± 1	139 ± 1	$16\,806 \pm 39$	2113 ± 35	$24\,516 \pm 40$	3263 ± 60	2921 ± 51	$49\,619 \pm 103$	51 091
	$m_{\ell\ell} < 55$ GeV	1047 ± 3	109 ± 1	63 ± 1	4116 ± 19	831 ± 27	5527 ± 19	1163 ± 31	981 ± 25	$12\,618 \pm 55$	13 879
	$\Delta\phi_{\ell\ell} < 1.8$	976 ± 3	104 ± 1	55 ± 1	3751 ± 18	723 ± 25	5220 ± 19	241 ± 22	798 ± 23	$10\,732 \pm 48$	11 917
ggF-enriched $N_{jet} \geq 2$	$N_{jet} \geq 2$	987 ± 3	346 ± 1	1227 ± 1	$17\,138 \pm 20$	4310 ± 48	$894\,072 \pm 206$	$14\,995 \pm 70$	$10\,530 \pm 153$	$941\,044 \pm 271$	895 198
	$N_{b\text{-jet}} = 0$	851 ± 3	306 ± 1	382 ± 1	$14\,807 \pm 19$	3397 ± 44	$62\,786 \pm 59$	$12\,409 \pm 67$	3435 ± 62	$96\,834 \pm 118$	95 323
	$m_{\tau\tau} < (m_Z - 25)$ GeV	757 ± 3	267 ± 1	187 ± 1	8895 ± 15	1924 ± 36	$39\,525 \pm 46$	4358 ± 47	2170 ± 48	$56\,871 \pm 91$	56 165
	$m_{\ell\ell} < 55$ GeV	670 ± 2	238 ± 1	112 ± 1	2357 ± 8	830 ± 29	$10\,398 \pm 24$	2150 ± 31	879 ± 28	$16\,614 \pm 57$	17 165
	$\Delta\phi_{\ell\ell} < 1.8$ rad	644 ± 2	231 ± 1	104 ± 1	2216 ± 7	755 ± 27	9874 ± 23	1294 ± 25	777 ± 27	$14\,916 \pm 52$	15 506
	$VH(\to WW^*)$ veto	584 ± 2	227 ± 1	73 ± 1	2022 ± 7	690 ± 27	8921 ± 22	1199 ± 25	661 ± 25	$13\,493 \pm 50$	14 010
	VBF $H \to WW^*$ veto	405 ± 2	56 ± 1	56 ± 1	1490 ± 6	493 ± 24	6361 ± 18	942 ± 16	514 ± 22	9801 ± 41	9982
VBF-enriched $N_{jet} \geq 2$	Preselection (no p_T^{miss} requirement)	5626 ± 8	597 ± 1	2716 ± 3	$127\,465 \pm 115$	$20\,030 \pm 118$	$1\,158\,770 \pm 236$	$249\,641 \pm 419$	$32\,980 \pm 244$	$1\,600\,651 \pm 572$	1 585 575
	$N_{jet} \geq 2$	1062 ± 3	367 ± 1	1377 ± 2	$25\,133 \pm 30$	5149 ± 56	$916\,427 \pm 203$	$25\,425 \pm 104$	$11\,632 \pm 162$	$985\,454 \pm 288$	975 285
	$N_{b\text{-jet}} = 0$	914 ± 3	324 ± 1	467 ± 1	$21\,751 \pm 29$	4054 ± 51	$64\,087 \pm 58$	$21\,332 \pm 99$	3837 ± 69	$116\,499 \pm 147$	109 428
	$m_{\tau\tau} < (m_Z - 25)$ GeV	799 ± 3	278 ± 1	211 ± 1	$12\,600 \pm 23$	2177 ± 41	$39\,060 \pm 45$	7571 ± 69	2378 ± 52	$64\,770 \pm 109$	61 311
	$m_{jj} > 120$ GeV	488 ± 2	254 ± 1	106 ± 1	8545 ± 18	1485 ± 30	$26\,983 \pm 37$	4983 ± 56	1386 ± 41	$43\,993 \pm 87$	41 466
	Pass CJV	416 ± 2	235 ± 1	82 ± 1	7114 ± 17	1213 ± 27	$21\,266 \pm 33$	4230 ± 53	1091 ± 37	$35\,435 \pm 80$	33 802
	Pass OLV	202 ± 1	204 ± 1	33 ± 1	2383 ± 11	440 ± 16	7698 ± 20	1646 ± 41	354 ± 22	$12\,763 \pm 55$	12 189

4.5.2 ggF $N_{\text{jet}} = 0$

The selection requirements for the ggF $N_{\text{jet}} = 0$ category aim to reduce the background from mainly non-resonant WW by exploiting the lepton kinematics of the Higgs boson signal. After the preselection criteria and an $N_{\text{jet}} = 0$ requirement (for jets with $p_{\text{T}} > 30$ GeV), the following selection is defined:

- $\Delta\phi(\ell\ell, E_{\text{T}}^{\text{miss}})$ is required to be greater than $\pi/2$ to remove events where $E_{\text{T}}^{\text{miss}}$ is reconstructed in the same direction as the lepton pair;
- $p_{\text{T}}^{\ell\ell}$ is required to be greater than 30 GeV to reject mostly Z/γ^* events since the lepton pair will generally be back-to-back;
- A veto on b-tagged jets, $N_{b\text{-jet}} = 0$, is applied for jets with $20 < p_{\text{T}} < 30$ GeV to reject top quark events;
- $m_{\ell\ell}$ is required to be less than 55 GeV;
- $\Delta\phi_{\ell\ell}$ is required to be less than 1.8 radians.

Distributions comparing the shape of the signal and background processes, as well as the modelling of the data and MC predictions, for the observables used in the ggF $N_{\text{jet}} = 0$ category, are shown in Figure 4.15.

4.5.3 ggF $N_{\text{jet}} = 1$

There is a larger relative amount of background from top quark and Z/γ^* processes when requiring exactly one jet. The following selection requirements, after imposing the preselection criteria and an $N_{\text{jet}} = 1$ requirement (for jets with $p_{\text{T}} > 30$ GeV), define the ggF $N_{\text{jet}} = 1$ SR:

- A veto on b-tagged jets, $N_{b\text{-jet}} = 0$, is required for all jets with $p_{\text{T}} > 20$ GeV to reject top quark events;
- $\max(m_{\text{T}}^{\ell})$ is required to be larger than 50 GeV to reject Z/γ^* and multi-jet background events;
- $m_{\tau\tau}$ is required to be less than $(m_Z - 25)$ GeV to reject Z/γ^* events;
- $m_{\ell\ell}$ is required to be less than 55 GeV;
- $\Delta\phi_{\ell\ell}$ is required to be less than 1.8 radians.

Distributions comparing the shape of the signal and background processes, as well as the modelling of the data and MC predictions, for the observables used in the ggF $N_{\text{jet}} = 1$ selection are shown in Figure 4.16.

4.5.4 ggF-enriched $N_{\text{jet}} \geq 2$

The analysis strategy and selection requirements in the ggF-enriched $N_{\text{jet}} \geq 2$ category largely resemble those used in the Run 1 $H \to WW^*$ measurement, especially since events

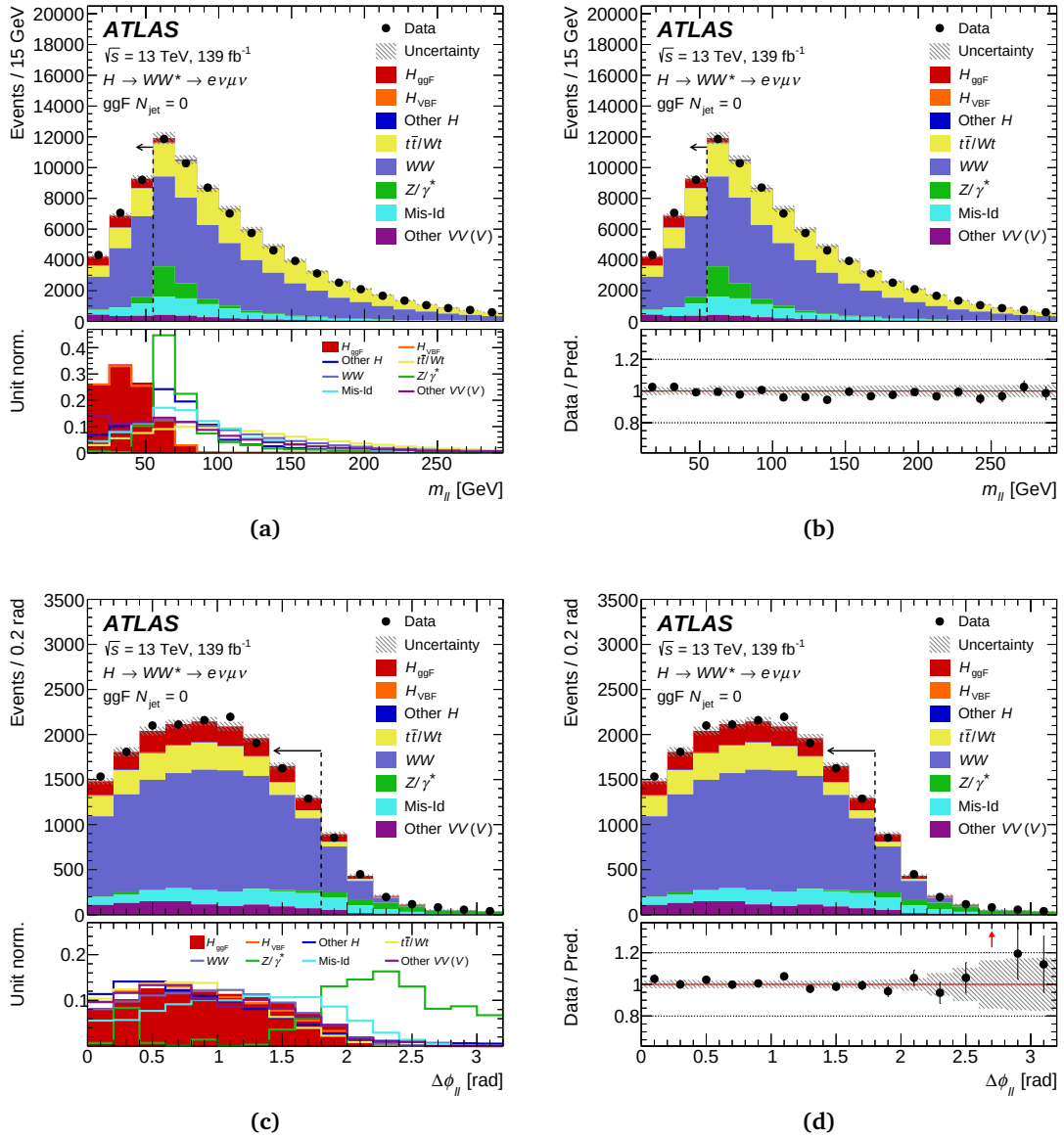

Figure 4.15: Distributions of $m_{\ell\ell}$ and $\Delta\phi_{\ell\ell}$ in the ggF $N_{\text{jet}} = 0$ category after applying all selection requirements except the requirements on $m_{\ell\ell}$ and $\Delta\phi_{\ell\ell}$, respectively. Comparisons of the shape of the signal and background processes are shown in (a) and (c), whilst comparisons of the modelling of the data and MC predictions are shown in (b) and (d). The vertical dashed lines and arrows identify the range of the distribution which is included in the selection. The uncertainty band represents the total normalisation uncertainty prior to performing the statistical analysis described in Chapter 6. The background processes are normalised according to the values in Table 4.6.

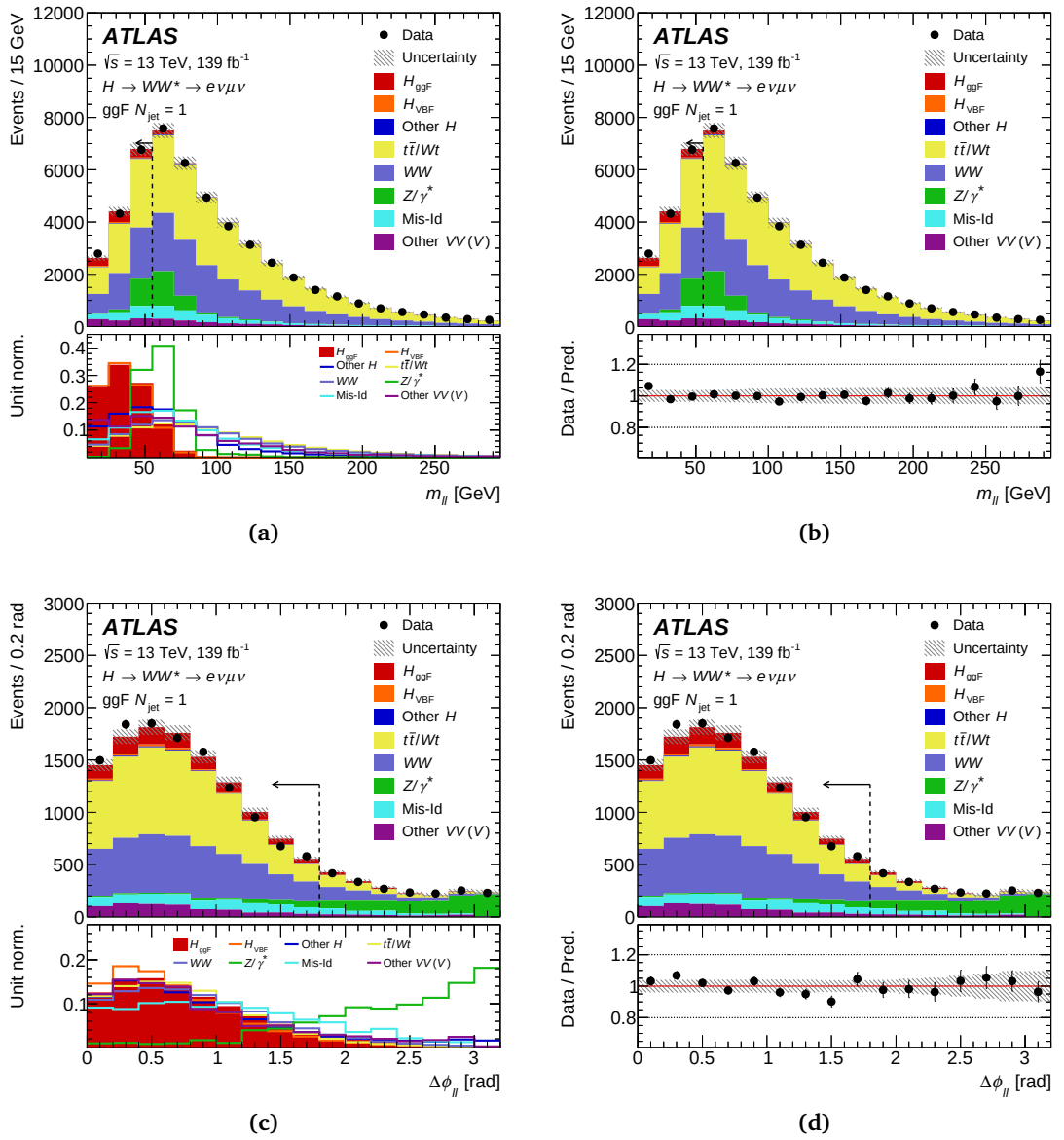

Figure 4.16: Distributions of $m_{\ell\ell}$ and $\Delta\phi_{\ell\ell}$ in the ggF $N_{\text{jet}} = 1$ category after applying all selection requirements except the requirements on $m_{\ell\ell}$ and $\Delta\phi_{\ell\ell}$, respectively. Comparisons of the shape of the signal and background processes are shown in (a) and (c), whilst comparisons of the modelling of the data and MC predictions are shown in (b) and (d). The vertical dashed lines and arrows identify the range of the distribution which is included in the selection. The uncertainty band represents the total normalisation uncertainty prior to performing the statistical analysis described in Chapter 6. The background processes are normalised according to the values in Table 4.6.

of this topology have not been studied in the full Run 2 data set, and target the large top quark background contamination of the total event yield in this category. After imposing the preselection criteria and an $N_{\text{jet}} \geq 2$ requirement (for jets with $p_{\text{T}} > 30$ GeV), the following selection requirements define the ggF-enriched $N_{\text{jet}} \geq 2$ SR:

- A veto on b-tagged jets, $N_{b\text{-jet}} = 0$, is required for all jets with $p_{\text{T}} > 20$ GeV to reject top quark events;
- $m_{\tau\tau}$ is required to be less than $(m_Z - 25)$ GeV to reject Z/γ^* events;
- $m_{\ell\ell}$ is required to be less than 55 GeV;
- $\Delta\phi_{\ell\ell}$ is required to be less than 1.8 radians.

Following the above selection requirements, an additional complication exists for the $N_{\text{jet}} \geq 2$ category specifically, since several production modes of the Higgs boson can give rise to the $\ell\ell + E_{\text{T}}^{\text{miss}} +$ jets final state. Namely, these are ggF and VBF production discussed already, but also VH production. Feynman diagrams at LO of the $\ell\ell + E_{\text{T}}^{\text{miss}} +$ jets final state produced through these three production modes are shown in Figure 4.17. Therefore, further selection requirements are implemented in the ggF-enriched $N_{\text{jet}} \geq 2$ category to ensure the selected events are mutually exclusive with the selected events in the VBF-enriched $N_{\text{jet}} \geq 2$ category, as well as removing $N_{\text{jet}} \geq 2$ events originating from the VH process. These selections are defined as follows:

- VH veto: $|m_{jj} - 85| > 15$ GeV `OR` $\Delta y_{jj} > 1.2$;
- VBF veto: fail central jet veto (CJV) `OR` fail outside lepton veto (OLV).

The VH veto removes events falling within a 15 GeV window of 85 GeV, since the invariant mass of the two jets, m_{jj}, should reconstruct the W or Z boson. Failing this requirement, events will still enter the ggF-enriched $N_{\text{jet}} \geq 2$ region if they are sufficiently separated by requiring $\Delta y_{jj} > 1.2$. This is because the two jets in the VH process should be produced centrally in the detector (i.e. at low values of rapidity) due to their originating from a massive vector boson recoiling from a Higgs boson.

The VBF veto exploits the topological differences between the production of a Higgs boson through VBF and through ggF in association with two or more jets. In the former case, the jets are typically very forward in the detector (i.e. they have large values of rapidity), whereas for ggF, the two jets are typically produced centrally in the detector by QCD processes. Failing the CJV means events with an additional jet located within the rapidity span of the two leading jets (in p_{T}) enter the ggF-enriched $N_{\text{jet}} \geq 2$ region. Failing the OLV ensures that events where the two leading leptons are not within the rapidity span of the two leading jets are also accepted into the ggF-enriched $N_{\text{jet}} \geq 2$ region.

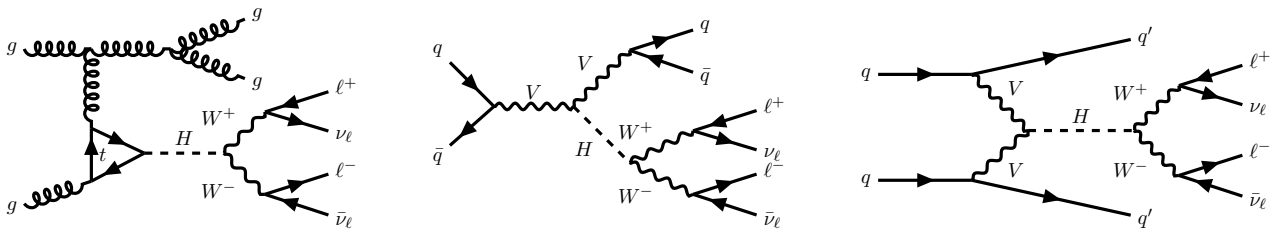

(a) ggF **(b)** VH **(c)** VBF

Figure 4.17: Example Feynman diagrams at LO showing the production of the $\ell\ell + E_{\mathrm{T}}^{\mathrm{miss}} +$ jets final state through (a) ggF, (b) VH, and (c) VBF.

It could also be possible to define mutual exclusivity between ggF-enriched $N_{\mathrm{jet}} \geq 2$ and VBF-enriched $N_{\mathrm{jet}} \geq 2$ events through a selection requirement on the DNN output distribution, since the ggF signal is included as a background process in the training. However, this reduces the usefulness of the measurements to the wider particle physics community since a selection requirement on a DNN is difficult to reproduce in a new theoretical calculation, for example. Additionally, the efficiency of the CJV is studied by varying the p_{T} threshold of the central jet. A value of 30 GeV is found to sufficiently reject background events in both ggF-enriched $N_{\mathrm{jet}} \geq 2$ and VBF-enriched $N_{\mathrm{jet}} \geq 2$ SRs, whilst also minimising the theoretical uncertainty in the signal modelling resulting from this selection requirement.

Distributions comparing the shape of the signal and background processes, as well as the modelling of the data and MC predictions, for the observables used in the ggF-enriched $N_{\mathrm{jet}} \geq 2$ selection are shown in Figure 4.18.

4.5.5 VBF-enriched $N_{\mathrm{jet}} \geq 2$

The selection requirements for events originating from the VBF production process exploit the topology of the process, which consists of two energetic jets with a large rapidity gap and where the decay products of the Higgs boson are centrally located in the detector. Similarly to the ggF-enriched $N_{\mathrm{jet}} \geq 2$ category, the major backgrounds include top quark processes, non-resonant WW, and Z/γ^*. However, given the lower cross section of the VBF production process and smaller signal event yields compared to the ggF categories, a multivariate analysis is used to fully exploit the expected topology and correlations between several observables in order to extract the VBF $H \to WW^* \to \ell\nu\ell\nu$ signal yield. The preselection of events follows the selection requirements in Table 4.3 except that there is no requirement on $p_{\mathrm{T}}^{\mathrm{miss}}$. After requiring $N_{\mathrm{jet}} \geq 2$ (for jets with $p_{\mathrm{T}} > 30$ GeV), the following selections define the VBF-enriched $N_{\mathrm{jet}} \geq 2$ SR:

- A veto on b-tagged jets, $N_{b\text{-jet}} = 0$, is required for all jets with $p_{\mathrm{T}} > 20$ GeV to reject top quark events;

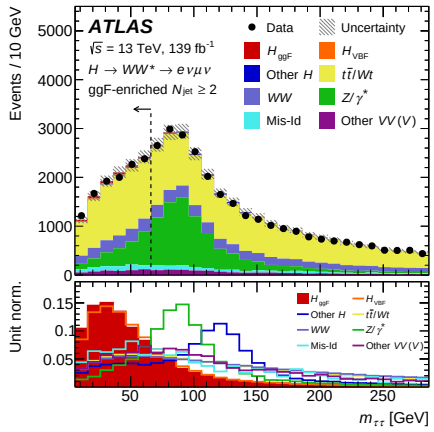

(a)

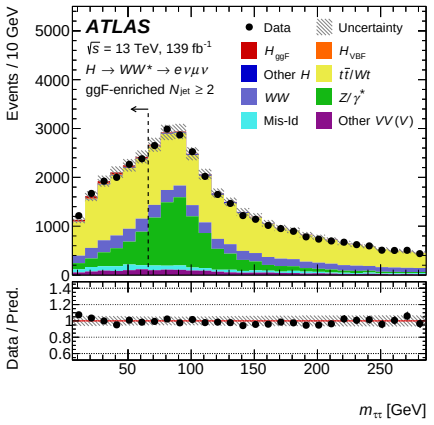

(b)

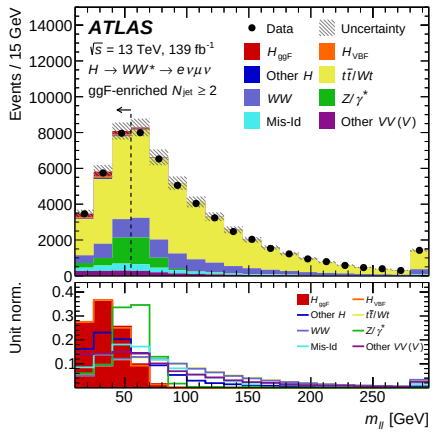

(c)

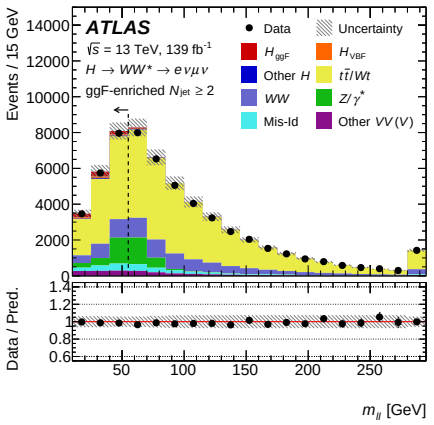

(d)

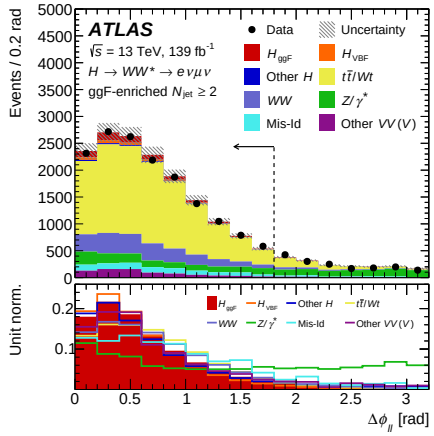

(e)

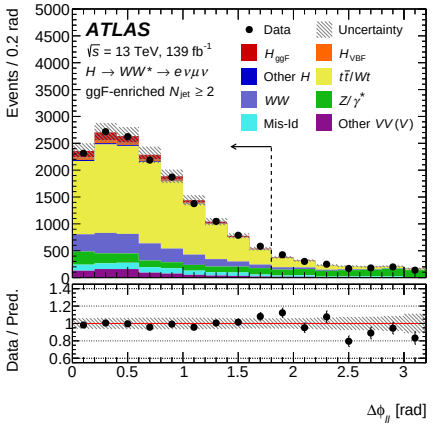

(f)

Figure 4.18: Distributions of $m_{\tau\tau}$, $m_{\ell\ell}$, and $\Delta\phi_{\ell\ell}$ in the ggF-enriched $N_{\text{jet}} \geq 2$ category shown after applying all selection requirements except the requirements on $m_{\tau\tau}$, $m_{\ell\ell}$ and $\Delta\phi_{\ell\ell}$, respectively. Comparisons of the shape of the signal and background processes are shown in (a), (c), and (e), whilst comparisons of the modelling of the data and MC predictions are shown in (b), (d), and (f). The vertical dashed lines and arrows identify the range of the distribution which is included in the selection. The uncertainty band represents the total normalisation uncertainty prior to performing the statistical analysis described in Chapter 6. The background processes are normalised according to the values in Table 4.6.

- $m_{\tau\tau}$ is required to be less than $(m_Z - 25)$ GeV to reject Z/γ^* events;
- The OLV and CJV are both required to pass. These requirements ensure that any events with jets with $p_{\mathrm{T}} > 30$ GeV lying in the rapidity span of the two leading jets, and with one or two leptons with rapidities outside the rapidity span of the two leading jets, are removed. Selected events in the VBF-enriched $N_{\mathrm{jet}} \geq 2$ SR are mutually exclusive with those in the ggF-enriched $N_{\mathrm{jet}} \geq 2$ SR with these requirements.
- m_{jj} is required to be greater than 120 GeV to remove events originating from the VH process.

A Deep Neural Network (DNN) is utilised as a further step to separate the Higgs boson signal from background processes, applied only in the VBF SR. The DNN is constructed using Keras [189] and TensorFlow [190]. Events are selected for training the DNN after applying the b-jet veto. Higgs boson production through VBF is considered the signal process, whilst all other processes are treated as background in the training, including ggF Higgs boson production. A total of fifteen kinematic observables are inputs to the DNN, which are selected to aid in the identification of events exhibiting the VBF topology, the topology of the $H \to WW^* \to \ell\nu\ell\nu$ decay, as well as to suppress background from top quark processes. The observables include:

- m_{jj}, Δy_{jj}, $\eta_{\ell}^{\mathrm{centrality}}$, the p_{T} of the three leading jets, and all combinations of $m_{\ell_i j_i}$ with $i = \{1, 2\}$, which target the expected VBF topology;
- $m_{\ell\ell}$, $\Delta\phi_{\ell\ell}$, and m_{T}, which target the expected $H \to WW^* \to \ell\nu\ell\nu$ topology;
- $p_{\mathrm{T}}^{\mathrm{tot}}$ and $E_{\mathrm{T}}^{\mathrm{miss}}$ significance, which target the suppression of top quark background events.

Distributions of two DNN input observables, m_{jj} and Δy_{jj}, comparing the shape of the signal and background processes, as well as the modelling of the data and MC predictions, are shown in Figure 4.19. The output of the DNN is a score in the range 0–1. The score represents a probability that an event is more like a VBF event. Events with scores closer to 1 comprise more of the Higgs boson signal, whilst events with scores closer to 0 are dominated by background events. Instead of m_{T}, the DNN output is used as the primary discriminating variable for the measurement of VBF production.

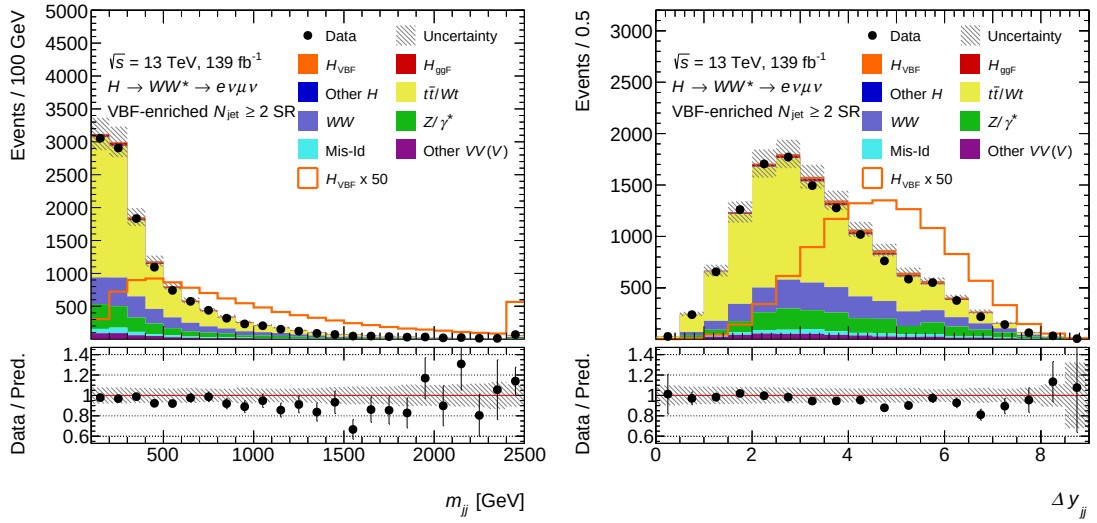

(a) **(b)**

Figure 4.19: Distributions comparing the modelling of data and MC predictions of (a) m_{jj} and (b) Δy_{jj} in the VBF-enriched $N_{\text{jet}} \geq 2$ SR. The distribution of the predicted VBF signal is shown by the solid line and is scaled by a factor of 50 for visualisation. The uncertainty band represents the total normalisation uncertainty prior to performing the statistical analysis described in Chapter 6. The background processes are normalised according to the values in Table 4.6.

Distributions of m_{T} and the DNN output comparing the modelling of the data and MC predictions are shown in Figure 4.20 after the application of all selection requirements defining the SRs.

After defining four SRs based on categories defined by jet multiplicity, the discrimination of the Higgs boson signal with respect to background processes is enhanced for the purpose of the statistical analysis (Chapter 6) by splitting the event yields of the SRs into smaller SRs with selection requirements on distributions of observables that are sensitive to the Higgs boson signal process. For the ggF $N_{\mathrm{jet}} = 0$ and ggF $N_{\mathrm{jet}} = 1$ SRs, the event yields are split into four further sub-SRs using boundaries defined by $m_{\ell\ell} = 30$ GeV and $p_{\mathrm{T}}^{\mathrm{sublead}} = 20$ GeV. The ggF-enriched $N_{\mathrm{jet}} \geq 2$ SR is split into two further sub-SRs using a boundary of $m_{\ell\ell} = 30$ GeV. This is determined by evaluating the expected precision of a measurement of the ggF signal strength using the ggF-enriched $N_{\mathrm{jet}} \geq 2$ regions only, including estimates of all sources of uncertainty[27]. The use of $m_{\ell\ell}$ is motivated by the fact that the event yield of the $H \to WW^* \to \ell\nu\ell\nu$ signal is expected to be larger at low values of $m_{\ell\ell}$, whilst the opposite is true for non-resonant WW production and other background processes. Similarly, the use of $p_{\mathrm{T}}^{\mathrm{sublead}}$ helps to distinguish the $H \to WW^* \to \ell\nu\ell\nu$ signal from the W+jets background. For the signal process, the sub-leading lepton typically has low p_{T} due to the fact that one of the W bosons is off-shell. Similarly, for W+jets processes where a jet or photon is incorrectly reconstructed as a lepton, or an off-shell photon produces a low-mass lepton pair with only one reconstructed lepton, the sub-leading lepton will also have low p_{T}. Typically however, the sub-leading lepton p_{T} for W+jets has a distribution that falls more rapidly than that for the $H \to WW^* \to \ell\nu\ell\nu$ signal [5]. There is no further categorisation of the VBF SR because the bins of the output DNN distribution that are most sensitive to the Higgs boson signal have a high signal-to-background ratio.

4.6 Background estimation

For many of the background processes which populate the selected event yields in this analysis, a data-driven approach is taken to estimate their yields (and/or the shape of the m_{T} or DNN output disitributions). This can be done using an entirely data-driven approach, which is the case for the W+jets and QCD multi-jet background processes, or with so-called *control regions* (CRs), which is the case for the non-resonant WW, top quark, and Z/γ^* background processes.

A CR for a specific background process is usually defined by inverting or modifying one of the event selection requirements of the SR, such that the newly defined region is enriched in the specific background process of interest and is kinematically similar to

[27] The use of futher sub-SRs split by $p_{\mathrm{T}}^{\mathrm{sublead}}$ in the ggF-enriched $N_{\mathrm{jet}} \geq 2$ region was shown to not increase the signal-to-background discrimination due to the smaller expected signal yields in this region.

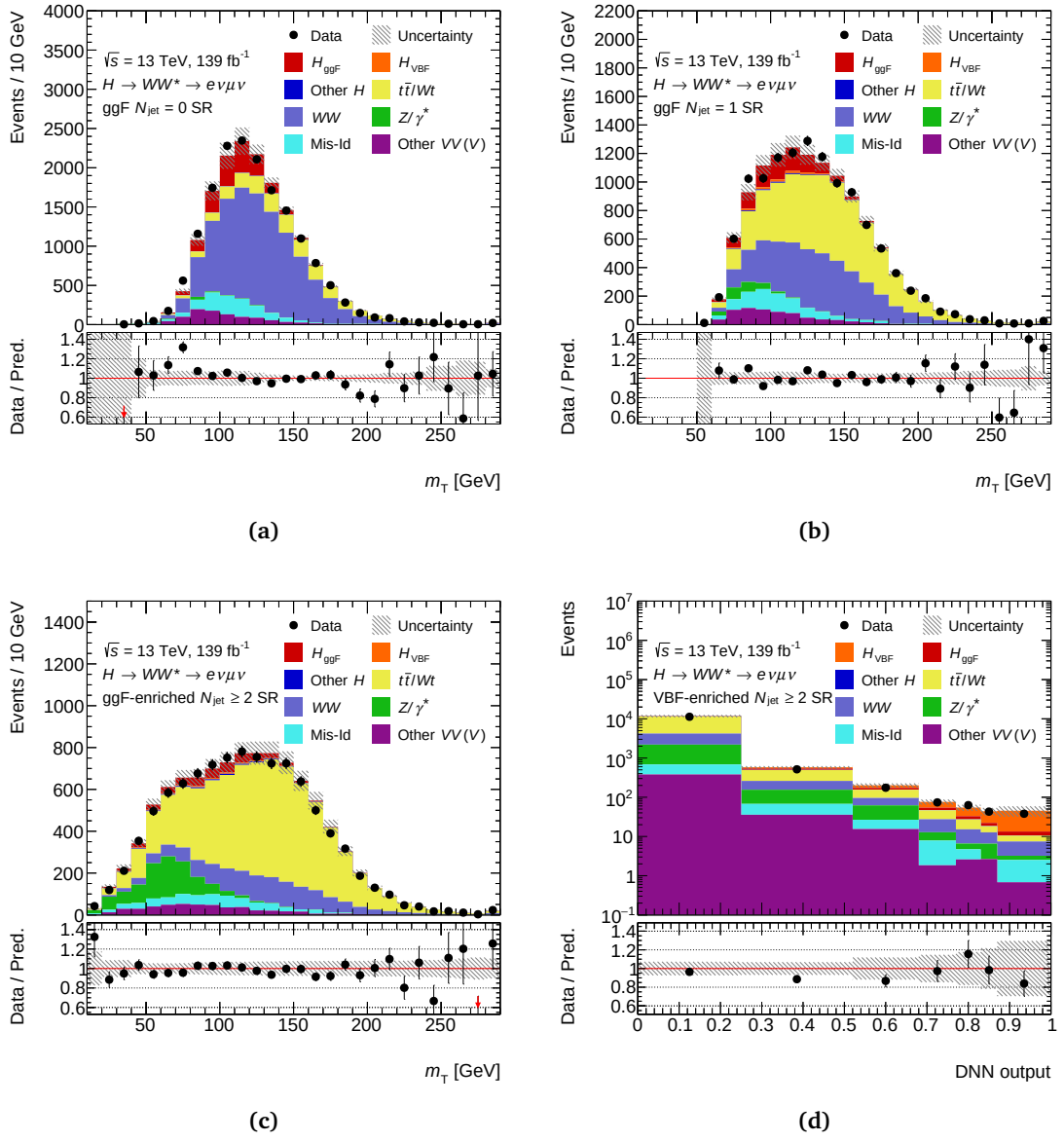

Figure 4.20: Distributions of m_{T} following all selection requirements in the (a) ggF $N_{\mathrm{jet}} = 0$, (b) ggF $N_{\mathrm{jet}} = 1$, and (c) ggF-enriched $N_{\mathrm{jet}} \geq 2$ SRs. The DNN output distribution is shown in (d) following all selection requirements of the VBF-enriched $N_{\mathrm{jet}} \geq 2$ SR. The sub-panel shows a comparison of the modelling of the data and the MC predictions. The uncertainty band represents the total normalisation uncertainty prior to performing the statistical analysis described in Chapter 6. The background processes are normalised according to the values in Table 4.6.

the SR. A *normalisation factor* (NF) for a specific background process, i, measured in a CR, is the ratio of the background-subtracted data yields and the event yields of process i predicted by MC simulation, and is defined by

$$\text{NF}_i = \frac{N^{\text{CR}}_{\text{data}} - N^{\text{CR}}_{\text{bkg}}}{N^{\text{CR}}_{i,\text{MC}}}, \tag{4.11}$$

where $N^{\text{CR}}_{\text{data}}$ is the data yield in the CR, $N^{\text{CR}}_{\text{bkg}}$ is the total yield of background processes other than process i (predicted with MC simulation or with data), and $N^{\text{CR}}_{i,\text{MC}}$ is the yield of process i in the CR as predicted by MC simulation. The estimated yield of process i in the SR, $N^{\text{SR}}_{i,\text{est.}}$, is obtained with

$$N^{\text{SR}}_{i,\text{est.}} = \text{NF}_i \times N^{\text{SR}}_{i,\text{MC}}, \tag{4.12}$$

where $N^{\text{SR}}_{i,\text{MC}}$ is the event yield of process i in the SR as predicted by MC simulation. Equation 4.12 can be manipulated in the following way:

$$\begin{aligned} N^{\text{SR}}_{i,\text{est.}} &= \frac{N^{\text{CR}}_{\text{data}} - N^{\text{CR}}_{\text{bkg}}}{N^{\text{CR}}_{i,\text{MC}}} \times N^{\text{SR}}_{i,\text{MC}} \\ &= (N^{\text{CR}}_{\text{data}} - N^{\text{CR}}_{\text{bkg}}) \times \frac{N^{\text{SR}}_{i,\text{MC}}}{N^{\text{CR}}_{i,\text{MC}}} \\ &= (N^{\text{CR}}_{\text{data}} - N^{\text{CR}}_{\text{bkg}}) \times \alpha^{\text{SR}}_i, \end{aligned} \tag{4.13}$$

where α^{SR}_i is an extrapolation factor. Since α^{SR}_i is a ratio of event yields predicted with MC simulation, many systematic uncertainties, which can originate from numerous experimental and theoretical sources, cancel in the ratio. The cancellation is largest when the SR and CR exhibit similar kinematics, hence the reason for minimally changing event selection requirements to define CRs. As such, systematic uncertainties on α^{SR}_i are small and the systematic uncertainties on the estimated event yields of backgrounds processes in the SR are significantly reduced. In this approach however, it is only the normalisation of background yields which is corrected with the use of the NF; inacuraccies in the modelling of the shape of the m_{T} and DNN output distributions are not corrected.

In this analysis, several CRs are defined for each analysis category and an NF is extracted to scale the background yields in each SR. Specifically, the normalisation of $qqWW$[28], top quark, and Z/γ^* processes are obtained using CRs. The yields and shape of distributions of other background processes, including non-WW diboson, triboson, $ggWW$, and non-ggF and VBF $H\to WW^*$ processes, are obtained using MC predictions. The event selection requirements defining the CRs are shown in Table 4.5. Generally, the defining requirements

[28]Only the rate of $qqWW$ is normalised by the CR instead of the sum of the $qqWW$ and $ggWW$ processes. This is because the $ggWW$ MC sample uses a calculation at lower order in QCD and therefore comes with large theoretical uncertainties. Not including the process in the normalisation ensures that large theoretical uncertainties assciated with the $ggWW$ sample are not linked to the normalisation factor.

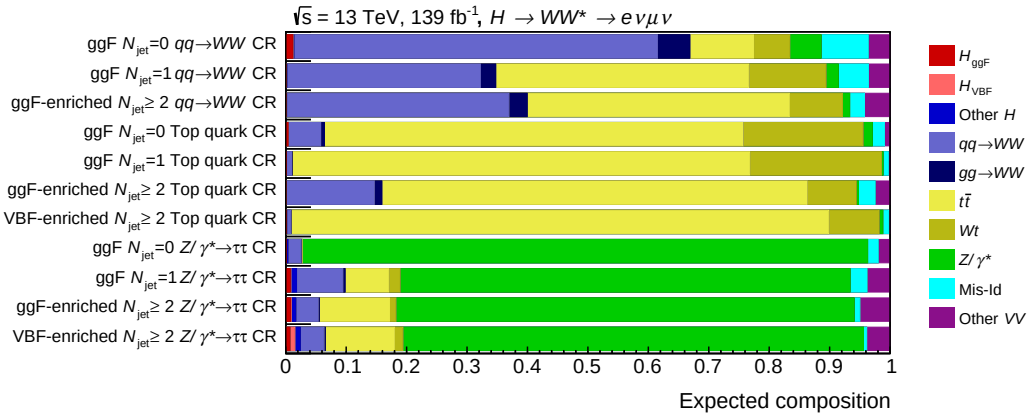

Figure 4.21: The composition of signal and background processes in each CR. The $qqWW$, top quark, and Z/γ^* background processes are normalised according to the values in Table 4.6.

of a CR are determined by ensuring the theoretical uncertainty in the extrapolation factor, α_i^{SR}, is minimised. For example, in defining CRs for the ggF-enriched $N_{\text{jet}} \geq 2$ category of events (a topology of events which had previously not been studied since the Run 1 measurement [6]), it is important to check if CR definitions are still optimal in this analysis will the full Run 2 data set. Typically, several different selection requirements are tested and the theoretical uncertainty of α_i^{SR} is computed for each test. This is the methodology by which the requirement of $m_{\ell\ell} < 55$ GeV is determined as a defining requirement of the Z/γ^* CR in the ggF-enriched $N_{\text{jet}} \geq 2$ category: it is more kinematically similar to the SR, which minimises the theoretical uncertainty in α_i^{SR}. Additionally, selection requirements defining CRs can be determined by removing regions of the data set poorly modelled by the MC simulation. Whilst this is subjective, MC simulation that is generally within 1σ of the observed data, considering the theoretical uncertainty in the MC prediction, is considered well-modelled. It is also important to verify that selection requirements do not also introduce artificial trends in the shape of distributions of observables. These considerations led to the definition of the Z/γ^* CR in the ggF-enriched $N_{\text{jet}} \geq 2$ category without placing a requirement on the $\Delta\phi_{\ell\ell}$ distribution, instead of a requirement of $\Delta\phi_{\ell\ell} > 2.8$ that was used in the Run 1 measurement [6].

The background NFs are determined along with the signal normalisations (signal strengths) in the statistical analysis described in Chapter 6. However, prior to performing the full statistical analysis, it is possible to estimate the values of the NFs using only the data from the CRs and a matrix inversion. The values of the NFs using this method are shown in Table 4.6 and are used to normalise the rate of the respective background processes in distributions and yield tables in this chapter (i.e. before Chapter 7). The expected signal and background compositions for each CR are shown in Figure 4.21 and the expected event yields are listed in Table 4.7.

Table 4.5: The selection criteria used to define the CRs in each analysis category defined by the jet multiplicity. The preselection requirements described in Section 4.5.1 are implicitly included in the CR selection requirements.

CR	$N_{\text{jet},(p_{\text{T}}>30\text{ GeV})} = 0$ ggF	$N_{\text{jet},(p_{\text{T}}>30\text{ GeV})} = 1$ ggF	$N_{\text{jet},(p_{\text{T}}>30\text{ GeV})} \geq 2$ ggF	$N_{\text{jet},(p_{\text{T}}>30\text{ GeV})} \geq 2$ VBF
$qq \to WW$	$N_{b\text{-jet},(p_{\text{T}}>20\text{ GeV})} = 0$			
	$\Delta\phi(\ell\ell, E_{\text{T}}^{\text{miss}}) > \pi/2$ $p_{\text{T}}^{\ell\ell} > 30$ GeV $55 < m_{\ell\ell} < 110$ GeV $\Delta\phi_{\ell\ell} < 2.6$	$m_{\ell\ell} > 80$ GeV		
		$\lvert m_{\tau\tau} - m_Z \rvert > 25$ GeV $\max(m_{\text{T}}^{\ell}) > 50$ GeV	$m_{\tau\tau} < m_Z - 25$ GeV $m_{\text{T2}} > 165$ GeV	
			fail central jet veto or fail outside lepton veto	
			$\lvert m_{jj} - 85 \rvert > 15$ GeV or $\Delta y_{jj} > 1.2$	
$t\bar{t}/Wt$	$N_{b\text{-jet},(20\text{ GeV}<p_{\text{T}}<30\text{ GeV})} > 0$	$N_{b\text{-jet},(p_{\text{T}}>30\text{ GeV})} = 1$ $N_{b\text{-jet},(20\text{ GeV}<p_{\text{T}}<30\text{ GeV})} = 0$	$N_{b\text{-jet},(p_{\text{T}}>20\text{ GeV})} = 0$	$N_{b\text{-jet},(p_{\text{T}}>20\text{ GeV})} = 1$
	$\Delta\phi(\ell\ell, E_{\text{T}}^{\text{miss}}) > \pi/2$ $p_{\text{T}}^{\ell\ell} > 30$ GeV $\Delta\phi_{\ell\ell} < 2.8$	$m_{\tau\tau} < m_Z - 25$ GeV		
		$\max(m_{\text{T}}^{\ell}) > 50$ GeV	$m_{\ell\ell} > 80$ GeV $\Delta\phi_{\ell\ell} < 1.8$ $m_{\text{T2}} < 165$ GeV	
			fail central jet veto or fail outside lepton veto	central jet veto outside lepton veto
			$\lvert m_{jj} - 85 \rvert > 15$ GeV or $\Delta y_{jj} > 1.2$	
Z/γ^*	$N_{b\text{-jet},(p_{\text{T}}>20\text{ GeV})} = 0$			
	$m_{\ell\ell} < 80$ GeV no $p_{\text{T}}^{\text{miss}}$ requirement		$m_{\ell\ell} < 55$ GeV	$m_{\ell\ell} < 70$ GeV
	$\Delta\phi_{\ell\ell} > 2.8$	$m_{\tau\tau} > m_Z - 25$ GeV		$\lvert m_{\tau\tau} - m_Z \rvert \leq 25$ GeV
		$\max(m_{\text{T}}^{\ell}) > 50$ GeV	fail central jet veto or fail outside lepton veto	central jet veto outside lepton veto
			$\lvert m_{jj} - 85 \rvert > 15$ GeV or $\Delta y_{jj} > 1.2$	

Table 4.6: NFs for background processes obtained using CR data and with matrix inversion. The uncertainties originate from the sample size of the CRs.

SR	$qqWW$	$t\bar{t}/Wt$	Z/γ^*
ggF $N_{\text{jet}} = 0$	1.09 ± 0.01	1.02 ± 0.01	0.95 ± 0.00
ggF $N_{\text{jet}} = 1$	0.88 ± 0.02	1.02 ± 0.00	0.88 ± 0.01
ggF-enriched $N_{\text{jet}} \geq 2$	0.73 ± 0.08	1.05 ± 0.03	0.90 ± 0.02
VBF-enriched $N_{\text{jet}} \geq 2$	–	0.99 ± 0.01	0.98 ± 0.03

Table 4.7: Event yields of signal and background processes for each CR. The yields correspond to the expectation from MC simulation. Yields for background processes measured with a CR are normalised according to the values in Table 4.6, whilst the yield for Mis-ID is obtained using the data-driven method described in Section 4.6.4. The uncertainties correspond to statistical uncertainty only.

CR	Category	H_{ggF}	H_{VBF}	WW	Other $VV(V)$	$t\bar{t}/Wt$	Z/γ^*	Mis-Id	Total Bkg.	Data
$qqWW$	ggF $N_{\text{jet}}=0$	303 ± 2	4 ± 0	$17\,542\pm47$	949 ± 19	4355 ± 19	1371 ± 56	2048 ± 39	$26\,266\pm87$	26 254
	ggF $N_{\text{jet}}=1$	6 ± 0	1 ± 0	$13\,494\pm37$	1397 ± 25	$21\,321\pm38$	816 ± 46	1945 ± 44	$38\,973\pm86$	38 911
	ggF-enriched $N_{\text{jet}}\geq2$	0 ± 0	0 ± 0	454 ± 3	48 ± 3	594 ± 6	14 ± 2	28 ± 6	1138 ± 10	1140
Top quark	ggF $N_{\text{jet}}=0$	45 ± 1	1 ± 0	678 ± 10	101 ± 7	9515 ± 25	142 ± 8	207 ± 17	$10\,644\pm34$	10 642
	ggF $N_{\text{jet}}=1$	63 ± 1	7 ± 0	663 ± 8	209 ± 8	$69\,903\pm67$	206 ± 16	621 ± 43	$71\,603\pm81$	71 598
	ggF-enriched $N_{\text{jet}}\geq2$	0 ± 0	0 ± 0	1057 ± 5	165 ± 7	5241 ± 17	25 ± 3	184 ± 16	6672 ± 25	6678
	VBF-enriched $N_{\text{jet}}\geq2$	28 ± 1	22 ± 0	219 ± 3	88 ± 8	$40\,129\pm44$	269 ± 10	404 ± 33	$41\,109\pm57$	41 112
Z/γ^*	ggF $N_{\text{jet}}=0$	144 ± 1	2 ± 0	2992 ± 19	2672 ± 52	258 ± 4	$127\,736\pm240$	2379 ± 88	$136\,037\pm261$	136 036
	ggF $N_{\text{jet}}=1$	90 ± 1	12 ± 0	977 ± 10	466 ± 19	1112 ± 8	9328 ± 80	342 ± 30	$12\,226\pm88$	12 222
	ggF-enriched $N_{\text{jet}}\geq2$	28 ± 0	5 ± 0	140 ± 2	181 ± 11	459 ± 5	2749 ± 20	34 ± 11	3563 ± 26	3624
	VBF-enriched $N_{\text{jet}}\geq2$	15 ± 0	17 ± 0	66 ± 1	83 ± 7	277 ± 4	1710 ± 18	11 ± 9	2148 ± 22	2114

4.6.1 Non-resonant WW background

$qqWW$ CRs are defined for each of the ggF $N_{\text{jet}} = 0$, ggF $N_{\text{jet}} = 1$, and ggF-enriched $N_{\text{jet}} \geq 2$ categories, which are used to normalise the rate of $qqWW$ in the respective SRs. The contribution of quark-induced and gluon-induced WW production to the total WW yield is around 90% and 10% in each SR, respectively. For the VBF-enriched $N_{\text{jet}} \geq 2$ analysis category, no CR is used to normalise the rate of $qqWW$ in the SR so both the rate and DNN output distribution are estimated from the theoretical prediction. The SRs in this analysis are defined at low values of $m_{\ell\ell}$ and $\Delta\phi_{\ell\ell}$, in line with the expectation of the Higgs boson signal. One or both of these requirements are inverted to target events comprising lepton pairs with larger invariant mass and opening angle in order to define CRs which are largely populated by $qqWW$ events.

ggF $N_{\text{jet}} = 0$

The ggF $N_{\text{jet}} = 0$ $qqWW$ CR is defined with the following modifications to the SR selection requirements:

- $m_{\ell\ell}$ is required to be between 55 and 110 GeV to ensure the CR is mutually exclusive to the SR and limit the contamination of the CR from top quark events.
- $\Delta\phi_{\ell\ell}$ is required to be less than 2.6 radians. The loosening of the $\Delta\phi_{\ell\ell}$ requirement maximises the total event yield to increase the precision of the sample size, whilst minimising the contamination of the event yield from Z/γ^* events.

The purity of the ggF $N_{\text{jet}} = 0$ $qqWW$ CR is 67% and the m_{T} distribution is shown in Figure 4.23a.

ggF $N_{\text{jet}} = 1$

The ggF $N_{\text{jet}} = 1$ $qqWW$ CR is defined with the following modifications to the SR selection requirements:

- Events where the hypothetical invariant mass of a τ-lepton pair, $m_{\tau\tau}$, falls within a 25 GeV window of the Z boson mass are rejected to reduce contamination from resonant $Z/\gamma^* \to \tau\tau$ production.
- $m_{\ell\ell}$ is required to be larger than 80 GeV which maintains exclusivity with the SR selection and reduces contamination from Z/γ^* events.
- The requirement on $\Delta\phi_{\ell\ell}$ is removed.

This selection results in a purity of 34% where the largest contamination arises from top quark processes. However, the ratio of WW and top quark processes in the CR is 0.63, which is similar to the ratio of $qqWW$ and top quark processes in the SR (0.71). This means that the composition of the $qqWW$ CR is representative of the SR and

the extrapolation uncertainty will be small. The m_{T} distribution of the ggF $N_{\mathrm{jet}} = 1$ $qqWW$ CR is shown in Figure 4.23b.

ggF-enriched $N_{\mathrm{jet}} \geq 2$

The largest background contamination originates from top quark processes in the ggF-enriched $N_{\mathrm{jet}} \geq 2$ category, even after rejecting events with an identified b-jet. It is challenging to disentangle top quark processes from non-resonant WW+jets such that the CR has a sufficiently high purity of WW and sample size. Nevertheless, a CR is defined in the ggF-enriched $N_{\mathrm{jet}} \geq 2$ category with the following modifications to the SR selection requirements:

- $m_{\ell\ell}$ is required to be larger than 80 GeV in order to maintain exclusivity with the SR selection, as well as to reduce the contamination of top quark and Z/γ^* events.
- The requirement on $\Delta\phi_{\ell\ell}$ is removed.
- m_{T2} is required to be larger than 165 GeV to further reduce the contamination from top quark events. In this region with $N_{b\text{-jet}} = 0$, events usually do not contain a true b-jet, or a mis-identified b-jet if they do. Additionally, several combinations of visible particle momenta are possible, with not all combinations corresponding to the correct decay branch. Therefore, several m_{T2} values are determined per event where the visible portion of each branch in the calculation consists of combinations of the leading and subleading leptons and jets. The final value of m_{T2} is the minimum of these calculations. The distribution of m_{T2} prior to this selection requirement is shown in Figure 4.22, where the proportion of $qqWW$ events increases in this range.

This selection results in a purity of 39%, with top quark background events comprising a substantial proportion of the total event yield. The m_{T} distribution of the ggF-enriched $N_{\mathrm{jet}} \geq 2$ $qqWW$ CR is shown in Figure 4.23c.

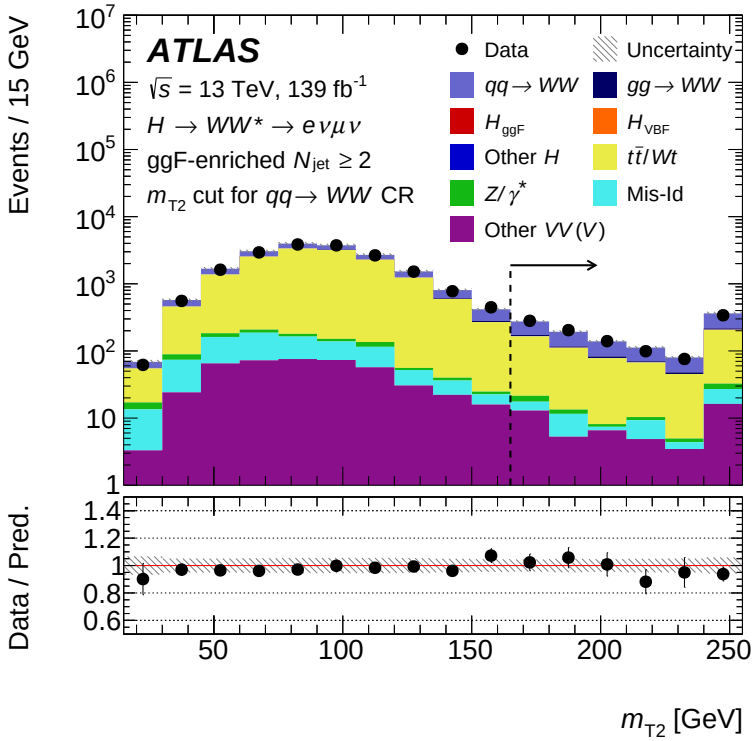

Figure 4.22: Distribution of m_{T2} following all selection requirements other than the selection on m_{T2} in the ggF-enriched $N_{\mathrm{jet}} \geq 2$ $qqWW$ CR. The sub-panel shows a comparison of the modelling of the data and the MC predictions. The uncertainty band represents the total normalisation uncertainty prior to performing the statistical analysis described in Chapter 6. The vertical dashed lines and arrows identify the range of the distribution which is included in the selection. The background processes are normalised according to the values in Table 4.6. The final bin includes events beyond the range of the plotted distribution.

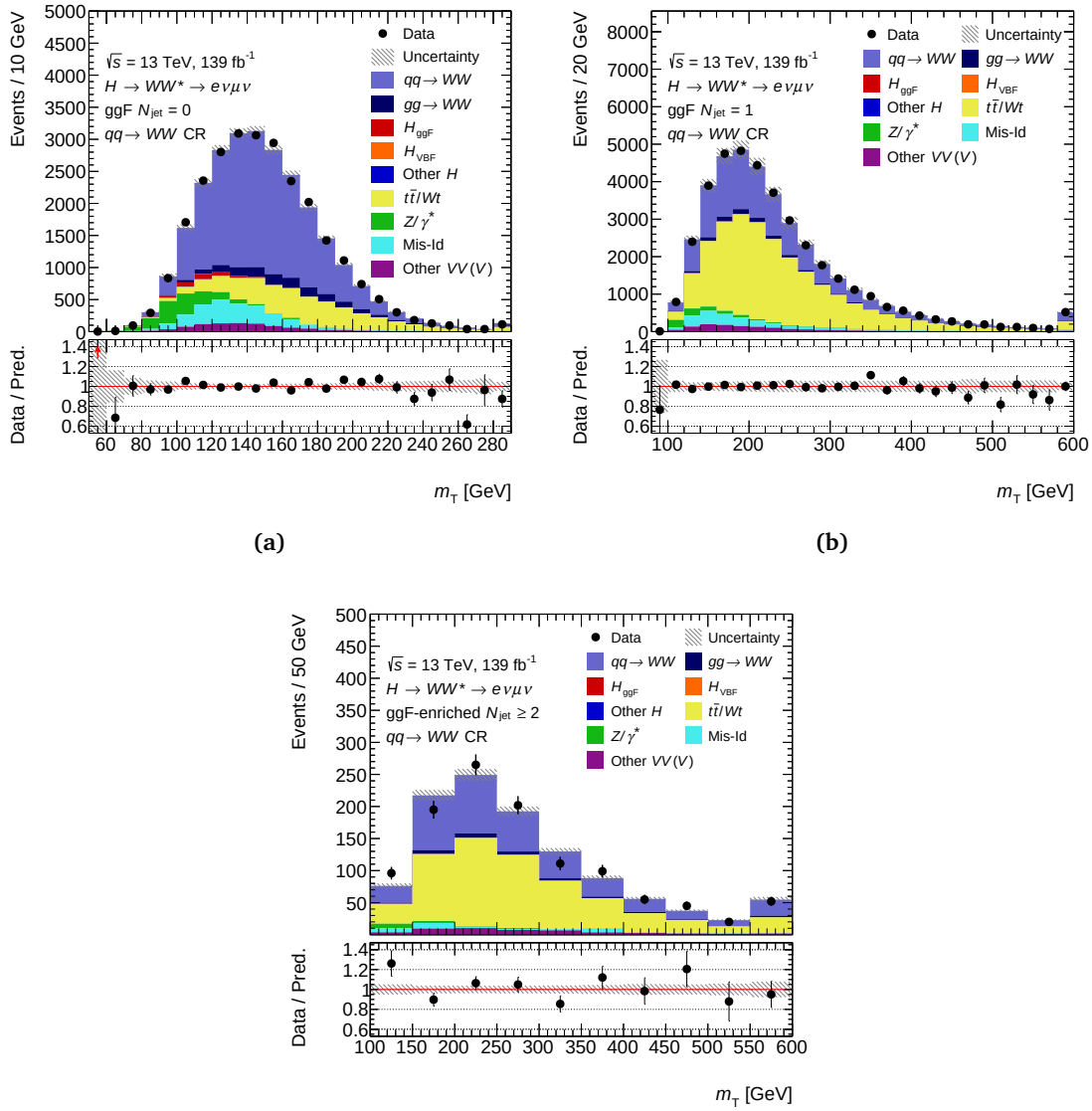

Figure 4.23: Distributions of m_{T} following all selection requirements in the (a) ggF $N_{\mathrm{jet}} = 0$, (b) ggF $N_{\mathrm{jet}} = 1$, and (c) ggF-enriched $N_{\mathrm{jet}} \geq 2$ $qqWW$ CRs. The sub-panel shows a comparison of the modelling of the data and the MC predictions. The uncertainty band represents the total normalisation uncertainty prior to performing the statistical analysis described in Chapter 6. The background processes are normalised according to the values in Table 4.6. The final bin includes events beyond the range of the plotted distribution.

4.6.2 Top quark background

Top quark CRs are defined for the ggF $N_{\text{jet}} = 0$, ggF $N_{\text{jet}} = 1$, ggF-enriched $N_{\text{jet}} \geq 2$, and VBF-enriched $N_{\text{jet}} \geq 2$ categories, which are used to normalise the combined rate of $t\bar{t}$ and Wt in the respective SRs. The selection requirements for the CRs typically invert the b-jet veto requirement which is used in all the SR selections, and in some cases the requirements on $m_{\ell\ell}$ and $\Delta\phi_{\ell\ell}$ are modified.

ggF $N_{\text{jet}} = 0$

The contribution of top quark events in the ggF $N_{\text{jet}} = 0$ category is small with respect to the other analysis categories since the decay of a top quark always includes a final state b-quark. The following SR selection requirements are modified for the ggF $N_{\text{jet}} = 0$ top quark CR:

- The analysis categories defined by jet multiplicity make use of jets which are reconstructed with a p_{T} larger than 30 GeV. A sufficient yield of top quark events and exclusivity with the SR selection is achieved by requiring that at least one jet with $20 < p_{\text{T}} < 30$ GeV is identified as a b-jet.
- The requirement on $m_{\ell\ell}$ is dropped and the requirement on $\Delta\phi_{\ell\ell}$ is loosened to 2.8 radians to ensure the sample size of the CR is sufficiently large.

These selection requirements result in a top quark CR with a purity of 89%. The m_{T} distribution of the ggF $N_{\text{jet}} = 0$ top quark CR is shown in Figure 4.24a.

ggF $N_{\text{jet}} = 1$

The top quark CR in the ggF $N_{\text{jet}} = 1$ category is defined with the following modifications to the SR selection requirements:

- The reconstructed jet with $p_{\text{T}} > 30$ GeV is required to be identified as a b-jet. Any jets with $20 < p_{\text{T}} < 30$ GeV are excluded from the b-jet identification. This requirement improves the similarity of the $t\bar{t}/Wt$ ratio in the CR with the ratio calculated in the SR and ensures that large uncertainties on the identification of low-p_{T} b-jets are not included in the extrapolation.
- The requirements on $m_{\ell\ell}$ and $\Delta\phi_{\ell\ell}$ are removed to increase the sample size of the CR.

The top quark CR is 98% pure. The m_{T} distribution of the ggF $N_{\text{jet}} = 1$ top quark CR is shown in Figure 4.24b.

ggF-enriched $N_{\text{jet}} \geq 2$

The highest prevalence of top quark events occurs in the $N_{\text{jet}} \geq 2$ categories. Given the inefficiencies in the identification of b-jets, a significant amount of top quark events remain

in the ggF-enriched $N_{\text{jet}} \geq 2$ SR after applying all selection requirements, including a b-jet veto. This means, however, that a top quark CR can be defined without requiring identified b-jets. The effect of this is that the extrapolation will not transport uncertainties due to b-tagging to a region where there is no use of b-tagging. The following modifications to the SR selection requirements are used to define the top quark CR:

- Exclusivity with the ggF-enriched $N_{\text{jet}} \geq 2$ SR is achieved by inverting the $m_{\ell\ell}$ requirement to $m_{\ell\ell} > 80$ GeV, a region populated by top quark events.
- m_{T2} is required to be less than 165 GeV so that the selected events are mutually exclusive with those selected for the $qqWW$ CR.

The purity of the top quark CR is 72%. The m_{T} distribution of the ggF-enriched $N_{\text{jet}} \geq 2$ top quark CR is shown in Figure 4.24c.

VBF-enriched $N_{\text{jet}} \geq 2$

The only modification to the VBF-enriched $N_{\text{jet}} \geq 2$ SR selection is that exactly one jet is required to have been identified as a b-jet. Not requiring an inclusive selection of b-tagged jets ensures that the flavour composition of the two leading jets in p_{T} is similar to those in the SR defined with a b-veto. The purity of the resulting selection is 97%. The DNN output distribution of the VBF-enriched $N_{\text{jet}} \geq 2$ top quark CR is shown in Figure 4.24d.

In defining top quark CRs, which are used to normalise the rate of the sum of the $t\bar{t}$ and Wt processes, the expected ratio of $t\bar{t}$ events to Wt events is compared between the SRs and CRs. If the sum of the $t\bar{t}$ and Wt yields is corrected in the CR, then the individual corrections to each individual process will result in the same combined correction if the proportion of $t\bar{t}$ and Wt yields is the same in the SR (neglecting any inacuraccies in the modelling of the shape of distributions). Figure 4.25 shows the proportion of $t\bar{t}$ and Wt events in each SR and CR. The ratio is most similar for the ggF-enriched $N_{\text{jet}} \geq 2$ and VBF-enriched $N_{\text{jet}} \geq 2$ regions, where top quark processes dominate the event yield.

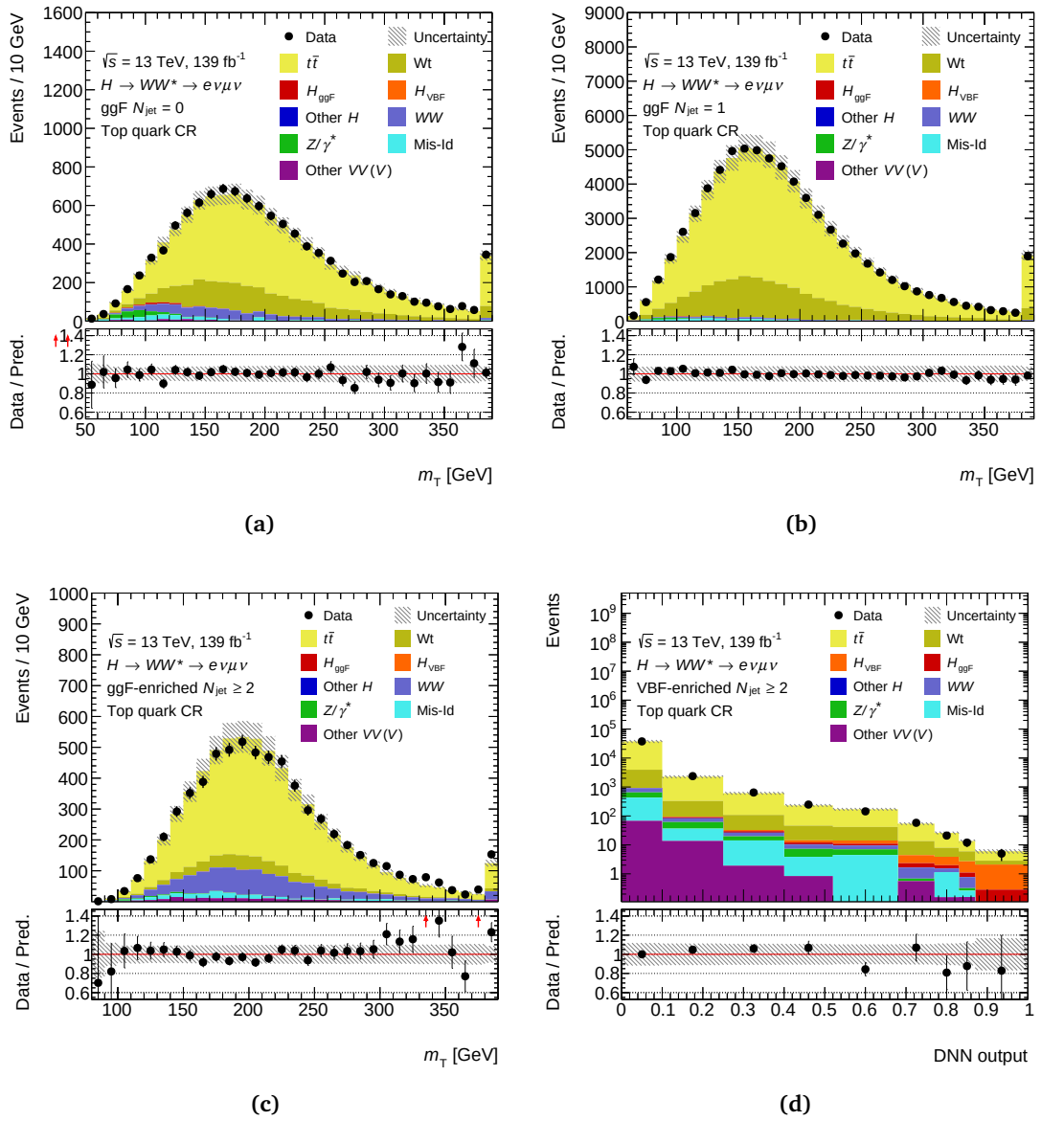

Figure 4.24: Distributions of m_{T} following all selection requirements in the (a) ggF $N_{\mathrm{jet}} = 0$, (b) ggF $N_{\mathrm{jet}} = 1$, and (c) ggF-enriched $N_{\mathrm{jet}} \geq 2$ top quark CRs. The DNN output distribution is shown in (d) for the VBF-enriched $N_{\mathrm{jet}} \geq 2$ top quark CR. The sub-panel shows a comparison of the modelling of the data and the MC predictions. The uncertainty band represents the total normalisation uncertainty prior to performing the statistical analysis described in Chapter 6. The background processes are normalised according to the values in Table 4.6. The final bin includes events beyond the range of the plotted distribution.

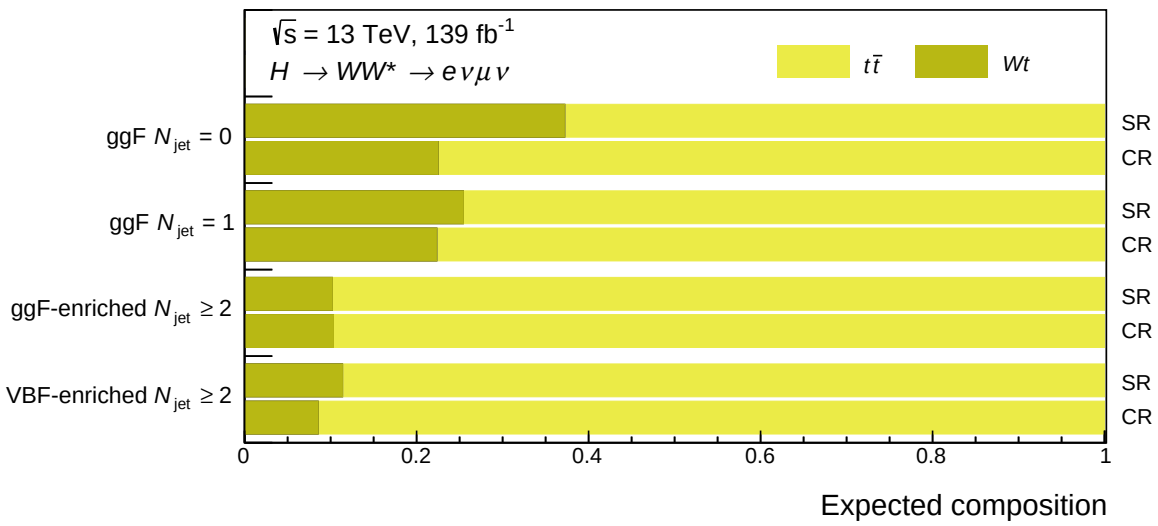

Figure 4.25: Proportion of $t\bar{t}$ and Wt events in each SR and CR. The yields are normalised according to the values in Table 4.6.

4.6.3 Z/γ^* background

CRs are defined for each of the ggF $N_{\text{jet}} = 0$, ggF $N_{\text{jet}} = 1$, ggF-enriched $N_{\text{jet}} \geq 2$, and VBF-enriched $N_{\text{jet}} \geq 2$ categories, which are used to normalise the Z/γ^* rate in the respective SRs.

ggF $N_{\text{jet}} = 0$

The following modifications are made to the signal selection requirements in order to define a Z/γ^* CR:

- the $p_{\text{T}}^{\text{miss}}$ requirement in the preselection is removed;
- $\Delta\phi_{\ell\ell}$ is required to be larger than 2.8 radians;
- $m_{\ell\ell}$ is required to be less than 80 GeV.

The purity of $Z/\gamma^* \to \tau\tau$ background resulting from the above selection requirements is 94%. The contribution from $Z/\gamma^* \to ee/\mu\mu$ events to the total Z/γ^* yield is 1.5%. The m_{T} distribution of the ggF $N_{\text{jet}} = 0$ Z/γ^* CR is shown in Figure 4.26a.

ggF $N_{\text{jet}} = 1$

The $N_{\text{jet}} = 1$ Z/γ^* CR is defined with the following modifications to the signal selection requirements:

- the $p_{\text{T}}^{\text{miss}}$ requirement in the preselection is removed;
- $m_{\ell\ell}$ is required to be less than 80 GeV;
- $m_{\tau\tau}$ is required to be larger than $(m_Z - 25)$ GeV.

For these selection requirements, the $Z/\gamma^* \to \tau\tau$ yield comprises 73% of the total prediction, and the contribution of $Z/\gamma^* \to ee/\mu\mu$ events is 3% of the total Z/γ^* yield. The m_{T} distribution of the ggF $N_{\text{jet}} = 1$ Z/γ^* CR is shown in Figure 4.26b.

ggF-enriched $N_{\text{jet}} \geq 2$

Similarly to the ggF $N_{\text{jet}} = 1$ Z/γ^* CR, exclusivity of the selected events with the ggF-enriched $N_{\text{jet}} \geq 2$ SR is achieved using an inversion of $m_{\tau\tau}$. The following modifications to the signal selection requirements are made:

- $m_{\tau\tau}$ is required to be larger than $(m_Z - 25)$ GeV;
- The requirement on $\Delta\phi_{\ell\ell}$ is removed.

The resulting purity of $Z/\gamma^* \to \tau\tau$ events is 76%. The contamination of $Z/\gamma^* \to ee/\mu\mu$ events to the total Z/γ^* yield is 0.8%. The m_{T} distribution of the ggF-enriched $N_{\text{jet}} \geq 2$ Z/γ^* CR is shown in Figure 4.26c.

VBF-enriched $N_{\text{jet}} \geq 2$

In the VBF-enriched $N_{\text{jet}} \geq 2$ category, a Z/γ^* CR is defined with the following modifications to the SR selection requirements:

- Events are selected within a mass window around the Z boson pole i.e $|m_{\tau\tau} - m_Z| < 25$ GeV to ensure the selected events are mutually exclusive with those selected for the SR;
- An additional selection requiring $m_{\ell\ell}$ to be less than 70 GeV is included to increase the $Z/\gamma^* \to \tau\tau$ purity.

The $Z/\gamma^* \to \tau\tau$ purity is 77%. The contamination of $Z/\gamma^* \to ee/\mu\mu$ events to the total Z/γ^* yield is 1.5%. The DNN output distribution of the VBF-enriched $N_{\text{jet}} \geq 2$ Z/γ^* CR is shown in Figure 4.26d.

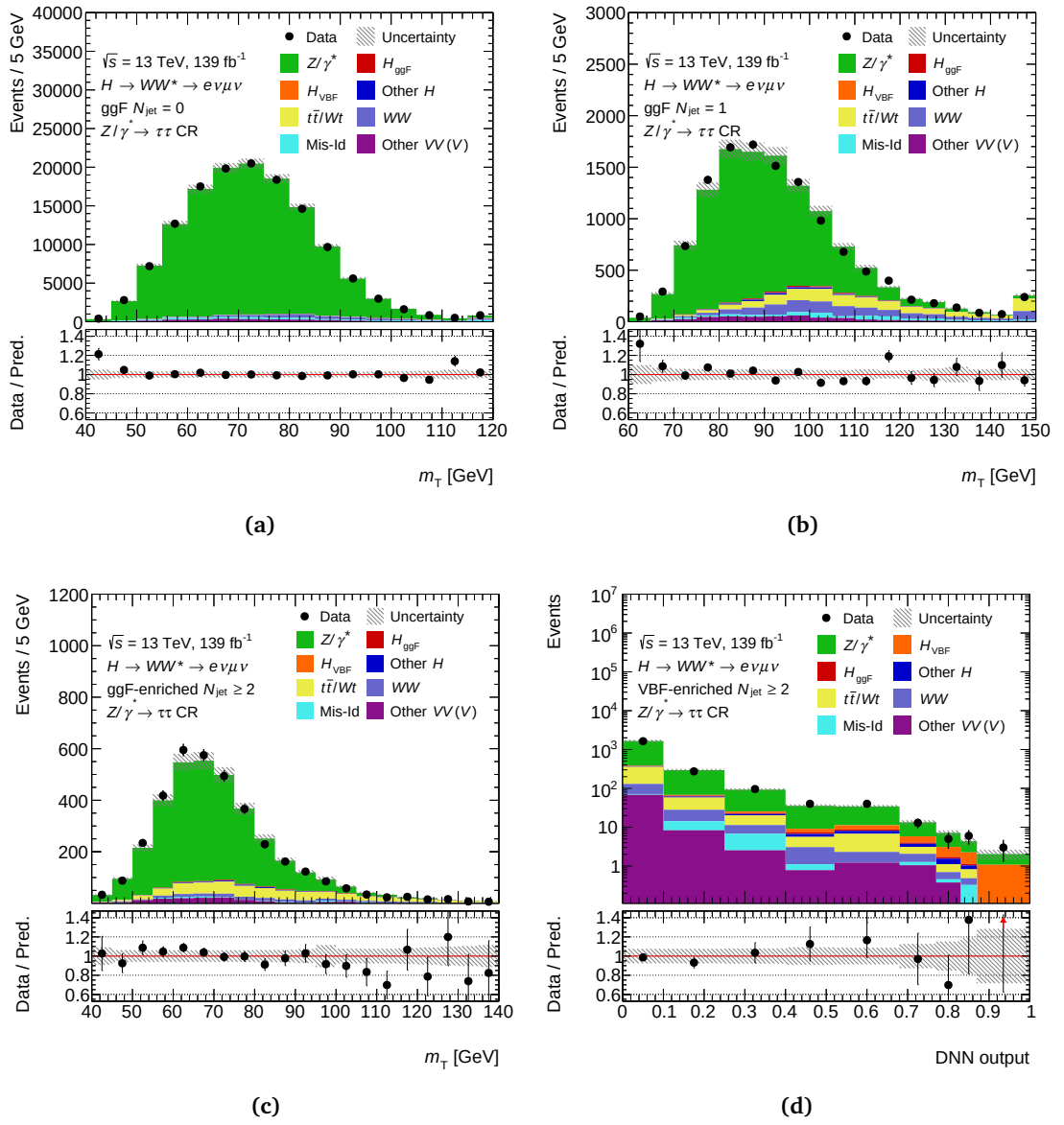

Figure 4.26: Distributions of m_{T} following all selection requirements in the (a) ggF $N_{\mathrm{jet}} = 0$, (b) ggF $N_{\mathrm{jet}} = 1$, and (c) ggF-enriched $N_{\mathrm{jet}} \geq 2$ Z/γ^* CRs. The DNN output distribution is shown in (d) for the VBF-enriched $N_{\mathrm{jet}} \geq 2$ Z/γ^* CR. The sub-panel shows a comparison of the modelling of the data and the MC predictions. The uncertainty band represents the total normalisation uncertainty prior to performing the statistical analysis described in Chapter 6. The background processes are normalised according to the values in Table 4.6. The final bin includes events beyond the range of the plotted distribution.

4.6.4 W+jets and QCD multi-jet background

The rate that a jet is mis-identified as a lepton is difficult to accurately model with simulation. This is because the rate depends on effects such as the flavour composition of jets, the evolution of a jet, as well as more extreme instances of the detector response. Additionally, infeasibly large MC samples would be needed to sufficiently model the fake lepton background in the analysis regions due to the low fraction of W+jets and QCD multi-jet events passing the event selection and object identification requirements. Instead, the estimation of the fake lepton background uses a data-driven approach called the *fake factor* method. The yield of events with fake leptons is estimated in the analysis regions by extrapolating from a CR which is enriched in fake lepton events. Such a region is formed by using lepton selection requirements that are less stringent than those nominally used in this analysis, but with otherwise identical selection requirements. The physics objects defined by the less stringent lepton selections are called *anti-identified* leptons (anti-ID; $\not{\ell}$). This is opposed to the physics objects defined by the nominal lepton selections (ID leptons; ℓ). The anti-ID selection is defined with a looser requirement on the lepton identification WP and removes any requirement on the lepton isolation WP. Exclusivity between the ℓ and $\not{\ell}$ objects is ensured by including a veto on ℓ objects in the $\not{\ell}$ definition.

The event yield in the fake lepton CR is scaled by the fake factor, f, which is defined as the ratio of the number of ID leptons to anti-ID leptons,

$$f = \frac{N^{\ell\ell}}{N^{\ell\not{\ell}}}. \tag{4.14}$$

The yield of events with at least one fake lepton in a region requiring two ID leptons ($\ell\ell$) is given by

$$N^{\ell\ell}_{>0\text{ fakes}} = f_2(N^{\ell\not{\ell}} - N^{\ell\not{\ell}}_{0\text{ fakes}}) + f_1(N^{\not{\ell}\ell} - N^{\not{\ell}\ell}_{0\text{ fakes}}) - f_1 f_2(N^{\not{\ell}\not{\ell}} - N^{\not{\ell}\not{\ell}}_{0\text{ fakes}}). \tag{4.15}$$

In this equation, N represents a yield of events after some set of selection requirements, with superscripts indicating the type of lepton selection criteria satisfied by each lepton. Variables without a subscript denote the yields in data, whilst the subscript *0 fakes* represents the yields of processes with two prompt leptons estimated with MC simulation. The fake factors are given by f_1 and f_2 for the leading and sub-leading lepton. The first two terms in Equation 4.15 estimate the yield of events with one fake lepton, whilst the third term estimates the yield of events with two fake leptons. This term corrects for double-counting in the first two terms for cases where the ID lepton could be a mis-identified lepton. The fake factors are derived as functions of lepton p_{T} for both electrons and muons, and the pseudorapidity, η, for muons, using a Z/γ^*+jets sample of events requiring three leptons. Corrections to the fake factors are derived to account for potential differences in the characteristics of the fake lepton candidate between two and

three lepton events, as well as the flavour composition of jets in Z/γ^*+jets and W+jets events. These corrections are derived using MC simulated samples and uncertainties on the fake factor are estimated by comparing differences in the estimate of the fake lepton yield between several different MC simulated samples.

4.7 Simplified template cross sections

The STXS framework is introduced in Section 2.4.4 as a method to measure quasi-fiducial differential cross sections as an evolution of measurements of the signal strength. A large and abstracted fiducial volume is defined and the fiducial cross section of Higgs boson production is divided by production process into several kinematic fiducial regions, called the STXS bins. The definition of the STXS bins relies on particle-level observables that are similar to the observables used in selection requirements at detector-level in order to maximise the experimental sensitivity to the Higgs boson production processes.

4.7.1 STXS stage 1.2

STXS bins are defined in stages, where a stage corresponds to a set of partitions of the Higgs boson production cross sections used to define mutually exclusive kinematic fiducial regions. The degree to which the production cross sections are partitioned is generally led by the current precision of the measurements with the data set available. The STXS measurements in this thesis use the so-called stage 1.2 definition [58].

Fiducial volume

The fiducial volume in which STXS stage 1.2 measurements are performed is defined at particle-level as follows:

Higgs boson

The Higgs boson is on-shell and its four-momentum is constructed from the sum of all of its decay particles. It is required to have a rapidity of $|y_{\mathrm{H}}| < 2.5$. The rapidity requirement is applied to minimise the extrapolation into unmeasured regions for measurements of the $H \to ZZ^*$ and $H \to \gamma\gamma$ decay modes, which make use of the precision charged-particle tracking capabilities of the ATLAS detector in the range $|\eta| < 2.5$. All STXS bins are defined with this rapidity requirement imposed.

Leptons

No requirements are applied to the p_{T} or rapidity of leptons. Final state leptons are said to be *dressed* since photons radiated by bremsstrahlung are added to the four-momenta of the lepton if they are within $\Delta R = 0.1$ of the lepton.

Jets

Jets are defined using the anti-k_t algorithm with a radius parameter of $R = 0.4$. All

final state particles with a lifetime greater than 10 ps produced in the hadronisation and showering of jets, including neutrinos, photons, and leptons from hadron decays, are included in the construction of jets. Particles associated with the decay of the Higgs boson are removed before jets are constructed. No requirements are applied to the rapidity of jets, although they must have $p_{\mathrm{T}} > 30$ GeV to reduce theoretical uncertainty on the partitioning by N_{jet} and to match a typical experimental threshold that suppresses pile-up contamination (e.g. the p_{T} threshold used in this analysis to count the number of jets in an event).

ggH STXS stage 1.2

The particle-level STXS bins corresponding to Higgs boson production through ggF production (termed ggH) are defined considering the production of the Higgs boson through an effective ggH coupling (Figure 2.7a). The stage 1.2 partition of the ggH cross section into mutually exclusive kinematic fiducial regions is illustrated in Figure 4.27 and defined by the following:

1. The ggH cross section is split into two bins delimited by $p_{\mathrm{T}}^{H} = 200$ GeV.
   - The $p_{\mathrm{T}}^{H} > 200$ GeV bin is designed to be sensitive to new physics and primarily consists of events with multiple jets. It is further subdivided into bins with boundaries at 300 GeV, 450 GeV, and 650 GeV.
   - The majority of the ggH cross section is contained within the $p_{\mathrm{T}}^{H} < 200$ GeV bin and the remainder of the ggH binning is defined within this bin.
2. The ggH cross section with $p_{\mathrm{T}}^{H} < 200$ GeV is then split into three bins according to the jet multiplicity: $N_{\text{jet}} = 0$, $N_{\text{jet}} = 1$, and $N_{\text{jet}} \geq 2$.
   - The $N_{\text{jet}} = 0$ bin is split into two bins delimited by $p_{\mathrm{T}}^{H} = 10$ GeV.
   - The $N_{\text{jet}} = 1$ bin is split into three bins delimited by $p_{\mathrm{T}}^{H} = 60$ GeV and $p_{\mathrm{T}}^{H} = 120$ GeV.
   - The $N_{\text{jet}} \geq 2$ bin is split into two bins delimited by $m_{jj} = 350$ GeV.
     - The majority of the ggH $N_{\text{jet}} \geq 2$ cross section populates the $m_{jj} < 350$ GeV bin. This bin is split into three bins, similarly to the $N_{\text{jet}} = 1$ binning, with boundaries at $p_{\mathrm{T}}^{H} = 60$ GeV and $p_{\mathrm{T}}^{H} = 120$ GeV.
     - The ggH cross section in the $m_{jj} > 350$ GeV bin is partitioned further with boundaries defined by $m_{jj} = 700$ GeV, $m_{jj} = 1000$ GeV, and $m_{jj} = 1500$ GeV, such that the partitioning is identical to the binning of the high-m_{jj} qqH bin described below. Two possible further bins of the ggH high-m_{jj} cross section are defined by $p_{\mathrm{T}}^{Hjj} = 25$ GeV.

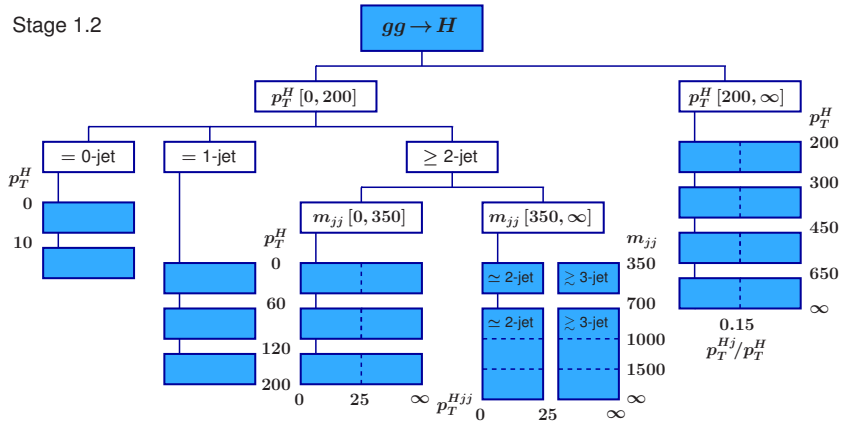

Figure 4.27: The partitioning of the ggH cross section defining STXS stage 1.2 [58]. The dashed lines indicate potential partitions of a bin in a future STXS stage.

Electroweak qqH STXS stage 1.2

The particle-level STXS bins targeting Higgs boson production through VBF are termed *electroweak qqH* production[29]. The same final state also arises from VH production with $V \to q\bar{q}$. These two production modes therefore represent the s-channel and t-channel contributions of the same process. Distinguishing the two is only possible with selection requirements on kinematic distributions to define regions enriched in one production mode. The stage 1.2 partition of the qqH cross section is illustrated in Figure 4.28 and defined by the following:

1. The qqH cross section is split into three bins according to the jet multiplicity: $N_{\text{jet}} = 0$, $N_{\text{jet}} = 1$, and $N_{\text{jet}} \geq 2$.
   - The $N_{\text{jet}} = 0$ and $N_{\text{jet}} = 1$ bins contain a very small amount of the qqH cross section and is difficult to distinguish from the ggH background.
   - The $N_{\text{jet}} \geq 2$ bin is split into two bins delimited by $m_{jj} = 350$ GeV.
     - The $m_{jj} < 350$ GeV bin is split into three bins with boundaries at $m_{jj} = 60$ GeV and $m_{jj} = 120$ GeV. The bin defined with $60 < m_{jj} < 120$ GeV targets the s-channel $V(\to q\bar{q})H$ production.
     - The majority of the qqH cross section populates the $m_{jj} > 350$ GeV bin.
   - The $m_{jj} > 350$ GeV is split into two bins delimited by $p_{\text{T}}^H = 200$ GeV, designed to mimic the p_{T}^H binning for the ggH bins.
     - The $m_{jj} > 350$ GeV bin contains most of the qqH cross section. There are further bins subdivided in m_{jj} with boundaries at $m_{jj} = 700$ GeV, $m_{jj} = 1000$ GeV, and $m_{jj} = 1500$ GeV. There is also a possible binning in p_{T}^{Hjj} with a boundary at $p_{\text{T}}^{Hjj} = 25$ GeV.

[29] The term *electroweak qqH* is also referred to as EW qqH or qqH.

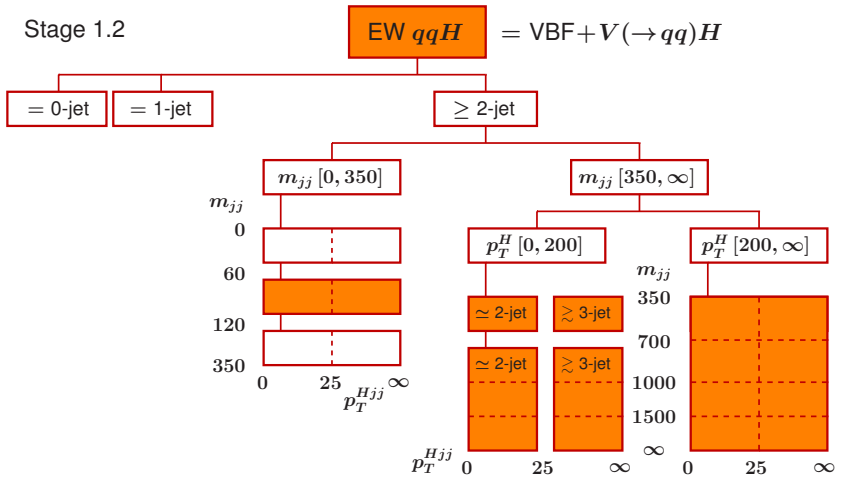

Figure 4.28: The partitioning of the qqH cross section defining STXS stage 1.2 [58]. The dashed lines indicate potential partitions of a bin in a future STXS stage.

4.7.2 Reduced STXS stage 1.2

In practice, no current measurement targeting a specific Higgs boson production and decay mode will have sufficient sensitivity to define many kinematic regions using reconstructed particle objects which are able to measure all bins of stage 1.2. Fortunately by construction, an analysis may merge bins and instead measure their sum, which can be freely decided within the analysis after considering the size of the available data set for each reconstructed SR targeting a specific STXS bin. In this analysis, several STXS bins are merged to form *reduced STXS stage 1.2*. STXS bins are successively merged until the expected precision of the measurement of the merged STXS bins is $\mathcal{O}(100\%)$. The reduced STXS stage 1.2 bins that are measured in this analysis are listed in Table 4.8, which describes the bins of the maximal STXS stage 1.2 bins that are merged (or not). Several bins of stage 1.2 are not included as part of a group of merged bins due to very little sensitivity or to reduce the correlation with several other bins. These are the qqH bins with $N_{\text{jet}} = 0$ and $N_{\text{jet}} = 1$, as well as the bins with $N_{\text{jet}} \geq 2$ and $m_{jj} < 350$ GeV. In these cases, the STXS bins assume the SM prediction as predicted by MC simulation.

4.7.3 STXS event selection

In order to measure the reduced STXS stage 1.2 bins defined in Table 4.8, several STXS SRs are defined using reconstructed objects. The selection requirements for the STXS SRs are required to match the particle-level definition of the reduced STXS stage 1.2 bins, such that an SR will be enriched in yields of (mostly) one STXS bin. The selection requirements are built on top of the selection requirements defining the four SRs previously defined. The names and definitions of the STXS SRs are given in Table 4.9, demonstrating which reduced STXS stage 1.2 bin is targeted by each SR. Distributions of reconstructed p_{T}^H in the ggF SRs are shown in Figure 4.29, whilst distributions of reconstructed p_{T}^H and m_{jj} in

Table 4.8: A list of reduced STXS stage 1.2 bins measured in this analysis and the corresponding STXS bins of the maximal stage 1.2 which are merged.

Reduced STXS stage 1.2 bin	**Corresponding STXS stage 1.2 bin(s)**
ggH-0j, low p_{T}^{H}	Merged ggH bins with $N_{\text{jet}} = 0$ and $p_{\mathrm{T}}^{H} < 10$ GeV or $p_{\mathrm{T}}^{H} > 10$ GeV
ggH-1j, very low p_{T}^{H}	ggH bin with $N_{\text{jet}} = 1$ and $p_{\mathrm{T}}^{H} < 60$ GeV
ggH-1j, low p_{T}^{H}	ggH bin with $N_{\text{jet}} = 1$ and $60 \leq p_{\mathrm{T}}^{H} < 120$ GeV
ggH-1j, med p_{T}^{H}	ggH bin with $N_{\text{jet}} = 1$ and $120 \leq p_{\mathrm{T}}^{H} < 200$ GeV
ggH, high p_{T}^{H}	Four merged ggH bins with $p_{\mathrm{T}}^{H} > 200$ GeV
ggH-2j, low p_{T}^{H}	Merged all ggH bins with $N_{\text{jet}} \geq 2$ and $p_{\mathrm{T}}^{H} < 200$ GeV
EW qqH-2j, low m_{jj}-low p_{T}^{H}	qqH bin with $N_{\text{jet}} \geq 2$, $350 \leq m_{jj} < 700$ GeV, and $p_{\mathrm{T}}^{H} < 200$ GeV
EW qqH-2j, med m_{jj}-low p_{T}^{H}	qqH bin with $N_{\text{jet}} \geq 2$, $700 \leq m_{jj} < 1000$ GeV, and $p_{\mathrm{T}}^{H} < 200$ GeV
EW qqH-2j, high m_{jj}-low p_{T}^{H}	qqH bin with $N_{\text{jet}} \geq 2$, $1000 \leq m_{jj} < 1500$ GeV, and $p_{\mathrm{T}}^{H} < 200$ GeV
EW qqH-2j, very high m_{jj}-low p_{T}^{H}	qqH bin with $N_{\text{jet}} \geq 2$, $m_{jj} > 1500$ GeV, and $p_{\mathrm{T}}^{H} < 200$ GeV
EW qqH-2j, high p_{T}^{H}	qqH bin with $N_{\text{jet}} \geq 2$, $m_{jj} > 350$ GeV, and $p_{\mathrm{T}}^{H} > 200$ GeV

the VBF-enriched $N_{\text{jet}} \geq 2$ SR are shown at in Figure 4.30.

The ggF $0j$, low p_{T}^{H} SR is defined with the same ggF $N_{\text{jet}} = 0$ selection requirements, but with $p_{\mathrm{T}}^{H} < 200$ GeV. This is because there are zero predicted events of the ggH-0j, low p_{T}^{H} bin with $p_{\mathrm{T}}^{H} > 200$ GeV, which means the ggF $0j$, low p_{T}^{H} SR is identical to the ggF $N_{\text{jet}} = 0$ SR defined in Section 4.5.2. Furthermore, this means that the ggH, high p_{T}^{H} bin comprises exclusively $N_{\text{jet}} = 1$ and $N_{\text{jet}} \geq 2$ events. As can be seen in Table 4.9, two SRs are defined to target the ggH, high p_{T}^{H} bin, split by N_{jet}.

For the VBF STXS SRs, no improvement in sensitivity is observed by using separate DNNs to separate the reduced STXS stage 1.2 bins in each reconstructed SR so the same DNN described in Section 4.5.5 is used for each VBF STXS SR.

The expected composition of each reconstructed STXS SR as a function of the reduced STXS stage 1.2 bins is shown in Figure 4.31, where the yields of each reduced STXS stage 1.2 bin are normalised to the total signal yield in each reconstructed STXS SR. Each reconstructed STXS SR is generally pure in the corresponding reduced STXS stage 1.2 bins. There is a relatively large migration of ggH-0j, low p_{T}^{H} events into the ggF $1j$, very low p_{T}^{H} SR, which is due to the jet energy resolution and pile-up, where a jet with $p_{\mathrm{T}} < 30$ GeV at particle-level could get reconstructed with $p_{\mathrm{T}} > 30$ GeV.

For the purpose of performing the STXS measurement, some of the STXS SRs undergo a further categorisation into sub-SRs, similarly to the further categorisation used for the inclusive regions. The categorisation of the event yields defined by $m_{\ell\ell} = 30$ GeV and

Table 4.9: A list of the STXS SRs and their selection requirements that are used to measure the reduced STXS stage 1.2 bins in Table 4.8.

STXS signal region	Selection requirements
ggF $0j$, low p_{T}^{H}	ggF $N_{\mathrm{jet}} = 0$ selection plus $p_{\mathrm{T}}^{H} < 200$ GeV
ggF $1j$, very low p_{T}^{H}	ggF $N_{\mathrm{jet}} = 1$ selection plus $p_{\mathrm{T}}^{H} < 60$ GeV
ggF $1j$, low p_{T}^{H}	ggF $N_{\mathrm{jet}} = 1$ selection plus $60 \leq p_{\mathrm{T}}^{H} < 120$ GeV
ggF $1j$, med p_{T}^{H}	ggF $N_{\mathrm{jet}} = 1$ selection plus $120 \leq p_{\mathrm{T}}^{H} < 200$ GeV
ggF $1j$, high p_{T}^{H}	ggF $N_{\mathrm{jet}} = 1$ selection plus $p_{\mathrm{T}}^{H} > 200$ GeV
ggF $2j$, low p_{T}^{H}	ggF-enriched $N_{\mathrm{jet}} \geq 2$ selection plus $p_{\mathrm{T}}^{H} < 200$ GeV
ggF $2j$, high p_{T}^{H}	ggF-enriched $N_{\mathrm{jet}} \geq 2$ selection plus $p_{\mathrm{T}}^{H} > 200$ GeV
VBF $2j$, very low m_{jj}	VBF-enriched $N_{\mathrm{jet}} \geq 2$ selection plus $p_{\mathrm{T}}^{H} < 200$ GeV and $350 \leq m_{jj} < 700$ GeV
VBF $2j$, low m_{jj}	VBF-enriched $N_{\mathrm{jet}} \geq 2$ selection plus $p_{\mathrm{T}}^{H} < 200$ GeV and $700 \leq m_{jj} < 1000$ GeV
VBF $2j$, med m_{jj}	VBF-enriched $N_{\mathrm{jet}} \geq 2$ selection plus $p_{\mathrm{T}}^{H} < 200$ GeV and $1000 \leq m_{jj} < 1500$ GeV
VBF $2j$, high m_{jj}	VBF-enriched $N_{\mathrm{jet}} \geq 2$ selection plus $p_{\mathrm{T}}^{H} < 200$ GeV and $m_{jj} > 1500$ GeV
VBF $2j$, high p_{T}^{H}	VBF-enriched $N_{\mathrm{jet}} \geq 2$ selection plus $p_{\mathrm{T}}^{H} > 200$ GeV and $m_{jj} > 350$ GeV

$p_{\mathrm{T}}^{\mathrm{sublead}} = 20$ GeV is retained for the ggF $0j$, low p_{T}^{H} SR. The event yield in the ggF $2j$, low p_{T}^{H} and ggF $2j$, high p_{T}^{H} SR are also split at $m_{\ell\ell} = 30$ GeV. The categorisation by $m_{\ell\ell} = 30$ GeV and $p_{\mathrm{T}}^{\mathrm{sublead}} = 20$ GeV is removed for the $N_{\mathrm{jet}} = 1$ STXS SRs because of the sample sizes of the SRs. No further categorisation of the VBF STXS SRs is performed. Figure 4.32 shows the correspondence between the particle-level reduced STXS stage 1.2 bins and the reconstruction-level sub-SRs that enter the statistical analysis (Chapter 6) of the STXS measurement.

4.7.4 STXS background estimation

The estimation of background processes for the STXS measurement follows the same principle as the SR selection. The CRs for the $qqWW$, top quark, and Z/γ^* background processes of each analysis category are used as a starting point for the STXS CRs. Further selection requirements on p_{T}^{H} or m_{jj} are included for the STXS CRs such that the background rate in an STXS SR is normalised with a corresponding NF from a dedicated CR with the same selection requirement on p_{T}^{H} or m_{jj}. For the VBF STXS SRs targeting the qqH STXS bins, it is difficult to maintain a large sample size of background events in the highest m_{jj} bins. Therefore, only three STXS CRs are defined, for both the top quark and Z/γ^* background, to normalise the rate of these backgrounds in the five VBF STXS SRs. The CRs are instead defined by: $350 \leq m_{jj} < 700$ GeV and $p_{\mathrm{T}}^{H} < 200$ GeV, $m_{jj} > 700$ GeV and $p_{\mathrm{T}}^{H} < 200$ GeV, and $m_{jj} > 350$ GeV and $p_{\mathrm{T}}^{H} > 200$ GeV. The values of the NFs for each STXS CR, estimated using the CR data and matrix inversion, are shown in Table 4.10.

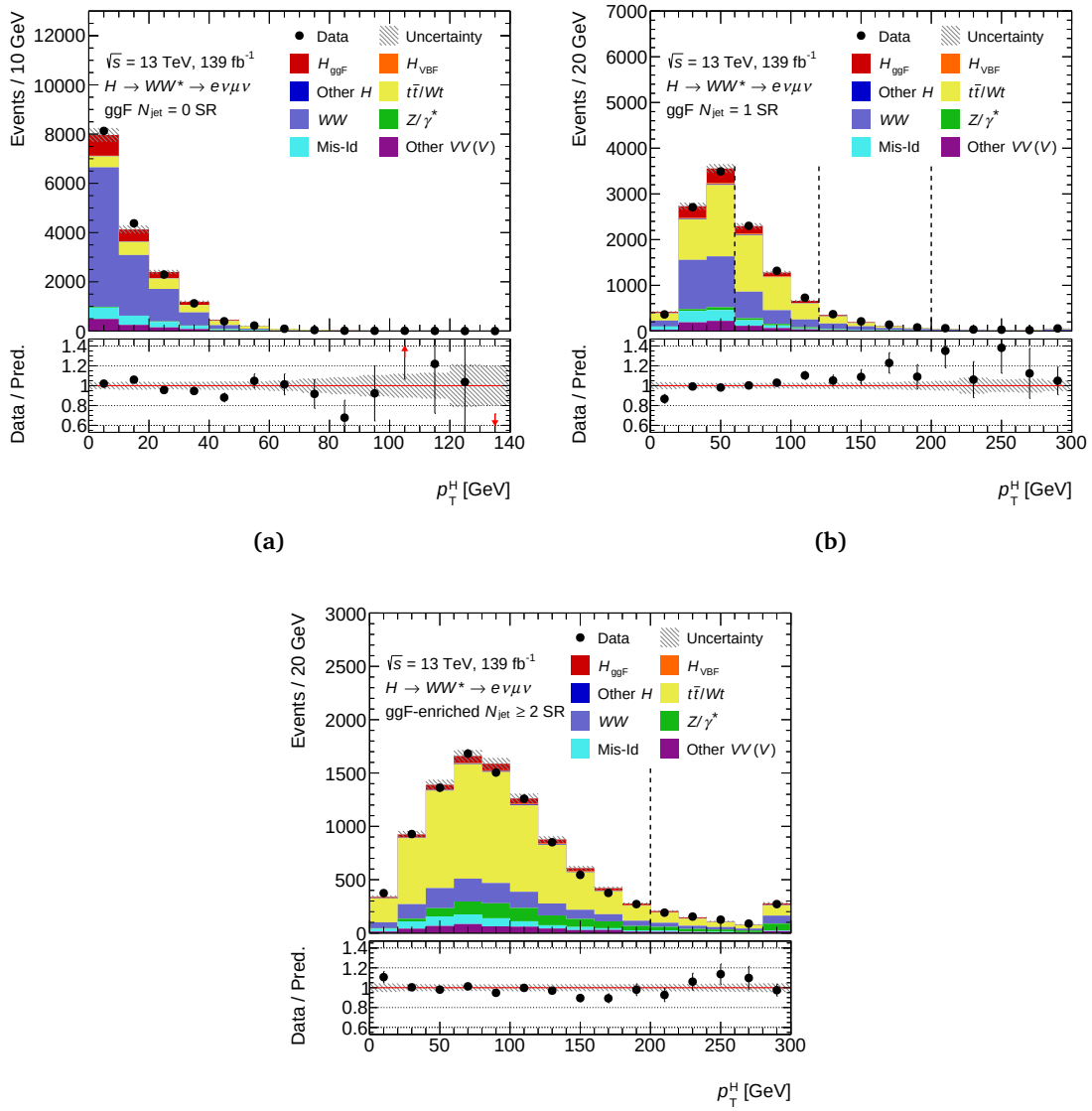

Figure 4.29: Distributions of reconstructed p_{T}^{H} in the (a) ggF $N_{\text{jet}} = 0$, (b) ggF $N_{\text{jet}} = 1$, and (c) ggF-enriched $N_{\text{jet}} \geq 2$ SRs. The black lines indicate the delineation of the SRs into the STXS SRs, corresponding to the definition of the particle-level STXS bins. The uncertainty band represents the total normalisation uncertainty prior to performing the statistical analysis described in Chapter 6. The background processes are normalised according to the values in Table 4.6. The final bin includes events beyond the range of the plotted distribution.

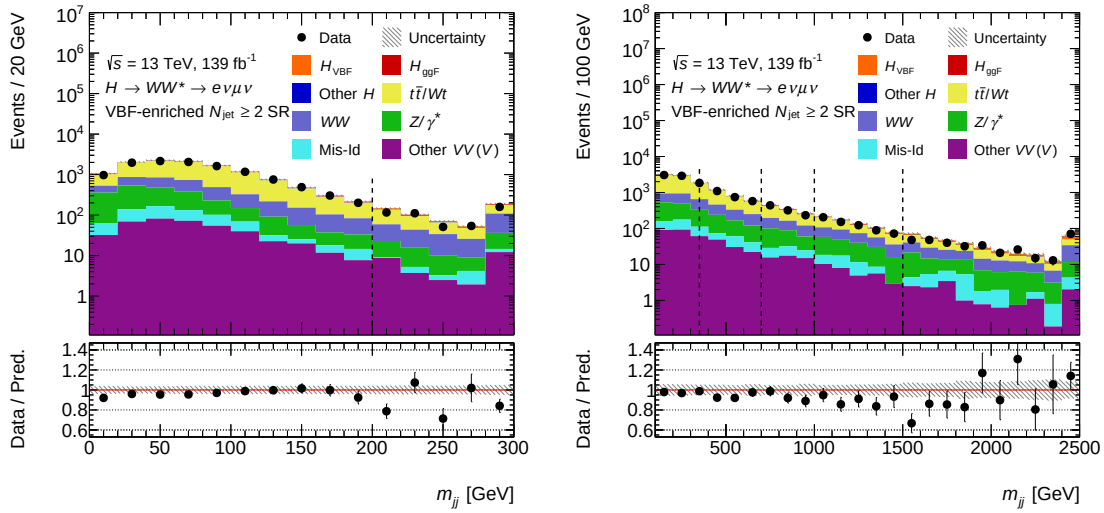

(a) **(b)**

Figure 4.30: Distributions of reconstructed (a) p_{T}^{H} and (b) m_{jj} in the VBF-enriched $N_{\mathrm{jet}} \geq 2$ SR. The black lines indicate the delineation of the SRs into the STXS SRs and correspond to the definition of the STXS bins. The uncertainty band represents the total normalisation uncertainty prior to performing the statistical analysis described in Chapter 6. The background processes are normalised according to the values in Table 4.6. The final bin includes events beyond the range of the plotted distribution.

Table 4.10: NFs for backgrounds obtained using STXS CR data and with matrix inversion. The uncertainties originate from the sample size of the CRs.

Region	$qqWW$	$t\bar{t}/Wt$	Z/γ^*
ggF $0j$, low p_{T}^{H}	1.09 ± 0.01	1.02 ± 0.01	0.95 ± 0.01
ggF $1j$, very low p_{T}^{H}	0.83 ± 0.02	1.04 ± 0.01	0.86 ± 0.02
ggF $1j$, low p_{T}^{H}	0.90 ± 0.04	1.02 ± 0.01	0.90 ± 0.03
ggF $1j$, med p_{T}^{H}	1.01 ± 0.06	0.99 ± 0.01	1.00 ± 0.07
ggF $1j$, high p_{T}^{H}	1.07 ± 0.07	0.91 ± 0.05	0.99 ± 0.16
ggF $2j$, low p_{T}^{H}	0.74 ± 0.10	1.06 ± 0.03	0.90 ± 0.02
ggF $2j$, high p_{T}^{H}	0.75 ± 0.22	0.99 ± 0.17	0.92 ± 0.05
VBF $2j$, $350 \leq m_{jj} < 700$ GeV and $p_{\mathrm{T}}^{H} < 200$ GeV	–	1.02 ± 0.01	1.01 ± 0.06
VBF $2j$, $m_{jj} > 700$ GeV and $p_{\mathrm{T}}^{H} < 200$ GeV	–	1.01 ± 0.03	0.90 ± 0.10
VBF $2j$, $m_{jj} > 350$ GeV and $p_{\mathrm{T}}^{H} > 200$ GeV	–	0.94 ± 0.04	1.04 ± 0.12

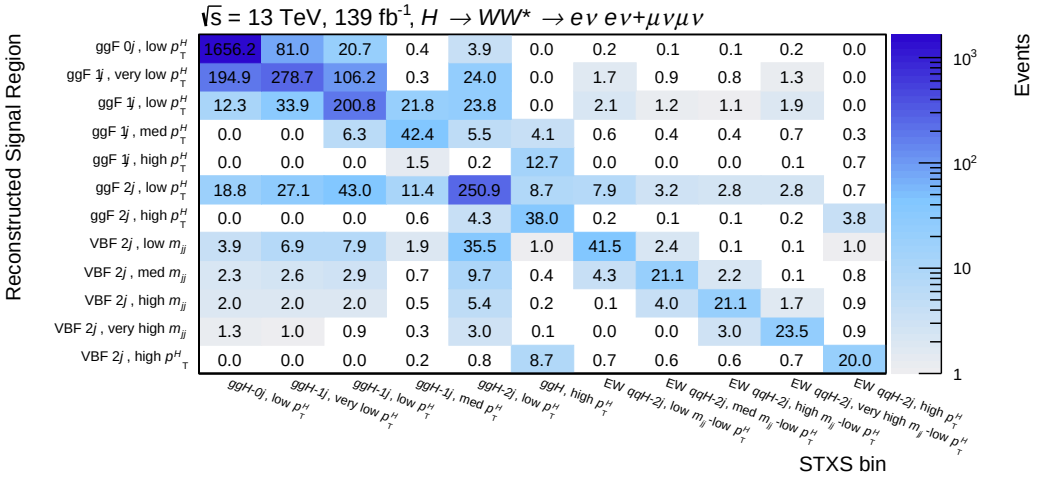

(a)

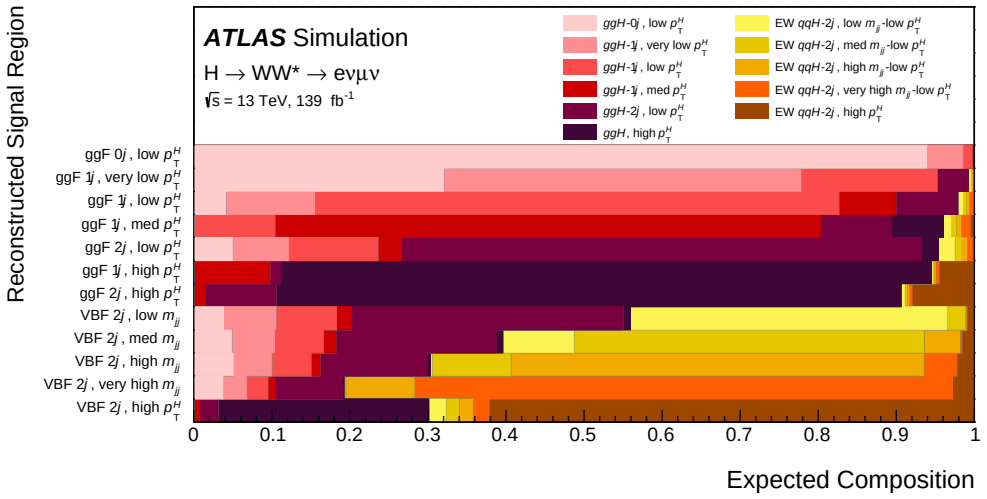

(b)

Figure 4.31: The expected signal yields (a) and relative signal composition (b) as a function of reduced STXS stage 1.2 bins for each reconstructed STXS SR.

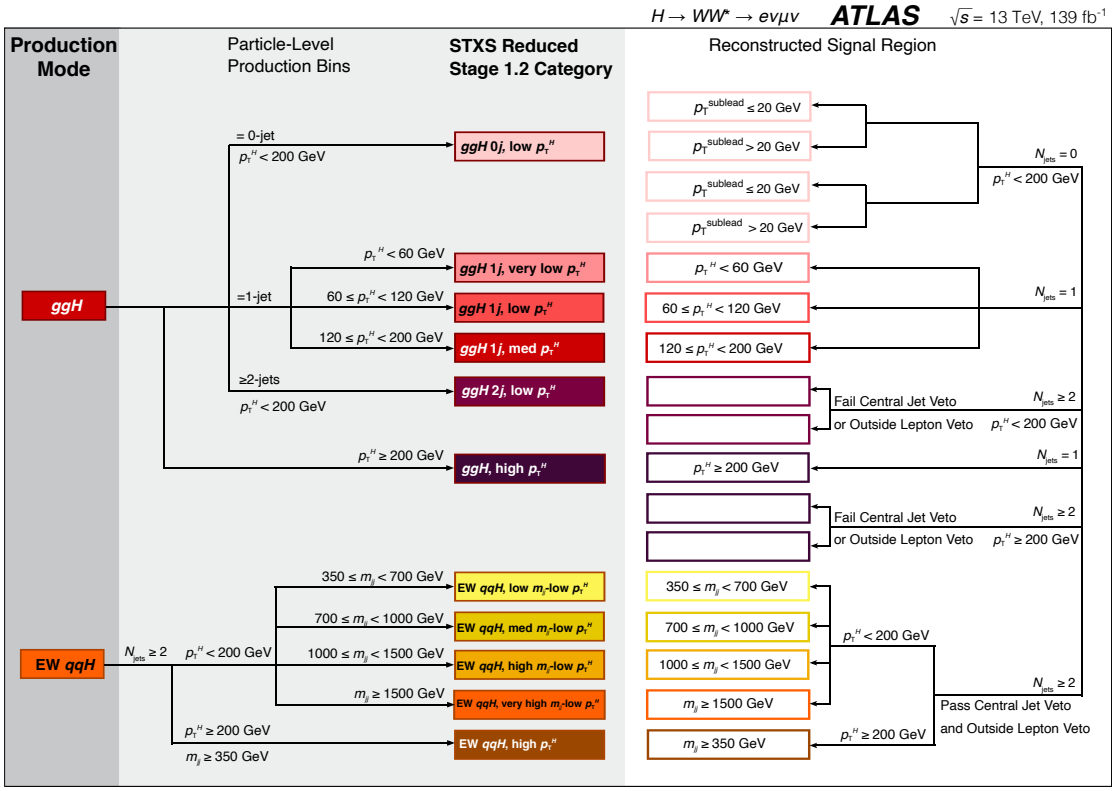

Figure 4.32: The correspondence of the particle-level reduced STXS stage 1.2 bins (left) with the reconstruction-level (sub-)SRs which are used in the statistical analysis for the STXS measurement (right). The colour of each SR on the right indicates the reduced STXS stage 1.2 bin targeted by the SR.

5
Systematic uncertainties

The reconstruction and calibration of the objects used in this analysis is a complex chain of algorithms and techniques. It is impossible to reconstruct the original energy and momenta of all particles in an event with absolute precision, nor is the data set used for the measurements infinitely large. There is therefore uncertainty in the measurements which originates from a number of sources. These uncertainties can be classed into two categories: a statistical component and a systematic component. The former class of uncertainties arises from natural fluctuation in the observed data set and expected event yields due to finite MC sample sizes. The latter class of uncertainties originates from the reconstruction and calibration of objects in the detector (*experimental uncertainties*) as well as from the modelling of signal and background processes in the simulation (*theoretical uncertainties*). Systematic uncertainties are estimated in all analysis regions and for most signal and background processes, for both the normalisation of processes and the shape of the m_{T} and DNN output distributions. This chapter describes the systematic uncertainties that affect this analysis, where experimental and theoretical uncertainties are outlined in Sections 5.1 and 5.2, respectively.

5.1 Experimental uncertainties

Experimental uncertainties are defined as the uncertainties relating to the inability to perfectly model the detector response, as well as to reconstruct and calibrate objects with absolute precision. The uncertainties are derived by several dedicated performance groups, independent of this particular analysis, and cover many sources. Typically, the dedicated performance groups provide a set of uncertainties which are smaller in number than the number of uncertainties in the original calibration measurement. Usually, this is done with an eigenvalue decomposition. This process ensures that the complexity of the statistical analysis performed in Chapter 6 is reduced.

The uncertainties provided by the performance groups are propagated through each MC-simulated sample. These variations can change the four-momentum of an object, leading

to migrations of events between regions and bins, or they can change an efficiency scale factor of an event or object. In both cases, these uncertainties will lead to changes in the expected acceptance of events or in the extrapolation of a background estimate from a CR. The difference between the nominal yield and the varied yield induced by a single source of experimental uncertainty, or difference between nominal and varied distributions, is taken to be the $\pm 1\sigma$ variation of that uncertainty source. A complete list of the experimental uncertainties, as well as a description of their source, is shown in Table 5.1.

Leptons

Systematic uncertainties for electrons and muons are derived separately given the differences in their reconstruction. Uncertainties are derived for the reconstruction, identification, isolation, and trigger efficiencies. Uncertainties are also derived on the energy scale and resolution. An additional uncertainty is derived for muons on the impact parameter cuts used in the track-to-vertex association (TTVA). Electron and muon uncertainties are derived as a function of p_{T} and η using a *tag and probe* method with $Z \to \ell\ell$ events [91, 92, 113, 114].

Jets

The calibration of the jet energy scale (JES) and jet energy resolution (JER) introduces systematic uncertainties on jets, which are typically measured as a function of p_{T} and η. Several sources of uncertainty are derived for each step of the JES calibration, including pile-up removal, the in-situ calibration, the η-intercalibration, flavour composition, and punch-through jets. The JER uncertainties arise from the different in-situ methods used to derive the JER, which include Z/γ^*+jets, γ+jets, and dijet measurements. Uncertainties arising from the comparison of data and modelling of the simulation are derived for both JES and JER. An additional scale factor uncertainty is derived to account for the modelling of the JVT efficiency [94, 98].

Heavy-flavour tagging

Systematic uncertainties on the identification and tagging of the jet flavour are included on the data-to-MC scale factors. The uncertainties are derived separately for b-, c-, and light-flavour jets. The uncertainties on the identification of b-jets are more significant than those for c- and light-jets, and are derived as a function of jet p_{T} using dileptonic $t\bar{t}$ events. Additional uncertainties are included to model the extension of b-tagging to high p_{T}, as well as the extension of b-tagging to τ-lepton jets [103].

Missing transverse momentum

Systematic uncertainties relating to the reconstruction of $E_{\mathrm{T}}^{\mathrm{miss}}$ and $p_{\mathrm{T}}^{\mathrm{miss}}$ arise from both the hard objects and the soft term. The inputs to the calculation of $E_{\mathrm{T}}^{\mathrm{miss}}$ and $p_{\mathrm{T}}^{\mathrm{miss}}$ are the calibrated electron, muon, and jet objects, and thus their systematic uncertainties are

considered in the $E_{\mathrm{T}}^{\mathrm{miss}}$ and $p_{\mathrm{T}}^{\mathrm{miss}}$ calculation. Systematic uncertainties on the soft term are derived using $Z \to \mu\mu$ events and with the variable $\vec{p}_{\mathrm{T}}^{\,\mathrm{hard}}$, which is the vector p_{T} sum of the hard objects. Uncertainties affecting the scale and resolution of the soft term are related to the longitudinal and transverse components of this quantity [108, 109].

Luminosity

The uncertainty on the total integrated luminosity is estimated to be 1.7% for the full Run 2 data set of 139 fb^{-1}, collected during the years 2015–2018 [191]. This uncertainty is derived using a dedicated detector, LUCID-2, for the luminosity measurement [192].

Pileup

Simulated samples are generally produced with a pile-up profile that does not necessarily reflect the pile-up profile in the observed data set (since the pile-up profile in the observed data set is not known until after the data set is collected). The simulated samples are re-weighted to match the pile-up profile measured in the observed data set. A systematic uncertainty on this procedure is derived by increasing and decreasing the pile-up scale factor by 4%.

Systematic uncertainty name	Description of uncertainty source
	Event
LUMI	uncertainty on total integrated luminosity
PRW_DATASF	uncertainty on pile-up modelling and re-weighting
	Electrons
EL_EFF_Trigger_Total_1NPCOR_PLUS_UNCOR	trigger efficiency uncertainty
EL_EFF_Reco_Total_1NPCOR_PLUS_UNCOR	reconstruction efficiency uncertainty
EL_EFF_ID_TotalCorrUncertainty	identification efficiency uncertainty
EL_EFF_ID_CorrUncertaintyNP(0...15)	identification efficiency uncertainty split into 16 components
EL_EFF_ID_SIMPLIFIED_UncorrUncertaintyNP(0...17)	identification efficiency uncertainty split into 18 components
EL_EFF_Iso_Total_1NPCOR_PLUS_UNCOR	isolation efficiency uncertainty
EG_SCALE_ALL	energy scale uncertainty
EG_SCALE_AF2	
EG_RESOLUTION_ALL	energy resolution uncertainty
	Muons
MUON_EFF_TrigStatUncertainty	trigger efficiency uncertainty
MUON_EFF_TrigSystUncertainty	
MUON_EFF_RECO_STAT	reconstruction and identification efficiency uncertainty for muons with $p_{\mathrm{T}} > 15$ GeV
MUON_EFF_RECO_SYS	
MUON_ISO_STAT	isolation efficiency uncertainty
MUON_ISO_SYS	
MUON_TTVA_STAT	track-to-vertex association efficiency uncertainty
MUON_TTVA_SYS	
MUON_ID	momentum resolution uncertainty of inner detector
MUON_MS	momentum resolution uncertainty of muon spectrometer
MUON_SCALE	momentum scale uncertainty
MUON_SAGITTA_RHO	charge dependent momentum scale uncertainty
MUON_SAGITTA_RESBIAS	
	Jets
JET_EffectiveNP_Detector(1...2)	energy scale uncertainty from the in situ calibration split into several components
JET_EffectiveNP_Mixed(1...3)	
JET_EffectiveNP_Modelling(1...4)	
JET_EffectiveNP_Statistical(1...6)	
JET_EtaIntercalibration_Modeling	energy scale uncertainty on η-intercalibration (modelling)
JET_EtaIntercalibration_TotalStat	energy scale uncertainty on η-intercalibration (statistics/method)
JET_EtaIntercalibration_NonClosure_highE	energy scale uncertainty on η-intercalibration (non-closure)
JET_EtaIntercalibration_NonClosure_negEta	
JET_EtaIntercalibration_NonClosure_posEta	
JET_Pileup_OffsetMu	energy scale uncertainty on pile-up (μ-dependent)
JET_Pileup_OffsetNPV	energy scale uncertainty on pile-up (N_{PV}-dependent)
JET_Pileup_PtTerm	energy scale uncertainty on pile-up (p_{T} term)
JET_Pileup_RhoTopology	energy scale uncertainty on pile-up (density ρ)
JET_Flavor_Composition	energy scale uncertainty on flavour composition
JET_Flavor_Response	energy scale uncertainty on flavour response of sample
JET_BJES_Response	energy scale uncertainty on b-jets
JET_PunchThrough_MC16	energy scale uncertainty for punch-through jets
JET_SingleParticle_HighPt	energy scale uncertainty for the behaviour of high-p_{T} jets
JET_JER_DataVsMC_MC16	energy resolution uncertainties
JET_JER_EffectiveNP(1...11)	
JET_JER_EffectiveNP_12restTerm	
JET_JvtEfficiency	JVT efficiency uncertainty
	Flavour tagging
FT_EFF_Eigen_B	b-tagging efficiency uncertainties: 3 components for b-jets, 3 for c-jets and 4 for light jets
FT_EFF_Eigen_C	
FT_EFF_Eigen_L	
FT_EFF_Eigen_extrapolation	b-tagging efficiency uncertainty on the extrapolation to high-p_{T} b- and c-jets
FT_EFF_Eigen_extrapolation_from_charm	b-tagging efficiency uncertainty on τ-lepton jets
	$E_{\mathrm{T}}^{\mathrm{miss}}$ and $p_{\mathrm{T}}^{\mathrm{miss}}$
MET_SoftTrk_ResoPara	track-based soft term related longitudinal resolution uncertainty
MET_SoftTrk_ResoPerp	track-based soft term related transverse resolution uncertainty
MET_SoftTrk_Scale	track-based soft term related longitudinal scale uncertainty
MET_JetTrk_Scale	$p_{\mathrm{T}}^{\mathrm{miss}}$ uncertainty due to tracks in jets

Table 5.1: Summary of the experimental systematic uncertainty sources which are considered in the analysis.

5.2 Theoretical uncertainties

Theoretical uncertainties are a class of uncertainties that are introduced into the measurements due to the inability to perfectly predict and model the signal and background processes. Since several programmes are used for predictions of event yields and the m_{T} or DNN output shape, with each implementing particular algorithms and parameter values, the use of a different programme for the same prediction can result in a different prediction. Theoretical uncertainties are generally derived on the absolute theoretical prediction of a process for the most significant processes in all analysis regions. For processes which are estimated using a CR, there is cancellation of uncertainties in the extrapolation factor from the CR to the (sub-)SRs. The theoretical uncertainty sources that are considered in this analysis, as well as a description of their estimation and approximate values, are summarised in Table 5.2.

5.2.1 Sources of theoretical uncertainty

Theoretical uncertainty originates from a number of sources in the steps of MC event generation. These sources can generally be divided into those that relate to the perturbative QCD calculation and those that relate to algorithmic differences in converting the perturbative QCD calculations into particle- and detector-level predictions.

Renormalisation and factorisation scale uncertainties

Theoretical uncertainty relating to missing higher orders in the perturbative calculations (*QCD scale uncertainty*) is estimated by changing the renormalisation and factorisation scales, μ_{R} and μ_{F}, respectively, by a factor of 2 or $1/2$. Specifically, a set of seven variations is defined by considering all variations of μ_{R} and μ_{F} around the nominal μ_{R} and μ_{F}, constrained by the requirement that $0.5 \leq \mu_{\mathrm{R}}/\mu_{\mathrm{F}} \leq 2$. The QCD scale uncertainty, $\delta\sigma^{\text{QCD scale}}$, in a particular analysis region is defined as the maximum variation of the envelope generated by the seven different variations of μ_{R} and μ_{F},

$$\delta\sigma^{\text{QCD scale}} = \max_{\text{var}}[\sigma_{\text{var}}/\sigma_{\text{nom}}], \tag{5.1}$$

where σ_x (with $x = \{\text{var},\ \text{nom}\}$) represents the yields (or histograms) obtained using one of the variations of μ_{R} and μ_{F} (*var*) or the nominal μ_{R} and μ_{F} (*nom*).

PDF and α_{S}

Uncertainty in the PDF sets and the value of α_{S} that is used for the generation of theoretical predictions arises from several sources. Firstly, experimental uncertainty in the PDF fit, as well as the uncertainty due to the assumed functional form of the PDF, needs to be propagated through measurements. Secondly, the experimental uncertainty in the estimation of α_{S}, which is typically measured at the scale of the Z boson mass, needs to

Table 5.2: A list of theoretical uncertainties that are derived for each process in this analysis. The values of the uncertainties refer to the size of the uncertainty in the SRs or the uncertainty on the extrapolation factor from CRs to SRs where a background process is estimated using a CR. The range of values reflects differences in the uncertainty values between the different analysis regions. Parameters and variables are defined in the text.

Process	Source of uncertainty	Description of uncertainty estimate	Uncertainty estimate [%]
ggF	QCD scale	Variations of μ_R and μ_F, N_{jet} migrations (STXS: also p_T^H and m_{jj} migrations)	5−17
	Matching	Comparison of POWHEG+PYTHIA 8 with MADGRAPH5_aMC@NLO+PYTHIA 8	1−4
	Shower (UEPS)	Comparison of POWHEG+PYTHIA 8 with POWHEG+HERWIG 7	1−7
	PDF	Standard deviation of a set of 30 PDF4LHC15 variations	2−3
	α_S	Comparison of two α_S variations	1−3
VBF	QCD scale	Variations of μ_R and μ_F, N_{jet} migrations (STXS: also p_T^H and m_{jj} migrations)	1−2
	Matching	Comparison of POWHEG+PYTHIA 8 with MADGRAPH5_aMC@NLO+HERWIG 7	6−16
	Shower (UEPS)	Comparison of POWHEG+PYTHIA 8 with POWHEG+HERWIG 7	4−9
	PDF	Standard deviation of a set of 30 PDF4LHC15 variations	1−2
	α_S	Comparison of two α_S variations	0.1−1
Other Higgs	Theoretical prediction	$\pm 50\%$ normalisation uncertainty	
$qqWW$	QCD scale	Envelope of seven $\{\mu_R, \mu_F\}$ variations	0.1−1
	PDF	Standard deviation of a set of 100 NNPDF3.0NLO replicas	∼0.1
	α_S	Comparison of two α_S variations	∼0.1
	Matching (CKWW)	Variation of Q_{cut} parameter	0.1−1
	Resummation	Variation of QSF parameter by factor 2	0.1−4
	Parton shower recoil	Comparison of two parton shower recoil schemes (CSSKIN)	1−3
$ggWW$	Theoretical prediction	Normalisation uncertainty. ggF $N_{jet} < 2$: NLO calculation; $N_{jet} \geq 2$: $-50/+100\%$	
Electroweak WW	QCD scale	Envelope of seven $\{\mu_R, \mu_F\}$ variations	1−6
	PDF	Standard deviation of a set of 100 NNPDF3.0NLO replicas	∼0.3
	α_S	Comparison of two α_S variations	∼0.2
	Shower	Comparison of MADGRAPH5_aMC@NLO interfaced to PYTHIA 8 and HERWIG 7	1−8
	EW correction	$\pm 15\%$ normalisation uncertainty	
$t\bar{t}/Wt$	Matching	Comparison of POWHEG+PYTHIA 8 with MADGRAPH5_aMC@NLO+PYTHIA 8	0.1−8
	Shower (UEPS)	Comparison of POWHEG+PYTHIA 8 with POWHEG+HERWIG 7	1−12
	QCD scale	Envelope of seven $\{\mu_R, \mu_F\}$ variations	0.1−1
	ISR	Comparison with Var3c A14 tune variation (variation of α_S)	0.1−1
	FSR	Variation of μ_R by factor of 2 in parton shower	0.1−6
	PDF	Standard deviation of a set of 100 NNPDF3.0NLO replicas	0.1−1
	$t\bar{t}/Wt$ interference	Comparison of DR and DS schemes (Wt only)	1−4
Z/γ^*+jets	Generator	Comparison of SHERPA 2.2.1 with MADGRAPH5_aMC@NLO+PYTHIA 8	1−25
	QCD scale	Envelope of seven $\{\mu_R, \mu_F\}$ variations	5−9
	PDF	Standard deviation of a set of 100 NNPDF3.0NLO replicas	0.1−1
	α_S	Comparison of two α_S variations	0.1−1
$V\gamma$	Theoretical prediction	$-50/+100\%$ normalisation uncertainty	
Non-WW diboson	Theoretical prediction	$\pm 12\%$ normalisation uncertainty	
VVV	Theoretical prediction	$\pm 12\%$ normalisation uncertainty	

be considered. The derivation of PDF uncertainties is different depending on whether NNPDF3.0NLO or PDF4LHC15 is used in the generation of an MC sample. In the former case, an ensemble of 100 PDF sets, in addition to the central PDF set, is provided. The central PDF set is the mean of the 100 PDF sets, so that a PDF uncertainty, $\delta\sigma^{\text{PDF}}$, is defined as the standard deviation, given by

$$\delta\sigma^{\text{PDF}} = \sqrt{\frac{1}{99}\sum_{i=1}^{100}(\sigma_i - \sigma_0)^2}, \tag{5.2}$$

where σ_i and σ_0 represent yields (or histograms) in a particular analysis region obtained using PDF set i and the central PDF set, respectively. For PDF4LHC15, a set of 30 Hessian-reduced error PDFs are provided, motivated by the fact that a PDF can be described by several parameters that may be varied individually to generate a new PDF. The PDF uncertainty, $\delta\sigma^{\text{PDF}}$, in this case is

$$\delta\sigma^{\text{PDF}} = \sqrt{\frac{1}{30}\sum_{i=1}^{30}(\sigma_i - \sigma_0)^2}, \tag{5.3}$$

with the same definitions of σ_i and σ_0 as in Equation 5.2.

Additionally, both PDF sets are produced using a nominal value of the strong coupling constant, α_{S}, of $\alpha_{\text{S}}(m_Z^2) = 0.1180$. An uncertainty on α_{S}, $\delta\sigma^{\alpha_{\text{S}}}$, is estimated by comparing the yields (or histograms) obtained using two different values of α_{S},

$$\delta\sigma^{\alpha_{\text{S}}} = \pm\frac{|\sigma_{\alpha_{\text{S}}^{\text{up}}} - \sigma_{\alpha_{\text{S}}^{\text{down}}}|}{2}, \tag{5.4}$$

where $\sigma_{\alpha_{\text{S}}^{\text{up}}}$ and $\sigma_{\alpha_{\text{S}}^{\text{down}}}$ represent the yields (or histograms) obtained with a PDF using an increased or decreased value of α_{S}. In the case of NNPDF3.0NLO, the up and down variations are 0.1190 and 0.1170, whilst in the case of PDF4LHC15 the variations are 0.1195 and 0.1165.

Matching and merging

In general, separate programmes are used to calculate the hard scatter and model the UEPS. An uncertainty arises when two programmes are interfaced, which depends on the programme. Firstly, an uncertainty arises in the case where double-counting of jets is removed when combining events with different jet multiplicities (merging), or secondly in the case when an NLO or NNLO calculation is interfaced to a parton shower (matching). Typically, uncertainties of this source are derived by fixing the programme used to model the UEPS but changing the programme to calculate the hard scatter. For example, when POWHEG is used to generate the hard scatter, the alternative programme is MADGRAPH5_aMC@NLO. As such, the uncertainty, $\delta\sigma^{\text{M}}$, is given by

$$\delta\sigma^{\text{M}} = \pm|\sigma_{\text{var}} - \sigma_{\text{nom}}|, \tag{5.5}$$

where σ_{var} and σ_{nom} represent the yields (or histograms) obtained using the alternative and nominal programme to generate the hard scatter, respectively. When SHERPA is used, the merging of matrix elements with differing jet multiplicities is performed using the MEPS@NLO algorithm [47–50] (based on the CKKW algorithm), which makes use of an arbitrary scale of $Q_{\text{cut}} = 20$ GeV to separate the matrix element from the parton shower. A merging uncertainty is derived by comparing the yields obtained when changing Q_{cut} to 15 and 30 GeV. A further uncertainty is derived for SHERPA by varying the resummation scale, which regulates the upper cutoff of the parton shower (the QSF parameter).

Parton shower and hadronisation model

Uncertainty due to the parton shower and hadronisation model (UEPS) arises since different algorithms are implemented by PYTHIA, HERWIG, and SHERPA. In general, a UEPS uncertainty is derived for a particular process and analysis region by using the same hard scatter calculation but where the generated events are instead interfaced with an alternate programme. For example, when PYTHIA is used to model the UEPS, the alternative programme is typically HERWIG. As such, the UEPS uncertainty, $\delta\sigma^{\text{UEPS}}$, is given by the formula in Equation 5.5. In the case that SHERPA is used, which models both the hard scatter and the UEPS, an uncertainty is derived by using a different algorithm to model the momentum recoil in the parton shower evolution (the CSSKIN parameter).

5.2.2 Process-specific theoretical uncertainties

For almost all processes considered in this analysis, uncertainties are derived for at least the following sources: QCD scale, PDF, α_{S}, UEPS, and matching. In some instances, the estimation of the UEPS and matching uncertainty may differ for a particular process and some processes may have uncertainties derived for additional sources.

Higgs boson signal

The theoretical uncertainty that is derived for the Higgs boson signal processes, ggF and VBF, depends on the type of measurement performed, whether that be signal strength measurements or cross section measurements[30]. In signal strength measurements, theoretical uncertainty affects the absolute normalisation of the theoretical prediction and also the acceptance of events. In cross section measurements, theoretical uncertainty affects only the acceptance.

The analysis is categorised by jet multiplicity, but variations of μ_{R} and μ_{F} within each jet-binned region can underestimate the perturbative QCD uncertainty due to missing higher-order corrections to the exclusive cross section predictions. The perturbative QCD

[30] Hereafter, these measurements are referred to as μ-style and σ-style measurements, respectively (note that the STXS measurements are exclusively σ-style measurements).

Table 5.3: Representative normalisation uncertainties on the absolute yields of the ggF and VBF $H \to WW^* \to \ell\nu\ell\nu$ processes for each source of uncertainty in the analysis regions. The column labelled *QCD scale* represents the quadrature sum of several sources of uncertainty, as described in the text. An entry of "–" refers to an uncertainty that is less than 0.1%.

Region	Uncertainty source in region [%]									
	ggF					VBF				
	QCD scale	UEPS	Matching	PDF	α_S	QCD scale	UEPS	Matching	PDF	α_S
Inclusive measurement										
ggF $N_{\text{jet}} = 0$	5.2	3.9	–	2.7	1.0	1.5	9.1	16.4	1.8	0.9
ggF $N_{\text{jet}} = 1$	9.0	4.4	–	2.0	2.9	1.0	3.6	6.3	1.7	0.7
ggF-enriched $N_{\text{jet}} \geq 2$	13.7	6.9	4.0	1.9	3.2	1.2	6.1	6.1	1.7	0.5
VBF-enriched $N_{\text{jet}} \geq 2$	16.6	0.7	0.9	1.7	3.2	1.4	4.7	8.2	1.7	0.4
STXS measurement										
ggF $0j$, low p_{T}^H	5.2	3.9	–	2.7	1.0	1.5	9.1	16.4	1.8	0.9
ggF $1j$, very low p_{T}^H	8.1	3.7	–	2.2	2.7	1.1	4.1	10.9	1.8	0.8
ggF $1j$, low p_{T}^H	11.8	4.9	–	1.9	3.3	1.0	4.2	7.3	1.7	0.7
ggF $1j$, med p_{T}^H	14.9	8.6	–	1.8	3.4	1.0	2.3	5.4	1.7	0.5
ggF $1j$, high p_{T}^H	36.5	6.5	–	2.2	3.3	1.0	3.7	11.2	1.8	0.2
ggF $2j$, low p_{T}^H	14.8	7.2	0.6	1.9	3.2	1.1	5.5	6.1	1.7	0.5
ggF $1j$, high p_{T}^H	22.6	4.1	20.1	2.5	3.3	1.7	9.7	6.2	1.7	0.2
VBF $2j$, very low m_{jj}	14.6	4.8	7.8	1.8	3.2	1.5	3.9	9.8	1.8	0.6
VBF $2j$, low m_{jj}	18.5	1.2	6.2	1.6	3.2	1.5	4.2	7.1	1.8	0.5
VBF $2j$, med m_{jj}	13.7	3.6	12.1	1.4	3.2	1.6	7.0	9.6	1.8	0.4
VBF $2j$, high m_{jj}	14.0	10.8	15.1	1.2	3.2	1.7	7.4	1.0	2.1	0.2
VBF $2j$, high p_{T}^H	21.0	5.9	11.8	2.2	3.3	1.6	3.9	9.7	1.8	0.1

uncertainty in exclusive regions of jet multiplicity, as well as on the migrations between regions of different jet multiplicity, is more accurately estimated using a method described in Ref. [53]. Additional sources of uncertainty are considered, including the effect of the top quark mass, m_t, in cross section predictions (which is relevant for Higgs boson $p_{\text{T}} \gtrsim 2m_t$ when the top quark loop is resolved), and the contamination of the ggF process in the VBF region. In the STXS measurements, further uncertainties are derived to account for migration of events across m_{jj} and p_{T}^H boundaries, as well as the N_{jet} boundaries. The normalisation uncertainties for each source of uncertainty considered for the ggF and VBF production of a Higgs boson are shown in Table 5.3. For Higgs boson production processes other than ggF or VBF $H \to WW^*$, a normalisation uncertainty of $\pm 50\%$ is assigned to the analysis regions within a jet-binned category. Lastly, an uncertainty of 2.16% is present in μ-style measurements reflecting the uncertainty in the $H \to WW^*$ branching ratio that includes the uncertainty in the Higgs boson mass [53].

Non-resonant WW

The matching, resummation, and algorithmic parton shower uncertainties for non-resonant WW are derived by considering variations of the CKKW, QSF, and CSSKIN parameters within the SHERPA event generator. Given limited sample sizes of the alternative SHERPA samples with full detector simulation, the uncertainties for matching,

Table 5.4: Representative normalisation uncertainties considered for the $qqWW$ and EW WW processes for each source of uncertainty in the analysis regions. The uncertainty on the extrapolation factor, $\Delta\alpha$, is shown in cases where the processes are normalised with CRs, otherwise the uncertainties on the absolute yields are shown. An entry of "–" refers to an uncertainty that is less than 0.1%.

Region	Uncertainty source									
	$qqWW$						EW WW ($qq \to WWqq$)			
	QCD scale	CKWW	QSF	CSSKIN	PDF	α_S	QCD scale	UEPS	PDF	α_S
Inclusive measurement										
	$\Delta\alpha$ [%]									
ggF $N_{\text{jet}} = 0$	–	0.1	0.1	0.7	0.1	0.1	0.7	1.0	0.1	–
ggF $N_{\text{jet}} = 1$	0.4	1.1	3.8	0.6	0.1	0.1	3.8	1.9	–	0.2
ggF-enriched $N_{\text{jet}} \geq 2$	0.7	0.2	1.5	3.0	–	0.1	5.5	7.6	0.3	0.2
	Uncertainty in region [%]									
VBF-enriched $N_{\text{jet}} \geq 2$	$+19.5/-14.2$	6.1	6.9	3.2	1.0	1.9	$+6.9/-6.2$	3.1	1.5	0.1
STXS measurement										
	$\Delta\alpha$ [%]									
ggF $0j$, low p_{T}^H	–	0.1	0.1	0.7	0.1	0.1	0.7	1.0	0.1	–
ggF $1j$, very low p_{T}^H	1.3	1.0	6.9	0.4	0.1	0.1	1.1	2.5	–	0.1
ggF $1j$, low p_{T}^H	0.1	2.2	0.2	0.6	0.1	0.1	2.9	0.1	0.2	0.1
ggF $1j$, med p_{T}^H	0.2	0.4	1.1	3.2	0.1	–	2.9	0.4	0.1	0.1
ggF $1j$, high p_{T}^H	0.4	5.5	7.1	4.0	–	–	3.0	6.8	0.3	0.1
ggF $2j$, low p_{T}^H	0.1	1.3	2.1	2.7	0.1	–	5.8	10.5	0.3	0.2
ggF $2j$, high p_{T}^H	0.3	1.4	1.5	1.8	0.4	–	3.0	0.7	0.3	–
	Uncertainty in region [%]									
VBF $2j$, very low m_{jj}	$+21.2/-15.5$	6.8	5.4	7.9	1.0	2.0	$+1.6/-2.0$	6.8	1.3	0.3
VBF $2j$, low m_{jj}	$+16.2/-11.9$	5.1	13.7	5.2	1.1	1.8	$+4.6/-4.5$	3.1	1.4	0.2
VBF $2j$, med m_{jj}	$+12.3/-9.4$	15.5	3.3	7.5	1.2	1.5	$+7.3/-6.5$	2.3	1.5	0.1
VBF $2j$, high m_{jj}	$+9.6/-7.2$	9.3	12.0	8.8	1.6	1.4	$+12.6/-10.3$	2.1	2.0	0.1
VBF $2j$, high p_{T}^H	$+31.0/-21.5$	0.6	10.5	4.3	1.1	2.2	$+9.2/-7.8$	5.4	1.7	–

resummation, and parton shower are estimated at particle-level. The normalisation uncertainties for each source of uncertainty considered for the $qqWW$ and EW WW processes are shown in Table 5.4.

The $ggWW$ process is not normalised using a CR, meaning the estimation of $ggWW$ relies solely on the theoretical prediction. The sample is accurate to LO in QCD for up to one additional parton emission, so a large normalisation uncertainty of $-50/+100\%$ is associated to the $ggWW$ process in the ggF-enriched $N_{\text{jet}} \geq 2$ and VBF-enriched $N_{\text{jet}} \geq 2$ analysis regions. In the ggF $N_{\text{jet}} = 0$ and ggF $N_{\text{jet}} = 1$ regions, QCD scale uncertainties are assigned to the $ggWW$ yields in the SRs and CRs using an NLO calculation produced with MATRIX [193].

Top quark

Two additional uncertainties are derived for the $t\bar{t}$ and Wt processes in order to estimate the effect of strong force radiation in the initial state (ISR) and final state (FSR). The

Table 5.5: Representative normalisation uncertainties considered for the $t\bar{t}$ process for each source of uncertainty in the analysis regions. The uncertainty on the extrapolation factor, $\Delta\alpha$, is shown. An entry of "–" refers to an uncertainty that is less than 0.1%.

Region	Uncertainty source, $\Delta\alpha$ [%]												
	$t\bar{t}$						Wt						
	QCD scale	UEPS	Matching	ISR	FSR	PDF	QCD scale	UEPS	Matching	ISR	FSR	PDF	$t\bar{t}/Wt$ int.
Inclusive measurement													
ggF $N_{\text{jet}} = 0$	0.6	2.5	0.2	–	3.4	–	0.1	3.9	1.3	0.7	3.7	0.1	2.5
ggF $N_{\text{jet}} = 1$	1.1	1.3	2.0	0.4	4.2	0.1	0.5	9.1	8.4	0.2	4.7	0.1	1.1
ggF-enriched $N_{\text{jet}} \geq 2$	1.2	2.0	3.4	0.1	0.3	0.2	0.6	3.4	5.4	1.3	5.7	0.1	3.9
VBF-enriched $N_{\text{jet}} \geq 2$	0.2	4.1	0.7	0.7	3.3	0.4	0.4	12.4	5.1	0.6	2.3	0.3	1.6
STXS measurement													
ggF $0j$, low p_{T}^{H}	0.6	2.5	0.2	–	3.4	–	0.1	3.9	1.3	0.7	3.7	0.1	2.5
ggF $1j$, very low p_{T}^{H}	0.7	0.1	3.2	0.2	3.6	–	0.3	10.9	10.2	0.2	5.3	0.1	1.5
ggF $1j$, low p_{T}^{H}	0.9	1.8	2.5	0.4	4.5	0.1	0.3	6.5	6.8	0.1	4.7	0.1	0.3
ggF $1j$, med p_{T}^{H}	3.2	7.0	6.6	1.6	4.4	0.1	2.5	13.4	0.6	3.1	0.7	–	0.5
ggF $1j$, high p_{T}^{H}	16.7	9.9	38.5	5.4	11.6	0.2	5.5	20.0	9.3	2.3	0.2	0.2	9.2
ggF $2j$, low p_{T}^{H}	1.0	2.0	3.8	–	0.1	0.2	0.5	4.0	5.9	1.8	3.7	–	4.3
ggF $2j$, high p_{T}^{H}	0.6	2.2	3.6	1.1	3.7	0.1	0.7	2.2	3.7	4.5	34.4	0.6	13.1
VBF $2j$, very low m_{jj}	0.1	4.3	1.0	0.7	4.2	0.3	0.3	14.6	8.7	0.1	4.3	0.2	0.9
VBF $2j$, low m_{jj}	0.5	3.3	2.3	0.3	1.5	0.4	1.0	1.2	11.5	1.3	–	0.3	7.0
VBF $2j$, med m_{jj}	0.5	2.4	2.1	0.7	1.8	0.7	0.4	2.3	9.1	3.2	7.1	0.6	1.4
VBF $2j$, high m_{jj}	0.4	3.8	5.2	2.2	0.2	1.1	1.1	4.2	16.5	2.5	11.6	1.4	24.9
VBF $2j$, high p_{T}^{H}	1.8	3.6	7.2	0.7	5.3	0.4	1.0	41.8	8.3	5.4	5.1	0.1	20.4

uncertainty on the amount of ISR in $t\bar{t}$ and Wt events is estimated by comparing two additional samples to the nominal sample, where the *Var3c* variation in the ATLAS A14 PYTHIA tune is used [164]. This corresponds to two samples generated with an increase or decrease of α_{S} in the initial state parton shower. For the uncertainty on the amount of FSR, μ_{R} is varied by a factor of 2 in the final state parton shower.

In addition, an uncertainty is estimated for the Wt process to account for the interference between the $t\bar{t}$ and Wt processes. At NLO, Wt production includes Feynman diagrams producing $gg \to tWb$ with either one on-shell top quark (e.g. one gluon splits to $t\bar{t}$, the other to $b\bar{b}$, and a top and bottom quark annihilate to a W boson) or two on-shell top quarks (which is exactly the $t\bar{t}$ process at LO). When using such a calculation, a subtraction scheme must be used to avoid double-counting, and this can be performed either at the amplitude level or at the cross section level. The *diagram removal* (DR) scheme sets the amplitude of the doubly-resonant diagrams to zero, which removes the $t\bar{t}$–Wt interference term and non-resonant tWb as well as the overlap with the LO $t\bar{t}$ process. The *diagram subtraction* (DS) scheme instead subtracts the squared amplitude of the doubly-resonant diagrams from the calculation, thereby retaining the $t\bar{t}$–Wt interference term. An uncertainty that estimates the size of the interference is derived by comparing the event yields of the nominal Wt sample (which uses the DR scheme) with an alternative Wt sample that uses the DS scheme [175, 194]. The normalisation uncertainties for each source of uncertainty considered for the $t\bar{t}$ and Wt processes are shown in Table 5.5.

Table 5.6: Representative normalisation uncertainties considered for the Z/γ^* process for each source of uncertainty in the analysis regions. The uncertainty on the extrapolation factor, $\Delta\alpha$, is shown. An entry of "–" refers to an uncertainty that is less than 0.1%.

Region	Uncertainty source, $\Delta\alpha$ [%]			
	QCD scale	Generator	PDF	α_S
Inclusive measurement				
ggF $N_{\text{jet}} = 0$	8.7	24.9	0.3	0.3
ggF $N_{\text{jet}} = 1$	5.7	10.8	0.6	0.2
ggF-enriched $N_{\text{jet}} \geq 2$	5.9	1.2	0.1	0.2
VBF-enriched $N_{\text{jet}} \geq 2$	6.9	23.8	0.5	0.3
STXS measurement				
ggF $0j$, low p_{T}^H	8.7	24.9	0.3	0.3
ggF $1j$, very low p_{T}^H	9.8	11.4	0.4	0.4
ggF $1j$, low p_{T}^H	0.8	4.9	0.6	0.1
ggF $1j$, med p_{T}^H	3.1	5.9	0.3	0.2
ggF $1j$, high p_{T}^H	3.9	55.3	0.6	0.3
ggF $2j$, low p_{T}^H	6.4	0.7	0.2	0.3
ggF $2j$, high p_{T}^H	3.4	5.1	0.1	0.1
VBF $2j$, very low m_{jj}	5.8	12.4	0.4	0.4
VBF $2j$, low m_{jj}	5.6	30.2	0.5	0.1
VBF $2j$, med m_{jj}	9.0	61.3	0.6	0.3
VBF $2j$, high m_{jj}	6.9	26.9	0.8	0.2
VBF $2j$, high p_{T}^H	1.7	21.6	0.1	0.1

Z/γ^*

A so-called *generator* uncertainty is estimated for the Z/γ^* background, which compares the predictions of the nominal SHERPA sample with the predictions of MADGRAPH5_aMC@NLO+PYTHIA 8. This uncertainty covers both the matrix element calculation as well as the UEPS. The normalisation uncertainties for each source of uncertainty considered for the Z/γ^* process are shown in Table 5.6.

Other diboson and triboson

Theoretical uncertainty on the absolute normalisation of the MC predictions is derived for remaining backgrounds of small magnitude. A normalisation uncertainty of $\pm 12\%$ is associated with the non-WW and VVV background processes in each analysis region, whilst a $-50/+100\%$ uncertainty is associated with the $V\gamma$ process in each analysis region. These values are obtained using the three-lepton data sample that is used to derive fake factors (Section 4.6.4).

6
Statistical analysis

A statistical analysis of the data and expected signal and background events in the SRs and CRs is performed using the formalism of *maximum likelihood estimation*, which allows one to make meaningful statements and inferences about the SM. The analysis proceeds by constructing a statistical model with the HISTFITTER [195] software, which is based on the ROOFIT [196] software. In this analysis, a binned likelihood function constitutes the statistical model and is described by a set of parameters, $\boldsymbol{\alpha} = (\boldsymbol{\mu}, \boldsymbol{\theta})$, where $\boldsymbol{\mu}$ are signal strengths and $\boldsymbol{\theta}$ is a vector of *nuisance parameters* (NPs). The signal strengths are termed *parameters of interest* (POIs) since it is the primary goal of the measurements to make statistical inference on these parameters, whilst the NPs are those parameters which must be included in the model in order to sufficiently account for systematic uncertainties. A description of the likelihood function and the setup for the inclusive and STXS measurements is given in Section 6.1. The method through which several hypotheses about nature can be tested is described in Section 6.2. Lastly, several tools which can be used to validate the performance of the statistical analysis are outlined in Section 6.3.

6.1 Maximum likelihood estimation

The likelihood function is a function of the data set and quantifies the probability of obtaining a specific set of parameter values given the data set. It is written as

$$\mathcal{L}(\boldsymbol{\mu}, \boldsymbol{\theta}) = \mathcal{L}(\boldsymbol{\mu}, \boldsymbol{\theta} | \boldsymbol{\mathcal{D}}) = f(\boldsymbol{\mathcal{D}}; \boldsymbol{\mu}, \boldsymbol{\theta}),$$

where $\boldsymbol{\mathcal{D}}$ is the observed data set. In this analysis, the likelihood function is defined by a product of four terms:

$$\begin{aligned} \mathcal{L}(\boldsymbol{\mu},\ \boldsymbol{\theta}) = & \prod_{i}^{N_{\text{SRs}}} \prod_{b}^{N_{\text{bins}}} \text{Pois}\left(N_{ib} \,\middle|\, \boldsymbol{\mu} \cdot \boldsymbol{S}_{ib}(\boldsymbol{\theta}) + \sum_{k}^{N_{\text{bkg}}} \beta_k \cdot B_{kib}(\boldsymbol{\theta}) \right) \\ & \times \prod_{l}^{N_{\text{CRs}}} \text{Pois}\left(N_l \,\middle|\, \boldsymbol{\mu} \cdot \boldsymbol{S}_l(\boldsymbol{\theta}) + \sum_{k}^{N_{\text{bkg}}} \beta_k \cdot B_{kl}(\boldsymbol{\theta}) \right) \\ & \times \prod_{t}^{\boldsymbol{\theta}} \text{Gaus}(\vartheta_t \mid \theta_t) \times \prod_{b}^{N_{\text{bins}}} \text{Pois}(\xi_b \mid \zeta_b \cdot \theta_b). \end{aligned} \tag{6.1}$$

The function of each term is as follows:

First term

The first term represents the product of Poisson functions describing the expected Higgs boson signal and k background yields, $\boldsymbol{S}(\boldsymbol{\theta})$ and $B_k(\boldsymbol{\theta})$, in each bin, b, of the SRs, i, given the observed data, N_{ib}. The Poisson distribution has the form $\text{Pois}(x;\nu) = \nu^x e^{-\nu}/x!$. The expected Higgs boson signal yield is given by $S_{jib} = \mathcal{L}_{ib} \times (\sigma_j \cdot \mathcal{B}_{H\to WW^*})^{\text{SM}} \times (A \cdot \epsilon)^{\text{SM}}_{jib}$ for production mode j[31], where the terms are described in Section 2.4.3. The terms $\boldsymbol{S}(\boldsymbol{\theta})$ and $B_k(\boldsymbol{\theta})$ are parameterised in terms of the NPs, $\boldsymbol{\theta}$, to take into account the effect of systematic uncertainties. The signal strengths, $\boldsymbol{\mu}$, normalise the expected Higgs boson signal yield whilst the yields of background processes estimated with a dedicated CR are normalised by the β_k, which are otherwise set to unity.

Second term

The second term represents the product of Poisson functions describing the expected Higgs boson signal and k background yields in each of the CRs, l. The CRs are used to measure the normalisation of the background processes targeted by each CR so only the total event yields are taken into account; CRs do not enter the likelihood function as binned distributions. The NFs, β_k, analogous to signal strengths, are included to scale the contributions of their respective background processes in each jet-binned SR and are dominantly extracted from this term of the likelihood function. These parameters are constrained in-situ during the minimisation of the likelihood.

Third term

The third term introduces NPs, $\boldsymbol{\theta}$, into the likelihood function that are used to constrain an associated systematic uncertainty, ϑ, with a Gaussian function of the form

$$\text{Gaus}(\vartheta_t|\theta_t) = \frac{1}{\sqrt{2\pi}} e^{-(\vartheta_t-\theta_t)^2/2}. \tag{6.2}$$

These constraint terms are normalised such that the nominal predictions of $\boldsymbol{S}_{ib}$ and B_{kib} are returned for $\theta_t = 0$, whilst $\theta_t = \pm 1$ returns the $\pm 1\sigma$ predictions corresponding to the systematic uncertainty ϑ_t.

Fourth term

The fourth term represents the product of Poisson functions which are included to model the finite sample size of the MC samples. These terms contain parameters, ξ_b, which parameterise the statistical uncertainty of the total sum of expected background event yields in each bin of the likelihood discriminant, according to a method proposed by Beeston and Barlow [197].

[31] Here, j represents ggF and VBF production for the inclusive measurement, or the eleven STXS bins for the STXS measurement.

The expected yields of the signal and background processes, generically termed N, are parameterised in terms of an NP, $N = N(\theta_t)$, associated with a systematic uncertainty. Many systematic uncertainties are incorporated into the likelihood function, so the parameterisation takes the form

$$N(\boldsymbol{\theta}) = N_0 \times \prod_t \nu(\theta_t), \tag{6.3}$$

where N_0 is the nominal expected yield of the process in question, and $\nu(\theta_t)$ is some function of θ_t. The exact form of the parameterisation of $\nu(\theta_t)$ depends on the systematic uncertainty associated to the NP, and whether an NP modifies the yields of a process, the shape of the discriminating variable, or both. It is obtained by computing event yields corresponding to the $\pm 1\sigma$ variations of each systematic uncertainty. For example, if an event yield varies by $\pm 5\%$ under a 1σ variation of a systematic uncertainty, then $\nu(\theta_t)$ evaluated at $\theta_t = \pm 1$ will return the event yield modified by $\pm 5\%$. The parameterisation between $\nu(\theta_t = \pm 1)$ is determined using a linear interpolation. Thus, systematic uncertainties are incorporated in the likelihood function, and their effects treated in a correlated way between different regions, by associating each systematic uncertainty to an NP and where the NPs are used to parameterise the expected signal and background yields, terms for which are included (in addition to the signal and background normalisation parameters) in every region (SRs and CRs). The assumed correlation of NPs between different regions, as well as their effect on a particular process, are not the same for all NPs: experimental systematic uncertainties affect all processes and are generally correlated between all regions in the likelihood function; theoretical uncertainty affecting the Higgs boson signal is also correlated between all regions; and theoretical uncertainty in the extrapolation factor for a background process measured in a CR are not correlated between regions of different jet multiplicity and production mode, as well as between CRs in the STXS measurement.

The construction of the likelihood function differs between the two sets of measurements in this analysis (the inclusive and STXS measurements). For the inclusive measurements, the SRs and their categorisations in $m_{\ell\ell}$ or $p_{\mathrm{T}}^{\mathrm{sublead}}$ are used. Two inclusive measurements are performed: the first is a measurement of ggF and VBF production where one parameter is associated to each production mode and scales the respective SM prediction; the second is a measurement where a single parameter is used to scale the sum of the SM predictions of ggF and VBF production. These are termed the 2 POI and 1 POI fits, respectively. For the STXS measurement, the STXS SRs and their categorisations in $m_{\ell\ell}$ or $p_{\mathrm{T}}^{\mathrm{sublead}}$ are used. A measurement of eleven POIs is performed, where one POI corresponds to one of the reduced STXS stage 1.2 bins. Table 6.1 shows the setup of the statistical analysis for each set of measurements, listing the SRs and types of CRs which enter the likelihood function, as well as the POIs measured with each setup.

The discriminating variable for all SRs in the likelihood function targeting the ggF production mode is the transverse mass, m_{T}. The event yields are distributed amongst six bins, covering the full m_{T} range, with the following binning: [< 90, 90–100, 100–110, 110–120, 120–130, > 130] GeV. The same binning of the m_{T} distribution is used for all ggF SRs in both the inclusive and STXS measurements. The choice of binning is similar to that used in previous measurements of $H \to WW^*$ [6, 7] and is designed to ensure the distribution of expected ggF events is flat in m_{T}, which reduces statistical fluctuation in the subtraction of background processes from the total yield. Several choices of bin boundaries and bin number were tested in a statistical analysis using only the ggF-enriched $N_{\mathrm{jet}} \geq 2$ regions, resulting in similar boundaries and number of m_{T} bins used in a statistical analysis of the ggF $N_{\mathrm{jet}} \leq 1$ regions. An identical binning of m_{T} is therefore chosen for all ggF regions for simple illustrative purposes and does not impact the results of the measurements significantly. For the VBF region, the output of the DNN functions as the input to the likelihood function using a binning that is defined using an algorithm that maximises the expected VBF Higgs boson signal significance. The algorithm returns seven bins with boundaries defined by [0.00–0.25, 0.25–0.52, 0.52–0.68, 0.68–0.77, 0.77–0.83, 0.83–0.87, 0.87–1.00] for the inclusive measurements, and four bins with boundaries defined by [0.00–0.50, 0.50–0.70, 0.70–0.84, 0.84–1.00] for the STXS measurement.

After constructing a likelihood function corresponding to one of the setups detailed in Table 6.1, estimates of the POIs and NPs are determined by maximising the likelihood function. Equivalently, minimising the negative log-likelihood function, $-\ln \mathcal{L}(\boldsymbol{\mu}, \boldsymbol{\theta})$, is computationally simpler and is the method implemented in software such as HistFitter [195]. The act of minimising the negative log-likelihood is often referred to as the *fit*. The resulting values and uncertainties of parameters in the likelihood function are referred to as *best-fit* or *post-fit*.

6.2 Hypothesis testing

Statistical inference given the observed data set and the theoretical modelling of signal and background processes is only possible if two *hypotheses* are compared. For the discovery of a signal process, the *null* hypothesis (a model that only describes the background) is tested with $\mu = 0$ whilst for the measurement of the signal process, the *alternate* hypothesis (a model that describes the signal and background) is tested with $\mu = 1$. Testing the null and alternate hypotheses proceeds by constructing the *profile likelihood ratio*, given by

$$\lambda(\mu) = \frac{\mathcal{L}(\mu, \hat{\hat{\boldsymbol{\theta}}}(\mu))}{\mathcal{L}(\hat{\mu}, \hat{\boldsymbol{\theta}})}, \tag{6.4}$$

Table 6.1: The setup of each statistical analysis, corresponding to the inclusive and STXS measurements, listing the SRs and CRs which enter the likelihood function, as well as the parameters of interest of each measurement.

Region	(sub-)SRs in likelihood function	CRs in likelihood function	POIs
Inclusive measurement			
ggF $N_{\text{jet}} = 0$	$m_{\ell\ell} < 30$ GeV, $p_{\text{T}}^{\text{sublead}} < 20$ GeV $m_{\ell\ell} < 30$ GeV, $p_{\text{T}}^{\text{sublead}} \geq 20$ GeV $m_{\ell\ell} \geq 30$ GeV, $p_{\text{T}}^{\text{sublead}} < 20$ GeV $m_{\ell\ell} \geq 30$ GeV, $p_{\text{T}}^{\text{sublead}} \geq 20$ GeV	$qqWW$, top quark, Z/γ^*	$\{\mu_{\text{ggF}}, \mu_{\text{VBF}}\}$, $\mu_{\text{ggF+VBF}}$
ggF $N_{\text{jet}} = 1$	$m_{\ell\ell} < 30$ GeV, $p_{\text{T}}^{\text{sublead}} < 20$ GeV $m_{\ell\ell} < 30$ GeV, $p_{\text{T}}^{\text{sublead}} \geq 20$ GeV $m_{\ell\ell} \geq 30$ GeV, $p_{\text{T}}^{\text{sublead}} < 20$ GeV $m_{\ell\ell} \geq 30$ GeV, $p_{\text{T}}^{\text{sublead}} \geq 20$ GeV	$qqWW$, top quark, Z/γ^*	
ggF-enriched $N_{\text{jet}} \geq 2$	$m_{\ell\ell} < 30$ GeV $m_{\ell\ell} \geq 30$ GeV	$qqWW$, top quark, Z/γ^*	
VBF-enriched $N_{\text{jet}} \geq 2$	No further categorisation	Top quark, Z/γ^*	
STXS measurement			
ggF $0j$, low p_{T}^H	$m_{\ell\ell} < 30$ GeV, $p_{\text{T}}^{\text{sublead}} < 20$ GeV $m_{\ell\ell} < 30$ GeV, $p_{\text{T}}^{\text{sublead}} \geq 20$ GeV $m_{\ell\ell} \geq 30$ GeV, $p_{\text{T}}^{\text{sublead}} < 20$ GeV $m_{\ell\ell} \geq 30$ GeV, $p_{\text{T}}^{\text{sublead}} \geq 20$ GeV	$qqWW$, top quark, Z/γ^*	$\{\mu_{ggH-0j,\text{ low } p_{\text{T}}^H}$, $\mu_{ggH-1j,\text{ very low } p_{\text{T}}^H}$, $\mu_{ggH-1j,\text{ low } p_{\text{T}}^H}$, $\mu_{ggH-1j,\text{ med } p_{\text{T}}^H}$, $\mu_{ggH-2j,\text{ low } p_{\text{T}}^H}$, $\mu_{ggH,\text{ high } p_{\text{T}}^H}$, $\mu_{\text{EW } qqH-2j,\text{ very low } m_{jj}-\text{low } p_{\text{T}}^H}$, $\mu_{\text{EW } qqH-2j,\text{ low } m_{jj}-\text{low } p_{\text{T}}^H}$, $\mu_{\text{EW } qqH-2j,\text{ med } m_{jj}-\text{low } p_{\text{T}}^H}$, $\mu_{\text{EW } qqH-2j,\text{ very high } m_{jj}-\text{low } p_{\text{T}}^H}$, $\mu_{\text{EW } qqH-2j,\text{ high } p_{\text{T}}^H}\}$
ggF $1j$, very low p_{T}^H	No further categorisation	$qqWW$, top quark, Z/γ^*	
ggF $1j$, low p_{T}^H		$qqWW$, top quark, Z/γ^*	
ggF $1j$, med p_{T}^H		$qqWW$, top quark, Z/γ^*	
ggF $1j$, high p_{T}^H		$qqWW$, top quark, Z/γ^*	
ggF $2j$, low p_{T}^H	$m_{\ell\ell} < 30$ GeV $m_{\ell\ell} \geq 30$ GeV	$qqWW$, top quark, Z/γ^*	
ggF $2j$, high p_{T}^H	$m_{\ell\ell} < 30$ GeV $m_{\ell\ell} \geq 30$ GeV	$qqWW$, top quark, Z/γ^*	
VBF $2j$, very low m_{jj}	No further categorisation	Top quark, Z/γ^*	
VBF $2j$, low m_{jj}		Top quark, Z/γ^*	
VBF $2j$, med m_{jj}			
VBF $2j$, high m_{jj}			
VBF $2j$, high p_{T}^H		Top quark, Z/γ^*	

where $\{\hat{\mu}, \hat{\boldsymbol{\theta}}\}$ is the set of parameter values which maximise the likelihood function (termed the *unconditional* fit), and $\hat{\hat{\boldsymbol{\theta}}}(\mu)$ are the values of the NPs which maximise the likelihood function for a given value of μ (termed the *conditional* fit). The value of $\lambda(\mu)$ is bound to the range $[0, 1]$, where $\lambda(\mu) \sim 1$ indicates maximal agreement between the tested value of μ and the observed data set. A *test statistic* is constructed, defined by $q_0 = -2 \ln \lambda(\mu)$, which is computationally more straightforward to determine. If the null or alternate hypotheses are compatible with the observed data set, the test statistic, q_0, will assume small values near zero. Conversely, increasing incompatibility between the tested hypotheses and the observed data set leads to increased values of q_0. The *p-value*, p_0, is constructed as a metric to quantify the amount of disagreement between the tested hypothesis and the observed data set. It is defined as the probability to obtain a value of q_0 at least as extreme as the observed value of q_0, q_0^{obs}, given the tested hypothesis:

$$p_0 = \int_{q_0^{\text{obs}}}^{\infty} f(q_0|\mu_{\text{tested}}) \mathrm{d}q_0, \tag{6.5}$$

where $f(q_0|\mu_{\text{tested}})$ is the probability density function of q_0 given the tested hypothesis with $\mu_{\text{tested}} = 0$ or 1, for discovery or measurement of the signal. The p-value allows one to exclude the hypothesis in question if the obtained p-value falls below some threshold, which in particle physics is considered to be $p_0 = 2.87 \times 10^{-7}$. This number is usually translated into a *significance*, Z_0, by using the fact the distribution of the q_0 is a χ^2 distribution with one degree of freedom (in the asymptotic limit) and using the inverse of the cumulative distribution of a standard Gaussian. A p-value of 2.87×10^{-7} translates to a significance of $Z_0 = 5$.

6.3 Validation tools

Given the complexity involved in constructing, performing, and understanding a likelihood fit, several common methods are employed to validate, diagnose potential issues in the statistical analysis, and visualise the results.

6.3.1 Pulls of nuisance parameters

The *pull* of an NP quantifies the deviation of the value of an NP from its input value, in units of its expected uncertainty, after performing the fit. The pull of an NP, θ is given by

$$\text{pull} = \frac{\hat{\theta} - \theta_0}{\sigma_{\theta_0}}, \tag{6.6}$$

where $\hat{\theta}$ is the value of θ obtained after the fit, and θ_0 and σ_{θ_0} are the value and uncertainty of θ before the fit (which are 0 and 1, by construction).

6.3.2 Estimates of uncertainties

The uncertainty of a parameter in the likelihood function after the fit can be obtained in two ways, either using the HESSE or MINOS algorithms. In the former case, the covariance matrix, V_{ij}, is built by deriving the inverse Hessian matrix from the likelihood function evaluated at its minimum. The covariance matrix is given by

$$V_{ij} = \left[- \frac{\partial^2 \log \mathcal{L}(\hat{\boldsymbol{\theta}})}{\partial\theta_i \partial\theta_j} \right]^{-1}, \tag{6.7}$$

where θ_i and θ_j represent two parameters in the likelihood model, and $\hat{\boldsymbol{\theta}}$ represents the maximum likelihood estimators of the parameters. The uncertainty on parameters are given by the square root of the diagonal elements of this matrix.

Related to the covariance matrix is the correlation matrix, ρ_{ij}. Correlations between parameters, or the dependency of one parameter on another, are introduced into the uncertainty estimates of the parameters due to the inversion of the Hessian matrix in Equation 6.7. The elements of the correlation matrix are constructed by normalising the elements of the covariance matrix by the variance of θ_i and θ_j, and are therefore bound to $[-1, 1]$. The correlation matrix is a useful tool to study the relationship between NPs in the likelihood function.

The approach taken by the HESSE algorithm to estimate parameter uncertainties is generally only valid in the vicinity of the function minimum. The MINOS algorithm instead makes use of the profile likelihood ratio,

$$-2\ln\lambda(\hat{\hat{\theta}}_i) = -2\ln\frac{\mathcal{L}(\hat{\boldsymbol{\theta}}(\theta_i = \hat{\hat{\theta}}_i))}{\mathcal{L}(\hat{\boldsymbol{\theta}})}, \tag{6.8}$$

where $\mathcal{L}(\hat{\boldsymbol{\theta}}(\theta_i = \hat{\hat{\theta}}_i))$ represents the *conditional* likelihood function with θ_i fixed, and $\mathcal{L}(\hat{\boldsymbol{\theta}})$ represents the fully *unconditional* likelihood function. An asymmetric 1σ confidence interval, $\sigma_i^{\pm}$, for the parameter θ_i is defined by determining the crossing points of $-2\ln\lambda(\hat{\hat{\theta}}_i) = 1$, so that the nominal value and uncertainty on the parameter θ_i is $\hat{\theta}_i{}^{+\sigma_i^+}_{-\sigma_i^-}$. This method of estimating the uncertainty on a parameter is said to *profile* said parameter. Parameters in the likelihood model with Gaussian constraint terms are said to be *overconstrained* if the uncertainty of the parameter is smaller after the fit than the uncertainty before ($[-1, 1]$), implying the likelihood model is more accurate than the initial estimate (usually from a different measurement).

6.3.3 Ranking of uncertainties

It is useful to quantify the importance of a singular uncertainty, or groups of uncertainties with a common source, on the total uncertainty of the parameter of interest, μ. In this

analysis, the ranking of uncertainties is achieved by using the method of *breakdowns*. In this method, two fits are performed and the uncertainties on the POI compared. The breakdown is given by

$$\text{breakdown} = \sqrt{\sigma^2_{\hat{\mu}} - \sigma^2_{\hat{\mu}'}}, \tag{6.9}$$

where $\sigma^2_{\hat{\mu}}$ is the uncertainty on the POI from the *unconditional* fit and $\sigma^2_{\hat{\mu}'}$ is the uncertainty on the POI from the *conditional* fit. The unconditional fit is the one in which the POI and all NPs are permitted to vary, whilst the conditional fit is so called since the uncertainty of interest (or group of uncertainties) is fixed to its value in the unconditional fit.

6.3.4 Asimov data set

The *Asimov data set* [198] is a data set that can be used to test and validate the statistical model. In this analysis, the development of the statistical model is performed *blind*. That is to say that the observed data in the SRs is not considered in developing the statistical analysis. Instead, the Asimov dataset is generated, the statistical analysis is refined and validated, and only then is the observed data used to extract the final results of the measurement. The yields of the Asimov data set correspond to the sum of the theoretical predictions of the signal and background processes considered in the analysis. As such, the pulls of NPs are zero and the values of the POI and background normalisations are unity, by construction. Performing the statistical analysis with the Asimov data set instead of the observed data set is important in order to construct a robust statistical model, estimate the expected precision of the measurement, and understand the performance of the statistical model, without introducing cognitive bias into the measurements.

6.3.5 Validation studies

In constructing a robust statistical model of the data set, many validation studies are performed using the tools described above. First, the statistical analysis is developed and optimised within each jet-binned region by performing separate fits using subsets of the different analysis regions listed in Table 6.1. For example, a fit can be performed using only the $N_{\text{jet}} \leq 1$ regions. In this case, the SM prediction of VBF production in these regions is assumed and μ_{ggF} is obtained. Generally, this approach allows for only one production mode measurement due to the fact that the SRs target different production modes. Similarly, measurements of μ_{ggF} and μ_{VBF} can be obtained in a fit using only the ggF-enriched $N_{\text{jet}} \geq 2$ and VBF-enriched $N_{\text{jet}} \geq 2$ regions, respectively. This approach means the expected sensitivity can be established for each subset of analysis regions and that the expected, and eventually observed results, are consistent with each subset. This method is also used to determine the number and definition of sub-SRs included in the fit, for example sub-SRs defined by $m_{\ell\ell}$ and $p_{\text{T}}^{\text{sublead}}$, for the regions used in both the inclusive and STXS measurements. The final fit setup for the inclusive and STXS measurement

makes use of sub-SRs which are found to maximise the expected precision of the signal normalisation with each jet-binned fit setup. Eventually, the statistical model developed for each jet-binned region is combined into a simultaneous fit to all event categories, as detailed in Table 6.1.

Second, whilst developing each statistical model, it is important to establish that NPs are not strongly constrained nor strongly pulled when the model eventually includes the observed SR data. Typically, *ranking plots* are generated, highlighting the pulls and breakdowns of individual NPs, ordered from those with the largest breakdown to smallest. These are generally studied using the statistical analysis performed with the Asimov data set. In the case that a particular NP is strongly constrained in this specific fit setup, it can be *decorrelated* between different regions and by its normalisation and shape components such that the constraint can be isolated and its origin understood. Once a well-validated statistical model in each jet-binned region is developed and merged into a simultaneous fit of all event categories, the fit using observed data can be performed and a ranking plot obtained, where in this case NPs can be pulled and the breakdowns could be different to the Asimov fit. Such an example is shown in Figure 6.1 which compares the pulls and breakdowns of the top 25 single NPs in a measurement of μ_{ggF} using the ggF-enriched $N_{\mathrm{jet}} \geq 2$ regions for both the Asimov and observed fits. The highest-ranked single NP is the matching uncertainty associated with the $t\bar{t}$ process. Originally, this NP was strongly constrained by about 50%. Performing studies as described above, the constraint was shown to originate from an imprecise estimate of the $t\bar{t}$ matching uncertainty, where the nominal and alternative generators used in the estimate had overlapping settings which overestimated the uncertainty. The development of an alternative sample which correctly accounted for differences only in the matrix element calculation reduced the constraint of this NP and ensured the fit model was more robust. Lastly, Figure 6.2 shows a ranking plot of the top 50 single NPs in the μ_{ggF} and μ_{VBF} signal strengths from the 2 POI simultaneous fit using observed data only. Developing and understanding the statistical analysis and performance of the fit within each jet-binned region ensures that the pulls and constraints of most NPs are reasonable and well-understood.

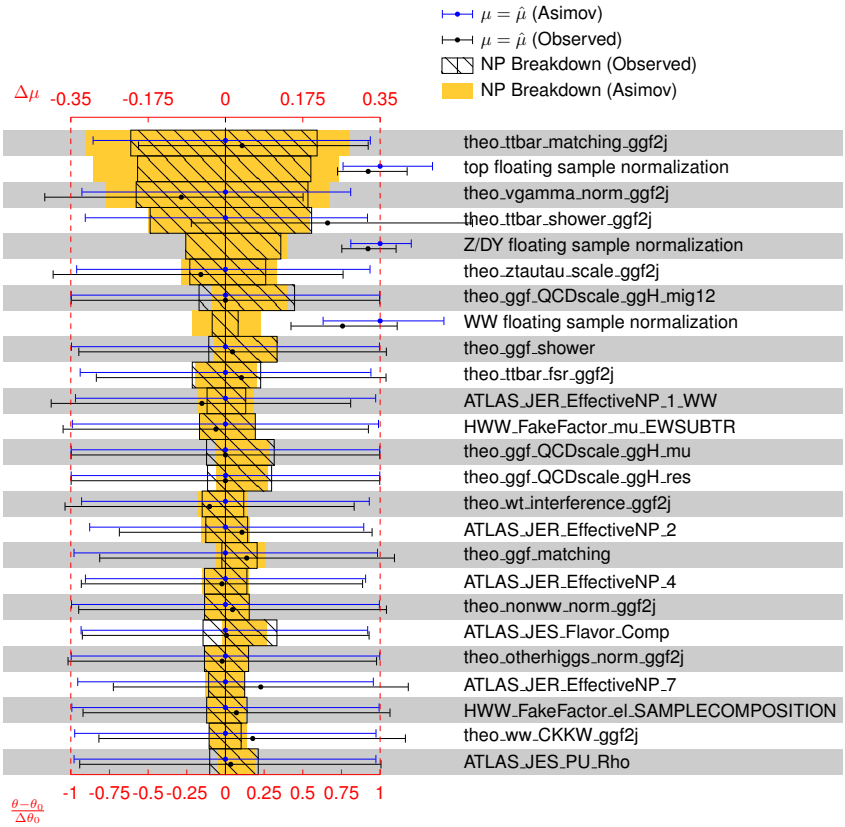

Figure 6.1: A ranking plot of the top 25 single NPs in a signal strength measurement of μ_{ggF} using only the ggF-enriched $N_{\mathrm{jet}} \geq 2$ regions listed in Table 6.1. The pulls of the NPs are compared between the Asimov (blue) and observed (black) statistical analyses, whilst the breakdown of each NP is shown for the Asimov (solid yellow) and observed (hatched black) statistical analyses.

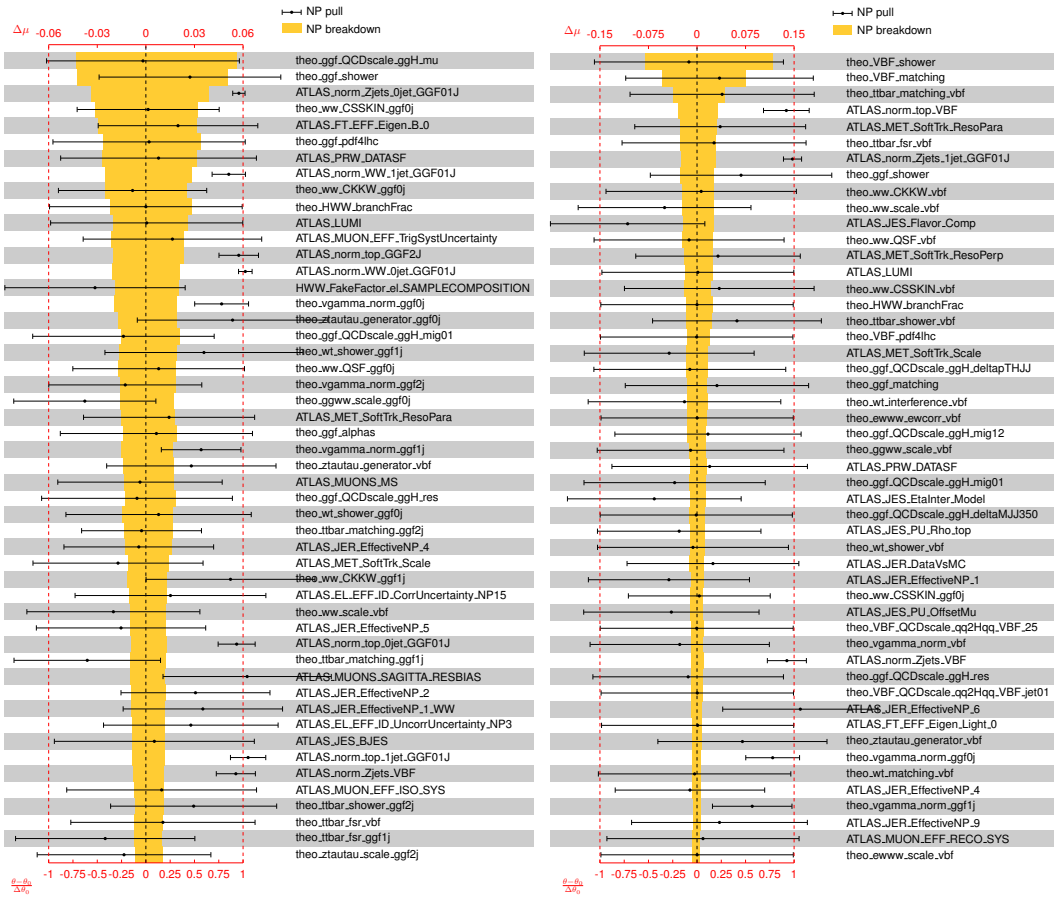

(a) **(b)**

Figure 6.2: Ranking plots of the top 50 single NPs in the (a) μ_{ggF} and (b) μ_{VBF} signal strength measurements using the observed data set. The pulls of NPs are shown in black whilst the breakdown of each NP is shown in solid yellow.

7
Results

After performing the minimisation of the likelihood function for the inclusive and STXS measurements, the values and uncertainties of the POIs are extracted, as well as several important distributions of observables in the analysis regions, constituting the results of the measurements. The results of the inclusive measurements (the 2 POI and 1 POI fits) are presented in Section 7.1 whilst the results of the STXS measurement are presented in Section 7.2. The results presented in this chapter are *post-fit*, since they are extracted after the minimisation of the likelihood function. They represent the combined effect of systematic and statistical uncertainties from all regions in the likelihood function and the correlations between them, as well as background and signal processes normalised according to the likelihood minimisation.

7.1 Inclusive measurements

The NFs for background processes estimated wth CRs, used to scale the respective predictions of background processes in each SR, are listed in Table 7.1. The NFs are consistent with unity within their respective uncertainties. The values of the NFs obtained from the minimisation of the likelihood function may differ from the values of the NFs used in Section 4.6. This is because the data in the SRs, as well as the effect of statistical and systematic uncertainties and their correlations, are taken into account during the likelihood minimisation. Only the CR data, with no consideration of systematic uncertainty, is used to estimate the NFs in Section 4.6. The values of the NFs obtained using these two methods are consistent, however. The post-fit yields of the signal and background processes in each SR are shown in Table 7.2.

Distributions of m_{T} and the DNN output are also obtained. Figure 7.1 shows the post-fit m_{T} distributions for the ggF $N_{\mathrm{jet}} = 0$, ggF $N_{\mathrm{jet}} = 1$, and ggF-enriched $N_{\mathrm{jet}} \geq 2$ SRs, as well as for the combination of the event yields in the ggF SRs. The post-fit DNN output distribution in the VBF-enriched $N_{\mathrm{jet}} \geq 2$ SR is shown in Figure 7.2. In both Figures 7.1 and 7.2, one bottom panel shows the ratio of the data yields to the sum of the post-fit

Table 7.1: The post-fit NFs which scale the respective yields of the predicted background processes in the SRs. The uncertainties include the combined effect and correlations of systematic and statistical uncertainties.

Category	$qqWW$	$t\bar{t}/Wt$	Z/γ^*
ggF $N_{\text{jet}} = 0$	$1.02^{+0.07}_{-0.07}$	$0.93^{+0.22}_{-0.17}$	$0.96^{+0.07}_{-0.06}$
ggF $N_{\text{jet}} = 1$	$0.85^{+0.16}_{-0.15}$	$1.05^{+0.19}_{-0.16}$	$0.98^{+0.10}_{-0.09}$
ggF-enriched $N_{\text{jet}} \geq 2$	$0.81^{+0.34}_{-0.33}$	$0.96^{+0.23}_{-0.18}$	$0.98^{+0.18}_{-0.17}$
VBF-enriched $N_{\text{jet}} \geq 2$	–	$0.92^{+0.33}_{-0.21}$	$0.93^{+0.23}_{-0.19}$

Table 7.2: Post-fit event yields of data and MC predictions for signal and background processes in each SR. The yields in the last bin of the DNN output are presented to illustrate the high signal-to-background ratio in this bin. The uncertainties reflect the combined effect of all statistical and systematic uncertainties.

Process	$N_{\text{jet}} = 0$ ggF	$N_{\text{jet}} = 1$ ggF	$N_{\text{jet}} \geq 2$ ggF	$N_{\text{jet}} \geq 2$ VBF	
				Inclusive	DNN: $[0.87, 1.0]$
H_{ggF}	2100 ± 220	1100 ± 130	440 ± 90	209 ± 40	2.6 ± 0.9
H_{VBF}	23 ± 9	103 ± 30	46 ± 12	180 ± 40	28.8 ± 5.5
Other Higgs	40 ± 20	55 ± 28	55 ± 27	29 ± 15	0.04 ± 0.02
WW	9700 ± 350	3500 ± 410	1500 ± 470	2100 ± 340	4.6 ± 1.2
$t\bar{t}/Wt$	2200 ± 210	5300 ± 340	6100 ± 500	7600 ± 370	2.6 ± 0.8
Z/γ^*	140 ± 50	280 ± 40	930 ± 70	1300 ± 300	0.6 ± 0.1
Other $VV(V)$	1400 ± 130	840 ± 100	470 ± 90	380 ± 80	0.6 ± 0.1
Mis-Id	1200 ± 130	720 ± 90	470 ± 50	330 ± 40	1.7 ± 0.2
Total	$16\,770 \pm 130$	$11\,940 \pm 110$	$10\,030 \pm 100$	$12\,200 \pm 180$	42.0 ± 5.1
Observed	16 726	11 917	9 982	12 189	38

MC predictions. For the ggF distributions, an additional bottom panel compares the data yields after subtracting the post-fit MC predictions of background processes with the yields of the predicted signal distribution of a SM Higgs boson. For the VBF distribution, the same quantity is shown in the bottom panel but where the background-subtracted yields are divided by the total background yields, in order to illustrate the discrimination power of the DNN. In all cases, the post-fit signal rates and shapes of the m_{T} and DNN output distributions are in good agreement with the data.

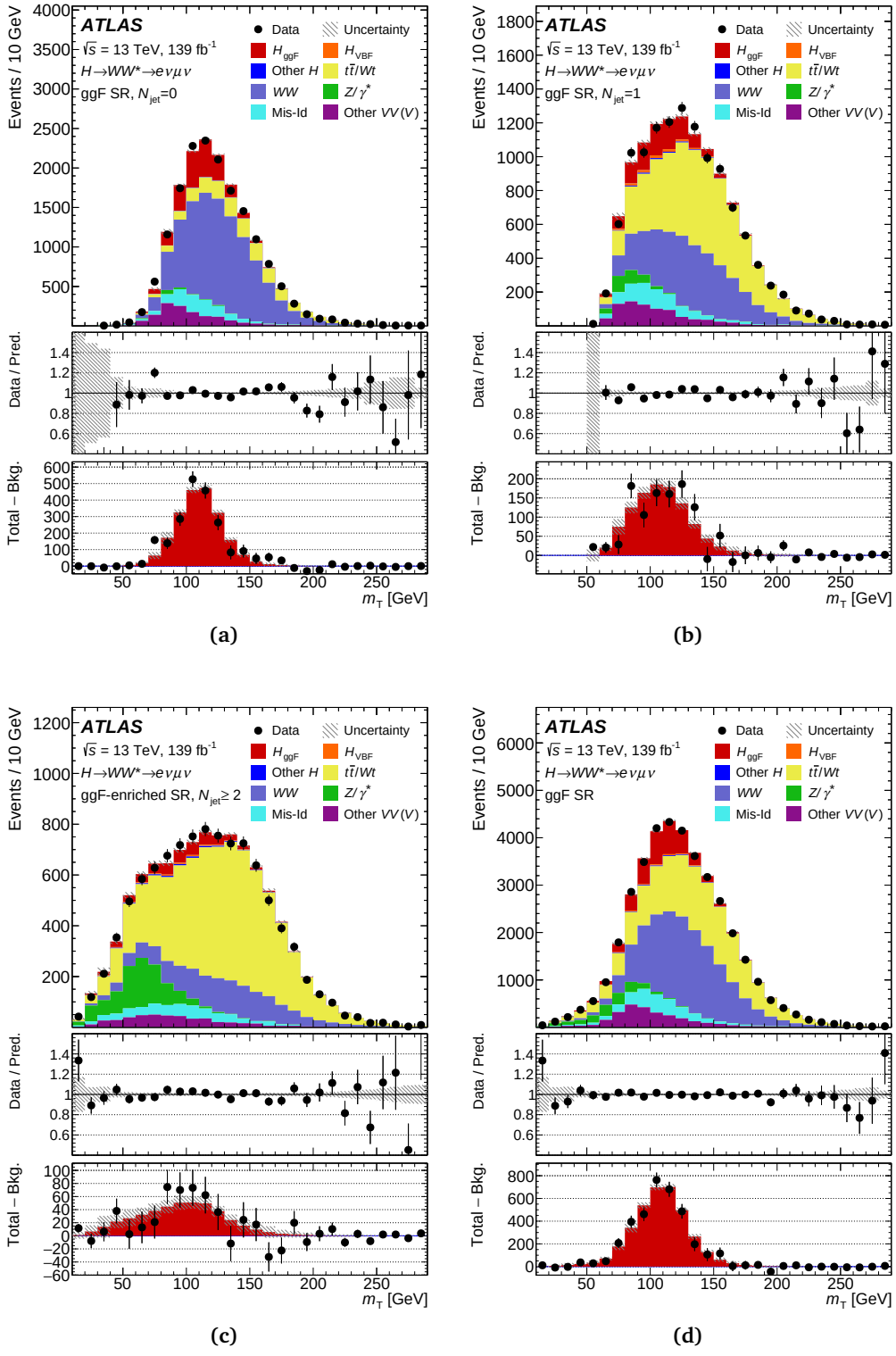

Figure 7.1: Post-fit distributions of m_{T} in the (a) ggF $N_{\mathrm{jet}} = 0$, (b) ggF $N_{\mathrm{jet}} = 1$, (c) ggF-enriched $N_{\mathrm{jet}} \geq 2$, and (d) combined ggF regions. The final bin of the distributions includes events beyond the range of the plotted distributions. The error band shows the total post-fit uncertainty. The middle panel displays the ratio of the data yields to the sum of the post-fit signal and background yields. The bottom panel displays the difference between the data yields (with post-fit background yields subtracted) compared to the measured Higgs boson signal yields.

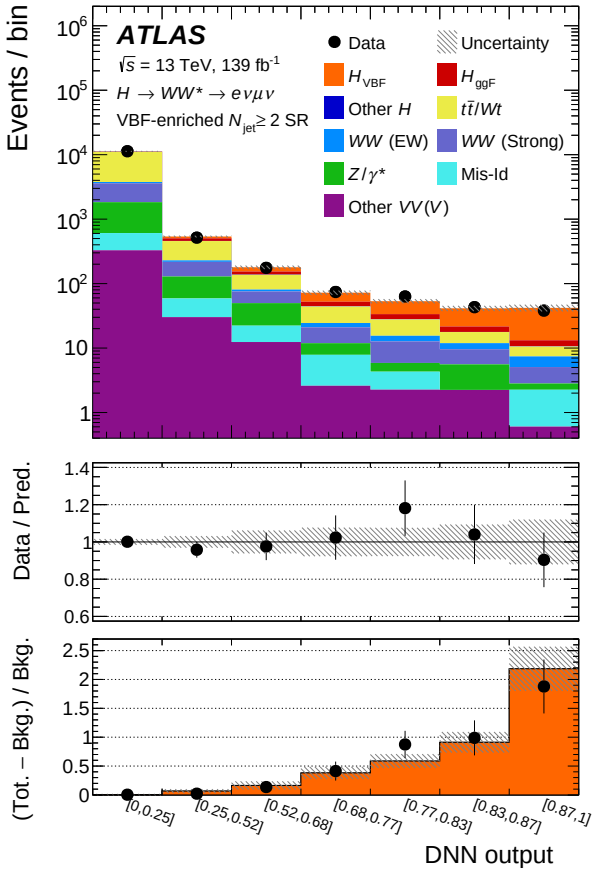

Figure 7.2: Post-fit distribution of the DNN output in the VBF-enriched $N_{\text{jet}} \geq 2$ SR. The error band shows the total post-fit uncertainty. The middle panel shows the ratio of the data yields to the sum of the post-fit signal and background yields. The bottom panel displays the Higgs boson signal-to-background ratio.

For the simultaneous measurement of the ggF and VBF production modes of the Higgs boson (the 2 POI fit), the POIs are μ_{ggF} and μ_{VBF}. The expectation of the signal strengths using the Asimov data set is determined to be

$$\begin{aligned}\mu_{\mathrm{ggF}} &= 1.00\ ^{+0.15}_{-0.14} \\ &= 1.00\ ^{+0.06}_{-0.06}\ (\mathrm{stat.})\ ^{+0.08}_{-0.07}\ (\mathrm{exp.})\ ^{+0.08}_{-0.06}\ (\mathrm{sig.})\ ^{+0.10}_{-0.09}\ (\mathrm{bkg.}) \qquad (7.1)\\ \mu_{\mathrm{VBF}} &= 1.00\ ^{+0.24}_{-0.21} \\ &= 1.00\ ^{+0.14}_{-0.14}\ (\mathrm{stat.})\ ^{+0.09}_{-0.08}\ (\mathrm{exp.})\ ^{+0.15}_{-0.11}\ (\mathrm{sig.})\ ^{+0.10}_{-0.09}\ (\mathrm{bkg.}), \qquad (7.2)\end{aligned}$$

for the ggF and VBF production modes, respectively. The measured values of the signal strengths using the full Run 2 data set are found to be

$$\begin{aligned}\mu_{\mathrm{ggF}} &= 1.15\ ^{+0.16}_{-0.15} \\ &= 1.15 \pm 0.06\ (\mathrm{stat.})\ ^{+0.09}_{-0.08}\ (\mathrm{exp.})\ ^{+0.09}_{-0.07}\ (\mathrm{sig.})\ ^{+0.08}_{-0.07}\ (\mathrm{bkg.}) \qquad (7.3)\\ \mu_{\mathrm{VBF}} &= 0.92\ ^{+0.24}_{-0.20} \\ &= 0.92\ ^{+0.14}_{-0.13}\ (\mathrm{stat.})\ ^{+0.08}_{-0.07}\ (\mathrm{exp.})\ ^{+0.15}_{-0.11}\ (\mathrm{sig.})\ ^{+0.09}_{-0.08}\ (\mathrm{bkg.}), \qquad (7.4)\end{aligned}$$

for the ggF and VBF production modes, respectively. In both measurements, the total uncertainty is decomposed into several groups of uncertainty sources using the breakdown method, and includes statistical uncertainty (*stat.*), experimental systematic uncertainty (*exp.*), systematic uncertainty due to the modelling of the Higgs boson signal process (*sig.*), and the systematic uncertainty due to the modelling of the background processes (*bkg.*). Both measurements are consistent with the expectation of an SM Higgs boson within the uncertainties.

The statistical significance of the measurements is estimated by performing separate fits using subsets of the different analysis regions listed in Table 6.1, as described in Section 6.3.5. The statistical significance is obtained by considering the null hypothesis that only background processes are expected i.e. that zero SM Higgs boson signal events are expected. The statistical significances of measurements with different analysis regions, corresponding to different production modes and jet multiplicity bins, are shown in Table 7.3. The statistical significances from previous ATLAS measurements [5, 7] using the same approach are also included to serve as a comparison. Improvements in the statistical significances obtained in this thesis differ with respect to the previous measurements shown for several reasons. First, the increase in the size of the data set used in this thesis decreases the statistical uncertainty in each measurement. Second, increased understanding and improvements in the reconstruction and identification of physics objects and the use of state-of-the-art MC predictions involving one or several higher order terms in the perturbative expansion reduce the systematic uncertainty inherent in each measurement. Third, advanced analysis techniques involving machine learning aid in the

classification of signal and background events, further reducing the systematic uncertainty in the VBF-enriched $N_{\text{jet}} \geq 2$ measurement.

The analysis strategy of the ggF $N_{\text{jet}} \leq 1$ regions is largely similar to the analysis with 36 fb^{-1} of Run 2 data, therefore the increase in the statistical significance in the results in this thesis are primarily a result of the first and second reasons described above. For the ggF-enriched $N_{\text{jet}} \geq 2$ measurement, the increase in the statistical significance is also a result of the first and second reasons. Events of this type of topology were last included in a measurement using $\sim$25 fb^{-1} of data collected at $\sqrt{s} = 7$–8 TeV. The event selection defining SRs and CRs in the ggF-enriched $N_{\text{jet}} \geq 2$ category in this measurement is similar to the previous measurement. However, the statistical significance is not larger in this analysis because the increase in the inclusive top quark production cross section from 7 to 13 TeV is larger than the increase in the inclusive Higgs boson production cross section by about a factor of 1.5 (Figure 4.1). Future increases to the statistical significance of the ggF-enriched $N_{\text{jet}} \geq 2$ measurement would be a result of adopting a different analysis strategy, for example through finding a more efficient classification of ggF-enriched $N_{\text{jet}} \geq 2$ and VBF-enriched $N_{\text{jet}} \geq 2$ events than through the CJV or OLV, as well as more effectively rejecting top quark background events. The improvement in the statistical significance of the VBF-enriched $N_{\text{jet}} \geq 2$ measurement is also affected by the first and second reasons, but is primarily driven by the third reason: the use of the DNN and its number and type of input variables significantly improves the classification of events containing VBF production of a Higgs boson. The combined effect of these points lead to the first observation of VBF production in the $H \to WW^*$ decay mode using the ATLAS detector and the re-observation of ggF production in the $H \to WW^*$ decay mode well beyond the threshold of 5σ.

Measurements of the Higgs boson using the WW^* decay mode are also performed by the CMS Collaboration using the full Run 2 data set, corresponding to an integrated luminosity of 138 fb^{-1} as recorded by the CMS detector [199]. The analysis strategy of the CMS measurement is more comprehensive than the measurements presented in this thesis using ATLAS data since event categories with same-flavour leptons are included and a simultaneous measurement of the WH and ZH production cross sections is performed (in addition to ggF and VBF) using dedicated event categories targeting these production modes. Nevertheless, the signal strengths of ggF and VBF production are $0.92^{+0.11}_{-0.10}$ and $0.71^{+0.28}_{-0.25}$, respectively, demonstrating a similar precision with the results in this thesis. The observed (expected) signal significances are 10.5 $(11.8)\sigma$ and 3.15 $(4.74)\sigma$ for the ggF and VBF measurement, respectively. The measurement of ggF production by CMS is likely more precise due to the inclusion of same-flavour leptons and a wider use of machine learning techniques in the signal classification. The measurement of VBF production

Table 7.3: The expected and observed values of significance obtained from separate fits using three sets of regions in this current analysis, as well as the same values obtained with the most recent previous measurements of these regions. The SM VBF process is assumed for the calculation of significance for the ggF regions, and vice versa. The calculation of significance is carried out for two separate regions targeting ggF production, $N_{\text{jet}} \leq 1$ and $N_{\text{jet}} \geq 2$.

	Now		Previous measurements		
Regions	Expected	Observed	Expected	Observed	Luminosity ($\mathcal{L}$) and energy ($\sqrt{s}$)
ggF $N_{\text{jet}} \leq 1$	8.5	9.4	5.3	6.0	$\mathcal{L} = 36.1$ fb^{-1}, $\sqrt{s} = 13$ TeV [7]
ggF-enriched $N_{\text{jet}} \geq 2$	1.6	2.2	1.2	1.4	$\mathcal{L} = 24.8$ fb^{-1}, $\sqrt{s} = 7$–8 TeV [5]
VBF-enriched $N_{\text{jet}} \geq 2$	5.8	6.2	2.6	1.8	$\mathcal{L} = 36.1$ fb^{-1}, $\sqrt{s} = 13$ TeV [7]

is less precise than the measurement reported in this thesis which is likely due to the performance of the DNN used in this analysis.

The simultaneous measurement of the cross section of ggF and VBF production of a Higgs boson proceeds similarly to the signal strength measurement, except that the systematic uncertainty due to the modelling of the signal processes only accounts for the change in acceptance of the event selection requirements. Each $\sigma_i \cdot \mathcal{B}_{H\to WW^*}$ can be obtained straightforwardly by multiplying the measured σ-style signal-strengths, $\hat{\mu}$, by the SM prediction, $(\sigma_i \cdot \mathcal{B}_{H\to WW^*})_{\text{SM}}$. The ggF and VBF production cross sections multiplied by the $H\to WW^*$ branching ratio, $\sigma_{\text{ggF}} \cdot \mathcal{B}_{H\to WW^*}$ and $\sigma_{\text{VBF}} \cdot \mathcal{B}_{H\to WW^*}$, are measured to be

$$\begin{aligned}\sigma_{\text{ggF}} \cdot \mathcal{B}_{H\to WW^*} &= 12.0 \pm 1.4 \text{ pb} \\ &= 12.0 \pm 0.6 \text{ (stat.)}^{+0.9}_{-0.8} \text{ (exp.)} \, ^{+0.6}_{-0.5} \text{ (sig.)} \pm 0.8 \text{ (bkg.) pb} \qquad (7.5) \\ \sigma_{\text{VBF}} \cdot \mathcal{B}_{H\to WW^*} &= 0.75 \, ^{+0.19}_{-0.16} \text{ pb} \\ &= 0.75 \pm 0.11 \text{ (stat.)} \, ^{+0.07}_{-0.06} \text{ (exp.)} \, ^{+0.12}_{-0.08} \text{ (sig.)} \, ^{+0.07}_{-0.06} \text{ (bkg.) pb}, \qquad (7.6)\end{aligned}$$

where the total uncertainty in the cross section measurements is similarly decomposed into several groups of systematic uncertainty sources using the breakdown method. The cross section measurements are consistent with the SM predictions of 10.4 ± 0.5 pb and 0.81 ± 0.02 pb for the ggF and VBF production modes [53], respectively.

The two-dimensional contours depicting the 68% and 95% confidence levels of $\sigma_{\text{ggF}} \cdot \mathcal{B}_{H\to WW^*}$ and $\sigma_{\text{VBF}} \cdot \mathcal{B}_{H\to WW^*}$, as well as the obtained values, are shown in Figure 7.3. The results indicate good agreement with the SM prediction, and that there is a small anti-correlation of 5% between the measured cross sections.

A combined cross section measurement is performed (the 1 POI fit) for the sum of the ggF

and VBF production cross section, $\sigma_{\text{ggF+VBF}} \cdot \mathcal{B}_{H\to WW^*}$, which is measured to be

$$\begin{aligned}\sigma_{\text{ggF+VBF}} \cdot \mathcal{B}_{H\to WW^*} &= 12.3 \pm 1.3 \text{ pb} \\ &= 12.3 \pm 0.6 \text{ (stat.)} \, ^{+0.8}_{-0.7} \text{ (exp.)} \, \pm 0.6 \text{ (sig.)} \, \pm 0.7 \text{ (bkg.) pb.} \quad (7.7)\end{aligned}$$

The combined cross section measurement is in agreement with the SM prediction of 11.3 ± 0.5 pb [53]. Figure 7.4 shows the obtained ggF, VBF, and combined production cross sections and their uncertainties, multiplied by the $H\to WW^*$ branching ratio and normalised to the corresponding SM prediction. The p-value for the 2 POI and 1 POI measurements are 53% and 45%, respectively, demonstrating good agreement with the hypothesis of a Higgs boson with SM interactions.

Lastly, the total uncertainty in each measurement of $\sigma_{\text{ggF+VBF}} \cdot \mathcal{B}_{H\to WW^*}$, $\sigma_{\text{ggF}} \cdot \mathcal{B}_{H\to WW^*}$, and $\sigma_{\text{VBF}} \cdot \mathcal{B}_{H\to WW^*}$ is decomposed into several groups comprising common sources of uncertainty. The relative impact of these groups of uncertainty are shown in Table 7.4. It is observed that all three measurements are limited by systematic uncertainties. More specifically, the systematic uncertainty originating from the modelling of signal and background processes in MC simulation (theoretical uncertainty) is larger than the experimental systematic uncertainty in all measurements. Decomposing the theoretical uncertainty into several contributions categorised by process, it can be seen that the modelling of the signal process is the largest contribution in each measurement. In the ggF measurement, the QCD scale uncertainty is the single source of uncertainty with the largest effect and is a result of the categorisation of event yields by jet multiplicity. The modelling of the UEPS in the signal MC prediction is the second single source of uncertainty with the largest effect. In the VBF measurement, the modelling of the UEPS and the matching of the matrix element calculation to the UEPS are the two single sources of uncertainty with the largest effect. Their effect is large due to the change in acceptance induced by the CJV selection requirement as well as the change in shape of the DNN output distribution (kinematic observables such as m_{jj}, Δy_{jj}, and $p_{\text{T}}^{\text{tot}}$ are sensitive to the UEPS modelling, which are used as input variables to the DNN). Other theoretical uncertainties which have a large contribution to the measurements include the modelling of WW and top quark background processes. For the WW background, it is the modelling of the m_{T} distribution in the ggF analysis regions which limits the ggF measurement. For the top quark background, the matching of the $t\bar{t}$ matrix element calculation to the UEPS is a large contribution due to the contamination of $t\bar{t}$ background events populating the ggF-enriched $N_{\text{jet}} \geq 2$ and VBF-enriched $N_{\text{jet}} \geq 2$ regions.

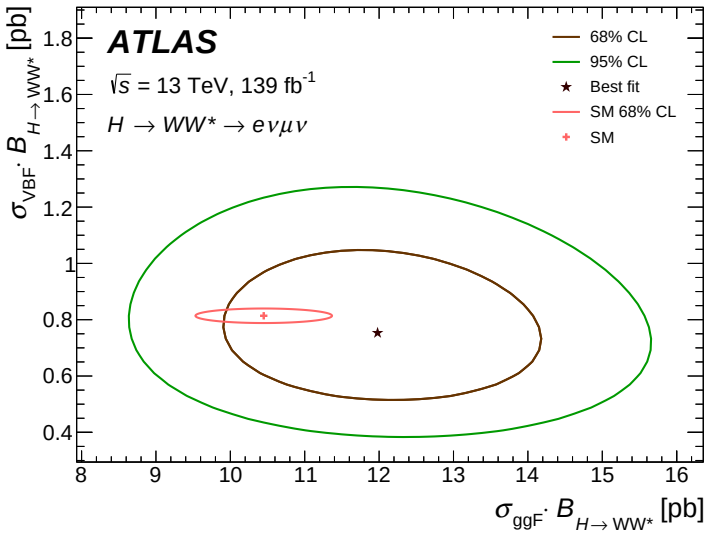

Figure 7.3: Two-dimensional likelihood contours of the 68% and 95% confidence levels for the measurements of $\sigma_{\mathrm{ggF}} \cdot \mathcal{B}_{H\to WW^*}$ and $\sigma_{\mathrm{VBF}} \cdot \mathcal{B}_{H\to WW^*}$. The 68% confidence level for $(\sigma_{\mathrm{ggF}} \cdot \mathcal{B}_{H\to WW^*})_{\mathrm{SM}}$ and $(\sigma_{\mathrm{VBF}} \cdot \mathcal{B}_{H\to WW^*})_{\mathrm{SM}}$ [53] is shown by the red ellipse.

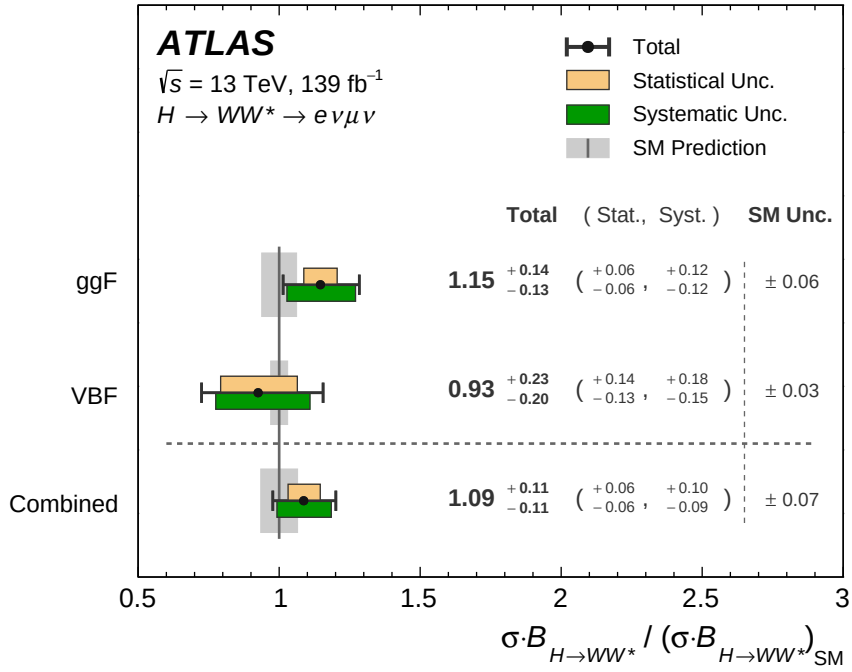

Figure 7.4: Measurements of $\sigma_i \cdot \mathcal{B}_{H\to WW^*}$, with $i = \{\mathrm{ggF},\ \mathrm{VBF},\ \mathrm{ggF}+\mathrm{VBF}\ (\mathrm{Combined})\}$, normalised to the corresponding SM prediction. The total uncertainty is shown, as well as the decomposition of the uncertainty into a statistical and systematic component, derived using the breakdown method. The grey bands highlight the theoretical uncertainty in the respective SM predictions.

Table 7.4: Decomposition of the total uncertainty in the measurements of $\sigma_{\text{ggF+VBF}} \cdot \mathcal{B}_{H\to WW^*}$, $\sigma_{\text{ggF}} \cdot \mathcal{B}_{H\to WW^*}$, and $\sigma_{\text{VBF}} \cdot \mathcal{B}_{H\to WW^*}$ into groups of uncertainty with common sources, estimated using the breakdown method and divided by the measured cross sections. The quadrature sum of the groups of uncertainty may differ from the total uncertainty due to the effect of correlations between uncertainties and parameters in the fit.

Source	$\frac{\Delta\sigma_{\text{ggF+VBF}}\cdot\mathcal{B}_{H\to WW^*}}{\sigma_{\text{ggF+VBF}}\cdot\mathcal{B}_{H\to WW^*}}$ [%]	$\frac{\Delta\sigma_{\text{ggF}}\cdot\mathcal{B}_{H\to WW^*}}{\sigma_{\text{ggF}}\cdot\mathcal{B}_{H\to WW^*}}$ [%]	$\frac{\Delta\sigma_{\text{VBF}}\cdot\mathcal{B}_{H\to WW^*}}{\sigma_{\text{VBF}}\cdot\mathcal{B}_{H\to WW^*}}$ [%]
Data statistical uncertainties	4.6	5.1	15
Total systematic uncertainties	9.5	11	18
MC statistical uncertainties	3.0	3.8	4.9
Experimental uncertainties	5.2	6.3	6.7
Flavour Tagging	2.3	2.7	1.0
Jet energy scale	0.9	1.1	3.7
Jet energy resolution	2.0	2.4	2.1
$E_{\text{T}}^{\text{miss}}$	0.7	2.2	4.9
Muons	1.8	2.1	0.8
Electrons	1.3	1.6	0.4
Fake factors	2.1	2.4	0.8
Pile-up	2.4	2.5	1.3
Luminosity	2.1	2.0	2.2
Theoretical uncertainties	6.8	7.8	16
ggF	3.8	4.3	4.6
VBF	3.2	0.7	12
WW	3.5	4.2	5.5
Top	2.9	3.8	6.4
Z/γ^*	1.8	2.3	1.0
Other $VV(V)$	2.3	2.9	1.5
Other Higgs	0.9	0.4	0.4
Background normalisations	3.6	4.5	4.9
$qqWW$	2.2	2.8	0.6
Top quark	1.9	2.3	3.4
Z/γ^*	2.7	3.1	3.4
TOTAL	10	12	23

7.2 STXS measurement

In the STXS measurement, a total of 11 cross sections are measured simultaneously. The cross section of each measured STXS bin, divided by the corresponding SM prediction, is shown in Figure 7.5. The total uncertainty on each cross section, and its decomposition into a statistical and systematic component using the breakdown method, is displayed. The absolute values of the measured cross sections including a finer decomposition of the total uncertainty are shown in Table 7.5. A p-value of 53% is obtained for the STXS measurement where the null hypothesis assumes SM Higgs boson production and decay, thus demonstrating good agreement with the SM.

The measured contribution of several sources of uncertainty to the total uncertainty of each measured cross section is illustrated in Figure 7.6. The contributions are broken down into a statistical uncertainty, theoretical uncertainty on the total background,

theoretical uncertainty on the Higgs boson signal processes, and experimental uncertainty. The theoretical uncertainty on the SM prediction is also shown. These contributions are divided by the predicted SM cross section for each STXS bin. It is apparent from Figures 7.5 and 7.6 that the uncertainties on the EW qqH bins and the ggH bins with higher p_{T}^{H} are dominantly due to the limited size of the available data set. Otherwise, the precision on the ggH bins with low p_{T}^{H} is largely limited by the theoretical uncertainty on the total background, as well as the experimental uncertainty.

Finally, the measured correlations between the parameters in the likelihood function representing the normalisation of the yield of each STXS bin are shown in Figure 7.7, of which the largest anti-correlation of -32% is between the parameters representing the EW qqH-2*j*, high p_{T}^{H} and ggH, high p_{T}^{H} yields. The anti-correlation is due to the corresponding STXS SRs containing a sum of events from these particle-level STXS bins.

The full Run 2 CMS measurement of the Higgs boson using the WW^{*} decay mode [199] also reports measurements in the STXS framework. Although the CMS measurement includes several dedicated VH bins, the number of measured ggH and EW qqH bins is less than the number measured in this thesis. The precision of the VBF measurement in this thesis and the performance of the DNN allows this analysis to measure more bins targeting EW qqH production, especially at high m_{jj}. However, the CMS measurement is able to probe the regions of high p_{T}^{H} in ggH production more so than the measurement in this thesis, which is likely due to the inclusion of event categories with same-flavour leptons.

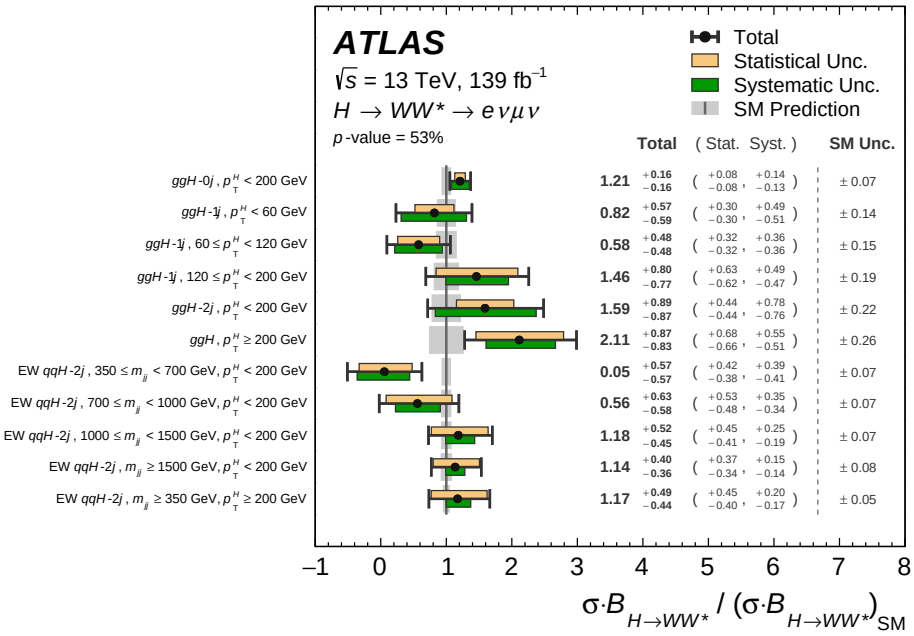

Figure 7.5: Measured cross sections and uncertainties of each STXS bin, divided by the respective SM prediction. The total uncertainty is decomposed into systematic uncertainty and statistical uncertainty components, using the breakdown method. The theoretical uncertainty on the SM prediction for each STXS bin is shown in grey.

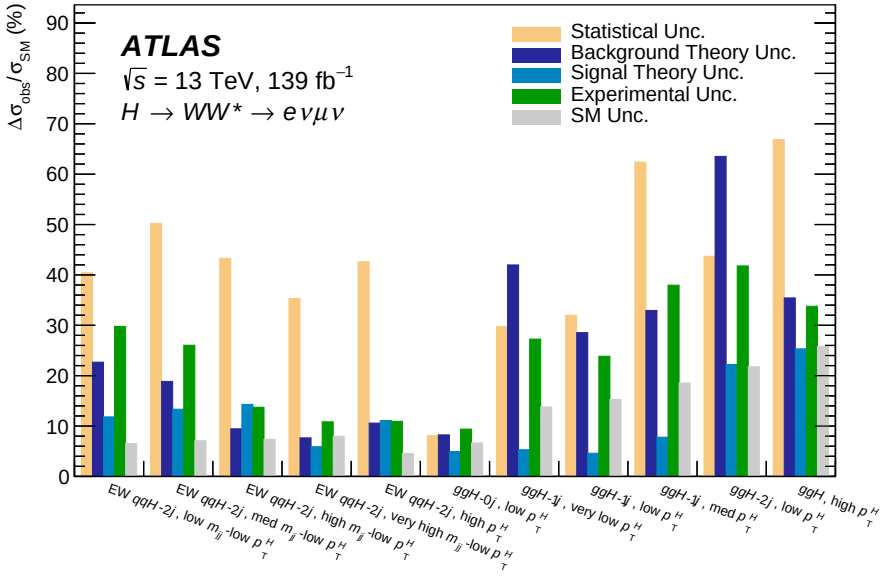

Figure 7.6: Decomposition of the total uncertainty for the measured cross section in each STXS bin into statistical uncertainty, theoretical uncertainty on the total background, theoretical uncertainty on the signal processes, and experimental uncertainty, using the breakdown method. The contribution of each group of uncertainties is divided by the predicted SM cross section for each STXS bin. The theoretical uncertainty for each STXS bin is shown in grey.

Table 7.5: Absolute measured cross section values and the associated uncertainties in each STXS bin. The decomposition of the total uncertainty into several groups of uncertainty is made using the breakdown method.

STXS bin ($\sigma_i \times \mathcal{B}_{H\to WW^*}$)	Value	Uncertainty [fb]					SM prediction
	[fb]	Total	Stat.	Exp.	Sig.	Bkg.	[fb]
ggH-0*j*, low p_{T}^H $p_{\mathrm{T}}^H < 200$ GeV	7100	$^{+950}_{-910}$	$^{+480}_{-470}$	$^{+570}_{-530}$	$^{+320}_{-260}$	$^{+490}_{-480}$	5870 ± 390
ggH-1*j*, very low p_{T}^H $p_{\mathrm{T}}^H < 60$ GeV	1140	$^{+800}_{-820}$	$^{+420}_{-410}$	$^{+380}_{-380}$	$^{+80}_{-70}$	$^{+570}_{-600}$	1400 ± 190
ggH-1*j*, low p_{T}^H $60 \leq p_{\mathrm{T}}^H < 120$ GeV	540	$^{+470}_{-470}$	$^{+310}_{-310}$	$^{+230}_{-230}$	$^{+42}_{-47}$	$^{+270}_{-280}$	970 ± 150
ggH-1*j*, med p_{T}^H $120 \leq p_{\mathrm{T}}^H < 200$ GeV	230	$^{+130}_{-120}$	$^{+100}_{-100}$	$^{+60}_{-60}$	$^{+10}_{-10}$	$^{+50}_{-50}$	160 ± 30
ggH-2*j*, low p_{T}^H $p_{\mathrm{T}}^H < 200$ GeV	1610	$^{+900}_{-890}$	$^{+440}_{-440}$	$^{+430}_{-420}$	$^{+300}_{-150}$	$^{+640}_{-650}$	1010 ± 220
ggH, high p_{T}^H $p_{\mathrm{T}}^H > 200$ GeV	260	$^{+100}_{-100}$	$^{+80}_{-80}$	$^{+40}_{-40}$	$^{+40}_{-20}$	$^{+40}_{-40}$	122 ± 31
EW qqH-2*j*, low m_{jj}-low p_{T}^H $350 \leq m_{jj} < 700$ GeV, $p_{\mathrm{T}}^H < 200$ GeV	6	$^{+63}_{-62}$	$^{+46}_{-42}$	$^{+31}_{-34}$	$^{+11}_{-14}$	$^{+24}_{-26}$	109 ± 7
EW qqH-2*j*, med m_{jj}-low p_{T}^H $700 \leq m_{jj} < 1000$ GeV, $p_{\mathrm{T}}^H < 200$ GeV	31	$^{+35}_{-33}$	$^{+30}_{-27}$	$^{+15}_{-14}$	$^{+8}_{-7}$	$^{+11}_{-10}$	56 ± 4
EW qqH-2*j*, high m_{jj}-low p_{T}^H $1000 \leq m_{jj} < 1500$ GeV, $p_{\mathrm{T}}^H < 200$ GeV	60	$^{+26}_{-23}$	$^{+23}_{-21}$	$^{+7}_{-7}$	$^{+9}_{-5}$	$^{+5}_{-5}$	51 ± 4
EW qqH-2*j*, very high m_{jj}-low p_{T}^H $m_{jj} > 1500$ GeV, $p_{\mathrm{T}}^H < 200$ GeV	57	$^{+20}_{-18}$	$^{+18}_{-17}$	$^{+5}_{-5}$	$^{+3}_{-3}$	$^{+4}_{-4}$	50 ± 4
EW qqH-2*j*, high p_{T}^H $m_{jj} > 350$ GeV, $p_{\mathrm{T}}^H > 200$ GeV	37	$^{+16}_{-14}$	$^{+14}_{-13}$	$^{+4}_{-3}$	$^{+4}_{-3}$	$^{+3}_{-3}$	32 ± 1

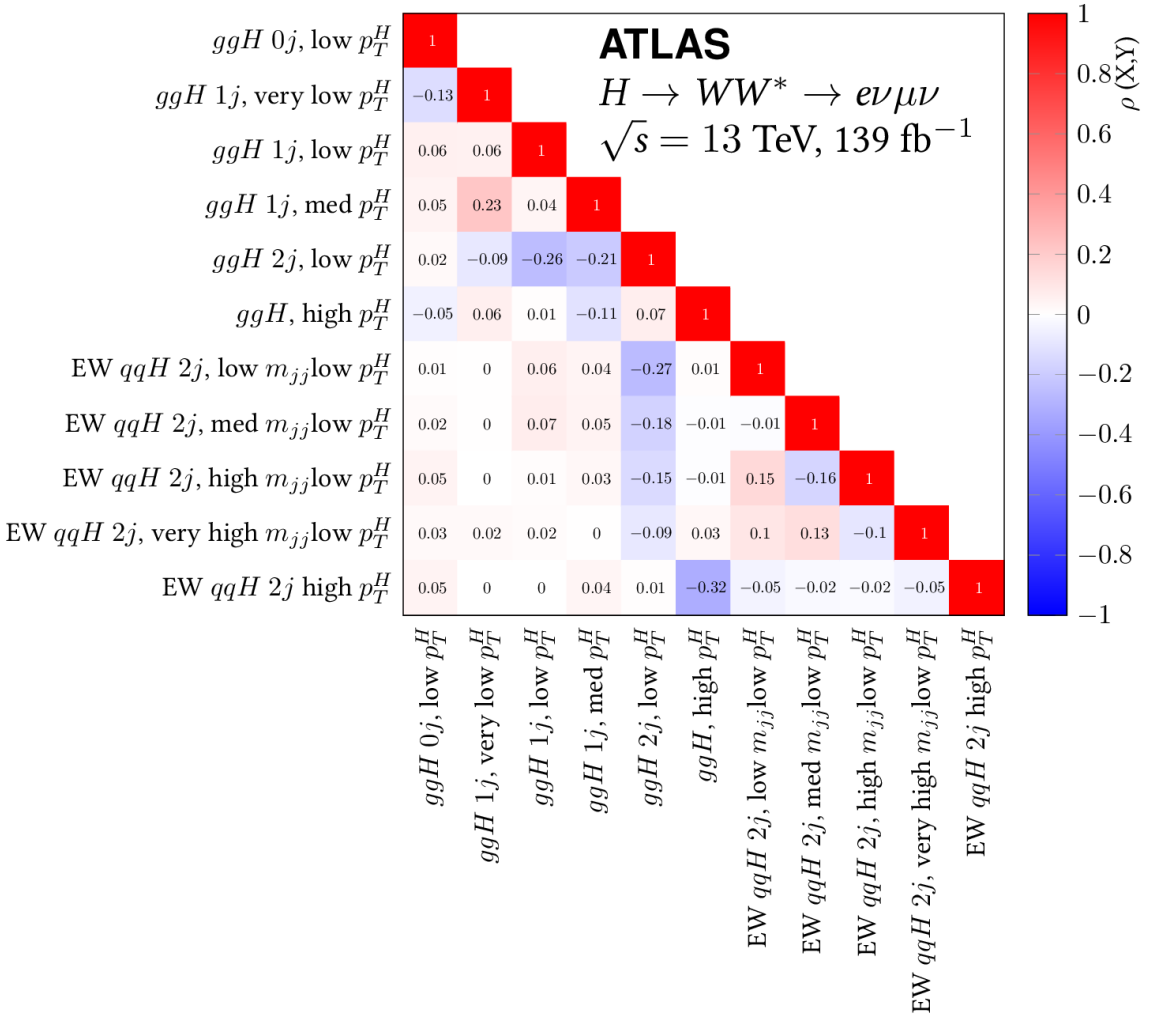

Figure 7.7: Correlation matrix of the parameters in the likelihood function representing the normalisation of the signal yield of each STXS bin.

8
Improvements and prospects

The measurements presented in this thesis constitute the most precise measurements of ggF and VBF production of a Higgs boson in the $H \to WW^*$ decay mode performed with the ATLAS detector to date. However, several improvements could be incorporated into future measurements to further improve the precision of the measurements, particularly for the STXS measurement. First, in Section 8.1, a study is described which aims to reduce the large top quark background in the ggF-enriched $N_{\text{jet}} \geq 2$ SR by improving the rejection of b-jets. Second, in Section 8.2, a preliminary study is outlined which could lead to improvements in the statistical uncertainty of the STXS bins, particularly the ggH, high p_{T}^{H} cross section, by including leptons of the same flavour in the measurement. Lastly, prospects for future measurements of the $H \to WW^*$ decay mode are suggested in Section 8.3.

8.1 Optimising the b-jet tagging efficiency

Top quark background events comprise $\approx 62\%$ of the total event yield in the ggF-enriched $N_{\text{jet}} \geq 2$ SR, constituting the largest background in this region and resulting in the largest effect on the uncertainty of the signal strength in this region from top quark theoretical uncertainties. Following the nominal analysis strategy, a fit is performed using the ggF-enriched $N_{\text{jet}} \geq 2$ SRs partitioned at $m_{\ell\ell} = 30$ GeV and the ggF-enriched $N_{\text{jet}} \geq 2$ CRs for $qqWW$, top quark, and Z/γ^* background processes. A signal strength, μ, is obtained and is found to be

$$\begin{aligned} \mu_{\text{obs.}} &= 1.22\ ^{+0.60}_{-0.54} \\ &= 1.22\ ^{+0.26}_{-0.26}\ (\text{stat.})\ ^{+0.26}_{-0.20}\ (\text{exp.})\ ^{+0.28}_{-0.11}\ (\text{sig.})\ ^{+0.39}_{-0.38}\ (\text{bkg.}), \end{aligned} \tag{8.1}$$

whilst the expected signal strength using an Asimov data set is found to be

$$\begin{aligned} \mu_{\text{exp.}} &= 1.00\ ^{+0.64}_{-0.62} \\ &= 1.00\ ^{+0.27}_{-0.27}\ (\text{stat.})\ ^{+0.25}_{-0.23}\ (\text{exp.})\ ^{+0.27}_{-0.06}\ (\text{sig.})\ ^{+0.46}_{-0.49}\ (\text{bkg.}). \end{aligned} \tag{8.2}$$

The modelling of the background predictions constitutes the largest source of uncertainty and is dominated by the modelling of the $t\bar{t}$ background process. Nominally, the rejection

of top quark background in the ggF-enriched $N_{\text{jet}} \geq 2$ SR is achieved by requiring $N_{b\text{-jet}} = 0$. This quantity is an event-level observable, defined as the number of jets in an event that are identfied as a b-jet by the DL1r b-tagging algorithm, using a fixed-cut WP with an efficiency of 85% for identifying b-jets evaluated with simulated $t\bar{t}$ events.

A new observable is defined, $\max(\text{DL1r})$, which determines the maximum DL1r score out of all jets in an event, and is defined by

$$\max(\text{DL1r}) = \max_{j \in \text{jets}} \left[\ln \left(\frac{p_b}{f_c p_c + (1 - f_c) p_l} \right) \right], \tag{8.3}$$

where the quantities p_b, p_c, p_l, and f_c, as well as the formula which is maximised, are the same as those in Eq. 3.10. This observable is continuously distributed as opposed to $N_{b\text{-jet}}$ and is shown in Figure 8.1 after making the initial preselection requirements and a requirement of at least two reconstructed jets with $p_{\text{T}} > 30$ GeV. Larger values of $\max(\text{DL1r})$ indicate events that are likely to contain true b-jets, whilst smaller values indicate events that are likely to not contain any true b-jets. Making a selection requirement on the distribution of this observable therefore functions similarly to the $N_{b\text{-jet}} = 0$ selection requirement, such that the event yield of Higgs boson signal (with no true b-jets) is enhanced with respect to the top quark background (with exactly two true b-jets). The bottom panel of Figure 8.1 shows the integrated ratio of Higgs boson signal events to the square root of total background events, indicating the location where the significance of the Higgs boson signal yield is largest with respect to the background yields. In this case, making a selection requirement of $\max(\text{DL1r}) < -0.73$ would result in the largest Higgs boson signal significance. A comparison of the event yields of the Higgs boson signal and background processes for the nominal selection requirement ($N_{b\text{-jet}} = 0$) and using a selection requirement of $\max(\text{DL1r}) < -0.73$ is shown in Table 8.1. This shows that the Higgs boson signal yield reduces by $\sim$19% when using a requirement on $\max(\text{DL1r})$, but that there is a larger reduction of $\sim$43% and $\sim$35% for the top quark and total background yields.

A fit is performed, similarly to above, considering events selected (and systematic uncertainties that are re-derived) using a requirement of $\max(\text{DL1r}) < -0.73$ instead of $N_{b\text{-jet}} = 0$ in all SRs and CRs. The fit is performed using an Asimov data set. The expected signal strength obtained using this setup is

$$\begin{aligned} \mu_{\max(\text{DL1r})} &= 1.00\ ^{+0.59}_{-0.55} \\ &= 1.00\ ^{+0.27}_{-0.27}\ (\text{stat.})\ ^{+0.25}_{-0.21}\ (\text{exp.})\ ^{+0.27}_{-0.08}\ (\text{sig.})\ ^{+0.40}_{-0.40}\ (\text{bkg.}), \end{aligned} \tag{8.4}$$

which is to be compared to the expected signal strength using the nominal ggF-enriched $N_{\text{jet}} \geq 2$ selection requirements in Eq. 8.2. The uncertainty in the expected signal strengths

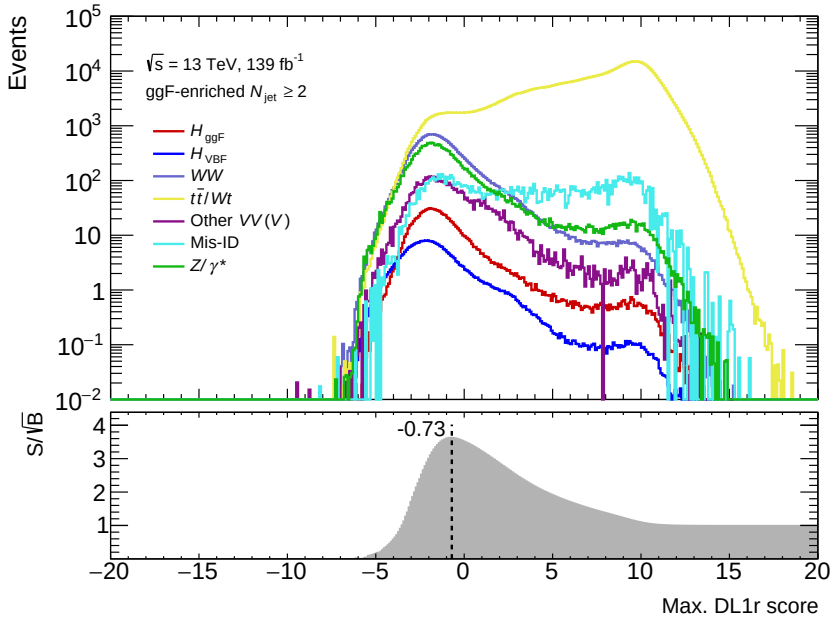

Figure 8.1: The distribution of the $\max(\mathrm{DL1r})$ observable for the signal and background processes. The distribution is shown after the preselection requirements listed in Table 4.3 and requiring at least two reconstructed jets with $p_{\mathrm{T}} > 30$ GeV. The signal and background processes are normalised according to the theoretical predictions from the MC simulation. The bottom panel shows the integrated ratio of the signal yield to the square root of the total background yield, $S/\sqrt{B}$. The value of $\max(\mathrm{DL1r})$ which results in the largest value of the integrated $S/\sqrt{B}$ is indicated.

is decomposed further into finer groups of several uncertainty sources, which are compared in Table 8.2. The expected total uncertainty is reduced from $\sim$63% to $\sim$57%. The effect on the signal strength uncertainty due to the uncertainty associated with the modelling of the $t\bar{t}$ process is reduced from $\sim$38% to $\sim$28%. The effect of other sources of systematic uncertainty do not change appreciably between the two measurements.

Whilst the uncertainty on the ggF-enriched $N_{\mathrm{jet}} \geq 2$ signal strength is still large and dominated by the theoretical modelling uncertainty, this study shows that optimising the identification of b-jets in this topology is useful to improve the precision of the signal strength measurement. For a more accurate approach, a calibration would need to performed in order to be able to use a continuously distributed b-tagging observable. This method would also likely be advantageous for the STXS measurement, where only two ggH STXS bins are presently measured with $N_{\mathrm{jet}} \geq 2$. In conjunction with other advanced techniques, such as multivariate analysis, the precision of the measurements could be significantly improved. This would mean that more granular STXS measurements could be performed, thus probing the Higgs boson in more extreme regions of the data set, and constraining the possibilities of new physics phenomena further.

Table 8.1: Event yields of signal and background processes in the ggF-enriched $N_{\text{jet}} \geq 2$ SR which are obtained using the nominal selection requirements described in Section 4.5.4 or using a requirement of $\max(\text{DL1r}) < -0.73$. The normalisation of signal and background yields assumes the theoretical predictions from the MC simulation. The uncertainties correspond to the statistical uncertainty of the MC samples.

Selection	H_{ggF}	H_{VBF}	Other H	WW	Other $VV(V)$	$t\bar{t}/Wt$	Z/γ^*	Mis-Id	Total Bkg.
Nominal $N_{b\text{-jet}} = 0$	405 ± 2	56 ± 1	56 ± 0	1990 ± 8	493 ± 24	6030 ± 18	1040 ± 17	514 ± 22	$10\,070 \pm 42$
$\max(\text{DL1r}) < -0.73$	330 ± 2	47 ± 1	41 ± 0	1590 ± 7	382 ± 23	3420 ± 14	807 ± 16	343 ± 18	6540 ± 36

Table 8.2: The expected total uncertainty in the measurement of the ggF-enriched $N_{\text{jet}} \geq 2$ signal strength, obtained using the nominal selection requirements or using $\max(\text{DL1r}) < -0.73$, decomposed into groups of uncertainty with common sources, estimated using the breakdown method. The quadrature sum of the groups of uncertainty may differ from the total uncertainty due to the effect of correlations.

Selection	Nominal	$\max(\text{DL1r})$
Source	$\Delta\mu$ [%]	
Total	62.7	57.1
Total systematics	58.8	52.7
Data statistics	26.9	26.9
MC statistics	14.0	12.8
Theoretical uncertainties	51.0	43.9
ggF	16.5	17.2
VBF	0.6	1.0
$H \to WW^*$ branching ratio	2.2	2.3
$t\bar{t}$	37.9	27.8
Wt	7.4	7.6
Z/γ^*	10.9	16.4
WW	6.8	8.1
Other $VV(V)$	25.9	21.9
Other Higgs	4.9	5.0
Experimental systematic uncertainties	19.1	19.1
Flavour Tagging	1.3	4.2
Jet energy scale	11.1	10.5
Jet energy resolution	13.0	12.3
$E_{\text{T}}^{\text{miss}}$	5.3	6.0
Muons	4.9	7.1
Electrons	2.1	2.3
Fake factors	9.2	8.6
Pile-up	1.9	0.8
Luminosity	2.4	2.5
Background normalisations	31.1	27.2
Top normalisation	27.8	20.7
Z/γ^* normalisation	11.5	17.6
$qqWW$ normalisation	7.8	6.9

8.2 Same-flavour leptons

The measurements presented in this thesis have focused solely on final states with *different-flavour* (DF) leptons. However, interactions of leptons with gauge bosons are independent of the lepton flavour in the SM (lepton flavour universality). This means that the $H \to WW^*$ process will decay to final states with *same-flavour* (SF) leptons at the same rate as final states with DF leptons. Particularly in the STXS measurement, the precision of several of the cross sections is dominantly due to the limited sample size of the selected

events, including the ggH, high p_{T}^{H} cross section uncertainty. This cross section targets events originating from possible new phenomena that are not in the SM. Including SF leptons in the measurement could improve the precision of this particular cross section and thus better constrain the possible effect of new phenomena in this Higgs boson decay mode. In this preliminary study, the same MC-simulated samples that are detailed in Section 4.2 are used. Importantly for this study, the Z/γ^* background comprises two MC-simulated samples: a low mass (LM) and a high mass (HM) sample, where the samples are generated in the ranges $10 < m_{\ell\ell} < 40$ GeV and $m_{\ell\ell} > 40$ GeV, respectively. Only the statistical uncertainty due to the size of the selected event samples is considered.

8.2.1 Event selection

The strategy to select Higgs boson signal events with SF leptons in the final state follows that of the selection of Higgs bosons with DF leptons, described in Section 4.5. SRs are similarly defined in categories of jet multiplicity (for jets with $p_{\mathrm{T}} > 30$ GeV), which target the ggF and VBF production modes. The SRs are constructed using selection requirements made on several observables to maximise the event yield from the Higgs boson signal and minimise the contamination from background processes. The selection requirements for SRs with SF leptons are shown in Table 8.3. Similarly to the event selection for the DF channel (Table 4.3), there is a preselection common to all SRs, followed by several requirements to reject background events and exploit the expected kinematics of the Higgs boson signal process.

The largest background in the SF channel is the production of SF-lepton pairs, $Z/\gamma^* \to ee/\mu\mu$, which has a cross section that is several orders of magnitude larger than the Higgs boson signal. This can be seen from the preselection distributions for several observables shown in Figure 8.2. Since the Z/γ^* process occurs with zero real $E_{\mathrm{T}}^{\mathrm{miss}}$, several requirements ensure there is a large amount of likely real $E_{\mathrm{T}}^{\mathrm{miss}}$ in any selected event and that the angles of decay products in the final state are compatible with the existence of real $E_{\mathrm{T}}^{\mathrm{miss}}$. Given the large background contamination from Z/γ^* events, its normalisation should be obtained using data from a CR. Possible CRs can be designed by partitioning the distributions of $m_{\ell\ell}$ and $\Delta\phi_{\ell\ell}$ such that the selected events are mutually exclusive with those selected for the SRs. It would be advantageous to measure the normalisation of Z/γ^* in both a low and a high $m_{\ell\ell}$ regime, since the energy scale of the processes is different in these regions (e.g. whether the energy scale is dominated by the dilepton system or additional jets). Further, the modelling of these regions (performed with separate MC samples) is different, motivating separate measurements of the normalisations of the two $m_{\ell\ell}$ regions.

The expected composition of the SF-lepton SRs and CRs is shown in Figure 8.3. Generally,

Category	$N_{\text{jet},(p_T>30\text{ GeV})} = 0$ ggF	$N_{\text{jet},(p_T>30\text{ GeV})} = 1$ ggF	$N_{\text{jet},(p_T>30\text{ GeV})} \geq 2$ ggF	$N_{\text{jet},(p_T>30\text{ GeV})} \geq 2$ VBF
Preselection	Two isolated, same-flavour leptons ($\ell = e, \mu$) with opposite charge $p_{\text{T}}^{\text{lead}} > 22$ GeV , $p_{\text{T}}^{\text{sublead}} > 15$ GeV $m_{\ell\ell} > 12$ GeV, $\lvert m_{\ell\ell} - m_Z \rvert > 15$ GeV $E_{\text{T}}^{\text{miss}}$ significance > 4, $N_{b\text{-jet}} = 0$			
Background rejection	$\Delta\phi(\ell\ell, E_{\text{T}}^{\text{miss}}) > 1.57$ $p_T^{\ell\ell} > 30$ GeV	$\max(m_{\text{T}}^{\ell}) > 50$ GeV $m_{\tau\tau} < m_Z - 25$ GeV	$\Delta\phi(\ell\ell, E_{\text{T}}^{\text{miss}}) < 2$ $m_{\tau\tau} < m_Z - 25$ GeV	
	$E_{\text{T}}^{\text{miss}}$ significance > 4.5 $\Delta\phi_{\ell\ell} > 0.3$ or $m_{\ell\ell} > 20$ GeV		$m_{\ell\ell} > 20$ GeV	
VBF topology	-		$m_{jj} < 350$ GeV or $\Delta y_{jj} < 3$ or $p_{\text{T}}^{\text{tot}} > 15$ GeV or fail CJV	$m_{jj} > 350$ GeV, $\Delta y_{jj} > 3$, $p_{\text{T}}^{\text{tot}} < 15$ GeV, pass CJV pass OLV
$H \to WW^*$ topology	$m_{\ell\ell} < 55$ GeV $\Delta\phi_{\ell\ell} < 1.8$			
LM $Z/\gamma^* \to \ell\ell$ CR	($\Delta\phi_{\ell\ell} < 0.3$ and $m_{\ell\ell} < 20$ GeV)		$m_{\ell\ell} < 20$ GeV	fail OLV
HM $Z/\gamma^* \to \ell\ell$ CR	$55 < m_{\ell\ell} < 75$ GeV			

Table 8.3: The selection criteria on observables to define SRs and CRs with the SF-lepton final state. Definitions of the observables are found in Section 4.4.

the LM CRs are relatively pure in LM Z/γ^* events, whilst the HM CRs have a relatively large contamination from top quark processes and other multi-boson backgrounds. The SRs are still largely dominated by Z/γ^* background events.

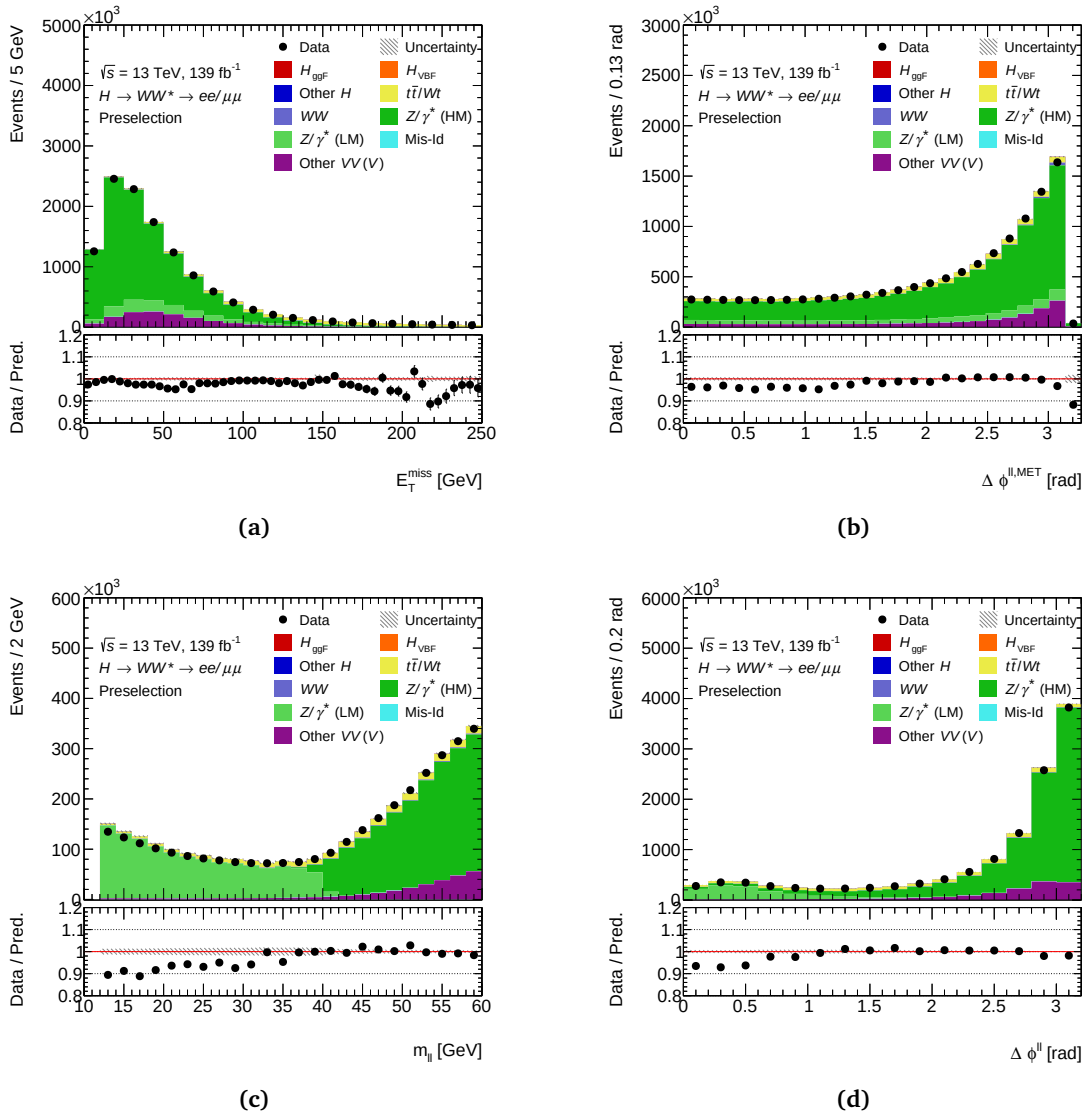

(a) **(b)**

(c) **(d)**

Figure 8.2: Distributions comparing the modelling of the data and MC predictions for several observables used in the SF channel shown at preselection but before any requirement is made on $E_{\mathrm{T}}^{\mathrm{miss}}$. The uncertainty band represents the statistical uncertainty due to the finite size of the MC samples. The background processes are normalised according to their theoretical predictions from the MC simulation. The yields of the Z/γ^* background process are split into two MC samples generated at high mass (HM: $m_{\ell\ell} > 40$ GeV) and low mass (LM: $m_{\ell\ell} < 40$ GeV). The mis-modelling of the low-$m_{\ell\ell}$ region motivates separate $Z/\gamma^* \to \ell\ell$ CRs for the LM and HM samples.

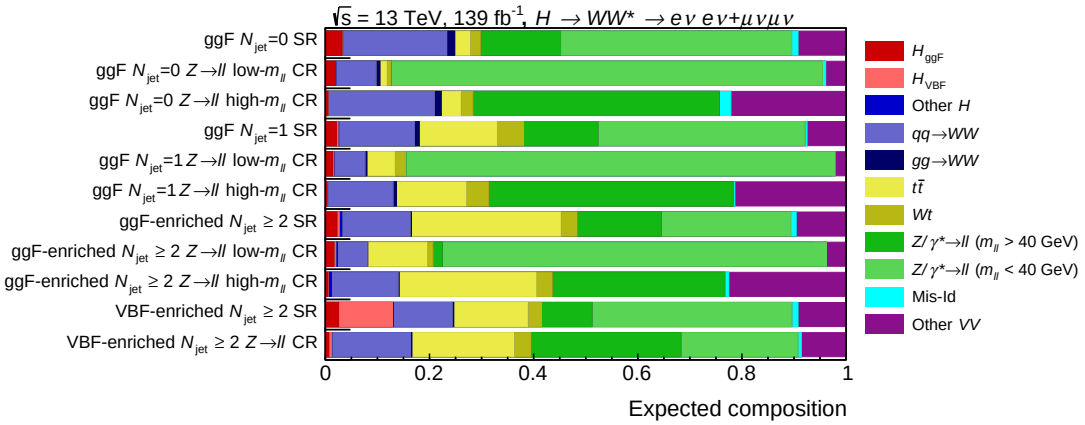

Figure 8.3: The expected composition of the signal and background processes in each SF-lepton SR and CR. Each process is normalised according to the theoretical prediction from the MC simulation.

8.2.2 STXS sensitivity

In order to estimate the statistical precision of the STXS measurement including SF leptons in combination with DF leptons, SRs and CRs are defined for SF leptons that correspond to the measured STXS bins, identical to the strategy described in Section 4.7. This is done by splitting the SRs and CRs into regions defined by selection requirements on reconstructed p_{T}^{H} and m_{jj} such that they are populated by the corresponding signal yield of the STXS bin. The expected distribution of the particle-level Higgs boson signal event yields across the reconstructed STXS SRs is shown in Figure 8.4a, whilst the relative signal yield fraction of each STXS SR is shown in Figure 8.4b. The former shows that $\approx$43 SF-lepton signal events from the ggH, high p_{T}^{H} STXS bin are expected in the corresponding STXS SRs, which is very similar to the $\approx$50 DF events expected in the same STXS bin (Figure 4.31a). Additionally, the purity of each STXS SR is relatively high, with the largest migration of signal events occurring in the VBF STXS SRs.

A statistical analysis is performed which is largely identical to that described in Chapter 6. The m_{T} distribution is used as the final discriminant in each SF-lepton STXS SR to obtain the normalisation of each STXS bin. The binning of the m_{T} distribution is similarly identical. The use of sub-SRs defined by requirements on $m_{\ell\ell}$ and $p_{\mathrm{T}}^{\mathrm{sublead}}$ is retained in the ggF $N_{\mathrm{jet}} = 0$ and ggF-enriched $N_{\mathrm{jet}} \geq 2$ STXS SRs. An Asimov data set is constructed and a fit is performed that contains eleven POIs, each corresponding to the normalisation of the event yield of one STXS bin. No systematic uncertainty is included in this study; the expected uncertainty on the normalisation of each STXS bin is due to the statistical uncertainty arising from the sample size of each SR and CR.

The expected statistical precision of each STXS bin is shown in Table 8.4 for three

Table 8.4: The expected statistical precision of the STXS bins, normalised to the SM predictions, when considering DF leptons only, SF leptons only, and thirdly, SF and DF leptons together.

Parameter	DF	SF	SF+DF
$\mu_{ggH-0j,\ \text{low}\ p_{\text{T}}^{H}}$	$1.00^{+0.08}_{-0.08}$	$1.00^{+0.36}_{-0.36}$	$1.00^{+0.08}_{-0.08}$
$\mu_{ggH-1j,\ \text{very low}\ p_{\text{T}}^{H}}$	$1.00^{+0.30}_{-0.30}$	$1.00^{+2.13}_{-2.12}$	$1.00^{+0.30}_{-0.30}$
$\mu_{ggH-1j,\ \text{low}\ p_{\text{T}}^{H}}$	$1.00^{+0.32}_{-0.32}$	$1.00^{+2.07}_{-2.07}$	$1.00^{+0.31}_{-0.31}$
$\mu_{ggH-1j,\ \text{med}\ p_{\text{T}}^{H}}$	$1.00^{+0.60}_{-0.59}$	$1.00^{+1.43}_{-1.40}$	$1.00^{+0.56}_{-0.55}$
$\mu_{ggH-2j,\ \text{low}\ p_{\text{T}}^{H}}$	$1.00^{+0.42}_{-0.42}$	$1.00^{+1.96}_{-1.95}$	$1.00^{+0.41}_{-0.41}$
$\mu_{ggH,\ \text{high}\ p_{\text{T}}^{H}}$	$1.00^{+0.65}_{-0.63}$	$1.00^{+0.89}_{-0.87}$	$1.00^{+0.54}_{-0.53}$
$\mu_{\text{EW}\ qq2H-2j,\ \text{low}\ m_{jj}-\text{low}\ p_{\text{T}}^{H}}$	$1.00^{+0.51}_{-0.47}$	$1.00^{+3.06}_{-2.91}$	$1.00^{+0.50}_{-0.47}$
$\mu_{\text{EW}\ qq2H-2j,\ \text{med}\ m_{jj}-\text{low}\ p_{\text{T}}^{H}}$	$1.00^{+0.56}_{-0.51}$	$1.00^{+3.07}_{-2.83}$	$1.00^{+0.55}_{-0.50}$
$\mu_{\text{EW}\ qq2H-2j,\ \text{high}\ m_{jj}-\text{low}\ p_{\text{T}}^{H}}$	$1.00^{+0.48}_{-0.43}$	$1.00^{+3.04}_{-2.78}$	$1.00^{+0.47}_{-0.43}$
$\mu_{\text{EW}\ qq2H-2j,\ \text{very high}\ m_{jj}-\text{low}\ p_{\text{T}}^{H}}$	$1.00^{+0.36}_{-0.33}$	$1.00^{+2.31}_{-2.03}$	$1.00^{+0.36}_{-0.33}$
$\mu_{\text{EW}\ qq2H-2j,\ \text{high}\ p_{\text{T}}^{H}}$	$1.00^{+0.43}_{-0.38}$	$1.00^{+1.04}_{-0.95}$	$1.00^{+0.41}_{-0.37}$

cases: first, considering DF leptons only; second, considering SF leptons only; and lastly, considering both SF and DF leptons together. The results indicate that the statistical uncertainty on the ggH, high p_{T}^{H} cross section reduces by 11%, corresponding to a relative reduction of 17%, when including SF leptons in the measurement. The statistical uncertainty of other STXS bins using SF leptons is significantly larger than that of the STXS bins using DF leptons which is due to the large contamination from Z/γ^{*} background events. The use of MVA techniques, such as a DNN like that used in the VBF analysis described in Section 4.5.5, could significantly improve the rejection of Z/γ^{*} background and further increase the statistical precision of the ggH, high p_{T}^{H} cross section, as well as that of other STXS bins. Further, the systematic uncertainty associated with SF leptons remains to be investigated. Nevertheless, this study shows that the addition of SF leptons could improve the precision of further measurements in the $H\rightarrow WW^{*}$ decay mode, particularly in the high p_{T}^{H} regime.

8.3 Prospects

The precision of the measurements presented in this thesis are limited by systematic uncertainty. Therefore, the precision of future measurements strongly depends on the analysis strategy: significant improvement to the measurement precision will only be possible by the combined effect of several analysis improvements and advances in theoretical calculations and the programmes used to model the signal and background processes. In addition to the improvements highlighted in the previous two sections,

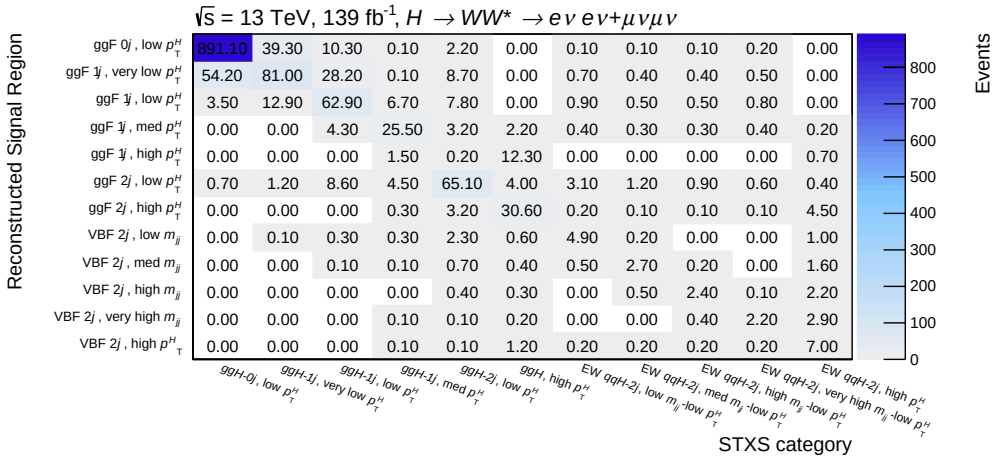

(a)

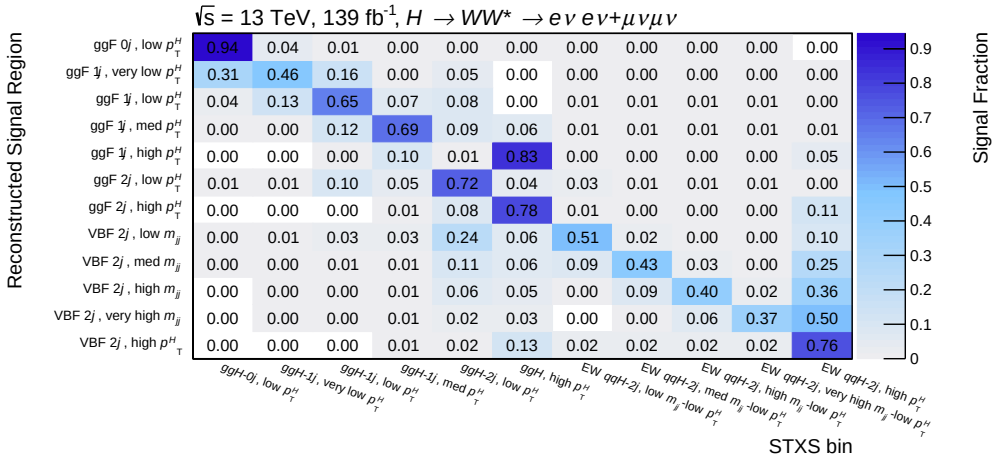

(b)

Figure 8.4: The expected SF-lepton signal yields (a) and relative signal composition (b) as a function of reduced STXS stage 1.2 bins for each reconstructed STXS SR.

several changes to the analysis strategy could be further studied and adopted to reduce the effect of systematic uncertainty:

- The modelling of the parton shower is one of the largest single sources of uncertainty in both the ggF and VBF measurement. It would be beneficial to understand the origin of large differences in the signal kinematics in the parton shower or if the analysis strategy selects a very exclusive region of the data set, introducing large extrapolation uncertainty to the inclusive cross section measurement.

- The QCD scale uncertainty is the single largest source of uncertainty in the ggF measurement. This would be improved through increased orders of α_S in the theoretical calculation of ggF production and improved understanding in estimating the systematic uncertainty due to missing higher orders in exclusive jet multiplicity bins.

- The $qqWW$ theoretical uncertainty is the largest source of background uncertainty in the measurement of ggF production. The dependency of the theoretical uncertainty in the $qqWW$ background estimate could be studied as a function of $m_{\ell\ell}$ and $\Delta\phi_{\ell\ell}$, since the selection requirements on these observables defining the SRs tageting ggF Higgs boson production have not been studied since the Run 1 measurement [5].

- Theoretical background uncertainty on the signal normalisation could be dependent on both the bin width and number of m_{T} bins, which are identical for all ggF regions, and it could be verified if additional overflow and underflow bins could reduce their effect.

- The non-WW multiboson background is currently estimated using the theoretical prediction from MC simulation but a CR could be used instead to estimate the rate of these processes and reduce the effect of theoretical uncertainty.

- The theoretical uncertainty associate with the top quark background has the largest effect on the signal normalisation in the ggF-enriched $N_{\mathrm{jet}} \geq 2$ and VBF-enriched $N_{\mathrm{jet}} \geq 2$ regions. A reduction of the top quark contamination in these regions could involve improved rejection of b-jets, additional selection requirements on new observables that can efficiently separate top quark and Higgs boson events, or performing a simultaneous measurement of the top quark production cross section and b-jet identification efficiency in data.

- It could be possible to adopt advanced machine learning techniques to classify the ggF signal, the VBF signal, and background processes, and develop the appropriate statistical analysis using the outputs of this classifier instead of using the CJV and OLV.

- Lastly, the majority of the sensitivity to the ggF-enriched $N_{\mathrm{jet}} \geq 2$ measurement is from events with exactly two reconstructed jets. A partition of the ggF-enriched $N_{\mathrm{jet}} \geq 2$ STXS bins and SRs by $p_{\mathrm{T}}^{Hjj} < 25$ GeV (typically $N_{\mathrm{jet}} \geq 2$ events) and $p_{\mathrm{T}}^{Hjj} > 25$ GeV (typically $N_{\mathrm{jet}} \geq 3$ events) could reduce the effect of theoretical uncertainty in the current extrapolation of the measurement across these STXS bins.

The above considerations, in addition to the improvements elaborated in Sections 8.1 and 8.2, could lead to a future precision below approximately 10% for the ggF measurement and below 20% for the VBF measurement, as well as improving the precision of individual STXS bins.

9
Conclusions

This thesis presents measurements of ggF and VBF production cross sections of the Higgs boson using the $H \to WW^* \to \ell\nu\ell\nu$ decay mode. The measurements make use of the full LHC Run 2 data set, corresponding to an integrated luminosity of 139 fb^{-1}, collected by the ATLAS detector from pp collisions generated at $\sqrt{s} = 13$ TeV during the years 2015–2018. The events selected for analysis are categorised based on jet multiplicity and production mode, increasing the signal-to-background discrimination of individual regions. Large contamination of the selected event yields from background processes, including non-resonant WW, top quark, and Z/γ^* processes, are measured using dedicated CRs to constrain their normalisation within each jet-binned region. In the ggF analysis regions, the transverse mass, m_{T}, is used as the discriminating observable in the statistical analysis, whilst advanced analysis techniques involving DNNs are used in the VBF region, where the output DNN distribution is used as the discriminating variable in the statistical analysis. The ggF and VBF production cross sections multiplied by the $H \to WW^*$ branching ratio, $\sigma_{\mathrm{ggF}} \cdot \mathcal{B}_{H\to WW^*}$ and $\sigma_{\mathrm{VBF}} \cdot \mathcal{B}_{H\to WW^*}$, are measured to be

$$\begin{aligned} \sigma_{\mathrm{ggF}} \cdot \mathcal{B}_{H\to WW^*} &= 12.0 \pm 1.4 \text{ pb} \\ \sigma_{\mathrm{VBF}} \cdot \mathcal{B}_{H\to WW^*} &= 0.75 \,^{+0.19}_{-0.16} \text{ pb} \end{aligned} \tag{9.1}$$

and the measurement of combined ggF and VBF production is measured to be

$$\sigma_{\mathrm{ggF+VBF}} \cdot \mathcal{B}_{H\to WW^*} = 12.3 \pm 1.3 \text{ pb}. \tag{9.2}$$

These measurements are in good agreement with the SM predictions of 10.4 ± 0.5 pb, 0.81 ± 0.02 pb, and 11.3 ± 0.5 pb, respectively. The precision of the measurements in this decay mode are now at the level of 12% and 23% for ggF and VBF production, respectively, which make these the most precise measurements of the $H \to WW^* \to \ell\nu\ell\nu$ process performed with the ATLAS detector to date. The uncertainty is limited by the theoretical modelling of the Higgs boson signal processes, as well as the theoretical modelling of important background processes, including non-resonant WW and top quark processes. Nevertheless, the measurements presented in this thesis result in a statistical significance of over 9σ for the ggF production mode, whilst the VBF production mode has

been observed for the first time in measurements using the $H \to WW^*$ decay mode with a statistical significance of 6.2σ.

The size of the full Run 2 data set and the precision with which the ggF and VBF production modes are measured means the analysis can be extended to measure ggF and VBF production of the $H \to WW^* \to \ell\nu\ell\nu$ process in eleven distinct kinematic fiducial regions, defined in the STXS framework, for the first time. This means measurements of the p_{T}^{H} and m_{jj} distributions are performed and regions of these distributions which are sensitive to new physics phenomena are directly probed. The precision of the cross section measurements at high p_{T}^{H} and m_{jj} are predominantly limited by the sample size of the selected events, whilst at lower p_{T}^{H} and lower m_{jj}, the precision is predominantly limited by the theoretical modelling of the signal and background processes. The cross section measurements in the STXS framework are, however, in good agreement with the SM predictions and have a probability of compatibility with the SM of 53%.

Reducing the uncertainty in future measurements of ggF and VBF production of the Higgs boson in the $H \to WW^* \to \ell\nu\ell\nu$ decay mode will be challenging since many of the simulated MC samples are state-of-the-art, with several higher order terms already included. Instead, more use of data (instead of relying on theoretical predictions) could be employed to estimate more background processes, for instance for non-WW multi-boson processes. Additionally, whilst multivariate analysis techniques were employed in the VBF measurement, further use of these techniques could be used to enhance the separation of signal and background, especially in several of the STXS SRs, although the impact of the signal and background modelling uncertainties should be carefully assessed.

This thesis additionally presents two possible improvements that could be incorporated in future measurements, which include the use of an optimised rejection of events containing b-jets and the inclusion of same-flavour leptons to the selected event yields. The former aims to reduce the significant contamination from top quark background events in the ggF-enriched $N_{\mathrm{jet}} \geq 2$ SR. A new observable is constructed, the maximum score of the b-tagging algorithm in an event, equivalent to a veto on the presence of a b-jet in an event. Making a selection requirement on this observable increases the rejection of top quark background events whilst maintaining a high signal selection efficiency and leads to an improvement of $\approx 10\%$ in the measurement of ggF production using only events from the ggF-enriched $N_{\mathrm{jet}} \geq 2$ region. The inclusion of SF leptons could improve the precision of the high p_{T}^{H} cross section measurement, where SF leptons will add an approximately equal number of Higgs boson signal events to DF leptons. Considering a preliminary set of selection requirements and the statistical uncertainty due to the sample size of selected events shows that an expected $\approx 10\%$ improvement could be achieved on the statistical

precision of the ggH, high p_{T}^{H} cross section. However, background from $Z/\gamma^{*} \to ee/\mu\mu$ events dominate the event yields with SF leptons due to its large cross section. Advanced analysis techniques could be used to increase the rejection of this background and further improve the precision of measurements using SF leptons.

Finally, whilst the measurements in this thesis give sizeable credibility to the mechanism through which fundamental particles acquire mass, and confirming the predicted Higgs boson exhibits SM-like interactions, larger data sets will continue to be produced by the LHC and recorded by the ATLAS detector. As such, more granular STXS measurements could be performed, probing possible new physics phenomena more sensitively, and examining the Higgs boson in kinematically unexplored regions of the data. Coupled with advanced analysis techniques, the precision and range of future measurements make the $H \to WW^{*}$ decay mode a challenging but valuable tool for measurements of the Higgs boson with the ATLAS detector. Ten years on from its discovery, there is still much to be learnt about the Higgs boson and its role within the Standard Model.

Bibliography

[1] ATLAS Collaboration, *Observation of a new particle in the search for the Standard Model Higgs boson with the ATLAS detector at the LHC*, Phys. Lett. B **716** (2012) 1, arXiv: 1207.7214 [hep-ex].

[2] CMS Collaboration, *Observation of a new boson at a mass of 125 GeV with the CMS experiment at the LHC*, Phys. Lett. B **716** (2012) 30, arXiv: 1207.7235 [hep-ex].

[3] LHCb Collaboration, *Test of lepton universality in beauty-quark decays*, Nature Phys. **18** (2022) 277, arXiv: 2103.11769 [hep-ex].

[4] Muon g–2 Collaboration, *Measurement of the Positive Muon Anomalous Magnetic Moment to 0.46 ppm*, Phys. Rev. Lett. **126** (14 2021) 141801.

[5] ATLAS Collaboration, *Observation and measurement of Higgs boson decays to WW^* with the ATLAS detector*, Phys. Rev. D **92** (2015) 012006, arXiv: 1412.2641 [hep-ex].

[6] ATLAS Collaboration, *Measurements of the Higgs boson production and decay rates and coupling strengths using pp collision data at $\sqrt{s} = 7$ and 8 TeV in the ATLAS experiment*, Eur. Phys. J. C **76** (2016) 6, arXiv: 1507.04548 [hep-ex].

[7] ATLAS Collaboration, *Measurements of gluon-gluon fusion and vector-boson fusion Higgs boson production cross-sections in the $H \to WW^* \to e\nu\mu\nu$ decay channel in pp collisions at $\sqrt{s} = 13$ TeV with the ATLAS detector*, Phys. Lett. B **789** (2019) 508, arXiv: 1808.09054 [hep-ex].

[8] S. L. Glashow, *Partial-symmetries of weak interactions*, Nucl. Phys. **22** (1961) 579.

[9] A. Salam, *Weak and Electromagnetic Interactions*, Conf. Proc. C **680519** (1968) 367.

[10] S. Weinberg, *A Model of Leptons*, Phys. Rev. Lett. **19** (21 1967) 1264.

[11] G. 't Hooft and M. Veltman, *Regularization and renormalization of gauge fields*, Nuclear Physics B **44** (1972) 189.

[12] A. Pich, "The Standard Model of Electroweak Interactions", *2010 European School of High Energy Physics*, 2012, arXiv: 1201.0537 [hep-ph].

[13] J. Ellis, "Higgs Physics", *2013 European School of High-Energy Physics*, 2015, arXiv: 1312.5672 [hep-ph].

[14] A. Djouadi, "The anatomy of electro-weak symmetry breaking I: The Higgs boson in the standard model", 2008, arXiv: hep-ph/0503172.

[15] G. Altarelli, "Collider Physics within the Standard Model: a Primer", 2013, arXiv: 1303.2842 [hep-ph].

[16] S. F. Novaes, "Standard model: An Introduction", *10th Jorge Andre Swieca Summer School: Particle and Fields*, 1999, arXiv: hep-ph/0001283.

[17] M. Schwartz, *Quantum Field Theory and the Standard Model*, 2013.

[18] E. Noether, *Invariante Variationsprobleme*, Nachrichten von der Gesellschaft der Wissenschaften zu Göttingen, Mathematisch-Physikalische Klasse (1918) 235, URL: http://eudml.org/doc/59024.

[19] E. Fermi, *Tentativo di una Teoria Dei Raggi* , Il Nuovo Cimento (1924-1942) **11** (2008) 1.

[20] C. S. Wu, E. Ambler, R. W. Hayward, D. D. Hoppes, and R. P. Hudson, *Experimental Test of Parity Conservation in Beta Decay*, Phys. Rev. **105** (4 1957) 1413.

[21] G. Arnison et al., *Experimental Observation of Isolated Large Transverse Energy Electrons with Associated Missing Energy at $\sqrt{s} = 540$ GeV*, Phys. Lett. B **122** (1983) 103.

[22] M. Banner et al., *Observation of Single Isolated Electrons of High Transverse Momentum in Events with Missing Transverse Energy at the CERN anti-p p Collider*, Phys. Lett. B **122** (1983) 476.

[23] G. Arnison et al., *Experimental observation of lepton pairs of invariant mass around 95 GeV/c^2 at the CERN SPS collider*, Physics Letters B **126** (1983) 398.

[24] P. Bagnaia et al., *Evidence for $Z^0 \to e^+e$ at the CERN pp collider*, Physics Letters B **129** (1983) 130.

[25] J. Goldstone, A. Salam, and S. Weinberg, *Broken Symmetries*, Phys. Rev. **127** (3 1962) 965.

[26] F. Englert and R. Brout, *Broken Symmetry and the Mass of Gauge Vector Mesons*, Phys. Rev. Lett. **13** (9 1964) 321.

[27] P. W. Higgs, *Broken symmetries, massless particles and gauge fields*, Phys. Lett. **12** (1964) 132.

[28] P. W. Higgs, *Broken Symmetries and the Masses of Gauge Bosons*, Phys. Rev. Lett. **13** (16 1964) 508, URL: https://link.aps.org/doi/10.1103/PhysRevLett.13.508.

[29] G. S. Guralnik, C. R. Hagen, and T. W. B. Kibble, *Global Conservation Laws and Massless Particles*, Phys. Rev. Lett. **13** (20 1964) 585.

[30] P. W. Higgs, *Spontaneous Symmetry Breakdown without Massless Bosons*, Phys. Rev. **145** (4 1966) 1156.

[31] T. W. B. Kibble, *Symmetry Breaking in Non-Abelian Gauge Theories*, Phys. Rev. **155** (5 1967) 1554.

[32] N. Cabibbo, *Unitary Symmetry and Leptonic Decays*, Phys. Rev. Lett. **10** (12 1963) 531, URL: https://link.aps.org/doi/10.1103/PhysRevLett.10.531.

[33] M. Kobayashi and T. Maskawa, *CP-Violation in the Renormalizable Theory of Weak Interaction*, Progress of Theoretical Physics **49** (1973) 652, URL: https://doi.org/10.1143/PTP.49.652.

[34] V. N. Gribov and L. N. Lipatov, *Deep inelastic ep scattering in perturbation theory*, Sov. J. Nucl. Phys. **15** (1972) 438.

[35] L. N. Lipatov, *The parton model and perturbation theory*, Yad. Fiz. **20** (1974) 181.

[36] G. Altarelli and G. Parisi, *Asymptotic Freedom in Parton Language*, Nucl. Phys. B **126** (1977) 298.

[37] Y. L. Dokshitzer, *Calculation of the Structure Functions for Deep Inelastic Scattering and e^+e^- Annihilation by Perturbation Theory in Quantum Chromodynamics.*, Sov. Phys. JETP **46** (1977) 641.

[38] J. Pumplin et al., *New generation of parton distributions with uncertainties from global QCD analysis*, JHEP **07** (2002) 012, arXiv: hep-ph/0201195, URL: https://doi.org/10.1088/1126-6708/2002/07/012.

[39] A. Sherstnev and R. S. Thorne, *Parton Distributions for LO Generators*, Eur. Phys. J. C **55** (2008) 553, arXiv: 0711.2473 [hep-ph].

[40] R. D. Ball et al., *Parton distributions with LHC data*, Nucl. Phys. B **867** (2013) 244, arXiv: 1207.1303 [hep-ph].

[41] J. Butterworth et al., *PDF4LHC recommendations for LHC Run II*, J. Phys. G **43** (2016) 023001, arXiv: 1510.03865 [hep-ph].

[42] T. Sjöstrand et al., *An introduction to PYTHIA 8.2*, Comput. Phys. Commun. **191** (2015) 159, arXiv: 1410.3012 [hep-ph].

[43] J. Bellm et al., *Herwig 7.0/Herwig++ 3.0 release note*, Eur. Phys. J. C **76** (2016) 196, arXiv: 1512.01178 [hep-ph].

[44] T. Gleisberg, S. Hóche, F. Krauss, M. Schónherr, S. Schumann, et al., *Event generation with SHERPA 1.1*, JHEP **02** (2009) 007, arXiv: 0811.4622 [hep-ph].

[45] J. Alwall, R. Frederix, S. Frixione, V. Hirschi, F. Maltoni, et al., *The automated computation of tree-level and next-to-leading order differential cross sections, and their matching to parton shower simulations*, JHEP **07** (2014) 079, arXiv: 1405.0301 [hep-ph].

[46] S. Alioli, P. Nason, C. Oleari, and E. Re, *A general framework for implementing NLO calculations in shower Monte Carlo programs: the POWHEG BOX*, JHEP **06** (2010) 043, arXiv: 1002.2581 [hep-ph].

[47] S. Höche, F. Krauss, M. Schönherr, and F. Siegert, *A critical appraisal of NLO+PS matching methods*, JHEP **09** (2012) 049, arXiv: 1111.1220 [hep-ph].

[48] S. Hoeche, F. Krauss, M. Schonherr, and F. Siegert, *QCD matrix elements + parton showers: The NLO case*, JHEP **04** (2013) 027, arXiv: 1207.5030 [hep-ph].

[49] S. Catani, F. Krauss, R. Kuhn, and B. R. Webber, *QCD Matrix Elements + Parton Showers*, JHEP **11** (2001) 063, arXiv: hep-ph/0109231.

[50] S. Höche, F. Krauss, S. Schumann, and F. Siegert, *QCD matrix elements and truncated showers*, JHEP **05** (2009) 053, arXiv: 0903.1219 [hep-ph].

[51] S. Höche, "Introduction to parton-shower event generators", 2015, arXiv: 1411.4085 [hep-ph].

[52] LHC Higgs Cross Section WG, "LHC Higgs Cross Section WG Picture Gallery", URL: https://twiki.cern.ch/twiki/bin/view/LHCPhysics/LHCHWGCrossSectionsFigures?redirectedfrom=LHCPhysics.LHCHXSWGCrossSectionsFigures.

[53] D. de Florian et al., *Handbook of LHC Higgs Cross Sections: 4. Deciphering the Nature of the Higgs Sector*, **2/2017** (2016), arXiv: 1610.07922 [hep-ph].

[54] M. Boggia et al., *The HiggsTools handbook: a beginners guide to decoding the Higgs sector*, Journal of Physics G: Nuclear and Particle Physics **45** (2018) 065004.

[55] ATLAS Collaboration, *Fiducial and differential cross sections of Higgs boson production measured in the four-lepton decay channel in pp collisions at $\sqrt{s} = 8$ TeV with the ATLAS detector*, Phys. Lett. B **738** (2014) 234, arXiv: 1408.3226 [hep-ex].

[56] CMS Collaboration, *Measurement of differential and integrated fiducial cross sections for Higgs boson production in the four-lepton decay channel in pp collisions at $\sqrt{s} = 7$ and 8 TeV*, JHEP **04** (2016) 005, arXiv: 1512.08377 [hep-ex].

[57] J. R. Andersen et al., "Les Houches 2015: Physics at TeV Colliders Standard Model Working Group Report", *9th Les Houches Workshop on Physics at TeV Colliders*, 2016, arXiv: 1605.04692 [hep-ph].

[58] N. Berger et al., *Simplified Template Cross Sections - Stage 1.1*, (2019), arXiv: 1906.02754 [hep-ph].

[59] The ATLAS Collaboration, *A detailed map of Higgs boson interactions by the ATLAS experiment ten years after the discovery*, Nature **607** (2022) 52, URL: https://doi.org/10.1038/s41586-022-04893-w.

[60] The CMS Collaboration, *A portrait of the Higgs boson by the CMS experiment ten years after the discovery*, Nature **607** (2022) 60, URL: https://doi.org/10.1038/s41586-022-04892-x.

[61] ATLAS Collaboration, *A search for the dimuon decay of the Standard Model Higgs boson with the ATLAS detector*, Phys. Lett. B **812** (2021) 135980, arXiv: 2007.07830 [hep-ex].

[62] ATLAS Collaboration, *Direct constraint on the Higgs-charm coupling from a search for Higgs boson decays into charm quarks with the ATLAS detector*, (2022), arXiv: 2201.11428 [hep-ex].

[63] ATLAS Collaboration, *Study of the spin and parity of the Higgs boson in diboson decays with the ATLAS detector*, Eur. Phys. J. C **75** (2015) 476, arXiv: 1506.05669 [hep-ex], Erratum: Eur. Phys. J. C **76** (2016) 152.

[64] CMS Collaboration, *Constraints on the spin-parity and anomalous HVV couplings of the Higgs boson in proton collisions at 7 and 8 TeV*, Phys. Rev. D **92** (2015) 012004, arXiv: 1411.3441 [hep-ex].

[65] ATLAS Collaboration, *Test of CP invariance in vector-boson fusion production of the Higgs boson in the $H \to \tau\tau$ channel in proton–proton collisions at $\sqrt{s} = 13$ TeV with the ATLAS detector*, Phys. Lett. B **805** (2020) 135426, arXiv: 2002.05315 [hep-ex].

[66] CMS Collaboration, *Analysis of the CP structure of the Yukawa coupling between the Higgs boson and τ leptons in proton–proton collisions at $\sqrt{s} = 13$ TeV*, (2021), arXiv: 2110.04836 [hep-ex].

[67] L. Evans and P. Bryant, *LHC Machine*, JINST **3** (2008) S08001.

[68] J. Haffner, *The CERN accelerator complex. Complexe des accélérateurs du CERN*, (2013), General Photo, URL: https://cds.cern.ch/record/1621894.

[69] G. Barr, R. Devenish, R. Walczak, and T. Weidberg, *Particle Physics in the LHC Era*, 2016.

[70] ATLAS Collaboration, *Reconstruction of primary vertices at the ATLAS experiment in Run 1 proton–proton collisions at the LHC*, Eur. Phys. J. C **77** (2017) 332, arXiv: 1611.10235 [hep-ex].

[71] ATLAS Collaboration, *ATLAS data quality operations and performance for 2015–2018 data-taking*, JINST **15** (2020) P04003, arXiv: 1911.04632 [physics.ins-det].

[72] ATLAS Collaboration, "Luminosity Public Results Run 2", URL: https://twiki.cern.ch/twiki/bin/view/AtlasPublic/LuminosityPublicResultsRun2.

[73] ATLAS Collaboration, *The ATLAS Experiment at the CERN Large Hadron Collider*, JINST **3** (2008) S08003.

[74] A. M. Rodriguez Vera and J. Pequenao, "ATLAS Detector Magnet System", 2021, URL: https://cds.cern.ch/record/2770604.

[75] J. Pequenao, "Computer generated image of the ATLAS inner detector", 2008, URL: https://cds.cern.ch/record/1095926.

[76] J. Pequenao, "Computer Generated image of the ATLAS calorimeter", 2008, URL: https://cds.cern.ch/record/1095927.

[77] J. Pequenao, "Computer generated image of the ATLAS Muons subsystem", 2008, URL: https://cds.cern.ch/record/1095929.

[78] ATLAS Collaboration, "Run 2 Public DAQ plots", URL: https://twiki.cern.ch/twiki/bin/view/AtlasPublic/ApprovedPlotsDAQ.

[79] S. Mehlhase, *ATLAS detector slice (and particle visualisations)*, (2021), URL: https://cds.cern.ch/record/2770815.

[80] ATLAS Collaboration, *Performance of the ATLAS track reconstruction algorithms in dense environments in LHC Run 2*, Eur. Phys. J. C **77** (2017) 673, arXiv: 1704.07983 [hep-ex].

[81] ATLAS Collaboration, *Early Inner Detector Tracking Performance in the 2015 Data at $\sqrt{s} = 13$ TeV*, ATL-PHYS-PUB-2015-051, 2015, URL: https://cds.cern.ch/record/2110140.

[82] R. Frühwirth, *Application of Kalman filtering to track and vertex fitting*, Nuclear Instruments and Methods in Physics Research Section A: Accelerators, Spectrometers, Detectors and Associated Equipment **262** (1987) 444.

[83] T. G. Cornelissen et al., *The global χ^2 track fitter in ATLAS*, J. Phys.: Conf. Ser. **119** (2008) 032013.

[84] ATLAS Collaboration, *Vertex Reconstruction Performance of the ATLAS Detector at $\sqrt{s} = 13$ TeV*, ATL-PHYS-PUB-2015-026, 2015, URL: https://cds.cern.ch/record/2037717.

[85] ATLAS Collaboration, "Updates of the ATLAS Tracking Event Data Model (Release 13)", 2007, URL: https://cds.cern.ch/record/1038095.

[86] ATLAS Collaboration, *Expected electron performance in the ATLAS experiment*, ATL-PHYS-PUB-2011-006, 2011, URL: https://cds.cern.ch/record/1345327.

[87] ATLAS Collaboration, *Topological cell clustering in the ATLAS calorimeters and its performance in LHC Run 1*, Eur. Phys. J. C **77** (2017) 490, arXiv: 1603.02934 [hep-ex].

[88] Walter Lampl et al., *Calorimeter Clustering Algorithms: Description and Performance*, ATL-LARG-PUB-2008-002, 2008, URL: https://cds.cern.ch/record/1099735.

[89] ATLAS Collaboration, *Improved electron reconstruction in ATLAS using the Gaussian Sum Filter-based model for bremsstrahlung*, ATLAS-CONF-2012-047, 2012, URL: https://cds.cern.ch/record/1449796.

[90] ATLAS Collaboration, *Electron reconstruction and identification in the ATLAS experiment using the 2015 and 2016 LHC proton–proton collision data at $\sqrt{s} = 13$ TeV*, Eur. Phys. J. C **79** (2019) 639, arXiv: 1902.04655 [hep-ex].

[91] ATLAS Collaboration, *Electron and photon performance measurements with the ATLAS detector using the 2015–2017 LHC proton–proton collision data*, JINST **14** (2019) P12006, arXiv: 1908.00005 [hep-ex].

[92] ATLAS Collaboration, *Muon reconstruction and identification efficiency in ATLAS using the full Run 2 pp collision data set at $\sqrt{s} = 13$ TeV*, Eur. Phys. J. C **81** (2021) 578, arXiv: 2012.00578 [hep-ex].

[93] ATLAS Collaboration, *Jet reconstruction and performance using particle flow with the ATLAS Detector*, Eur. Phys. J. C **77** (2017) 466, arXiv: 1703.10485 [hep-ex].

[94] ATLAS Collaboration, *Jet energy scale and resolution measured in proton–proton collisions at $\sqrt{s} = 13$ TeV with the ATLAS detector*, Eur. Phys. J. C **81** (2020) 689, arXiv: 2007.02645 [hep-ex].

[95] M. Cacciari, G. P. Salam, and G. Soyez, *The anti-k_t jet clustering algorithm*, JHEP **04** (2008) 063, arXiv: 0802.1189 [hep-ph].

[96] Matteo C. and G. P. Salam, *Pileup subtraction using jet areas*, Physics Letters B **659** (2008) 119.

[97] ATLAS Collaboration, *Tagging and suppression of pileup jets with the ATLAS detector*, ATLAS-CONF-2014-018, 2014, URL: https://cds.cern.ch/record/1700870.

[98] ATLAS Collaboration, *Performance of pile-up mitigation techniques for jets in pp collisions at $\sqrt{s} = 8$ TeV using the ATLAS detector*, Eur. Phys. J. C **76** (2016) 581, arXiv: 1510.03823 [hep-ex].

[99] ATLAS Collaboration, *Optimisation and performance studies of the ATLAS b-tagging algorithms for the 2017-18 LHC run*, ATL-PHYS-PUB-2017-013, 2017, URL: https://cds.cern.ch/record/2273281.

[100] ATLAS Collaboration, *Secondary vertex finding for jet flavour identification with the ATLAS detector*, ATL-PHYS-PUB-2017-011, 2017, URL: https://cds.cern.ch/record/2270366.

[101] ATLAS Collaboration, *Topological b-hadron decay reconstruction and identification of b-jets with the JetFitter package in the ATLAS experiment at the LHC*, ATL-PHYS-PUB-2018-025, 2018, URL: https://cds.cern.ch/record/2645405.

[102] ATLAS Collaboration, *Identification of Jets Containing b-Hadrons with Recurrent Neural Networks at the ATLAS Experiment*, ATL-PHYS-PUB-2017-003, 2017, URL: https://cds.cern.ch/record/2255226.

[103] ATLAS Collaboration, *ATLAS b-jet identification performance and efficiency measurement with $t\bar{t}$ events in pp collisions at $\sqrt{s} = 13$ TeV*, Eur. Phys. J. C **79** (2019) 970, arXiv: 1907.05120 [hep-ex].

[104] ATLAS Collaboration, *Measurement of b-tagging efficiency of c-jets in $t\bar{t}$ events using a likelihood approach with the ATLAS detector*, ATLAS-CONF-2018-001, 2018, URL: https://cds.cern.ch/record/2306649.

[105] ATLAS Collaboration, *Calibration of light-flavour b-jet mistagging rates using ATLAS proton–proton collision data at $\sqrt{s} = 13$ TeV*, ATLAS-CONF-2018-006, 2018, URL: https://cds.cern.ch/record/2314418.

[106] ATLAS Collaboration, *Optimisation of the smoothing of b-jet identification efficiency and mistag rate simulation-to-data scale factors in ATLAS*, ATL-PHYS-PUB-2020-004, 2020, URL: https://cds.cern.ch/record/2710598.

[107] ATLAS Collaboration, *E_T^{miss} performance in the ATLAS detector using 2015–2016 LHC pp collisions*, ATLAS-CONF-2018-023, 2018, URL: https://cds.cern.ch/record/2625233.

[108] ATLAS Collaboration, *Performance of missing transverse momentum reconstruction with the ATLAS detector using proton–proton collisions at $\sqrt{s} = 13$ TeV*, Eur. Phys. J. C **78** (2018) 903, arXiv: 1802.08168 [hep-ex].

[109] ATLAS Collaboration, "Missing transverse energy performance in 2017 data and Monte Carlo using PFlow Jets", URL: https://atlas.web.cern.ch/Atlas/GROUPS/PHYSICS/PLOTS/JETM-2018-002/.

[110] ATLAS and CMS Collaborations, *Combined Measurement of the Higgs Boson Mass in pp Collisions at $\sqrt{s} = 7$ and 8 TeV with the ATLAS and CMS Experiments*, Phys. Rev. Lett. **114** (2015) 191803, arXiv: 1503.07589 [hep-ex].

[111] Particle Data Group et al., *Review of Particle Physics*, Progress of Theoretical and Experimental Physics **2020** (2020), 083C01.

[112] ATLAS Collaboration, "Standard Model Summary Plots June 2021", 2021, URL: http://cds.cern.ch/record/2777014.

[113] ATLAS Collaboration, *Performance of electron and photon triggers in ATLAS during LHC Run 2*, Eur. Phys. J. C **80** (2020) 47, arXiv: 1909.00761 [hep-ex].

[114] ATLAS Collaboration, *Performance of the ATLAS muon triggers in Run 2*, (2020), arXiv: 2004.13447 [hep-ex].

[115] K. Hamilton, P. Nason, E. Re, and G. Zanderighi, *NNLOPS simulation of Higgs boson production*, JHEP **10** (2013) 222, arXiv: 1309.0017 [hep-ph].

[116] K. Hamilton, P. Nason, and G. Zanderighi, *Finite quark-mass effects in the NNLOPS POWHEG+MiNLO Higgs generator*, JHEP **05** (2015) 140, arXiv: 1501.04637 [hep-ph].

[117] P. Nason, *A New method for combining NLO QCD with shower Monte Carlo algorithms*, JHEP **11** (2004) 040, arXiv: hep-ph/0409146.

[118] S. Frixione, P. Nason, and C. Oleari, *Matching NLO QCD computations with Parton Shower simulations: the POWHEG method*, JHEP **11** (2007) 070, arXiv: 0709.2092 [hep-ph].

[119] C. Anastasiou et al., *High precision determination of the gluon fusion Higgs boson cross-section at the LHC*, JHEP **05** (2016) 058, arXiv: 1602.00695 [hep-ph].

[120] C. Anastasiou, C. Duhr, F. Dulat, F. Herzog, and B. Mistlberger, *Higgs Boson Gluon-Fusion Production in QCD at Three Loops*, Phys. Rev. Lett. **114** (2015) 212001, arXiv: 1503.06056 [hep-ph].

[121] F. Dulat, A. Lazopoulos, and B. Mistlberger, *iHixs 2 — Inclusive Higgs cross sections*, Comput. Phys. Commun. **233** (2018) 243, arXiv: 1802.00827 [hep-ph].

[122] R. V. Harlander and K. J. Ozeren, *Finite top mass effects for hadronic Higgs production at next-to-next-to-leading order*, JHEP **11** (2009) 088, arXiv: 0909.3420 [hep-ph].

[123] R. V. Harlander and K. J. Ozeren, *Top mass effects in Higgs production at next-to-next-to-leading order QCD: Virtual corrections*, Phys. Lett. B **679** (2009) 467, arXiv: 0907.2997 [hep-ph].

[124] R. V. Harlander, H. Mantler, S. Marzani, and K. J. Ozeren, *Higgs production in gluon fusion at next-to-next-to-leading order QCD for finite top mass*, Eur. Phys. J. C **66** (2010) 359, arXiv: 0912.2104 [hep-ph].

[125] A. Pak, M. Rogal, and M. Steinhauser, *Finite top quark mass effects in NNLO Higgs boson production at LHC*, JHEP **02** (2010) 025, arXiv: 0911.4662 [hep-ph].

[126] S. Actis, G. Passarino, C. Sturm, and S. Uccirati, *NLO Electroweak Corrections to Higgs Boson Production at Hadron Colliders*, Phys. Lett. B **670** (2008) 12, arXiv: 0809.1301 [hep-ph].

[127] S. Actis, G. Passarino, C. Sturm, and S. Uccirati, *NNLO Computational Techniques: The Cases $H \to \gamma\gamma$ and $H \to gg$*, Nucl. Phys. B **811** (2009) 182, arXiv: 0809.3667 [hep-ph].

[128] M. Bonetti, K. Melnikov, and L. Tancredi, *Higher order corrections to mixed QCD-EW contributions to Higgs boson production in gluon fusion*, Phys. Rev. D **97** (2018) 056017, [Erratum: Phys.Rev.D 97, 099906 (2018)], arXiv: 1801.10403 [hep-ph].

[129] P. Nason and C. Oleari, *NLO Higgs boson production via vector-boson fusion matched with shower in POWHEG*, JHEP **02** (2010) 037, arXiv: 0911.5299 [hep-ph].

[130] J. M. Campbell et al., *NLO Higgs Boson Production Plus One and Two Jets Using the POWHEG BOX, MadGraph4 and MCFM*, JHEP **07** (2012) 092, arXiv: 1202.5475 [hep-ph].

[131] R. Frederix and S. Frixione, *Merging meets matching in MC@NLO*, JHEP **12** (2012) 061, arXiv: 1209.6215 [hep-ph].

[132] M. Ciccolini, A. Denner, and S. Dittmaier, *Strong and electroweak corrections to the production of Higgs + 2 jets via weak interactions at the LHC*, Phys. Rev. Lett. **99** (2007) 161803, arXiv: 0707.0381 [hep-ph].

[133] M. Ciccolini, A. Denner, and S. Dittmaier, *Electroweak and QCD corrections to Higgs production via vector-boson fusion at the LHC*, Phys. Rev. D **77** (2008) 013002, arXiv: 0710.4749 [hep-ph].

[134] P. Bolzoni, F. Maltoni, S. O. Moch, and M. Zaro, *Higgs production via vector-boson fusion at NNLO in QCD*, Phys. Rev. Lett. **105** (2010) 011801, arXiv: 1003.4451 [hep-ph].

[135] M. L. Ciccolini, S. Dittmaier, and M. Kramer, *Electroweak radiative corrections to associated WH and ZH production at hadron colliders*, Phys. Rev. D **68** (2003) 073003, arXiv: hep-ph/0306234.

[136] O. Brein, A. Djouadi, and R. Harlander, *NNLO QCD corrections to the Higgs-strahlung processes at hadron colliders*, Phys. Lett. B **579** (2004) 149, arXiv: hep-ph/0307206.

[137] O. Brein, R. Harlander, M. Wiesemann, and T. Zirke, *Top-Quark Mediated Effects in Hadronic Higgs-Strahlung*, Eur. Phys. J. C **72** (2012) 1868, arXiv: 1111.0761 [hep-ph].

[138] A. Denner, S. Dittmaier, S. Kallweit, and A. Mück, *HAWK 2.0: A Monte Carlo program for Higgs production in vector-boson fusion and Higgs strahlung at hadron colliders*, Comput. Phys. Commun. **195** (2015) 161, arXiv: 1412.5390 [hep-ph].

[139] O. Brein, R. V. Harlander, and T. J. E. Zirke, *vh@nnlo - Higgs Strahlung at hadron colliders*, Comput. Phys. Commun. **184** (2013) 998, arXiv: 1210.5347 [hep-ph].

[140] L. Altenkamp, S. Dittmaier, R. V. Harlander, H. Rzehak, and T. J. E. Zirke, *Gluon-induced Higgs-strahlung at next-to-leading order QCD*, JHEP **02** (2013) 078, arXiv: 1211.5015 [hep-ph].

[141] R. V. Harlander, A. Kulesza, V. Theeuwes, and T. Zirke, *Soft gluon resummation for gluon-induced Higgs Strahlung*, JHEP **11** (2014) 082, arXiv: 1410.0217 [hep-ph].

[142] E. Bothmann et al., *Event Generation with Sherpa 2.2*, SciPost Phys. **7** (2019) 034, arXiv: 1905.09127 [hep-ph].

[143] NNPDF Collaboration, R.D. Ball et al., *Parton distributions for the LHC Run II*, JHEP **04** (2015) 040, arXiv: 1410.8849 [hep-ph].

[144] T. Gleisberg and S. Höche, *Comix, a new matrix element generator*, JHEP **12** (2008) 039, arXiv: 0808.3674 [hep-ph].

[145] S. Schumann and F. Krauss, *A parton shower algorithm based on Catani-Seymour dipole factorisation*, JHEP **03** (2008) 038, arXiv: 0709.1027 [hep-ph].

[146] F. Buccioni et al., *OpenLoops 2*, Eur. Phys. J. C **79** (2019) 866, arXiv: 1907.13071 [hep-ph].

[147] F. Cascioli, P. Maierhofer, and S. Pozzorini, *Scattering Amplitudes with Open Loops*, Phys. Rev. Lett. **108** (2012) 111601, arXiv: 1111.5206 [hep-ph].

[148] A. Denner, S. Dittmaier, and L. Hofer, *Collier: A fortran-based complex one-loop library in extended regularizations*, Comput. Phys. Commun. **212** (2017) 220, arXiv: 1604.06792 [hep-ph].

[149] S. Hoeche, S. Schumann, and F. Siegert, *Hard photon production and matrix-element parton-shower merging*, Phys. Rev. D **81** (2010) 034026, arXiv: 0912.3501 [hep-ph].

[150] F. Caola, K. Melnikov, R. Röntsch, and L. Tancredi, *QCD corrections to W^+W^- production through gluon fusion*, Phys. Lett. B **754** (2016) 275, arXiv: 1511.08617 [hep-ph].

[151] F. Cascioli et al., *Precise Higgs-background predictions: merging NLO QCD and squared quark-loop corrections to four-lepton + 0,1 jet production*, JHEP **01** (2014) 046, arXiv: 1309.0500 [hep-ph].

[152] M. Beneke, P. Falgari, S. Klein, and C. Schwinn, *Hadronic top-quark pair production with NNLL threshold resummation*, Nucl. Phys. B **855** (2012) 695, arXiv: 1109.1536 [hep-ph].

[153] M. Cacciari, M. Czakon, M. Mangano, A. Mitov, and P. Nason, *Top-pair production at hadron colliders with next-to-next-to-leading logarithmic soft-gluon resummation*, Phys. Lett. B **710** (2012) 612, arXiv: 1111.5869 [hep-ph].

[154] P. Bärnreuther, M. Czakon, and A. Mitov, *Percent-Level-Precision Physics at the Tevatron: Next-to-Next-to-Leading Order QCD Corrections to $q\bar{q} \to t\bar{t} + X$*, Phys. Rev. Lett. **109** (2012) 132001, arXiv: 1204.5201 [hep-ph].

[155] M. Czakon and A. Mitov, *NNLO corrections to top-pair production at hadron colliders: the all-fermionic scattering channels*, JHEP **12** (2012) 054, arXiv: 1207.0236 [hep-ph].

[156] M. Czakon and A. Mitov, *NNLO corrections to top pair production at hadron colliders: the quark-gluon reaction*, JHEP **01** (2013) 080, arXiv: 1210.6832 [hep-ph].

[157] M. Czakon, P. Fiedler, and A. Mitov, *Total Top-Quark Pair-Production Cross Section at Hadron Colliders Through $O(\alpha_S^4)$*, Phys. Rev. Lett. **110** (2013) 252004, arXiv: 1303.6254 [hep-ph].

[158] M. Czakon and A. Mitov, *Top++: A program for the calculation of the top-pair cross-section at hadron colliders*, Comput. Phys. Commun. **185** (2014) 2930, arXiv: 1112.5675 [hep-ph].

[159] N. Kidonakis, *Two-loop soft anomalous dimensions for single top quark associated production with a W^- or H^-*, Phys. Rev. D **82** (2010) 054018, arXiv: 1005.4451 [hep-ph].

[160] N. Kidonakis, "Top Quark Production", *Helmholtz International Summer School on Physics of Heavy Quarks and Hadrons*, 2014, arXiv: 1311.0283 [hep-ph].

[161] C. Anastasiou, L. J. Dixon, K. Melnikov, and F. Petriello, *High precision QCD at hadron colliders: Electroweak gauge boson rapidity distributions at NNLO*, Phys. Rev. D **69** (2004) 094008, arXiv: hep-ph/0312266.

[162] J. Butterworth et al., *PDF4LHC recommendations for LHC Run II*, J. Phys. **G43** (2016), arXiv: 1510.03865 [hep-ph].

[163] ATLAS Collaboration, *Measurement of the Z/γ^* boson transverse momentum distribution in pp collisions at $\sqrt{s} = 7$ TeV with the ATLAS detector*, JHEP **09** (2014) 145, arXiv: 1406.3660 [hep-ex].

[164] ATLAS Collaboration, *ATLAS Pythia 8 tunes to 7 TeV data*, ATL-PHYS-PUB-2014-021, 2014, URL: https://cds.cern.ch/record/1966419.

[165] M. Ciccolini, A. Denner and S. Dittmaier, *Strong and electroweak corrections to the production of Higgs + 2 jets via weak interactions at the LHC*, Phys. Rev. Lett. **99** (2007), arXiv: 0707.0381 [hep-ph].

[166] P. Bolzoni et al., *Higgs production via vector-boson fusion at NNLO in QCD*, Phys. Rev. Lett. **105** (2010), arXiv: 1003.4451 [hep-ph].

[167] A. Djouadi, J. Kalinowski, and M. Spira, *HDECAY: A Program for Higgs boson decays in the standard model and its supersymmetric extension*, Comput. Phys. Commun. **108** (1998) 56, arXiv: hep-ph/9704448.

[168] M. Spira, *QCD effects in Higgs physics*, Fortsch. Phys. **46** (1998) 203, arXiv: hep-ph/9705337.

[169] A. Djouadi, M. M. Muhlleitner, and M. Spira, *Decays of supersymmetric particles: The Program SUSY-HIT (SUspect-SdecaY-Hdecay-InTerface)*, Acta Phys. Polon. B **38** (2007) 635, ed. by K. Fialkowski and B. Muryn, arXiv: hep-ph/0609292.

[170] A. Bredenstein, A. Denner, S. Dittmaier, and M. M. Weber, *Radiative corrections to the semileptonic and hadronic Higgs-boson decays $H \to WW/ZZ \to 4$ fermions*, JHEP **02** (2007) 080, arXiv: hep-ph/0611234.

[171] A. Bredenstein, A. Denner, S. Dittmaier, and M. M. Weber, *Precise predictions for the Higgs-boson decay $H \to WW/ZZ \to 4$ leptons*, Phys. Rev. D **74** (2006) 013004, arXiv: hep-ph/0604011.

[172] A. Bredenstein, A. Denner, S. Dittmaier, and M. M. Weber, *Precision calculations for the Higgs decays $H \to ZZ/WW \to 4$ leptons*, Nucl. Phys. B Proc. Suppl. **160** (2006) 131, ed. by J. Blumlein, S. Moch, and T. Riemann, arXiv: hep-ph/0607060.

[173] G. Aad et al., *Combined Measurement of the Higgs Boson Mass in pp Collisions at $\sqrt{s} = 7$ and 8 TeV with the ATLAS and CMS Experiments*, Physical Review Letters **114** (2015).

[174] M. Czakon et al., *Top-pair production at the LHC through NNLO QCD and NLO EW*, JHEP **186** (2017).

[175] S. Frixione, E. Laenen, P. Motylinski, B. R. Webber, and C. D. White, *Single-top hadroproduction in association with a W boson*, JHEP **07** (2008) 029, arXiv: 0805.3067 [hep-ph].

[176] D. J. Lange, *The EvtGen particle decay simulation package*, Nucl. Instrum. Meth. A **462** (2001) 152.

[177] T. Sjöstrand, S. Mrenna, and P. Skands, *A brief introduction to PYTHIA 8.1*, Comput. Phys. Commun. **178** (2008) 852, arXiv: 0710.3820 [hep-ph].

[178] ATLAS Collaboration, *The Pythia 8 A3 tune description of ATLAS minimum bias and inelastic measurements incorporating the Donnachie–Landshoff diffractive model*, ATL-PHYS-PUB-2016-017, 2016, URL: https://cds.cern.ch/record/2206965.

[179] S. Agostinelli et al., *GEANT4: A Simulation toolkit*, Nucl. Instrum. Meth. A **506** (2003) 250.

[180] ATLAS Collaboration, *The ATLAS Simulation Infrastructure*, Eur. Phys. J. C **70** (2010) 823, arXiv: 1005.4568 [physics.ins-det].

[181] ATLAS Collaboration, *The ATLAS Collaboration Software and Firmware*, ATL-SOFT-PUB-2021-001, 2021, URL: https://cds.cern.ch/record/2767187.

[182] T. Plehn, D. L. Rainwater, and D. Zeppenfeld, *A method for identifying $H \to \tau\tau \to e^{\pm}\mu^{\pm}$ + missing p_T at the CERN LHC*, Phys.Rev. **D61** (2000) 093005, arXiv: hep-ph/9911385 [hep-ph].

[183] C. G. Lester and D. J. Summers, *Measuring masses of semi-invisibly decaying particles pair produced at hadron colliders*, Phys. Lett. **B463** (1999) 99, arXiv: hep-ph/9906349 [hep-ph].

[184] A. J. Barr, B. Gripaios, and C. G. Lester, *Measuring the Higgs boson mass in dileptonic W-boson decays at hadron colliders*, Journal of High Energy Physics **2009** (2009) 072.

[185] A. J. Barr and C. G. Lester, *A review of the mass measurement techniques proposed for the Large Hadron Collider*, Journal of Physics G: Nuclear and Particle Physics **37** (2010) 123001.

[186] CMS Collaboration, *Measurement of the top quark mass in the dileptonic $t\bar{t}$ decay channel using the mass observables $M_{b\ell}$, M_{T2}, and $M_{b\ell\nu}$ in pp collisions at $\sqrt{s} = 8$ TeV*, Phys. Rev. D **96** (2017) 032002, arXiv: 1704.06142 [hep-ex].

[187] ATLAS Collaboration, *Object-based missing transverse momentum significance in the ATLAS Detector*, ATLAS-CONF-2018-038, 2018, URL: https://cds.cern.ch/record/2630948.

[188] CMS Collaboration, *Missing transverse energy performance of the CMS detector*, JINST **6** (2011) P09001, arXiv: 1106.5048 [hep-ex].

[189] F. Chollet et al., *Keras*, https://keras.io, 2015.

[190] *TensorFlow: Large-Scale Machine Learning on Heterogeneous Systems*, Software available from tensorflow.org, 2015, URL: https://www.tensorflow.org/.

[191] ATLAS Collaboration, *Luminosity determination in pp collisions at $\sqrt{s} = 13$ TeV using the ATLAS detector at the LHC*, ATLAS-CONF-2019-021, 2019, URL: https://cds.cern.ch/record/2677054.

[192] G. Avoni et al., *The new LUCID-2 detector for luminosity measurement and monitoring in ATLAS*, JINST **13** (2018) P07017.

[193] M. Grazzini, S. Kallweit, M. Wiesemann, and J. Yeon Yook, *W^+W production at the LHC: NLO QCD corrections to the loop-induced gluon fusion channel*, Physics Letters B **804** (2020) 135399.

[194] ATLAS Collaboration, *Studies on top-quark Monte Carlo modelling for Top2016*, ATL-PHYS-PUB-2016-020, 2016, URL: https://cds.cern.ch/record/2216168.

[195] M. Baak et al., *HistFitter software framework for statistical data analysis*, Eur. Phys. J. **C75** (2015) 153, arXiv: 1410.1280 [hep-ex].

[196] W. Verkerke and D. Kirkby, *The RooFit toolkit for data modeling*, 2003, arXiv: physics/0306116 [physics.data-an].

[197] R. Barlow and C. Beeston, *Fitting using finite Monte Carlo samples*, Computer Physics Communications **77** (1993) 219, URL: https://www.sciencedirect.com/science/article/pii/001046559390005W.

[198] G. Cowan, K. Cranmer, E. Gross, and O. Vitells, *Asymptotic formulae for likelihood-based tests of new physics*, Eur. Phys. J. C **71** (2011) 1554, arXiv: 1007.1727 [physics.data-an], Erratum: Eur. Phys. J. C **73** (2013) 2501.

[199] *Measurements of the Higgs boson production cross section and couplings in the W boson pair decay channel in proton-proton collisions at $\sqrt{s} = 13$ TeV*, (2022), arXiv: 2206.09466 [hep-ex].

[200] ATLAS Collaboration, *Measurements of b-jet tagging efficiency with the ATLAS detector using $t\bar{t}$ events at $\sqrt{s} = 13$ TeV*, JHEP **08** (2018) 089, arXiv: 1805.01845 [hep-ex].

[201] ATLAS Collaboration, *Calibration of the ATLAS b-tagging algorithm in $t\bar{t}$ semileptonic events*, ATLAS-CONF-2018-045, 2018, URL: https://cds.cern.ch/record/2638455.

[202] ATLAS Collaboration, *Calibration of the performance of b-tagging for c and light-flavour jets in the 2012 ATLAS data*, ATLAS-CONF-2014-046, 2014, URL: https://cds.cern.ch/record/1741020.

[203] M.P. Wand and M.C. Jones, *Kernel Smoothing*, Chapman & Hall/CRC Monographs on Statistics & Applied Probability, Taylor & Francis, 1994, URL: https://books.google.ch/books?id=GTOOi5yE008C.

[204] T. Hastie, R. Tibshirani, and J.H. Friedman, *The Elements of Statistical Learning: Data Mining, Inference, and Prediction*, Springer series in Statistics, Springer, 2009, URL: https://books.google.ch/books?id=eBSgoAEACAAJ.

[205] S. Ghosh, *Kernel Smoothing: Principles, Methods and Applications*, Wiley, 2018, URL: https://books.google.ch/books?id=cl06DwAAQBAJ.

[206] R. J. Tibshirani and S. Rosset, *Excess Optimism: How Biased is the Apparent Error of an Estimator Tuned by SURE?*, Journal of the American Statistical Association **114** (2019) 697, URL: https://doi.org/10.1080/01621459.2018.1429276.

Appendices

A

Smoothing of b-jet identification efficiency and mistag rate scale factors

In Section 3.5.5, the identification of b-, c-, and light-flavour jets is performed using a number of algorithms that exploit several properties of b-hadrons. The probability that a b-tagging algorithm correctly identifies a b-jet is called the b-tagging efficiency, ϵ_b. In addition, b-taggers can also mistakenly identify c- or light-flavour jets as a b-jet and this is called the mistag rate. The probability for this to occur is ϵ_c and ϵ_l for c- and light-flavour jets, respectively. These parameters, ϵ_b, ϵ_c, and ϵ_l, quantify the performance of a b-tagging algorithm.

The performance of a b-tagging algorithm is measured in both simulation and data by dedicated analyses using samples of events enriched in either b-, c-, or light-flavour jets [103, 105, 200–202]. Fixed requirements on the output distribution of a b-tagging algorithm define so-called working points (WPs) which result in a particular b-tagging efficiency in simulated top quark pair events. Four single-cut WPs are defined, at 60%, 70%, 77%, and 85% b-tagging efficiency. Simulation-to-data scale factors (SFs) are derived as a function of jet p_{T} for each WP as the ratio of the measured b-jet tagging efficiency in data and simulation. The SFs are applied in physics measurements as a per-jet weight to jets in simulation.

The nominal values and systematic uncertainties of the measured SFs are smoothed as a function of p_{T} with a non-parametric regression technique before they are used in physics measurements, since it is assumed that the b-tagging efficiency is a smoothly varying function of jet kinematics. This is based on the further assumption that inaccuracy in the modelling of the detector response is not discontinuous as a function of the jet kinematics. The output of performing the smoothing of the SFs is a finely binned histogram which are used by physics analyses to correct jets in simulation. The smoothing method implemented in this work is local polynomial kernel regression [203], which is a type of non-parametric regression. This work has been published in Ref. [106] from which

the following description is based on.

A.1 Local polynomial kernel regression

The description of local polynomial kernel regression follows the description in Refs. [203–205]. The goal of the regression is to estimate a function that describes the relationship between the discrete SF measurements and the jet p_{T}, given that there are only n data points $(X_1, Y_1), \ldots, (X_n, Y_n)$, where X_i are the jet p_{T} values and Y_i are the discrete SF measurements with uncertainties. Typically in linear regression, a model is selected and a particular method (e.g. ordinary least squares minimisation) is used to estimate the parameters of the model. For example, if $m(x)$ is the regression function, it should match the conditional expectation at $x = X_i$:

$$m(x = X_i) = \mathbb{E}[Y_i | X_i]. \tag{A.1}$$

Kernel regression aims to estimate the function $m(x)$ at $x = X_i$ without specifying what the function should be. This is done by using a local polynomial approximation of the function $m(x)$ in the region around X_i, for example. The regression function is assumed to be continuous so that a Taylor expansion can be used around $x = X_i$ to find a pth-order polynomial,

$$m(x) = \sum_{j=0}^{p} (x - X_i)^j \beta_j(X_i) + R, \tag{A.2}$$

where R represents higher-order terms and

$$\beta_j(X_i) = \frac{m^{(j)}(x = X_i)}{j!}, \; j = 0, 1, \ldots, p, \tag{A.3}$$

where $m^{(j)}(x)$ is the jth derivative of $m(x)$ at X_i. Equation A.2 defines the statistical model and allows one to empirically find the full functions $\beta_i(x)$, given the set of input points. This can be done by minimising a sum of squares similar to a χ^2 but with interpolations between data points, where the kernel parameter h determines the weight given to nearby data points. The estimate is performed by minimising the weighted sum of squares

$$\sum_{i=1}^{n} K_h(x - X_i)[Y_i - \beta_0(x) - \beta_1(x)(x - X_i) - \cdots - \beta_p(x)(x - X_i)^p]^2, \tag{A.4}$$

where $K_h(x - X_i)$ is the kernel weight function with intrinsic parameter, h, called the bandwidth. The choice of kernel function and bandwidth value are arbitrary choices in kernel smoothing since the smoothness of the estimate of the regression function is defined by the properties of the kernel function. For fixed x, Equation A.4 is minimised with respect to each β. The estimates of each β give estimates of the regression function, $\hat{m}(x)$, and its derivatives, by definition. Although a polynomial of order p is fitted to the data in

the region around X_i, it is only used to evaluate the fit at a single point x. Mathematically, the following notation is defined: $\mathbf{Y} = (Y_1, \ldots, Y_n)^T$ is a vector of responses,

$$\mathbf{X}(x) = \begin{bmatrix} 1 & x - X_1 & \ldots & (x - X_1)^p \\ \vdots & \vdots & \ddots & \vdots \\ 1 & x - X_n & \ldots & (x - X_n)^p \end{bmatrix}, \tag{A.5}$$

which is a matrix of size $n \times (p + 1)$, and $\mathbf{W}(x) = \text{diag}[K_h(x - X_1), \ldots, K_h(x - X_n)]$ is a diagonal weight matrix of size $n \times n$. Additionally, a vector of the regression "coefficients" is defined as

$$\boldsymbol{\beta}(x) = (\beta_0(x), \ldots, \beta_p(x))^T, \tag{A.6}$$

which is implicitly a vector of the jth derivatives of $m(x)$, as in Equation A.3. Equation A.4 is then restated as

$$(\boldsymbol{Y} - \boldsymbol{X}(x)\boldsymbol{\beta}(x))^T \boldsymbol{W}(x)(\boldsymbol{Y} - \boldsymbol{X}(x)\boldsymbol{\beta}(x)). \tag{A.7}$$

Minimising Equation A.7 with respect to $\boldsymbol{\beta}(x)$ for fixed x leads to the solution

$$\hat{\boldsymbol{\beta}}(x) = (\boldsymbol{X}^T(x)\boldsymbol{W}(x)\boldsymbol{X}(x))^{-1}\boldsymbol{X}^T(x)\boldsymbol{W}(x)\boldsymbol{Y} \tag{A.8}$$

where $(\boldsymbol{X}^T(x)\boldsymbol{W}(x)\boldsymbol{X}(x))^{-1}$ is assumed to be invertible. The estimate of the regression function, $\hat{m}(x)$, is the zeroth coefficient, $\hat{\beta}_0(x)$, so

$$\hat{m}(x; p, h) = \boldsymbol{e}_1^T(\boldsymbol{X}^T(x)\boldsymbol{W}(x)\boldsymbol{X}(x))^{-1}\boldsymbol{X}^T(x)\boldsymbol{W}(x)\boldsymbol{Y}, \tag{A.9}$$

where e_1 is a vector of $(p + 1)$ rows with one in the first entry and zero elsewhere. The notation $\hat{m}(x; p, h)$ is to clarify that the estimate of the regression function not only depends on x, but also on the order of the polynomial that is fitted locally and the value of the bandwidth parameter in the kernel function. Equation A.9 shows explicitly that the estimated regression function, $\hat{m}(x; p, h)$, is linear in the vector of the discrete measured SFs for each X_i, $\boldsymbol{Y}$.

A.2 Bandwidth optimisation

The bandwidth, h, is a fundamental parameter of the kernel function that is arbitrarily chosen to adjust the degree to which the discrete measured SFs are smoothed. In this implementation, a first-order polynomial for the Taylor expansion is used, and a Gaussian function is used for the kernel function. The bandwidth in this case corresponds to the width of the Gaussian kernel function. A small value of the bandwidth means the local linear fitting in any p_{T} region is sensitive to data measurements close to it but not to data measurements far from it, resulting in an under-smooth estimate. Conversely, a large value of the bandwidth implies that the data measurements are all weighted equally

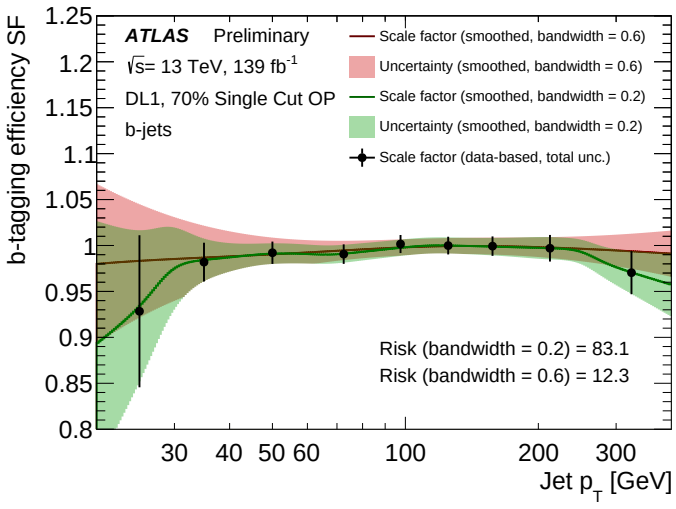

Figure A.1: b-tagging efficiency SFs for b-jets at the 70% WP. The smoothed curves are obtained using bandwidth values of 0.2 and 0.6, whilst the data is shown by the black points. The risk, as defined in Equation A.11, is shown on the figure for both smoothed curves.

[203, 204]. Thus, the choice of bandwidth value implies a particular assumption about the nature of the inaccuracy of the simulation to model the detector and the underlying physics processes. The effect of choosing two distinct bandwidth values is illustrated in Figure A.1, which shows the b-tagging efficiency SF for b-jets at the 70% WP smoothed with bandwidth values of 0.2 and 0.6.

The nominal smoothed value and relative uncertainty are shown in Figures A.2a and A.2b, respectively, for bandwidth values of 0.2, 0.6, and 2.0. In both cases, the difference between each smoothed curve is negligible in the bulk of the p_{T} spectrum, whilst the differences are much larger in the upper and lower extremes of the p_{T} range. The bandwidth is therefore optimised such that large and nonphysical variations are removed from the smoothed result, particularly in the more extreme regions of the p_{T} spectrum.

The number of degrees of freedom in the fit is the number of fitted parameters subtracted from the number of data measurements in ordinary least squares estimation. This is not always the case for non-parametric regression techniques. Generally, a non-parametric smoothing method is linear in the response variable and can be written as

$$\hat{\mathbf{m}}(X_i; h) = \mathbf{S}(X_i; h)\mathbf{Y}, \tag{A.10}$$

where $\hat{\mathbf{m}}(X_i; p, h)$ is a vector of the smoothed predictions at p_{T} values X_i, $\mathbf{Y}$ is a vector of the discrete SF measurements as a function of p_{T}, and $\mathbf{S}(X_i; h)$ is a smoothing matrix which transforms the discrete SF measurements into a smoothed continuous function. The smoothing matrix, $\boldsymbol{S}(X_i; h)$, has rank equal to the number of SF measurement points. By definition, the trace, $\mathrm{tr}(\boldsymbol{S}(X_i; h))$, is the number of basis functions [205], which implies

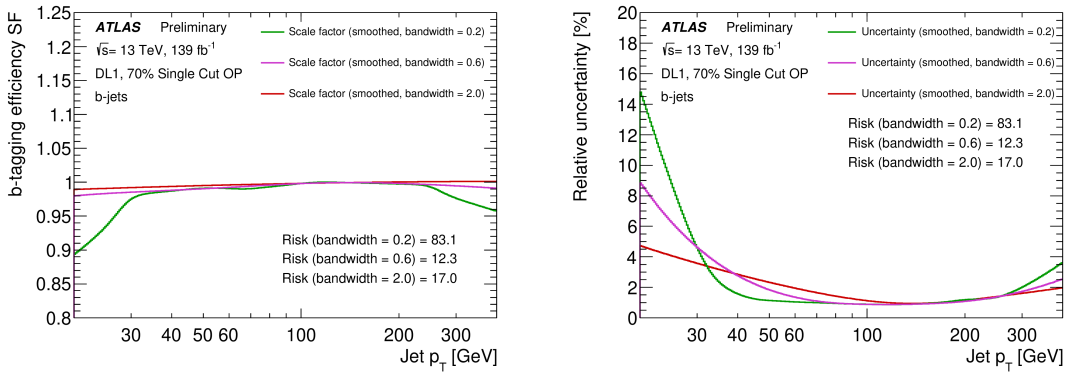

(a) **(b)**

Figure A.2: The nominal smoothed curves obtained with bandwidth values of 0.2, 0.6, and 2.0 are shown in (a). The corresponding relative uncertainties are shown for each smoothed curve in (b). The risk, as defined in Equation A.11, is shown on each figure for the three smoothed curves.

that this quantity gives the number of parameters in the fit.

In order to find an optimal value for the bandwidth, a method is developed based on minimising *Stein's unbiased risk estimator*, hereafter known as the risk [206]. The risk is defined as

$$\widehat{\mathrm{Err}}(h) = \sum_i \mathbb{E}[Y_i - \hat{m}(X_i; h)]^2 + 2\hat{\mathrm{df}}(h), \tag{A.11}$$

where $\mathbb{E}[Y_i - \hat{m}(X_i; p, h)]^2$ is the mean squared error between the data points and the estimate of the regression function at the data points, and $\hat{\mathrm{df}}(h)$ is the estimate of the effective degrees of freedom. The addition of the effective degrees of freedom in Equation A.11 avoids selecting the bandwidth that simply interpolates the SF measurements. Instead, the bandwidth obtained by minimising the risk represents a compromise between minimising the mean squared error and minimising the sensitivity of the fit to data fluctuations.

The effective number of degrees of freedom for a generic smoothing method is

$$\hat{\mathrm{df}}(h) = \mathrm{tr}(\boldsymbol{S}(X_i; h)). \tag{A.12}$$

This formula is valid in the case where the data are statistically uncorrelated, but this is not the case for the b-tagging efficiency SFs. In this case, a sample of events is selected by requiring more than one reconstructed jet per event where these selected jets may be in different jet p_{T} bins. The statistical uncertainty on the b-tagging efficiency measurement in jet p_{T} bin i may then have a nonzero correlation with the measurement in jet p_{T} bin j. In order to determine the effective degrees of freedom correctly taking into account the statistical correlations between b-tagging efficiency measurements in different bins of jet p_{T}, the statistical covariance matrix is reconstructed from the original measurement of the

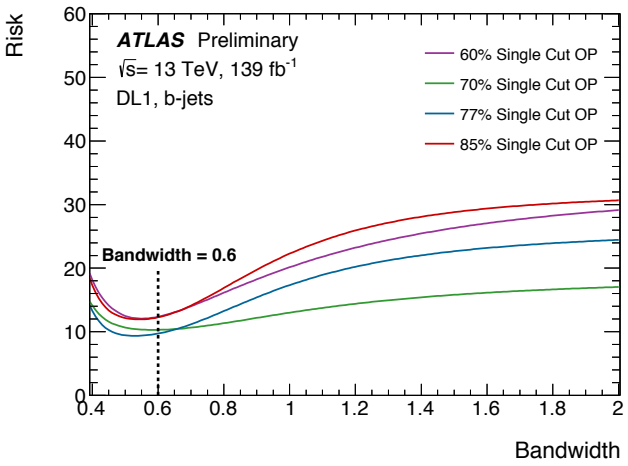

Figure A.3: The risk distribution, as defined in Equation A.11, determined as a function of bandwidth in the range $[0.4, 2.0]$ for the b-jet tagging efficiency scale factor for b-jets at the four WPs. The bandwidth that is selected as optimal is shown by the vertical line at 0.6.

b-tagging efficiencies. The eigenvectors of this matrix are found and are used to translate the smoothing matrix $\boldsymbol{S}$ in Equation A.10 into this basis and the trace is taken.

A.3 Results for b-jets

The risk, as defined in Equation A.11, is calculated as a function of the bandwidth in the range $[0.4, 2.0]$ for the b-jet tagging efficiency scale factor for b-jets at all four WPs. This is shown in Figure A.3. The minima of the risk distributions in Figure A.3 are found to be at bandwidths of 0.55, 0.60, 0.53, and 0.54 for the 60%, 70%, 77%, and 85% WPs, respectively. The optimal bandwidth for b-jet tagging efficiency SFs is defined as the average of the minimum risk values for the four WPs, rounded to the nearest significant digit, resulting in an optimal bandwidth of 0.6. The b-jet tagging efficiency SFs for b-jets, smoothed with a bandwidth of 0.6, are shown in Figure A.4 for each WP. The smoothed results of mistag rates for c- and light-jets are documented in Ref. [106].

The smoothed SF distributions in Figures A.4a–A.4d follow the trend of the data well. The uncertainty on the smoothed distribution ranges from 1–2% in the bulk of the distribution and 5–7% in the lowest p_{T} region, with a maximum discrepancy of approximately one standard deviation difference between the smoothed estimate and the data observed in the first bin. The uncertainty band on the smoothed distribution is derived from the quadrature sum of the smoothed distributions obtained after the nominal result is varied by the value of each systematic uncertainty and smoothed.

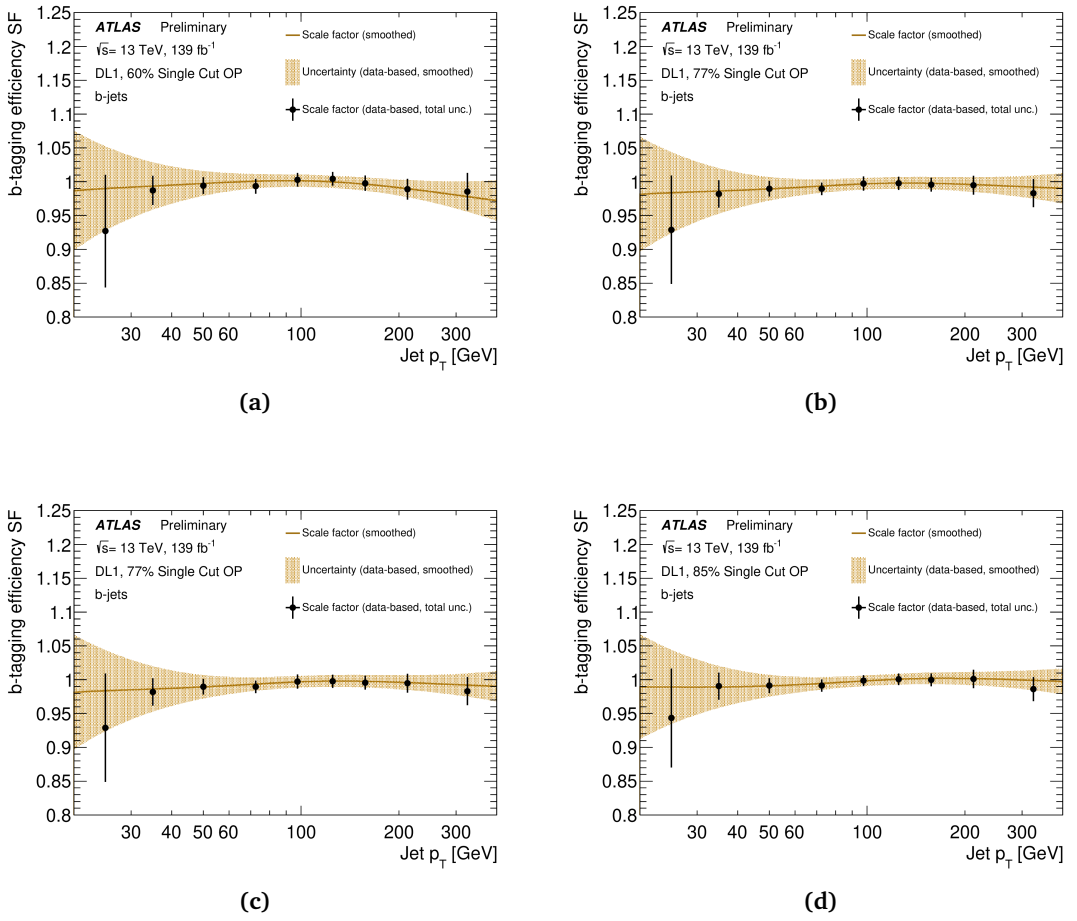

Figure A.4: b-tagging efficiency SFs for b-jets at the (a) 60%, (b) 70%, (c) 77%, and (d) 85% WPs. The binned SFs, and their total uncertainties, are shown by the black data points which are located at the geometric centre of each bin. The smoothed distribution and its uncertainty band are overlaid.

B

Invariant mass reconstruction of a τ-lepton pair

In Section 4.4, the observable $m_{\tau\tau}$ is introduced as the reconstructed invariant mass of a di-τ pair (or hypothetical pair otherwise) in order to suppress background from $Z/\gamma^* \to \tau\tau$ (and $H \to \tau\tau$) events. This appendix outlines the kinematics of these di-τ events and the method that is used to reconstruct the di-τ invariant mass.

The reconstruction is performed using the *collinear approximation* [182]. The method is based on two assumptions. First, that the τ-lepton decay particles are collinear with the τ-lepton direction. This is because the τ-leptons are Lorentz boosted since the Higgs boson mass is larger than the τ mass, and the decay particles are similarly Lorentz boosted. Second, that the only source of $E_{\mathrm{T}}^{\mathrm{miss}}$ in the event is due to the neutrinos from the τ-lepton decay. In practice, mis-measurement of objects invalidates this assumption, and thus the resolution of the reconstructed $m_{\tau\tau}$ is dependent on the resolution of the reconstructed $E_{\mathrm{T}}^{\mathrm{miss}}$.

Given these assumptions, the $\boldsymbol{E}_{\mathrm{T}}^{\mathrm{miss}}$ vector will always lie between the two τ-leptons (as it is the vector sum of the neutrino momenta). This is illustrated in Figure B.1, which shows the collinear approximation. The two neutrino momenta are understood to comprise the vector sum of the momenta of both neutrinos produced in the decay of a single τ-lepton.

Simple kinematic arguments are used to reconstruct the di-τ invariant mass. Starting with conservation of transverse momentum,

$$p_{\mathrm{T}}^{\tau_1} + p_{\mathrm{T}}^{\tau_2} = p_{\mathrm{T}}^{\ell_1} + p_{\mathrm{T}}^{\ell_2} + E_{\mathrm{T}}^{\mathrm{miss}}, \tag{B.1}$$

where $p_{\mathrm{T}}^{\tau_i}$ represents the transverse momentum of the ith τ-lepton, $p_{\mathrm{T}}^{\ell_i}$ represents the transverse momentum of the ith lepton from the τ-lepton decay. Due to the collinearity of all the decay particles, the momenta of the τ-leptons can be replaced with

$$p_{\mathrm{T}}^{\tau_i} = \frac{p_{\mathrm{T}}^{\ell_i}}{x_i}, \tag{B.2}$$

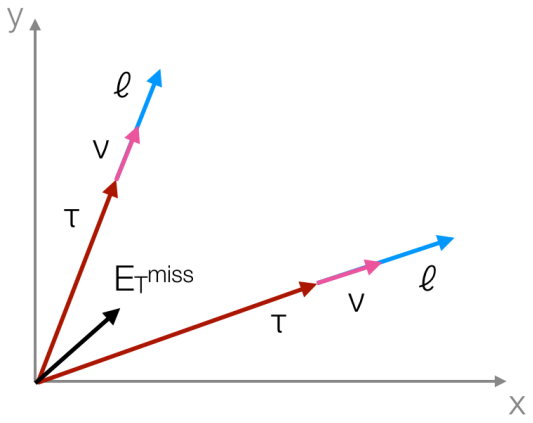

Figure B.1: Illustration of the transverse momentum vectors of two τ-lepton decays and the $\boldsymbol{E}_{\mathrm{T}}^{\mathrm{miss}}$ vector which are used in the collinear approximation.

where x_i represents the fraction of the ith τ-lepton momentum imparted to the lepton, bounded between zero and one. Splitting Equation B.1 into the x- and y- components, solutions for x_1 and x_2 can be found analytically, given by

$$x_1 = \frac{p_{\mathrm{x}}^{\ell_1} \cdot p_{\mathrm{y}}^{\ell_2} - p_{\mathrm{y}}^{\ell_1} \cdot p_{\mathrm{x}}^{\ell_2}}{p_{\mathrm{y}}^{\ell_2} \cdot E_{\mathrm{x}}^{\mathrm{miss}} - p_{\mathrm{x}}^{\ell_2} \cdot E_{\mathrm{y}}^{\mathrm{miss}} + p_{\mathrm{x}}^{\ell_1} \cdot p_{\mathrm{y}}^{\ell_2} - p_{\mathrm{y}}^{\ell_1} \cdot p_{\mathrm{x}}^{\ell_2}} \tag{B.3}$$

$$x_2 = \frac{p_{\mathrm{x}}^{\ell_1} \cdot p_{\mathrm{y}}^{\ell_2} - p_{\mathrm{y}}^{\ell_1} \cdot p_{\mathrm{x}}^{\ell_2}}{p_{\mathrm{x}}^{\ell_1} \cdot E_{\mathrm{y}}^{\mathrm{miss}} - p_{\mathrm{y}}^{\ell_1} \cdot E_{\mathrm{x}}^{\mathrm{miss}} + p_{\mathrm{x}}^{\ell_1} \cdot p_{\mathrm{y}}^{\ell_2} - p_{\mathrm{y}}^{\ell_1} \cdot p_{\mathrm{x}}^{\ell_2}} \tag{B.4}$$

The di-τ invariant mass, $m_{\tau\tau}$, neglecting all lepton masses, is found through:

$$m_{\tau\tau}^2 = (p_{\tau_1} + p_{\tau_2})^2 \approx 2 p_{\tau_1} p_{\tau_2} = 2 \cdot \left(\frac{p_{\ell_1} p_{\ell_2}}{x_1 x_2} \right) \tag{B.5}$$

$$= \frac{m_{\ell\ell}^2}{x_1 x_2}, \tag{B.6}$$

where p_{τ_i} and p_{ℓ_i} are the four-momenta of the ith τ-lepton and decay lepton, respectively, and $m_{\ell\ell}$ is the invariant mass of the lepton pair.

The collinear approximation of $m_{\tau\tau}$ is only applicable when the Higgs boson or Z boson has sufficiently large p_{T}. This can occur when the Higgs boson or Z boson recoils against additional hadronic activity in the event, such as a jet. This ensures the two τ-leptons are not back-to-back, since in this case the approximation breaks down. Additionally, for other backgrounds where the hypothetical di-τ invariant mass is reconstructed, such as top quark or non-resonant WW events, the boost to the top quarks and W bosons will not be sufficient to ensure that the $E_{\mathrm{T}}^{\mathrm{miss}}$ vector lies between the two leptons [182]. In this case, unphysical values of x_1 and x_2 will be found, leading to values of $m_{\tau\tau}$ inconsistent with $H/Z/\gamma^* \to \tau\tau$ decays.